

AD-787 192

THE GENERATION AND RADIATION OF SUPER-
SONIC JET EXHAUST NOISE: A PROGRESS
REPORT ON STUDIES OF JET NOISE GENERATION
AND RADIATION, TURBULENCE STRUCTURE
AND LASER VELOCIMETRY

Harry E. Plumblee, Jr.

Lockheed-Georgia Company

Prepared for:

Air Force Aero Propulsion Laboratory

June 1974

DISTRIBUTED BY:

NTIS

National Technical Information Service
U. S. DEPARTMENT OF COMMERCE
5285 Port Royal Road, Springfield Va. 22151

NOTICE

When Government drawings, specifications, or other data are used for any purpose other than in connection with a definitely related Government procurement operation, the United States Government thereby incurs no responsibility nor any obligation whatsoever; and the fact that the government may have formulated, furnished, or in any way supplied the said drawings, specifications, or other data, is not to be regarded by implication or otherwise as in any manner licensing the holder or any other person or corporation, or conveying any rights or permission to manufacture, use, or sell any patented invention that may in any way be related thereto.

ACCESSION for	
NTIS	White Section <input checked="" type="checkbox"/>
DIC	Ref. Section <input type="checkbox"/>
UNR. QUINCE	<input type="checkbox"/>
JUSTIFICATION	
BY	
DISTRIBUTION/AVAILABILITY CODES	
Dist. AVAIL. AND/OR SPECIAL	

Copies of this report should not be returned unless return is required by security considerations, contractual obligations, or notice on a specific document.

Unclassified
Security Classification

AD 787 192

DOCUMENT CONTROL DATA - R & D		
<i>(Security classification of title, body of abstract and indexing annotation must be entered when the overall report is classified)</i>		
1. ORIGINATING ACTIVITY (Corporate author)		2a. REPORT SECURITY CLASSIFICATION
Lockheed-Georgia Company Marietta, Georgia		Unclassified
		2b. GROUP
3. REPORT TITLE		
The Generation and Radiation of Supersonic Jet Noise: A Progress Report on Studies of Jet Noise Generation and Radiation, Turbulence Structure and Laser Velocimetry		
4. DESCRIPTIVE NOTES (Type of report and inclusive dates)		
Interim Report (November 1972 through February 1974)		
5. AUTHOR(S) (First name, middle initial, last name)		
Harry E. Plumblee, Jr.		
6. REPORT DATE	7a. TOTAL NO. OF PAGES	7b. NO. OF REFS
June 1974	190	148
8a. CONTRACT OR GRANT NO.	9a. ORIGINATOR'S REPORT NUMBER(S)	
F33615-73-C-2032	LG74ER0010	
b. PROJECT NO.	9b. OTHER REPORT NO(S) (Any other numbers that may be assigned this report)	
c. Task 14	AFAPL-TR-74-24	
d. Work Unit 08		
10. DISTRIBUTION STATEMENT		
Approved for Public Release; Distribution Unlimited.		
11. SUPPLEMENTARY NOTES	12. SPONSORING MILITARY ACTIVITY	
	Air Force Aero Propulsion Laboratory Wright-Patterson AFB, Ohio	
13. ABSTRACT		
<p>This progress report summarizes the major theoretical and experimental efforts performed during the first year of a two-year program sponsored by the Air Force and the Department of Transportation on the Generation and Radiation of Supersonic Jet Noise. Specific technical results are presented in the following areas:</p> <p>(1) the radiation of sound sources in a jet shear layer, as described by Lilley's theory of jet noise generation, (2) a theoretical study of the large scale noise producing structure of jets, (3) the design, construction and calibration of a high temperature anechoic facility for jet noise experiments, (4) a series of high temperature subsonic and supersonic jet noise experiments and the analysis of data from these experiments and (5) the design and development of a laser velocimeter for the measurement of mean flow velocity and orthogonal components of turbulence velocity with turbulence spectra, intensity, and correlations as standard outputs.</p>		

Reproduced by
NATIONAL TECHNICAL
INFORMATION SERVICE
U S Department of Commerce
Springfield VA 22151

DD FORM 1 NOV 65 1473

Unclassified
Security Classification

190

14.	KEY WORDS	LINK A		LINK B		LINK C	
		ROLE	WT	ROLE	WT	ROLE	WT
	1. Acoustics						
	2. Turbulence						
	3. Jet Noise						
	4. Laser Doppler Velocimetry						
	5. Supersonic Jets						

FOREWORD

This annual progress report was prepared by the Lockheed-Georgia Company, Marietta, Georgia, for the Air Force Aero Propulsion Laboratory, Wright-Patterson Air Force Base under Contract F33615-73-C-2032. The report covers work done in the period 6 November 1972 through 1 February 1974. The contract extends through 6 February 1975. The work described herein is part of the Air Force Aero Propulsion Laboratory's joint program with the Department of Transportation to define and control the noise emission of aircraft propulsion systems.

Mr. Paul Shahady of the Air Force Aero Propulsion Laboratory was the Project Engineer. The program is being conducted under Project 3066, Task 14.

Lockheed's Program Manager was Harry E. Plumblee, Jr.

Major contributors to the work presented in this report are: Robert H. Burrin, Peter D. Dean, Philip E. Doak, Michael J. Fisher, Sham S. Kapur, Geoffrey M. Lilley, William T. Mayo, Donald M. Meadows, Philip J. Morris, David M. Smith, H. K. "Bob" Tanna, Brian J. Tester, and M. Clay Whiffen.

The assistance of the following individuals is gratefully acknowledged: L. V. Mазzarella, who operated the test facilities and data acquisition facilities; R. E. Singleton, who prepared the mean flow velocity analysis and computer program and who initially worked on the compressible 2-D turbulence program; C. R. Huie, who helped in the buildup and operation of the laser velocimeter; J. H. Ivester and E. C. Mills, who designed the laser velocimeter processor electronics; H. G. Henderson, who developed the special disc controller for the data acquisition system; W. R. Powell, who did the electronics drafting; R. B. Harrison, J. C. Bailey and P. Aderholt, who constructed the new acoustic facilities; S. Y. Ruo, who participated in early portions of the acoustic analysis; J. P. McKenna, who kept up with the budget and other administrative details, and last, but certainly not least, most gracious appreciation is extended to Barbara C. Reagan, who did such a beautiful job of typing for all the manuscripts.

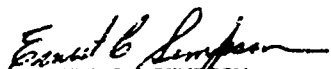
Gratitude is expressed to the University of Southampton for permitting Professor Philip E. Doak, Professor Geoffrey M. Lilley and Dr. Michael J. Fisher to participate in the performance of the research reported herein.

This report was submitted on 20 February 1974.

Publication of this report does not constitute Air Force approval of the report's findings or conclusions. It is published only for the exchange and stimulation of ideas.


PAUL A. SHAHADY
Project Engineer

FOR THE COMMANDER


ERNEST C. SIMPSON
Director, Turbine Engine Division

ABSTRACT

This is a mid-contract progress report of results on a two-year research program on supersonic jet noise generation and radiation. Specific topics covered are (i) the radiation of sound from sources in a jet shear layer, as described by Lilley's theory of jet noise generation, (ii) a theoretical study of the large-scale noise producing structure of jets, (iii) the design, construction and calibration of a high temperature anechoic facility for jet noise experiments, (iv) a series of high temperature subsonic and supersonic jet noise experiments and the analysis of data from these experiments, and (v) the design and development of a laser velocimeter for the measurement of mean flow velocity and orthogonal components of turbulence velocity with turbulence spectra, intensity and correlations as standard outputs.

TABLE OF CONTENTS

	<u>Page</u>
1. INTRODUCTION	1
2. PROGRAM OBJECTIVES	3
3. SUMMARY OF ACHIEVEMENTS	5
3.1 Jet Noise Theory	6
3.2 Turbulence/Source Function Theory	10
3.3 Acoustic Facilities	16
3.4 Jet Noise Experiments	20
3.5 Laser Velocimeter Design and Qualification	24
4. CONCLUSIONS	28
5. REFERENCES	30
APPENDICES	
I THEORETICAL STUDIES OF JET NOISE GENERATION AND RADIATION AND TURBULENCE/SOURCE FUNCTION BEHAVIOR	31
I-1 Critique of Acoustic and Source Models for the Generation of Noise by Turbulence	33
I-2 On the Theory of Jet Noise and Its Applications	37
I-3 On the Respective Roles of Helmholtz-Type Instabilities and Acoustic Propagation in Jet Noise Generation and Radiation	52
I-4 On Sound Radiation from Sources in Parallel Sheared Jet Flows	59
I-5 A Model for the Structure of Jet Turbulence as a Source of Noise	88
I-6 A Model for the Orderly Structure of Turbulence in a Two-Dimensional Shear Layer	107
I-7 The Momentum Potential Field Description of Fluctuating Fluid Motion as a Basis for a Unified Theory of Internally Generated Sound	115

TABLE OF CONTENTS (Con'td)

	<u>Page</u>
II A NEW ANECHOIC FACILITY FOR SUPERSONIC HOT JET NOISE RESEARCH AT LOCKHEED-GEORGIA	123
III EFFECT OF TEMPERATURE ON SUPERSONIC JET NOISE	143
IV LASER VELOCIMETER FOR SUPERSONIC JET TURBULENCE AND TURBULENCE SPECTRA RESEARCH	161

LIST OF FIGURES

<u>Figure No.</u>	<u>Title</u>	<u>Page</u>
1	Comparison of Plug Flow "Constant Particle Velocity Source" Directivities with MacGregor's ⁽¹⁴⁾ Measurements ($V_j/a_0 = 0.9$)	7
2	Variation of SPL_0 with Radial Position of Source: $M_R = 0.0$, $n = 0$	7
3	Variation of SPL_0 with Radial Position of Source: $M_R = 1.0$, $n = 0$	7
4	Variation of SPL_0 with Frequency: $n = 0$	9
5	Variation of SPL_1 with Frequency: $n = 1$	9
6	Measured Difference Spectra: $M_R = 1.0$	9
7	Theoretical Difference Spectra	9
8	Radial Distributions Axial Velocity Fluctuations and Shear Stress Parameter in the Developed Region of the Jet	11
9	Most Amplifying Frequencies for $n = 0$ and $n = 1$ Modes as a Function of Momentum Thickness	11
10	Effect of Initial Energy Amplitude on Jet Center-Line Velocity Decay	13
11	Effect of Single Mode Number on Jet Center-Line Velocity	13
12	Energy Density as a Function of Axial Location	13
13	Integrated Fluctuation Energy Flux for Single Frequency Components as a Function of Axial Location, $n = 1$	13
14	Curves of Amplification Rate Against Frequency for Two-Dimensional Compressible Shear Layer	15
15	Radial Distributions of $ \tilde{u} ^2$, $ \tilde{v} ^2$ and $\tilde{u}\tilde{v}$ for Two-Dimensional Compressible Shear Layer	15

LIST OF FIGURES (Cont'd)

<u>Figure No.</u>	<u>Title</u>	<u>Page</u>
16	Most Amplifying Frequencies as a Function of Axial Distance for Two-Dimensional Compressible Shear Layer	15
17	Plan View Schematic of the New Facility for Supersonic Hot Jet Noise Research	17
18	Completed Anechoic Room Viewed from Entrance Door	17
19	Results of Inverse-Square Law Tests with Point Sound Source	19
20	Results of Inverse-Square Law Tests with Cold Jet: $D = 2$ in., $V_j/a_0 = 0.85$, $\theta = 90^\circ$	19
21	Background/Instrumentation Noise and Cold Jet Noise Spectra at $\theta = 90^\circ$	19
22	Turbulent Mixing Noise and Internal Noise Spectra at $\theta = 45^\circ$, Cold and Hot	19
23	Experimental Program Chart	21
24	Master Spectra for Reynolds Shear Stress Noise and Temperature Fluctuation Noise	23
25	Laser System Block Diagram	25
26	LDV Test Configuration	25
27	Beam Splitter Assembly	25
28	Jet Turbulence - Comparison Between Laser Velocimeter and Hot-Wire Spectra	27
29	Processor Spectrum for 1 kHz FM Square Wave Excitation	27
30	Cross Spectral Density - Synthetic Data Compared with Theoretical Filter Frequency Response	27

I. INTRODUCTION

After the initial commercial development of the jet engine, it was obvious to anyone with perceptive ears that something had to be done about jet noise. This problem, of course, was observed by researchers throughout the world and after a very short time Lighthill produced his famous theory, Hubbard and Lassiter measured the noise of model jets which on the whole compared quite well with the Lighthill theory and Lilley and Westley discovered a series of jet noise suppression devices which produced substantial noise reduction and which were put into use by many of the commercial aircraft manufacturers throughout the world. Then, with great finesse, engine manufacturers developed the by-pass fan engine which further reduced jet noise and the cycle was complete. There was no further need for jet noise research since the problem had apparently been solved by elimination of the source.

However, as everyone knows, this was not the end of the problem. The world had been told from the early 1950's through the mid-60's that the noise of military jet fighters, transports and bombers should be ignored to the extent possible as that was the "sound of freedom". But stricter controls on noise of aircraft by governments throughout the world, development of even more powerful military jet engines and development of supersonic jet aircraft which could not use fanjet engines, by the United Kingdom, France, the USSR and the USA, put the problem of understanding and minimization of jet noise into even clearer focus - jet noise must be reduced.

Research on jet noise had not, of course, been completely halted as insinuated above. There were many hundreds of papers published, in the decade beginning in 1960, on all aspects of the problem. Lighthill continued to work in the field, at least until 1961 when he produced his Bakerian Lecture, and Ribner and his group did much to further understanding of the problem throughout the 1960's. In fact, the individual and group efforts produced many competing ideas on how jet noise and attendant noise problems were generated.

But in 1970, with the scheduled development of the B-1 bomber and the U. S. supersonic transport, the U. S. Air Force and the U. S. Department of Transportation decided that something other than fragmented research efforts on jet noise was required if clearer understanding of and substantial reduction of jet noise were to be achieved. As a result, a major program of jet noise research was initiated. The program was multi-phase, with three separate awards contracted for the Phase I program definition and team qualification efforts. At the end of one year of study, which resulted in a reasonably clear definition of the work necessary for an adequate theoretical and experimental understanding of how jet noise is generated and how it radiates (the Lockheed work is given in References 1 through 6), two contractors, Lockheed-Georgia and General Electric, were selected to implement their proposed programs of jet noise research.

The Lockheed program is a very fundamental theoretical and experimental study of jet noise generation and its subsequent radiation from the jet flow region. The emphasis on fundamentals has been consistently stressed throughout the study phase and the current program. The program is three phase, with concentration being on (i) development of a clearer theoretical understanding and description of the jet noise generation and radiation process, (ii) the measurement of data necessary for qualification of theoretical models and predictions, and (iii) development of the necessary instrumentation technology and operational instrumentation for the measurement of the requisite experimental data.

In what follows, a progress report is given for the first year's accomplishments. The program has been very intense and many results have been generated. A complete presentation of all the work conducted would be very lengthy and difficult to follow. Therefore, the most significant results, in several areas, have been distilled into technical papers and are presented in an extended appendix to this report. The highlights of these results are repeated in the body of this document. In addition, to qualify and clarify the overall direction of the program, the program objectives are outlined.

2. PROGRAM OBJECTIVES

The overall program objectives and specific technical objectives can be stated by a direct quote from the contract statement of work. It

The overall objective of this program is to develop the technology to significantly reduce supersonic aircraft propulsion noise with minimum associated performance and weight penalties. Emphasis is placed on afterburning and non-afterburning supersonic jet exhaust systems with operating conditions typical of supersonic transport (SST) and long range strategic (B-1) aircraft propulsion systems. The specific technical objectives of this program are to numerically solve the applicable turbulence and acoustic theories which describe jet noise generation and radiation for the subsonic and fully-expanded supersonic flow regime and to measure the necessary turbulence and acoustic parameters in order to verify the numerical predictions or to supply data for turbulence/noise theories, as necessary.

At the completion of the program definition phase, there were several specific program objectives determined as necessary for Lockheed's jet noise research program to meet the overall program objectives. These were:

- (1) the study of solutions to and limitations of and development of extensions to Lilley's theory of jet noise generation; this study would consist of (a) the further development of a deterministic large-scale model of turbulence as a source of jet noise, and (b) the study of numerical solutions to Lilley's theory for assumed jet noise source distributions and (c) the study of numerical solutions to Lilley's theory for jet noise source distributions computed from the deterministic turbulence model;
- (2) the development of and qualification of anechoic facilities suitable for measurement of far-field high-temperature supersonic jet noise without significant interference with the noise generation and radiation process.
- (3) the performance and analysis of data from jet noise and turbulence experiments necessary for validation of the theoretical models and predictions; in addition, these experiments are to provide the basis for new theoretical models as required; and
- (4) the development of optical instrumentation for providing the necessary turbulence data, in this case a laser velocimeter for the measurement of turbulence velocity intensity, scale, spectra and convection speeds, as well as mean flow velocity. In addition, the instrument must provide cross-spectra and

cross-correlation information from orthogonal turbulence components at a point.

The following section describes the progress toward meeting these objectives.

3. SUMMARY OF ACHIEVEMENTS

During the first half of this research program on supersonic jet noise generation and radiation, major steps were made toward the achievement of the stated program goals. In addition, no major problems were encountered in the work to date. Advances were made in all areas of research. Some of these are:

- o numerical solutions to Lilley's equation for a number of idealized source types and distributions have been completed and reasonable agreement with experiment is seen;
- o development of the incompressible axisymmetric jet turbulence/source function model and the computer program has been completed;
- o modifications to an existing facility to permit the measurement of far-field jet noise from high temperature supersonic jets in an anechoic free-field environment have been completed, and facility calibrations have been completed which conclusively prove that no problems exist which will contaminate the measured jet noise data;
- o a measurement program of the noise from high temperature supersonic jets has been completed, resulting in a new prediction model for noise from heated jets; and
- o one channel of the laser Doppler velocimeter has been completed and verified and it permits the measurement of all turbulence velocity quantities up to 20 kHz; this is one of the most significant achievements to date in the entire program; in addition, the two-channel LV optical system was completed and successful operation was verified.

A brief summary of major accomplishments during the past year, in each area of research is given in the following discussion. More complete details can be found in the appropriate appendix.

3.1 JET NOISE THEORY

A special form of Lilley's equation has been solved numerically to obtain the far-field directivity of acoustic radiation from a point source located within a parallel sheared jet flow; the results are in fair agreement with measurements.

Sound generated by velocity fluctuations in a turbulent jet interacts with the mean flow field along its propagation path through the jet. Lilley's equation describes explicitly both the sound-mean flow interaction effects, on a linear basis, and the sound generation which, in a parallel jet flow model, is represented by a quadratic function of the turbulent velocity fluctuations.

A special form of Lilley's equation has been solved numerically for an isothermal, parallel, sheared jet flow field to obtain the far-field directivity of acoustic radiation from a stationary point source located within the jet. The point source solutions can be checked by experiment, since it is not difficult to create a stationary point source in practice and these solutions can be used to construct a general solution for any source distribution.

Examples of point source radiation directivities are shown in Figure 1 for four frequencies; the radiation level exhibits a peak somewhere between 60° and 40° to the jet axis, depending on frequency, and thereafter decreases almost linearly with angle. The measured directivities, shown in the same figure, do not exhibit a peak but the calculated results are otherwise in fair agreement, particularly at the higher frequencies for angles shown outside the jet flow (that is, greater than 10°). The major discrepancy may be connected with our over-simplified parallel jet flow model since a peak does not appear in the theoretical directivity patterns obtained with diverging jet flow models; this aspect will be considered in future work.

The influence of sound mean flow interactions on the axisymmetric radiation level of a particular angle as a function of the radial position of the source and frequency ($f_1 - f_5$) is illustrated by Figure 2 (zero flow) and Figure 3 (jet Mach No. = 1, velocity profile is shown). In the absence of flow at low frequencies (f_1, f_2) the radiation level is independent of the source position but at Mach 1 the radiation level is increased by up to 40 dB. At the highest frequency the zero flow sensitivity is replaced by a large reduction in radiation level if the source is well inside the jet flow. The level increases linearly with source distance from the center-line but if we assume that the most significant sources are located near the lip-line ($r'/r_0 = 1$) then it can be seen that there is a smooth reduction in radiation level with increasing frequency, which is consistent with experimental observation at small angles to the jet axis.

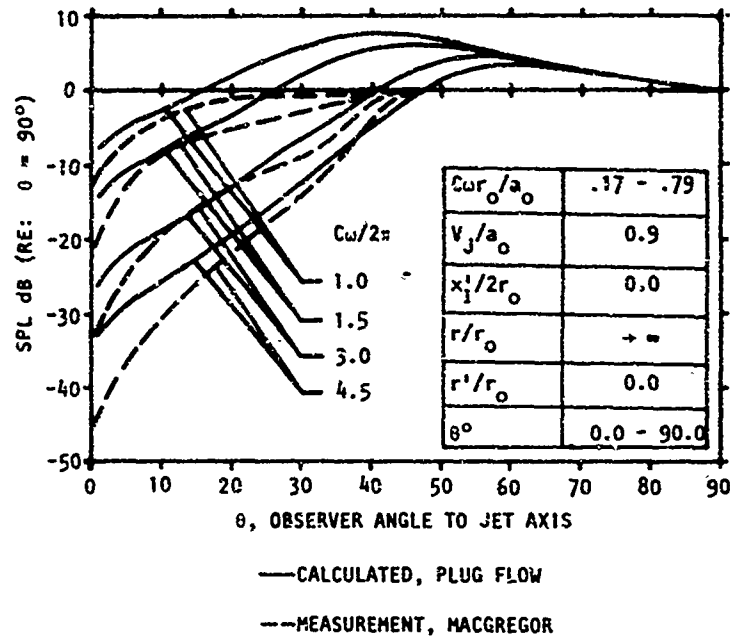


Fig. 1 Comparison of Plug Flow "Constant Particle Velocity Source" Directivities with MacGregor's (14) Measurements ($V_j/a_0 = 0.9$)

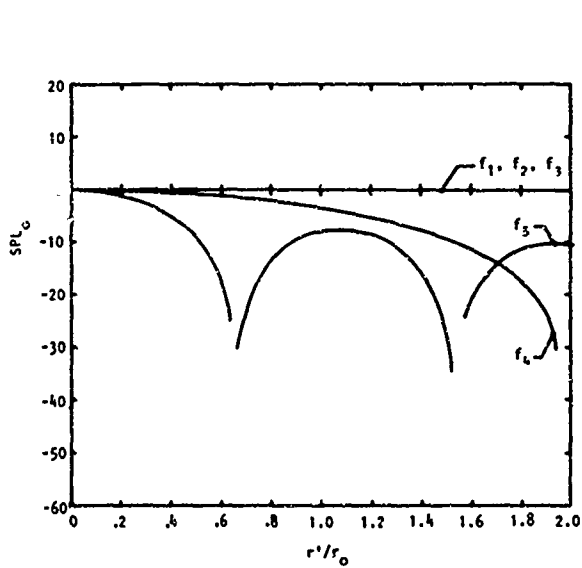


Fig. 2 Variation of SPL_0 with Radial Position of Source: $M_R = 0.0$, $n = 0$

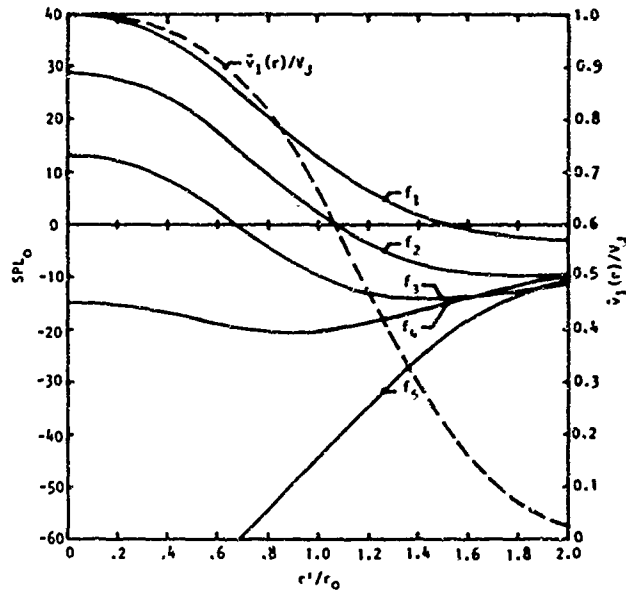


Fig. 3 Variation of SPL_0 with Radial Position of Source: $M_R = 1.0$, $n = 0$

Difference spectra solutions to Lilley's equation for a simplified version of the standard turbulence space-time covariance function are in good qualitative agreement with measurements.

The frequency dependence of non-axisymmetric radiation from a circular jet is different from that of the axisymmetric radiation in the absence of sound-mean flow interaction effects. To illustrate their influence we consider the case when the point source is on the lip-line of a Mach 1 jet; the variation of radiation level with frequency for five particular angles is shown in Figure 4 for axisymmetric radiation and in Figure 5 for the first non-axisymmetric mode. In the first figure there is a moderate low frequency "lift", which is negligible near 90° and a smooth reduction or attenuation at all angles as the frequency is increased. In Figure 5, the low frequency behavior is completely different: the non-axisymmetric radiation is well below that due to the axisymmetric radiation, as in the zero flow case (not shown). At higher frequencies sound-mean flow interactions produce the same effect; that is, a reduction in radiation levels with largest reductions at small angles. In principle all the non-axisymmetric modes contribute to the acoustic radiation from a turbulent jet.

In our first attempt at predicting the difference between measured radiation levels and the classical, theoretical, jet noise directivity pattern, as, for example, shown in Figure 6, we have assumed that the source function correlation length in the circumferential direction is small such that all the modes have equal excitation. The radiation is equal to a simulation of contributions from a finite number (but sufficiently large to ensure convergence) of modes to give the theoretical difference spectra shown in Figure 7 (for comparison with Figure 6). Now that all the significant modes have been taken into account, the theoretical difference spectra at large angles are nearly constant, while at smaller angles and at high frequencies the reduction or attenuation with increasing frequency remains. Both trends exist in the measured difference spectra but at low frequencies the general behavior is not reproduced in these theoretical results. This may be due to real source location effects not yet taken account and other crude assumptions on which this preliminary model is based rather than on any inherent limitations of Lilley's equation.

Detailed analysis and further results are given in Appendix I.

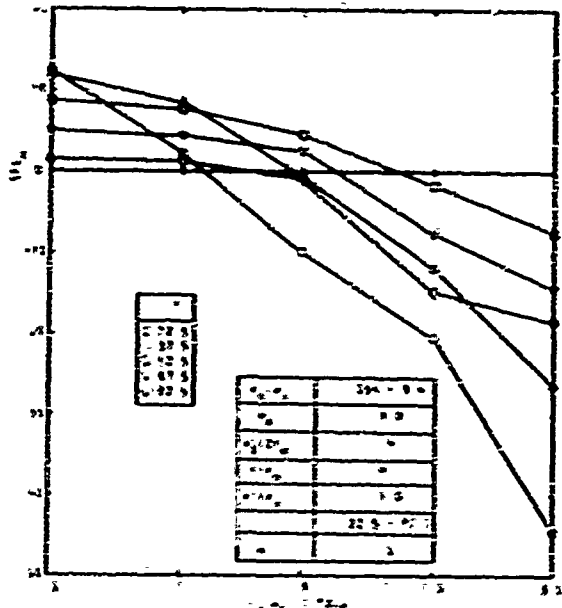


Fig. 4 Variation of SPL_0 with Frequency: $n = 0$

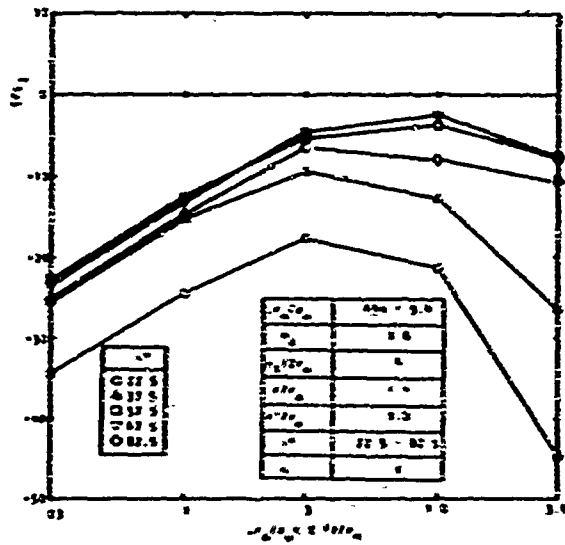


Fig. 5 Variation of SPL_1 with Frequency: $n = 1$

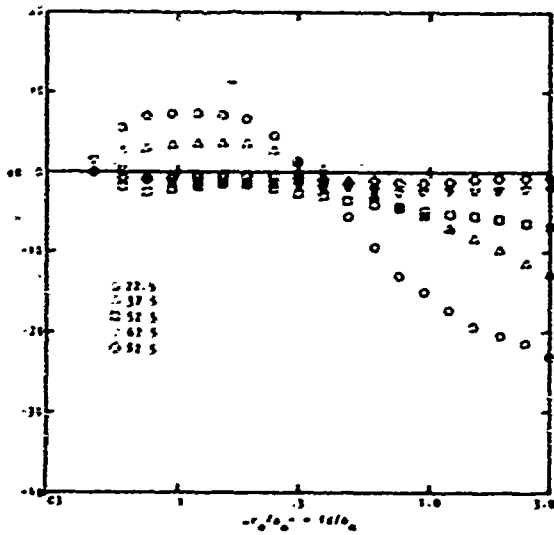


Fig. 6 Measured Difference Spectra: $M_R = 1.0$

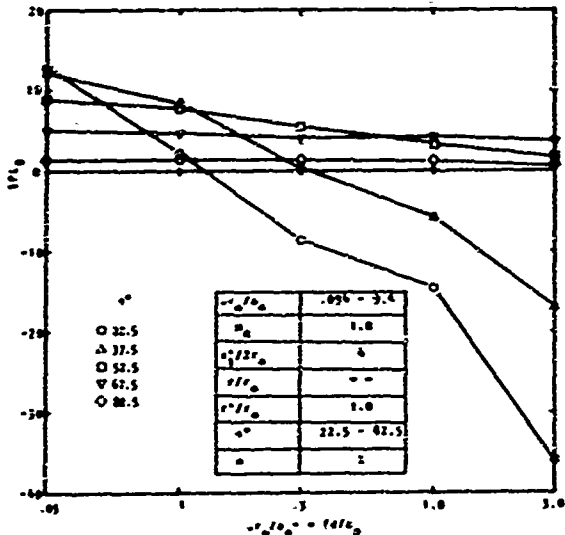


Fig. 7 Theoretical Difference Spectra

3.2 TURBULENCE/SOURCE FUNCTION THEORY

The large-scale noise producing structure of an axisymmetric incompressible jet is described in terms of the locally least stable mode of the primary jet flow.

The aim of this work has been to describe the large-scale noise producing structure of a turbulent jet. Recently, considerable evidence has been made available which indicates that the noise generated by a turbulent jet is closely related to a large-scale organized motion which results from instabilities of the primary flow. Experiments have demonstrated that the scale of these large eddy structures is much larger than that of the energy-containing eddies.

The velocity and pressure in the jet are separated into three components; the first is the time averaged component, the second a time-dependent organized fluctuation, and the third the background disorganized turbulence. The effect of the background turbulence is represented by an eddy viscosity.

The equations for the organized motion are Fourier decomposed and linearized and the mean flow is assumed to be locally parallel. The fluctuations are seen to locally satisfy the homogeneous stability equations. Thus, the organized motion is described by the spatially unstable modes which are eigensolutions to the stability equations. By analogy with stability theory it is plausible to assume that the structure of the jet is locally dominated by the most preferred mode or the most highly amplifying fluctuation at the location. The radial distributions of axial velocity fluctuations and shear stress parameter for the most unstable helical mode in the developed region of the jet are shown in Figure 8. The most amplifying frequency is a function of the local jet momentum thickness; this relationship is shown in Figure 9 for the axisymmetric and helical modes, $n = 0$ and $n = 1$. The higher frequencies are seen to dominate for small jet thicknesses and the low frequencies dominate in the developed jet region, where the jet thickness is large. At the end of the potential core, $b^* = .4128$, the Strouhal frequency of the dominant modes lies between .3 and .4. In the potential core region the dominant frequency is approximately inversely proportional to the local jet width and in the developed jet the frequency is proportional to \bar{u}_c^*/b^* . From the momentum equation \bar{u}_c^* is inversely proportional to the jet width b^* and so in the developed jet the dominant frequency is inversely proportional to the square of the jet width. These relationships agree well with those used by Ribner⁽⁷⁾ where the radian Strouhal frequency is between .3 and .4 at the end of the potential core and is inversely proportional to L in the annular mixing region and inversely proportional to L^2 in the developed jet where L is a characteristic length of a slice of the jet.

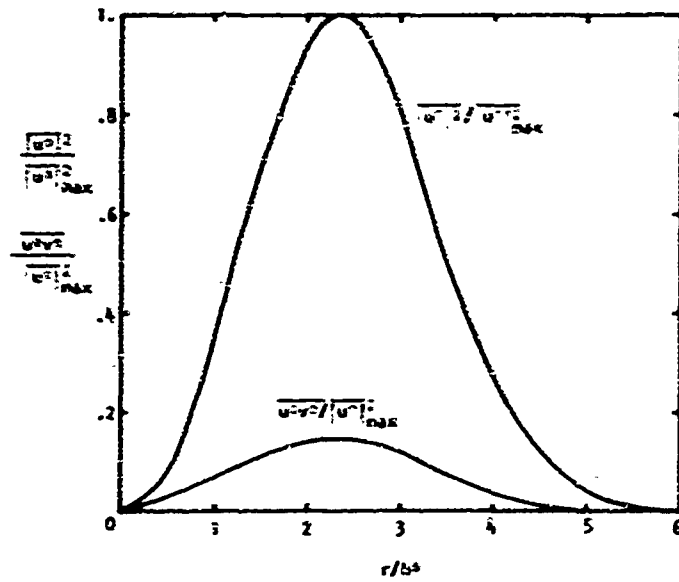


Fig. 8 Radial Distributions Axial Velocity Fluctuations and Shear Stress Parameter in the Developed Region of the Jet

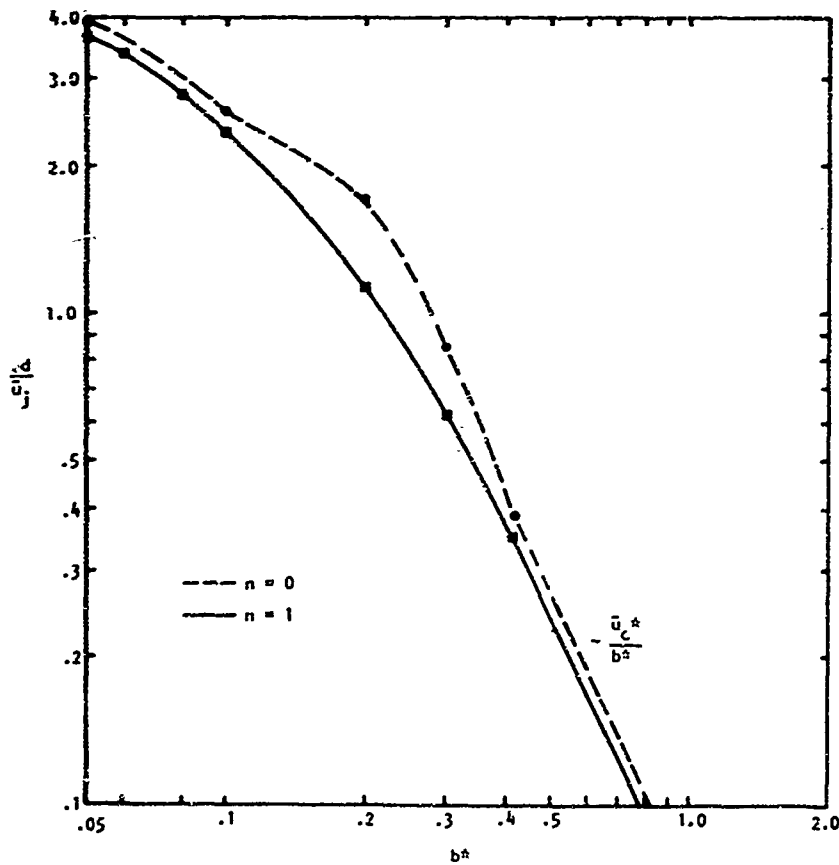


Fig. 9 Most Amplifying Frequencies for $n = 0$ and $n = 1$ Modes as a Function of Momentum Thickness

The downstream development of the mean flow, and growth in energy amplitude of the organized motion, are found by solutions to integral forms of the momentum and energy equations, in which the fluctuations are described locally by a sum of the least stable modes for each azimuthal mode number.

With the fluctuations described locally as a sum of the least stable modes for each azimuthal mode number, the downstream growth of the mean flow dimensions, jet center-line velocity decay, and turbulent energy may be calculated. The development of the mean flow is affected by the initial amplitude of the fluctuations though the maximum amplitude of the fluctuations varies only slightly for large changes in the initial conditions. The jet center-line velocity decay for equal initial fluctuation energy amplitudes of the axisymmetric and helical modes is shown in Figure 10. The center-line velocity decay is shown in Figure 11, where only a single azimuthal mode number is considered. The axisymmetric mode alone does not lead to sufficient energy loss by the mean flow whereas the helical, $n = 1$, mode leads to too large a decay in the jet center-line velocity. The center-line velocity decay computed by a well tested mean flow program is shown as the continuous line in the previous two figures.

A good indication of the amplitude of the velocity and pressure fluctuations is given by the integrated energy density flux. The downstream growth and decay of the energy density is shown in Figure 12. The amplitudes of the two azimuthal modes are almost equal in the annular mixing region of the jet but the helical mode dominates the developed region of the jet.

The downstream growth and decay of single frequency components is found by determining the local amplitude rate as a function of downstream distance, with the scale of the mean flow predetermined by the most amplifying mode analysis discussed above. The axial behavior of a number of different frequency components for the $n = 1$ mode, for a given equal initial amplitude, is shown in Figure 13. The higher frequency components grow very rapidly to a peak close to the jet exit before decaying at a similar rate, whereas the lower frequency components peak further downstream. The relative magnitudes of these frequency components may be determined since the magnitude of each component is known at the axial location where that frequency was most amplifying.

Further results and detailed analysis can be found in Appendix 1.5.

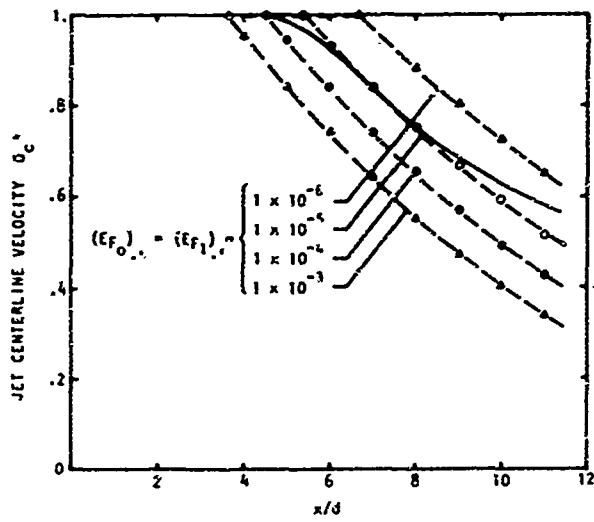


Fig. 10 Effect of Initial Energy Amplitude on Jet Center-Line Velocity Decay

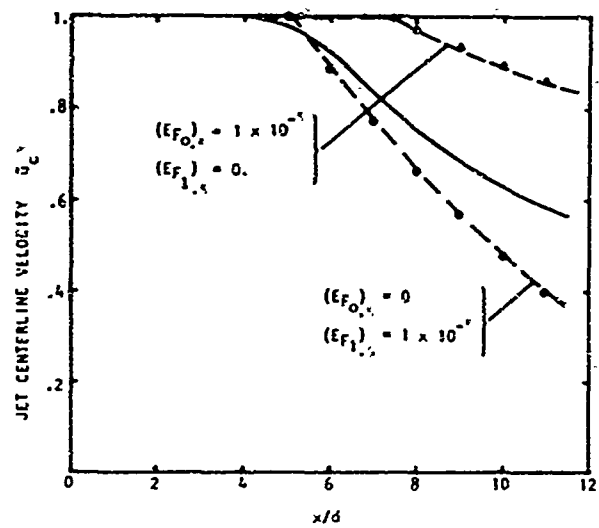


Fig. 11 Effect of Single Mode Number on Jet Center-Line Velocity Decay

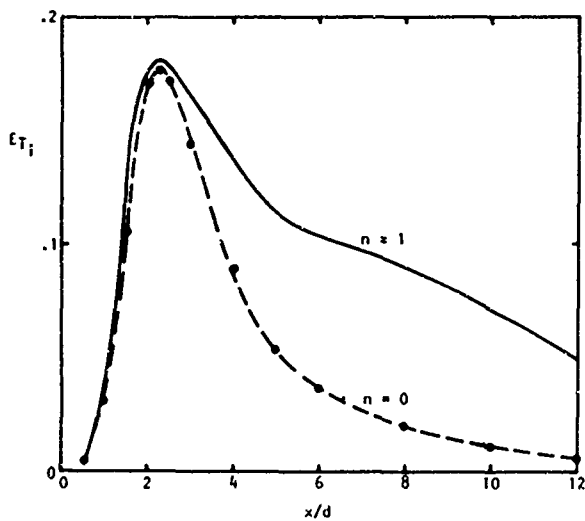


Fig. 12 Energy Density as a Function of Axial Location

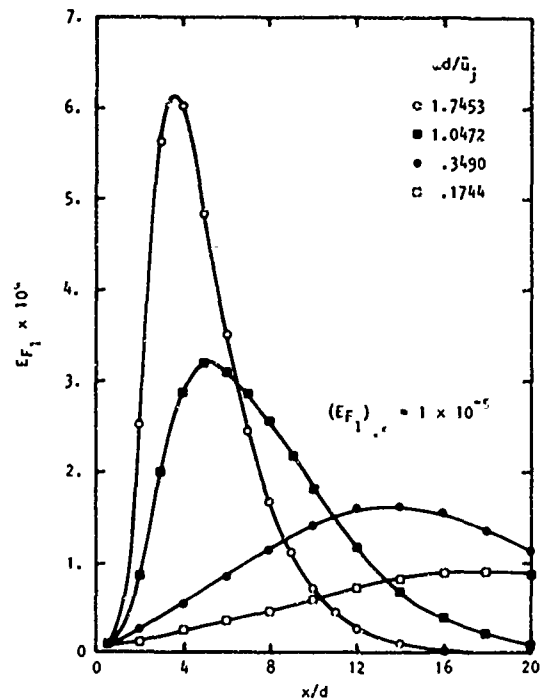


Fig. 13 Integrated Fluctuation Energy Flux for Single Frequency Components as a Function of Axial Location, $n = 1$

The development of a two-dimensional compressible shear layer is found from solutions to integral forms of the momentum, mechanical energy and thermal energy equations in which the fluctuations are described locally by the most unstable eigensolutions to the viscous compressible stability equations.

The compressible flow analysis enables the calculation of the effects of Mach number and temperature variations on the stability of the primary flow and hence on the organized fluctuations. Thus, it is possible to treat such problems as high speed, high temperature flows.

Linearization and Fourier transformation of the continuity, momentum and internal energy equations and the equation of state for the organized fluctuations leads to a set of coupled ordinary differential equations for the fluctuating velocity components, pressure, density and temperature. Together with the boundary conditions these equations form an eigenvalue problem. This is solved for specified velocity and temperature profiles of the mean flow.

Figure 14 shows the effect of the Mach number M_∞ and the temperature T_∞ of the high speed stream on the growth rate for two-dimensional fluctuations in a compressible shear layer whose mean velocity profile is of hyperbolic tangent form and where one stream is at rest. Increasing the temperature of the high speed stream is seen to reduce the frequency for maximum amplification. Increasing the Mach number of the high speed stream is seen to decrease the growth rates of the fluctuations.

The fluctuations are described locally by the most amplifying solutions of the compressible stability equations. The radial distributions of the mean square axial and transverse velocity fluctuations and the shear stress parameter \bar{uv} are shown in Figure 15.

The linear solutions are used, in the same manner as for the incompressible flow, in integral equations to determine the axial development of the free shear layer. The dominant frequency as a function of axial distance may then be calculated and this is shown in Figure 16. As in the case of the incompressible axisymmetric jet, the high frequencies are seen to dominate in the early stages of the development of the shear layer.

Further results and detailed analysis can be found in Appendix 1-6.

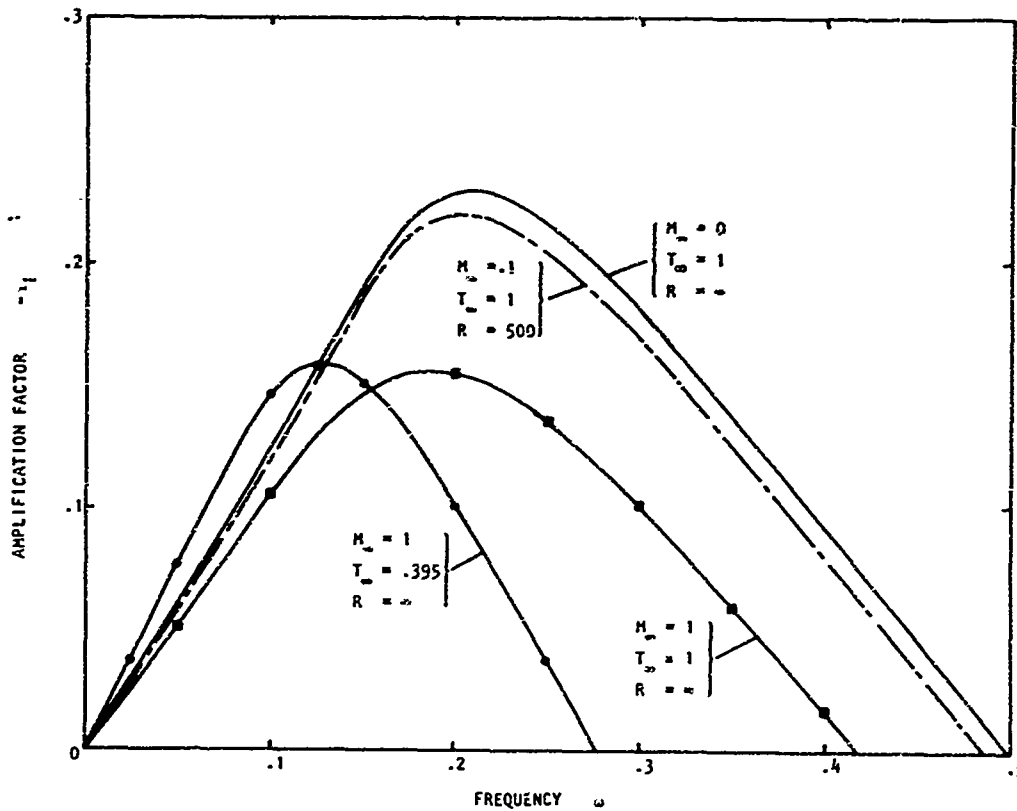


Fig. 14 Curves of Amplification Rate Against Frequency for Two-Dimensional Compressible Shear Layer

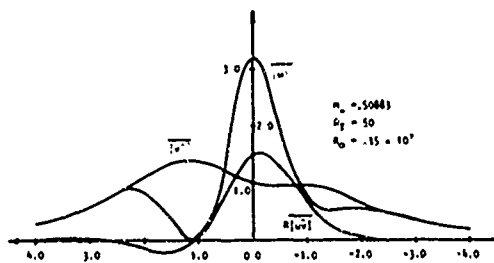


Fig. 15 Radial Distributions of $|\bar{u}'|^2$, $|\bar{v}'|^2$ and $\bar{u}'\bar{v}'$ for Two-Dimensional Compressible Shear Layer

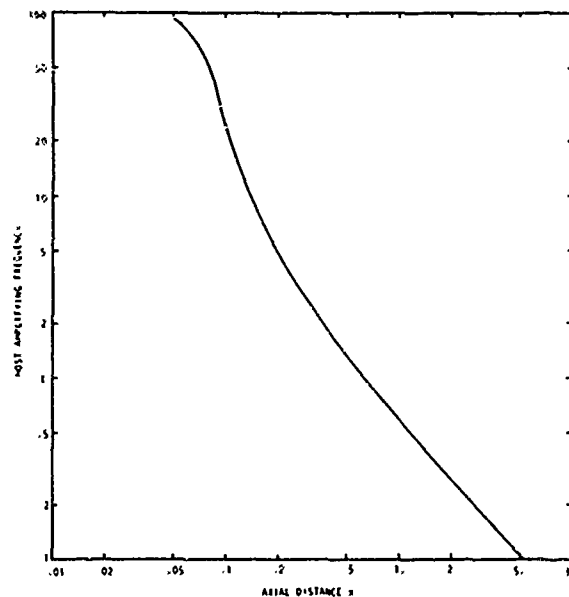


Fig. 16 Most Amplifying Frequencies as a Function of Axial Distance for Two-Dimensional Compressible Shear Layer

3.3 ACOUSTIC FACILITIES

A new facility, anechoic at all frequencies above 200 Hz, has been designed and constructed for investigating supersonic hot jet exhaust noise over a large envelope of jet operating conditions. It incorporates a specially designed exhaust collector that provides a free-field environment for any configuration under test.

The present facility was carefully designed accounting for inadequacies in other facilities and was guided by the stringent demands of jet noise research on this program. Prior to the design and construction of the facility, a one-sixth scale model of the anechoic room was constructed and a comprehensive series of flow visualization and temperature mapping experiments was conducted. The results of this model study dictated the design of the exhaust collector/muffler to provide entrainment air in quantities demanded by the jet operating conditions. The choice of acoustic wedge material and design was optimized by conducting an extensive series of performance evaluation tests in a specially built impedance tube.

A plan view of the complete hot jet noise facility is shown in Figure 17, and it is described in detail in Appendix II. A photograph of the completed facility as viewed through the entrance door is shown in Figure 18. Items of interest in the photograph are the exhaust collector, the microphone arc and the crane cover (in the lower left corner). The anechoic room measures 22' (long) x 20' (wide) x 28' (high) between structural walls, and the flame-retardant wedges are 18" long. The room is anechoic at all frequencies above 200 Hz. The hot air is supplied by a Marquardt Sudden Expansion (SUE) Propane Burner. At the present time, the test range of the facility for model jets of 2 inches diameter is up to 1500°F stagnation temperature and pressure ratios as high as 8. This range is adequate to permit the determination of temperature effects on jet noise, however, upon installation of a 300 KW electric heater between the muffler and the plenum sections, it will be possible to increase the range of stagnation temperature to 2000°F, giving a better high temperature limit for studying advanced systems.

The acoustically lined exhaust collector injects entrainment and room cooling air through the outer channel of the coaxial duct in quantities dictated by the particular jet operating condition, with no special forced-air injection or fan system. After passing through the air gap between the concrete wall and the false wall on the collector side of the room, this entrainment air then distributes symmetrically around the jet axis, thus keeping the air flow circulation velocities in the room to a minimum.

A "cherry-picker" crane is used to gain access to instrumentation and test installations for calibration, test set-up modifications, and maintenance, thus eliminating the need for access platforms and their attendant reflection problems. The crane is stowed by remote control under an anechoic cover during all test operations. The microphone arc is at 72 nozzle exit diameters, still outside the wedge near field. Noise data are normally taken in the range $15^\circ \leq \theta \leq 105^\circ$, but forward arc measurements to 150° can be accomplished by adding a plenum plug.

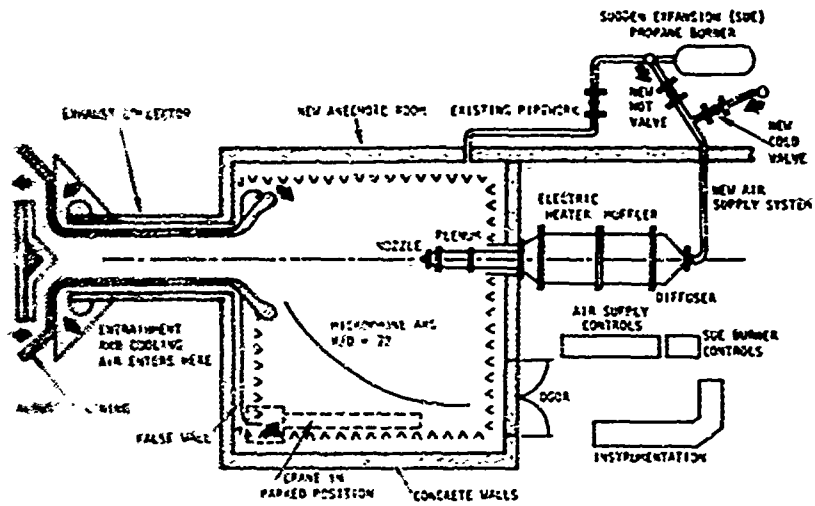


Fig. 17 Plan View Schematic of the New Facility for Supersonic Hot Jet Noise Research



Fig. 18 Completed Anechoic Room Viewed from Entrance Door

The facilities were subjected to rigorous performance evaluation tests, and it has been established that (i) at 72 nozzle diameters from the jet exit plane, the microphones are in the far-field of the jet exhaust at frequencies down to 200 Hz and (ii) the operation of the facility, both hot and cold, is not affected by internal noise, at least down to 350 fps.

In order to confirm the design criteria and to ensure the accuracy of the subsequent jet noise measurements, the facilities were subjected to rigorous performance evaluation tests at appropriate stages and the major findings are as follows.

The anechoic quality of the room and the far-field criteria were examined by conducting inverse-square law tests, first with a point sound source and later with a cold jet (distributed sound source). Typical results are presented in Figures 19 and 20 respectively. It can be seen that the cut-off frequency of the room is below 200 Hz and that at the proposed distance of 12 feet (72 nozzle diameters) from the nozzle exit plane, the microphones will be both in the *acoustic* as well as the *geometric* (or interference) far fields of the jet exhaust at all frequencies of interest (above 200 Hz).

The spectrum of background (or ambient) noise in the anechoic room is shown in Figure 21, together with the 90° cold jet noise spectra at various velocities. The low background noise does not affect the jet noise spectrum even at the lowest velocity (300 fps) tested. Further, the jet noise spectra for velocities up to 1000 fps follow the V_j^8 dependence, thus indicating the lack of any significant internal noise contribution.

The magnitude of the internally generated noise at a low value of jet exit velocity ratio ($V_j/a_0 = 0.32$), both cold and hot, was established by conducting a systematic study (see Appendix II) and a typical set of results is presented in Figure 22. It can be concluded that the internally generated noise, for cold as well as hot operation of the facility, is *not* significant at least down to $V_j/a_0 = 0.32$. All data for $V_j/a_0 > 0.32$ obtained from this jet noise rig represent true turbulent mixing noise, unaffected by internal noise. Due to limitations imposed by the measuring instrumentation noise, however, the lower limit of V_j/a_0 in jet noise experimental programs will be restricted to 0.35.

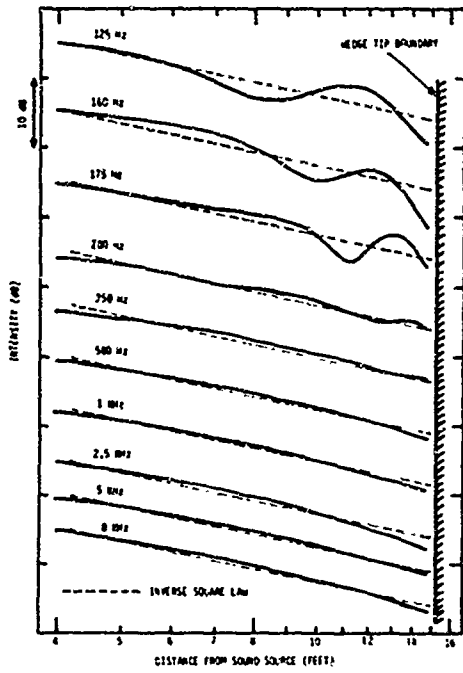


Fig. 19 Results of Inverse-Square Law Tests with Point Sound Source

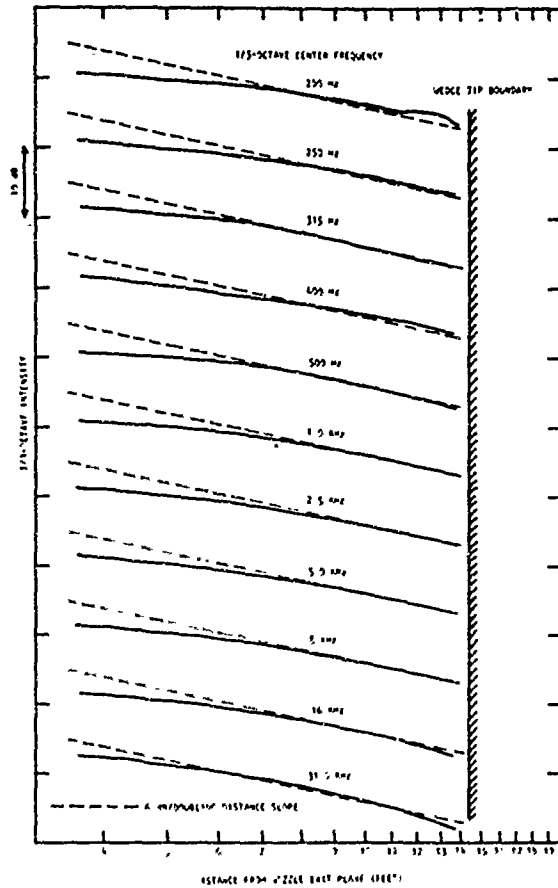


Fig. 20 Results of Inverse-Square Law Tests with Cold Jet: $D=2$ in., $V_j/a_0 = 0.85$, $\theta = 90^\circ$

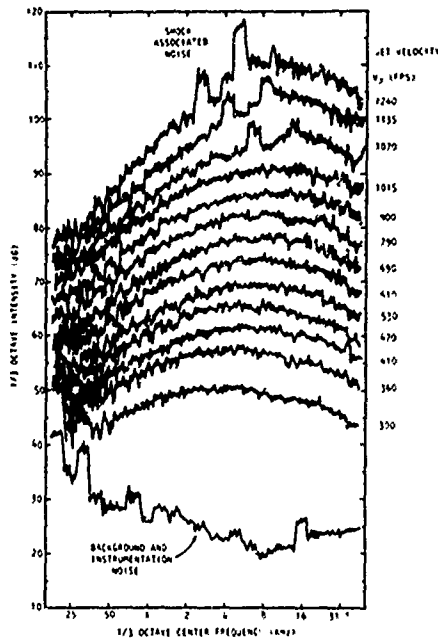


Fig. 21 Background/Instrumentation Noise and Cold Jet Noise Spectra at $\theta = 90^\circ$

	V_j/a_0	T_j/T_∞
A BACKGROUND = INSTRUMENTATION NOISE	0.32	1.0
B MIXING NOISE, COLD	0.32 (EFFECTIVE)	1.0
C BACKGROUND = INSTRUMENTATION + INTERNAL NOISE, COLD	0.32 (EFFECTIVE)	2.0
D MIXING NOISE, HOT	0.32 (EFFECTIVE)	2.0
E BACKGROUND = INSTRUMENTATION + INTERNAL NOISE, HOT	0.32 (EFFECTIVE)	2.0

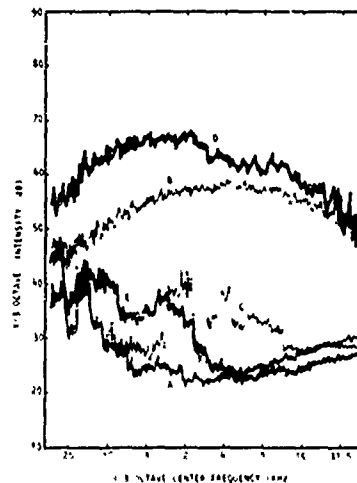


Fig. 22 Turbulent Mixing Noise and Internal Noise Spectra at $\theta = 45^\circ$. Cold and Hot.

3.4 JET NOISE EXPERIMENTS

The jet noise experimental program has extended the range of available turbulent mixing noise data to include velocities in the range $0.35 \leq V_J/a_0 \leq 2.8$ with jet stagnation temperature ratios in the range from unity to values in excess of 3.

The characteristics (spectra and directivity) of the sound field of supersonic, shock-free jets are studied experimentally by measuring the turbulent mixing noise in the far field from four 2-inch diameter nozzles, namely a convergent nozzle for pressure ratios up to 1.89 and three convergent-divergent nozzles having design Mach numbers of 1.4, 1.7 and 2.0, respectively. In order to avoid the contamination of data by shock-associated noise, these latter were operated only at their design pressure ratios (up to 7.4).

The experimental program chart (Figure 23) shows the ranges of jet static temperature ratio T_J/T_0 (and hence also jet density ratio ρ_J/ρ_0) and jet exit velocity ratio V_J/a_0 that could be obtained with the available ranges of stagnation temperature ratio T_R/T_0 and pressure ratio P_R/P_0 . The portion of the chart above the $T_R/T_0 = 3.6$ curve has been explored to date, while the portion below this curve represents the additional regime that will be available in the near future when the electric heater is installed. A total of 65 jet exit conditions (T_J/T_0 , V_J/a_0) were in fact chosen, and these are identified by test point numbers in Figure 23. It can be seen that by considering test points along each horizontal line it is possible to keep the jet efflux temperature constant while varying the jet velocity. Conversely, each vertical line maintains constant exit velocity while varying jet efflux temperature.

At this stage, the experimental results are being analyzed in order to obtain some knowledge of the physical origin of the observed effects and their accountability in terms of the Lighthill acoustic analogy approach and other prediction methods. In particular, the results at 90° to the jet axis have been successfully employed to establish the influence of flow temperature on mixing noise source strengths, as described in detail in Appendix III. Several difficulties are presented, however, in analyzing the results at other angles to the jet axis in terms of available models for convective amplification and refraction and work is in progress to try and resolve some of these difficulties.

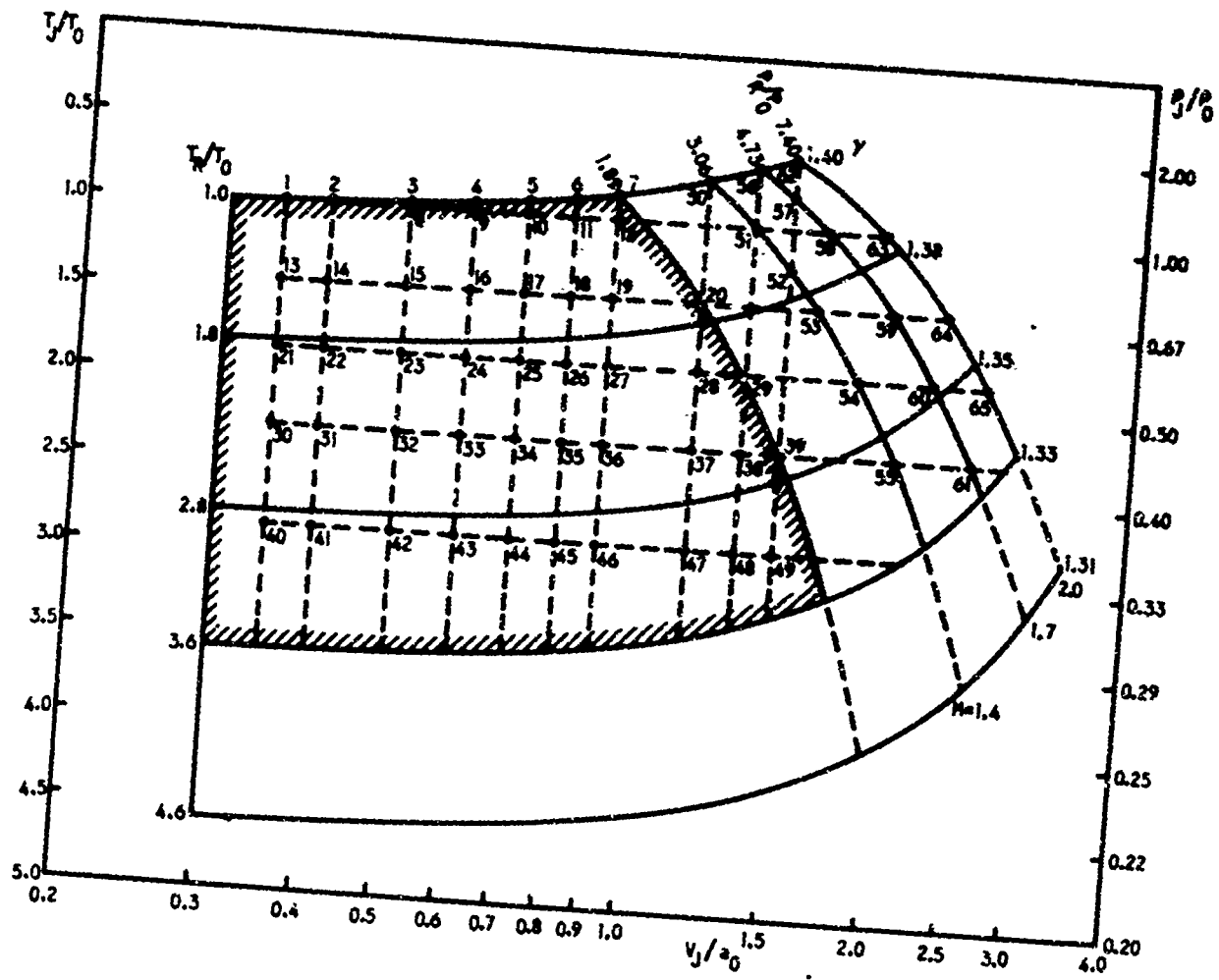


Fig. 23 Experimental Program Chart

The effects of temperature on turbulent mixing noise source strengths per se are established, a new model is hypothesized, and the final predictions in general agree with the measured spectra, at 90° to the jet axis, within 1 or 2 dB.

In order to avoid the additional problems of convective amplification and refraction, the influence of temperature on mixing noise source strengths is studied by examining the data at 90° to the jet axis only. In general, two sources of noise are apparent, one due to the familiar Reynolds shear stress fluctuations and a second attributable to density or temperature fluctuations promoted by the turbulent mixing of streams of dissimilar temperatures. This latter dominates the measured noise at low velocity and high temperature. Scaling laws for the spectra at 90° to the jet axis of these noise components are respectively

(i) Reynolds shear stress noise contribution:

$$S_m(\omega) = S_m(\omega_s) \left[\frac{T_s}{T_0} \right]^{-2} \left[\frac{V_J}{a_0} \right]^{7.5} = \overline{a^2(t)}, \quad \text{where } \frac{\omega}{\omega_s} = \frac{V_J}{a_0};$$

$S_m(\omega_s)$ is the master shear stress noise spectrum given in Figure 24 and for the majority of cases tested,

$$T_s/T_0 = 0.7 (T_J/T_0 - 1) + 1.$$

(ii) Temperature fluctuation noise contribution:

$$S_T(\omega) = S_T(\omega_s) \left[\frac{2\Delta T}{T_J} \right]^2 \left[\frac{V_J}{a_0} \right]^4 = \overline{b^2(t)}, \quad \text{where } \Delta T = (T_J - T_0);$$

$S_T(\omega_s)$ is the master temperature fluctuation noise spectrum given in Figure 24.

These sources are not statistically uncorrelated as previously supposed, but are, it appears, highly correlated. The resulting spectrum, when both are contributing sufficiently, must therefore be calculated from

$$S(\omega) = \overline{a^2(t)} + 2 \sqrt{\overline{a^2(t)}} \sqrt{\overline{b^2(t)}} + \overline{b^2(t)}$$

which assumes unity correlation between the sources, where $a(t)$ and $b(t)$ represent the amplitude dependence of the far field pressure from the Reynolds shear stress source and the temperature source respectively. The use of these relationships, in conjunction with the spectra given in Figure 24, is in general capable of predicting the measured spectra at 90° to the jet axis to an accuracy of 1 or 2 dB.

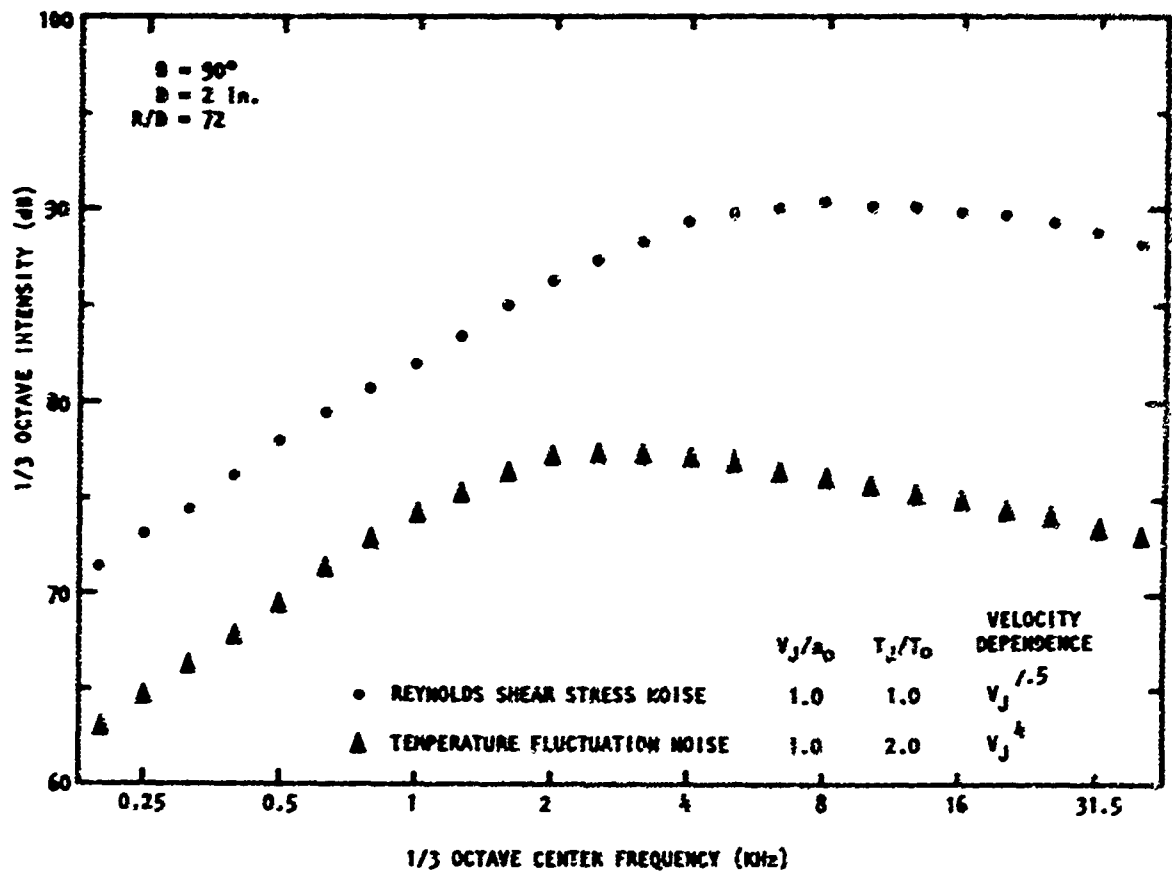


Fig. 24 Master Spectra for Reynolds Shear Stress Noise and Temperature Fluctuations Noise

3.5 LASER VELOCIMETER DESIGN AND QUALIFICATION

A laser velocimeter developed by the Lockheed-Georgia Company has successfully demonstrated the ability to measure instantaneous turbulence velocity in high velocity air flows at repetition rates as fast as 2.4 microseconds.

A laser velocimeter is an electro-optical system which measures localized velocities in a fluid flow field by detecting the laser light scattered by contaminant particles suspended in and moving with the fluid. Such systems are potentially capable of measuring instantaneous velocity vectors in a turbulent flow field over a velocity range from less than 1 inch/second to greater than Mach 4. The measurements do not disturb the flow field and are made in a localized region with cylindrical volume dimensions typically of 0.3 millimeters radius and one millimeter length. As a consequence of the feature of non-interference, a wide range of flow characteristics may be investigated without distorting or destroying the characteristic under study.

The Lockheed-Georgia Company has developed an advanced laser velocimeter (Figures 25 and 26) which provides the unique capability of measuring two simultaneous, orthogonal flow velocity vectors at very high repetition rates. The minimum time between samples is 3 microseconds and the maximum continuous throughput rate for valid data is 18.75 kHz. The velocimeter system operates over a velocity range from 1 to 4,000 fps with an instantaneous sample accuracy which varies linearly from .1% at 125 fps and below to 3.2% at 4,000 fps. The ability to achieve these capabilities is based on three major system features:

(1) a set of unique and highly efficient color separator/beam splitter optics (Figure 27) provide the basis for generating the multicolor laser beams necessary for multivector capability; the optics are self-aligning, extremely stable and virtually eliminate cross-talk between vector channels;

(2) extremely high speed processing electronics (using a 500 MHz clock rate), and error checking circuitry; and,

(3) direct coupling of the LV to an on-line, high data rate mini-computer which provides unusual flexibility in data formatting and in changing or adding outputs or calculations.

TWO AXIS LDV SYSTEM FOR TURBULENCE ANALYSIS

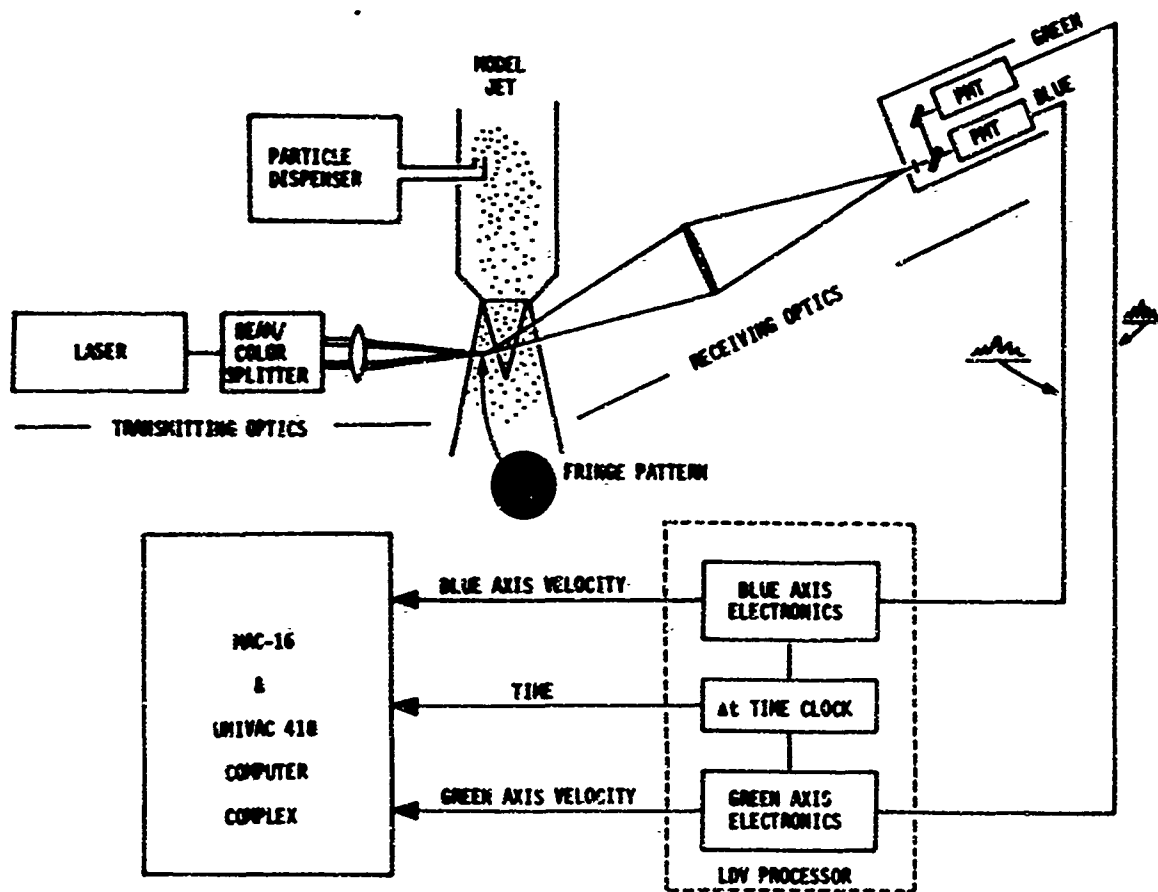


Fig. 25 Laser System Block Diagram

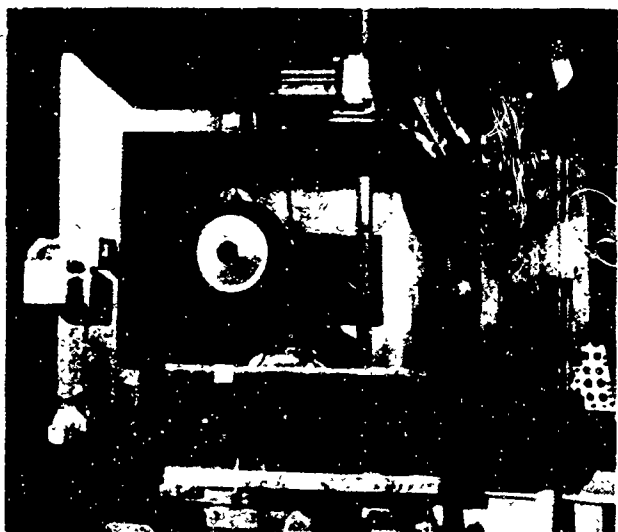


Fig. 26 LDV Test Configuration

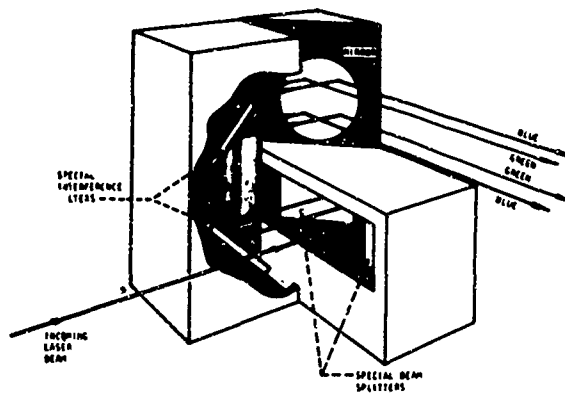


Fig. 27 Beam Splitter Assembly

Analysis of the instantaneous velocity data from the laser velocimeter results in a probability density distribution of the samples, mean velocity, standard deviation (turbulence intensity), auto and cross-correlation and power spectrum and cross-spectrum at frequencies up to 20 kHz. Valid comparisons have been made with hot-wire spectral data.

The on-line mini-computer is used to compute the mean, standard deviation and velocity distribution of the data for immediate reference. An advanced data processing algorithm processes the random-time samples acquired at sub-Nyquist average rates to produce the auto-correlation of each vector and their cross-correlation function. From these, the appropriate spectrum information is computed by Fast Fourier Transform. The power spectrum measured on one channel in an 0.63 inch jet is compared to that obtained by a hot-wire anemometer in Figure 28. The complete electronics and processing systems have been calibrated by using frequency modulated signals to replace the laser signal inputs while retaining the particle detection electronics for data sampling. Figure 29 shows the results due to a 1 kHz square wave modulation indicating harmonics of correct order and amplitude up to 20 kHz. This data was sampled at an average rate of 6,000 samples per second. Signals up to 50 kHz have been correctly processed in this manner. A simulated data set used to develop the original software concepts has been extensively used in studies to refine the data processing algorithm. Figure 30 shows the cross-spectral density from two simulated channels compared against the characteristics of the original signal. Data in the range 300 Hz to 50 kHz have been analyzed with this simulation.

After absolute calibration of measured velocity and turbulence intensity in the test jet have been completed, the LV will be used in support of the theoretical program to perform detailed spectral profiles of the test jet throughout its operating range.

A detailed discussion of the laser velocimeter design and qualification is given in Appendix IV.

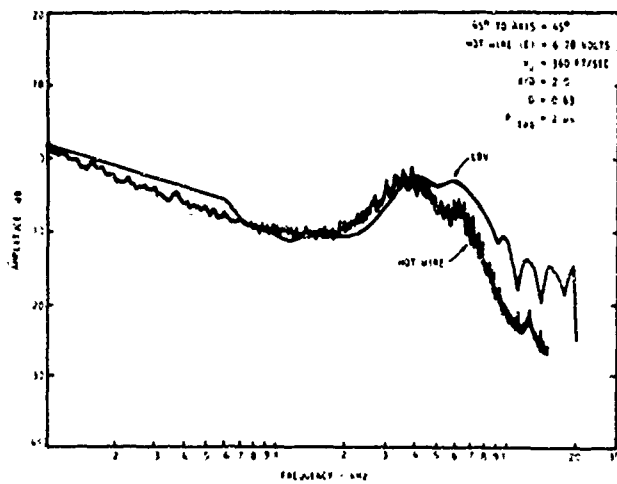


Fig. 28
 Jet Turbulence - Comparison
 Between Laser Velocimeter
 and Hot Wire Spectra

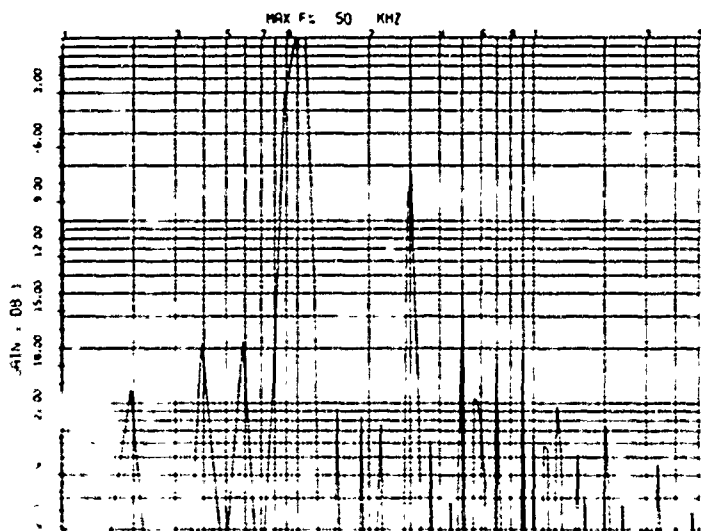


Fig. 29
 Processor Spectrum for
 1 kHz FM Square Wave
 Excitation

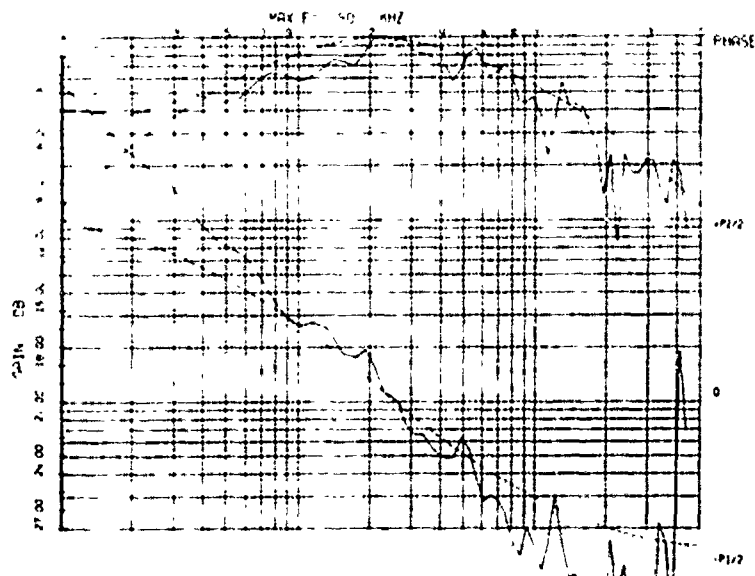


Fig. 30
 Cross Spectral Density -
 Synthetic Data Compared
 with Theoretical Filter
 Frequency Response

4. CONCLUSIONS

1. The homogeneous form of Lilley's equation is recognized to be the same as the equation which is used to investigate the stability of inviscid, compressible sheared flows. Thus, two types of solution can be obtained: the "acoustic solution" and the "unstable solution". Unstable solutions are being studied in our theoretical program to provide information for a model of the source function in Lilley's equation and are described elsewhere. The "acoustic solution" is the subject of this report.

2. Acoustic solutions to Lilley's equation can be constructed from an appropriate specification of the source function and point source or Green's function solutions.

3. The influence of sound-mean flow interaction-effects on the radiation level and directivity of point source solutions has been evaluated in some detail for subsonic parallel jet flows with realistic mean velocity profiles.

4. The directivity of modified point solutions are only in qualitative agreement with measurement and while questions remain concerning representation of the experimental source and the type of solution utilized here, consideration of theoretical results, obtained elsewhere, strongly suggests that a more realistic mean flow model is required.

5. A complete solution to Lilley's equation for a simplified version of the standard type of source function is evaluated in the form of difference spectra which are found to be in good qualitative agreement with measurement.

6. A model for the large-scale organized structure of a turbulent axisymmetric jet has been developed.

7. The model gives the radial, axial and azimuthal variations in the mean flow and the organized fluctuations. It also describes the dominant frequencies and wavenumber, and hence the phase velocities, as a function of position in the jet.

8. A similar model for the 2-D compressible shear layer has been developed.

9. An existing facility has been modified to provide an anechoic high temperature (presently 1500°F) jet noise test facility.

10. In the facility qualification tests, it was determined that rig internal noise was not a problem at velocities as low as 350 fps for hot and cold operation and that the microphones were in both the acoustic and geometric far fields.

11. A series of high temperature jet noise tests was conducted which extended the range of available jet noise data to temperature ratios in excess of 3.0 up to exhaust Mach numbers of 2.

12. Analysis of the jet noise data at 90° resulted in the development of a new model of noise due to temperature fluctuations. The data collapse to within 1 or 2 dB at all frequencies, within the complete test envelope.

13. An orthogonal two-channel laser velocimeter design and construction was completed and checked out. Signal outputs from the photomultiplier tubes proved that the two channel concept was valid.

14. The LV processor and analyzer system was completed and checked with simulated particle signals. All features of the processor and analysis program proved to be more than adequate.

15. In actual test runs in the high velocity jet, comparisons between the LV spectral output and a hot-wire spectrum proved that the Lockheed laser velocimeter is an operational system and that it meets or exceeds all design goals.

In conclusion, all scheduled objectives for the first half of the program have been successfully met without encountering significant difficulties. Thus, it can be concluded that the program goal of understanding the jet noise generation process can be accomplished by continuing to follow the original schedule of work, both theoretically and experimentally.

5. REFERENCES

1. Plumblee, H. E. and Doak, P. E., Summary of Supersonic Jet Noise Studies, Volume I, *The Generation and Radiation of Supersonic Jet Noise*. AFAPL-TR-72-53, July 1972.
2. Plumblee, H. E. and Burrin, R. H., Future Studies for Definition of Supersonic Jet Noise Generation and Reduction Mechanisms, Volume II, *The Generation and Radiation of Supersonic Jet Noise*. AFAPL-TR-72-53, July 1972.
3. Doak, P. E., Progress Toward a Unified Theory of Jet Engine Noise, Volume III, *The Generation and Radiation of Supersonic Jet Noise*. AFAPL-TR-72-53, July 1972.
4. Lilley, G. M., Plumblee, H. E., Strahle, W. C., Ruo, S. Y. and Doak, P. E., Theory of Turbulence Generated Jet Noise, Noise Radiation from Upstream Sources, and Combustion Noise, Volume IV, *The Generation and Radiation of Supersonic Jet Noise*. AFAPL-TR-72-53, July 1972.
5. Lush, P. A. and Burrin, R. H., An Experimental Investigation of Jet Noise Variation with Velocity and Temperature, Volume V, *The Generation and Radiation of Supersonic Jet Noise*. AFAPL-TR-72-53, July 1972.
6. Fisher, M. J., Mayo, W. T., Meadows, D. M., Burrin, R. H. and Beisel, G. E., Jet Flow Measurement and Analysis with Special Emphasis on Remote Sensing Devices, Volume VI, *The Generation and Radiation of Supersonic Jet Noise*. AFAPL-TR-72-53, July 1972.
7. Ribner, H. S., The Generation of Sound by Turbulent Jets. *Advances in Applied Mechanics*, 1964, Vol. III, pp. 103-182, Academic Press, New York.

APPENDIX I

THEORETICAL STUDIES OF JET NOISE GENERATION AND RADIATION AND TURBULENCE/SOURCE FUNCTION BEHAVIOR

- Critique of Acoustic and Source Models for the Generation of Noise by Turbulence, B. J. Tester and P. J. Morris.
- On the Theory of Jet Noise and Its Applications, B. M. Lilley, P. J. Morris and B. J. Tester⁽¹⁾.
- On the Respective Roles of Helmholtz-Type Instabilities and Acoustic Propagation in Jet Noise Generation and Radiation, P. E. Doak.
- On Sound Radiation from Sources in Parallel Sheared Jet Flows, B. J. Tester and R. H. Burrin⁽²⁾.
- A Model for the Structure of Jet Turbulence as a Source of Noise, P. J. Morris⁽³⁾.
- A Model for the Orderly Structure of Turbulence in a Two-Dimensional Shear Layer, S. S. Kapur and P. J. Morris.
- The Momentum Potential Field Description of Fluctuating Fluid Motion as a Basis for a Unified Theory of Internally Generated Sound, P. E. Doak⁽⁴⁾.

INTRODUCTION

This appendix contains papers and notes on theoretical aspects of our program written by members of the Lockheed team during the past year. Section I-2, an AIAA paper by Lilley *et al* serves, in part, to describe our theoretical program; but since this paper, and other papers included here, are essentially progress reports, a more general introduction is given to the two main aspects of our program: the acoustic model, based on Lilley's equation in Section I-1.1 and the turbulence source model and orderly structure model in Section I-1.2. A brief review of recent and contemporary work is given in each of these sections, a more general literature review has been recently published by Doak⁽⁵⁾.

⁽¹⁾ Published as AIAA Paper No. 73-987, October 1973.

⁽²⁾ Published as AIAA Paper No. 74-57, January 1974.

⁽³⁾ Published as AIAA Paper No. 74-1, January 1974.

⁽⁴⁾ Published as AIAA Paper No. 73-1000, October 1973.

⁽⁵⁾ Reference I, Appendix I-1.

1-1. CRITIQUE OF ACOUSTIC AND SOURCE MODELS FOR THE GENERATION OF NOISE BY TURBULENCE

B. J. Tester and P. J. Morris
Lockheed-Georgia Company
Marietta, Georgia

1-1.1 General Introduction to the Acoustic Model, Based on Lilley's Equation, and Its Relation to Other Contemporary Models

Our acoustic model, in some respects, plays a central role in the range of models currently under development elsewhere; for example, in a sense, it includes as special cases the model developed by Mani(2) based on a slug flow jet and the approximate analytic solutions to Phillips' equation obtained by Pao(3) for a sheared jet flow. On the other hand in these special cases and, indeed, in our work, the mean flow model is possibly too extensive in that the mean flow is uni-directional or parallel and hence is obviously at variance with the diverging or spreading properties of a real jet. From the analytic point of view the advantages of a parallel flow model are so overwhelming that, until recently, with the work of Schubert(4), Mungur et al.(5), and Liu and Maestrello(6) the diverging flow on acoustic radiation had been completely ignored. Here we compare the models and results from the aforementioned references with our own and also include the more recent work by Tam(7), which is essentially unique, at least from the acoustic viewpoint.

In general, the acoustic models are based on an inhomogeneous wave equation in say the fluctuating pressure, p ,

$$L(p) = A$$

where

$$L(p) = 0$$

is a type of (linear) wave equation which may include (i) the jet mean velocity and mean temperature as constants (Mani), as variables dependent on the radial coordinate (Phillips-Pao), plus (ii) radial gradients of the jet mean velocity and temperature (Lilley), plus (iii) jet mean velocity and temperature as functions of the axial coordinate as well as the radial coordinate (Schubert, Mungur, Liu). When these quantities are absent, it reduces to the classical wave equation which is the only acoustic equation used by Tam(7); that is, he does not attempt to utilize any type of inhomogeneous wave equation and uses only the classical wave equation outside the jet flow region.

Again when these quantities are absent, the inhomogeneous wave equation reduces to Lighthill's famous equation and the source function A takes on the well known form which is quadratic in the velocity fluctuations; it takes on a different form in Phillips' equation and yet another form in Lilley's equation although in the latter it is still quadratic in the velocity fluctuations. In Mani's model the source function is not related to the velocity fluctuations at all and in this sense his work falls into the category occupied by Schubert, Mungur and Liu where the source or excitation for their wave equations is the elementary point source. These works are not concerned with jet noise as such, that is the strength or distribution of

sound sources within the jet, but only with how the sound radiation from a source is affected by the jet mean flow field. The task of solving the Lighthill, Phillips or Lilley equations conveniently falls into two parts: (a) specification of the source function A and (b) solution of the inhomogeneous wave equation. The source function, it is assumed, can be accurately specified from a knowledge of the turbulent velocity fluctuations in the jet flow; our progress to date on the development of a model for the source function is described in Section 1-5 and a general introduction is given in Section 1-1.2. Here we consider the problem of solving the inhomogeneous wave equation for a given source function.

The relevance of the point source studies now becomes clear: since the wave equation is linear in the pressure fluctuations and the source function is not a deterministic function of space and time, the only realistic approach is to solve the equation with the source function replaced by that describing a stationary point source emitting a pulse at a particular time. Once this solution is obtained the required solution for a particular source function can be constructed by superposition. These intermediate, stationary point source solutions serve two other purposes:

(i) since in the absence of sound-mean flow interactions the radiation would be omni-directional, the directivity is a direct consequence of these interactions and is not obscured by source convection and source distribution interference effects, and

(ii) the solutions can be checked by experiment since it is not difficult to create a stationary point-source in practice.

Thus, one of the main purposes of Lilley's equation, to accurately represent sound-mean flow interactions, can be examined in detail and checked by experiment, independently of the source function for turbulent velocity fluctuations. This is why Section 1-4 concentrates on this type of solution.

We can now examine in more detail the contemporary models having shown that the point source models of Mani, Schubert, etc., are quite relevant.

Mani(2) uses an infinite parallel slug jet flow model and, as we have said, does not have a turbulence related source function but a point source which moves with the jet flow velocity from minus to plus infinity. Apart from this moving source feature his model is simply a special case of our flow model in the limit as the velocity profile tends to the top-hat slug profile, or, a good approximation to the profile at the jet nozzle. In his earlier work the source is of infinite life-time and the only information that could be obtained was the total acoustic power radiated, which of course obscures the important directivity effects. In current work the finite life-time point source is being examined so that meaningful directivity

patterns can be obtained. Mari's (2) work has been of considerable interest, partly because of the moving source feature, but this does tend to confuse source convection and sound-mean flow interaction effects. A stationary point analysis can be applied in a straightforward manner to the real case of interest: a turbulence-related source function whose space-time covariance is separable in a coordinate frame moving with some mean convection speed, as in Section 1-4.

Pao (8) has derived approximate analytical solutions to Phillips equation for a parallel, sheared jet flow which he claims should be valid for jet noise radiation at frequencies near and above the peak frequency as long as the jet velocity is greater than 0.6 times the ambient speed of sound. We believe that Phillips' equation is a special case of Lilley's equation in that solutions from each equation should coincide at high frequencies but we have not, as yet, proved this, either analytically or numerically. Pao (8) uses a source space-time covariance function of the type described in the next section although it is not clear whether this is of the standard, convected type or not. Pao (8) obtains some impressive agreement with measured directivity patterns of supersonic jet noise and rocket noise. Despite the many advantages of approximate analytic solutions we have chosen to concentrate on numerical solutions (see Section 1-4) to avoid any frequency restrictions and of course we use Lilley's equation instead of Phillips' since the latter equation does not contain the important shear-sound convection/refraction or diffraction term.

The point source models of Hungur et al (5) and Liu and Maestrello continue the work of Schubert (4) by investigating the radiation of sound from a source placed in a diverging mean flow. Section 1-4 shows that these models are at present more accurate than our present parallel flow model in predicting far-field directivity patterns (through comparisons with measurements carried out at UTIAS in recent years). We feel that this problem must be resolved; that is, we must improve the accuracy of our solutions in this respect before proceeding to construct general solutions to Lilley's inhomogeneous equation for realistic and detailed source functions.

Tam's work is different not only in the sense that he does not use any form of inhomogeneous wave equation to obtain an acoustic solution but also in that he uses, in fact, the homogeneous form of Lilley's equation to construct an orderly structure model of the jet turbulence. This apparent dichotomy is considered by Doak in Section 1-3. The fact that Lilley's equation has unstable solutions as well as well behaved acoustic solutions was the basis of Prof. J. E. P. Ffowcs Williams' criticisms of our work at the last review. We remain convinced, however, that the acoustic solutions are valid, particularly in the light of their good qualitative agreement with measurement and the excellent agreement when a diverging flow model is used (Section 1-4). Nevertheless, Tam's work is of considerable interest from the acoustic viewpoint in that he proposes two mechanisms for noise generation, unsteady entrainment by the diverging flow and unsteady vibration of the jet column. The radiation is calculated by matching the resultant unsteady velocity fluctuations normal to an imaginary cylindrical surface enclosing the jet flow with the

acoustic field in the outer, ambient medium. This approach is apparently at variance with the accepted physical concept that velocity fluctuations within the jet give rise to a volume source distribution, which at low jet Mach numbers, is of quadrupole order. Sound generated within the jet also gives rise to velocity fluctuations normal to that imaginary surface but these are not included by Tam (7) as such. Although his approach is valid in principle, its weakness lies in the need for an extremely accurate description of those surface velocity fluctuations such that the acoustic component is not lost. Both Lilley's equation and Phillips' equation are solved through a matching process but the imaginary surface is drawn completely outside the mean flow and source region such that only acoustic velocity fluctuations exist and these consist of a superposition of contributions due to radiation from the elemental sources representing the entire volume source distribution.

1-1.2 On the Choice of Source Function in the Radiation of Noise from a Jet

Let us examine the current state of the art with regard to the specification of the source terms. There are two distinct schools of thought, though there is no essential contradiction between the two. The first may be termed the 'eddy-model' and the second the 'wave-model'. The attractiveness of the former model is its simplicity and its ability to yield noise predictions which agree in many essential features with measurements. However, there is much experimental evidence that this 'eddy-model' is too restrictive and conceals the essential noise-generating components of the turbulence. This opinion has led to the use of the 'wave-model' in which the sources are described as coherent large-scale motions.

The original attempts at realism such as those used by Ribner, Lilley and others specified certain statistical properties of the flow. In this manner the cross-correlation between the velocity fluctuations in the direction of the observer can be expressed in terms of characteristic local frequency and length scales. An example of this technique is given by Lilley in Section 1-2. The actual values of these characteristic scales are always determined from experimental results. This model for the turbulence assumes that eddies are convected downstream at a certain convection speed and are considered to be approximately isotropic in a frame of reference moving with the convection speed. It is also assumed that the eddies are small and that the rms-value of the correlated quantities is constant within the correlation volume. Such a model for the structure of turbulence may be introduced as

$$\overline{v_i v_j}(\lambda, \tau) = v_0^2 \left\{ \left(1 - \frac{\lambda^2}{L_1^2}\right) \delta_{ij} + L_1^{-2} \lambda_i \lambda_j \right\} \exp \left[- \left\{ \left(\frac{\lambda}{L_1}\right)^2 + \left(\frac{\tau}{L_t}\right)^2 \right\} \right]$$

where λ is the spatial separation from the source, τ is the time delay, L_1 is the spatial scale of the turbulence and L_t is the time scale of the turbulence in a moving frame. This form is based on the velocity covariance tensor derived by Batchelor (9) for homogeneous turbulence in a uniform stream where

the longitudinal velocity correlation coefficient $f(\lambda)$ is given by

$$f(\lambda) = \exp \left[- \left(\frac{\lambda}{L_1} \right)^2 \right].$$

We note that

$$\begin{aligned} \overline{v_i v_j} (0,0) &= v_0^2 & i = j \\ &= 0 & i \neq j \end{aligned}$$

indicating the presence of only normal stress terms since the assumption of local isotropy requires that the mean flow be uniform. The experimental investigation by Fuchs⁽¹⁰⁾ has shown that the isotropic form of the overall correlation function is very much at variance with the measurements in a jet; in fact the correlation measurements indicate a strong periodic structure for the turbulence.

In spite of these shortcomings this model does permit the calculation of noise radiated by a jet and, as is shown in Section 1-2, much useful information can be obtained.

However it is important to notice that the characteristic frequency and length scales which are so crucial to the determination of radiated noise have, of necessity, to be obtained from experimental measurements. Changes in the flow properties by, for example, use of a different jet nozzle configuration, can also be expected to produce changes in the noise characteristics. Since the prediction of the radiated noise is our goal it is unfortunate that once again, of necessity, the frequency and length scales must be measured in the new flow. In the case of high speed turbulent flow the measurement of these scales has not been possible and only recently, with the use of optical devices such as the laser velocimeter developed in this program, have these measurements become feasible. In essence this technique has not advanced our ability to predict the radiated noise from a turbulent flow.

Where are there gaps in our understanding that need to be filled? Firstly, as we have discussed above, the problem must be formulated in a way which accounts for interaction between the sound and the flow which leads to such phenomena as refraction or diffraction. Secondly, it is essential to develop a model for the turbulence as a source of noise. It is this latter need that will be addressed here.

At the very least the model for the noise producing structure of the flow must enable computation of the local characteristic frequency and length scales as well as the amplitude of the fluctuations for use in a simplified description of the statistical properties. This elementary requirement releases the researcher from the need to conduct flow measurements for every change in the primary flow; that is, detailed predictions of the radiated noise can be made without the necessity for experimental input. Of course, this must not preclude measurements being made either as confirmation of the theoretical predictions or to provide further insight into the mechanisms of noise generation and radiation. The model for the turbulent structure described in Sections 1-5 and 1-6

provides the required information. The source function predicted by this analysis may be used in either a 'Lighthill analysis' or making use of Lilley's equation. Bergeron⁽¹¹⁾ has made some progress along these lines in his work on the aerodynamic sound of nearly incompressible boundary-layer turbulence.

The essence of the model presented in Sections 1-5 and 1-6 is that the noise-producing eddies in a turbulent flow may be described in terms of a large-scale, wave-like organized structure. (Large-scale in this context is in relation to both the scale of the energy-containing eddies in the flow and the local width of the mean flow.) This description of the turbulence also permits us to look at the noise radiation process as deterministic.

The use of a wave-model for the turbulent structure has been used by Tam⁽⁷⁾ and Michalke⁽¹²⁾. The motivation for Tam's model was his observation of schlieren pictures of a supersonic jet which seemed to exhibit a periodic structure in the developed region of the jet. Tam assumed that all the noise production could be associated with a single frequency corresponding to the observed periodicity. The predicted radiated noise using Tam's model gives good agreement for both the overall level and directivity. However, the observed spectrum of jet noise does not contain one single frequency component. Tam has argued that a degree of frequency spreading will occur, but it would be fortuitous if the combination of the noise spectrum of the highly coherent source and the spectrum of noise generated by the random background turbulence provided a smooth spectrum over all frequencies.

The work of Michalke⁽¹²⁾ was motivated by both the observed discrepancies between previous source models and measurements as well as the probable coincidence of the large-scale motions in a turbulent flow and the stability of this primary flow. The analysis shows that there is no essential contradiction between the eddy model and the wave model of jet turbulence though the assumption of the Gaussian form of overall correlation function leads to a special case of Michalke's more general expansion scheme. It is also found that the number of components of jet turbulence which are responsible for the jet noise is relatively limited being confined to the most coherent eddies.

Though it is not explicitly stated in the earlier works of Tam^(13,14) and Michalke⁽¹⁵⁾, they appear to rely on the phase velocity of the source, predicted by a linear theory, being supersonic. In this way the inner solution may be matched with the outer wave solution. This has led Tam^(7,13,14) to study a Mach 2.2 jet. However, in the manner that Tam⁽⁷⁾ has formulated the problem in his most recent work, this restriction to supersonic jets is not necessary. Since the amplitude of the sources is also changing in the axial direction, obeying a non-linear process, the sources will generate components in their wavenumber spectra which will give supersonic phase velocities. This means that if a non-linear theory is used there is no restriction of the Mach number of the jet flow. In Michalke's work⁽¹⁵⁾ it is felt that though linear theory alone is used, which for a subsonic jet would not permit noise radiation, the truncation of the growing linear mode at some spatial distance leads to an equivalent non-linear amplitude limitation and the wavenumber spectrum generated by this truncation

will lead to components with supersonic phase velocities.

The models for the turbulent structure developed in Sections 1-5 and 1-6 extend the work of Tam(7) and Michalke(12). In these models the large-scale structure is not limited to a single frequency as is the case in Tam's work but admits all possible frequencies. However, like Tam(7), but unlike Michalke(12), the model is non-linear and can lead to noise radiation by subsonic jets.

References

1. P. E. Doak, 1972. AFAPL-TR-72-53, Volume III. Progress toward a unified theory of jet engine noise.
2. R. Mani, 1973. AGARD CPP-131, Reference 10. The issue of convective amplification in jet noise.
3. S. P. Pao, 1973. J. Fluid Mech. 59, pp. 451-479. Aerodynamic noise emission for turbulent shear layers.
4. L. K. Schubert, 1972. J.A.S.A. 51, pp. 447-463. Numerical study of sound refraction by a jet flow. II. Wave acoustics.
5. P. M. Mungur, H. E. Plumblee and P. E. Doak. Submitted to J. Sound Vib. On the influence of jet flow on sound radiation.
6. C. H. Liu and L. Maestrello, 1974. AIAA Paper No. 74-5. Propagation of sound through a real jet flow field.
7. C. K. W. Tam, 1973. AIAA Paper No. 73-992. Supersonic jet noise generated by large-scale disturbances.
8. S. P. Pao, 1973. AIAA Paper No. 73-185. An analysis of jet noise directivity.
9. G. K. Batchelor, 1953, Cambridge Univ. Press. The theory of homogeneous turbulence.
10. H. V. Fuchs, 1972. J. Sound Vib., 23, pp. 77-99. Space correlations of the fluctuating pressure in subsonic turbulent jets.
11. R. F. Bergeron, 1973, J.A.S.A., 54, pp. 123-133. Aerodynamic sound and the low-wavenumber wall-pressure spectrum of nearly incompressible boundary-layer turbulence.
12. A. Michalke, 1972, Z. Flugwiss., 20, pp. 229-237. An expansion scheme for the noise from circular jets.
13. C. K. W. Tam, 1971. J. Fluid Mech., 46, pp. 757-768. Directional acoustic radiation from a supersonic jet generated by shear layer instability.
14. C. K. W. Tam, 1972, J. Fluid Mech., 51, pp. 69-95. On the noise of a nearly ideally expanded supersonic jet.
15. A. Michalke, 1970, Deutsche Luft-und Raumfahrt, FB 70-57. A wave model for sound generation in circular jets.

G. H. Lilley
Department of Aeronautics and Astronautics
University of Southampton, U.K.

P. J. Morris and B. J. Tester
Lockheed-Georgia Company
Marietta, Georgia

Abstract

In applications of Lighthill's theory of aerodynamic noise the strength of the sources depends on the local intensity of the turbulent fluctuations together with the intensity of the sound waves generated by the turbulence and their mutual interactions. These latter effects cannot readily be calculated and hence estimates of the noise spectrum and directivity cannot be obtained. In the present work Lighthill's acoustic analogy is replaced by a theoretical model more representative of the true flow and the turbulence fluctuations within it. In this model the problem is divided into an outer region and an inner region which includes the turbulent flow and its convection. Pressure fluctuations in the inner region are suitably matched with those in the outer. Two important results are obtained. Firstly, the generation of high frequency components is not controlled by the gradients of mean velocity and temperature within the flow and, secondly, that within a given frequency band of the far field radiation, only certain regions of the turbulent flow contribute to that radiated sound.

1-2.1 Introduction

Lighthill's theory (1), (2) of aerodynamic noise has been the foundation of our present knowledge on the generation of noise from jets. This theory was extended by Curle (3) to include surfaces within the flow field and by Ffowcs Williams (4) to include the effects of supersonic convection speeds. Many authors, notably Ribner (5), (6) and Lilley (7) have made efforts to include an adequate flow model in Lighthill's theory from which the distribution of the effective noise sources throughout the flow field can be evaluated. Although the Lighthill theory provides a suitable base for the correlation of the total acoustic power output from a jet with distributions of noise intensity and its spectra, in its usual form of application it does not predict the measured convective amplification, the high frequency spectrum at small angles to the jet axis and the changes in noise generation and propagation arising from changes in velocity and temperature gradients within the flow field as found in the careful experiments of Lush and others. Some success in modifying the basic theory of Lighthill to include some of these effects has been achieved by Ribner (8), Doak (9) and others, but these works are far from exhaustive and a more general treatment is clearly needed.

Since Lighthill's theory is an exact theory, it is difficult to argue on any lack of agreement between experiment and theory. Differences that do exist are of course apparent and are only due to the introduction of approximations to the theory in applying them to the calculation of the noise generated, its directivity and its spectrum from a

given jet configuration. This being so, progress in removing these apparent discrepancies has been slow. The difficulty lies in the fact that Lighthill's theory is based on an acoustic analogy whereby the turbulent flow in a jet mixing region, say, is replaced by an equivalent distribution of moving sources placed in a uniform medium at rest -- the sources move but not the fluid. The strength of the sources depends on the local intensity of the turbulent fluctuations together with the intensity of the sound waves generated by the turbulence and their mutual interaction. Thus, the equivalent source strength includes all such effects as refraction, diffraction and scattering. Thus, the major problem in applications of Lighthill's theory is uncovered, in that the source strength can only be found when the complete problem of noise generation is solved -- that is, the sound intensity as well as the turbulent fluctuations within the flow are known. Attempts at iterative methods of solution have so far not been very successful and have usually been limited to solutions covering jet exit Mach numbers which are subsonic and small. Other methods in which refraction in the higher frequencies is included as a correction to a solution in which the source strength is exclusively that associated with turbulent fluctuations only, are useful in distinguishing some of the major characteristics of the directivity of the sound generated. However, their validity at low frequencies is questionable. There is no doubt that these attempts at improving the Lighthill theory and its applications have only had marginal success and at present we are forced to use experimental data in all applied work, with theory merely assisting in providing a suitable background for the presentation of this data.

In the Lighthill theory the real turbulent flow is replaced by an equivalent distribution of quadrupole sources T_{ij} per unit volume in a uniform fluid at rest through which the sources may move but not the fluid. The approach to be followed in this paper involves splitting up the problem into an inner and outer problem. In the inner solution an adequate flow model of the jet flow is introduced which includes the mean flow structure and the convection properties of the turbulence. Our attempt here is to provide a general flow model which represents in a simple way the main features of the flow field on the assumption that it is not greatly contaminated by the sound field which it generates, and which propagates to the far field outside the flow. Of course in assuming that the instantaneous flow can be replaced by a time averaged flow field plus a locally pseudo-random fluctuating field, we immediately ignore the fact that over the bulk of the turbulent flow in a jet the flow is turbulently intermittent and its large-scale structure, at least, appears from experiment to be quasi-ordered. Although there is much conjecture at the present time on the correct interpretation of the experi-

mental data(10),(11), (12) available on the large-scale structure, nevertheless measurement and physical observations confirm broadly a growth of scale of the large-scale motion and a reduction of its characteristic frequency with distance downstream as might be deduced from the divergence, or linear growth, of the mean flow field. Thus unless sound generation in a turbulent flow is very intermittent in character and is specifically dependent only on the instantaneous flow field, it can be assumed that our flow model, in which the turbulent structure is evolving continuously and uniformly along the mixing region of the jet, can at least predict many of the governing features of the far-field sound intensity such as its directivity and spectrum.

The paper first reviews briefly the main characteristics of the far field sound intensity of a jet from Lighthill's formulation. Secondly, the generalized convective wave equation for the inner flow is discussed and the form of the solution of its characteristic (diffraction) equation is given and interpreted. Finally, the model for the flow field is further discussed and our attempts at describing the large-scale turbulent structure, including effects of flow divergence and non-linear interaction, are described.

1-2.2 Lighthill's Theory of Aerodynamic Noise Applied to Jets

In Lighthill's(1),(2) theory of aerodynamic noise the perturbation density $\rho - \rho_\infty$, throughout the entire medium, which is otherwise at rest, is given by the equation

$$\left[\frac{\partial^2}{\partial t^2} - a_\infty^2 \nabla^2 \right] \rho = \frac{\partial^2 T_{ij}}{\partial x_i \partial x_j} \quad (2.1)$$

where $T_{ij} = \rho v_i v_j + (p - \rho a_\infty^2) \delta_{ij} - \tau_{ij}$.

Lilley(13) has given an expanded form for the term in $(p - \rho a_\infty^2)$ but for the purposes of this section we can assume that T_{ij} is adequately represented by its first term, and in which the velocity components are the fluctuating components of velocity. The reason why the terms involving products of the mean velocity and fluctuating components of velocity are neglected is that (see Appendix 1-2A) such terms can be identified as being responsible for refraction and diffraction phenomena associated with the transmission and propagation of sound across the real flow field. In this analysis such effects are absent although their magnitude is included in the local value and distribution of T_{ij} . Clearly any analysis which neglects them can only be directed towards an estimate of the total acoustic power and its spectrum.

For a static jet the far-field spectrum of noise at a point \underline{x} at a frequency γ due to a distribution of quadrupoles of strength T_{ij} moving at an average Mach number $M = \bar{v}_1/a_\infty$ is found from the solution to Equation (2.1) to be

$$\tilde{B}(\underline{x}; \gamma) = \frac{\pi}{2a_\infty^8 x^2} \iiint \frac{d\underline{y}}{(1-M\cos\theta)} \iiint \frac{d\underline{\delta}}{(2\pi)^3} e^{-i\underline{\delta} \cdot \underline{k}} \quad (2.2)$$

$$\int \frac{d\underline{x}}{2\pi} \frac{\partial^4 P_{xx}}{\partial t^4} (\underline{y}; \underline{\delta}; \tau) e^{-i\underline{x} \cdot \underline{k}} \quad (2.2)$$

where $\underline{k} = -\gamma(\underline{x} - \underline{y})/a_\infty |\underline{x} - \underline{y}|$ is the wavenumber of the sound and is equal to that in the turbulence. The frequency is the Doppler shifted frequency

$$\omega = \gamma (1 - M \cos\theta) \quad (2.3)$$

where θ is the angle between the line joining the source at emission to the observer and the direction of the mean velocity of the sources (parallel to the jet axis). $\underline{\delta}$ is the separation in moving coordinates and τ is the retarded time separation given by

$$\tau = \frac{a_\infty \tau^2 |\underline{x} - \underline{y}| + \underline{\delta} \cdot (\underline{x} - \underline{y})}{a_\infty^2 |\underline{x} - \underline{y}| - M \cdot (\underline{x} - \underline{y})} \quad (2.4)$$

with τ^2 the time separation at the fixed observer. \underline{y} is the coordinate of the source at emission. P_{xx} is the space-time covariance of T_{ij} taken in the direction of source to observer.

Now the final two integrations on P_{xx} are equivalent to performing a four-dimensional Fourier transform on $P_{xx}(\underline{y}; \underline{\delta}; \tau)$ and can therefore be replaced by $\tilde{P}_{xx}(\underline{y}; \underline{k}; \omega)$ and Equation (2.2) has the equivalent form

$$\tilde{B}(\underline{x}; \gamma) = \frac{\pi}{2a_\infty^8 x^2} \iiint d\underline{y} \gamma^4 \tilde{P}_{xx}(\underline{y}; \underline{k}; \omega) \quad (2.5)$$

provided P_{xx} is a continuous function along with its derivatives and satisfies certain specific conditions. By the use of this relationship the automatic selection of that part of the turbulence wave number frequency spectrum function which is responsible for noise generation is achieved.

Equation (2.5) is an exact result for the spectrum of the far-field radiation if P_{xx} includes all effects of the disturbances in the flow. If the interference between the flow and the sound mode generated by it is neglected, as stated above, it can be expected that although little error will be introduced in the magnitude of P_{xx} its wave number vector in the turbulence will strictly not be that of the far-field sound. This effect will be greater at high than low frequencies. The relation between the wave number vectors in the turbulence and in the far-field sound can be found in the high frequency limit by ray theory, as suggested by Csanady(14) and others.

In order to clarify what type of results are obtained from this formulation based on Lighthill's model, we introduce the gross approximation that

$$P_{xx}(\underline{y}; \underline{\delta}; \tau) = P_{xx}(\underline{y}) R_1(\underline{y}; \underline{\delta}) R_2(\underline{y}; \tau) \quad (2.6)$$

The four-dimensional Fourier transforms lead to the functions

$$I_1(\underline{y}; \underline{k}) = \iiint \frac{d\underline{\delta}}{(2\pi)^3} e^{-i\underline{k} \cdot \underline{\delta}} R_1(\underline{y}; \underline{\delta}) \quad (2.7)$$

and

$$I_2(\underline{y};\omega) = \int \frac{d\underline{r}}{2\pi} e^{-i\underline{r}\omega} \frac{\partial^2 R_2}{\partial \underline{r}^2}(\underline{y};\underline{r}) \quad (2.8)$$

with

$$\underline{\omega} \cdot \underline{P}(\underline{y};\underline{k};\omega) = P_{xx}(\underline{y}) I_1 I_2 \quad (2.9)$$

If it is assumed that

$$R_2(\underline{y};\underline{r}) = \exp\{-\delta_1^2 \underline{r}_1^2 - \delta_2^2 \underline{r}_2^2 - \delta_3^2 \underline{r}_3^2\} \quad (2.10)$$

where $\delta_1 = \delta_1/\omega_1$, etc. and l_1, l_2, l_3 are scales of turbulence in the direction of the mainstream and transversely respectively,

and

$$R_2(\underline{y};\underline{r}) = \exp\{-\omega_0^2 \underline{r}^2\} \quad (2.11)$$

we find

$$I_1 I_2 = \frac{l_1 l_2 l_3 \omega^3}{16\pi^2 \omega_0} \exp\left\{-\frac{Y^2}{4\omega_0^2} C(M,\theta)\right\} \quad (2.12)$$

where

$$C(M,\theta) = (1-M\cos\theta) + \frac{\omega_0^2 l_1^2}{a_0^2} (\cos^2\theta + \frac{Z^2}{l_1^2} \sin^2\theta) \quad (2.13)$$

Although it can be argued at first sight that these gross approximations to measured values of P_{xx} are too crude to be of value; nevertheless, it can easily be demonstrated that in evaluating the far-field spectrum it is not the form of the function P_{xx} which is critical, but how the length scales l_1, l_2, l_3 , in the turbulence and the reference frequency, ω_0 , in the turbulence, all measured in the moving frame, vary in the downstream direction and across the flow. We also stress that we have used the correct form for the source function, namely, $\partial^2 P_{xx}/\partial \underline{r}^2$, which is consistent with our assumptions about the form of T_{ij} and that the mean properties of the turbulence are stationary functions of time.

Finally, we require an approximation for the amplitude function $P_{xx}(\underline{y})$. We put

$$P_{xx}(\underline{y}) = \bar{\rho}^2 (\overline{v_x^2})^2 \quad (2.14)$$

where $\bar{\rho}$ is a suitable average density and v_x is the component of turbulent velocity in the direction of the observer. If we write v_1^2 and v_2^2 for the turbulent components of velocity in the axial and transverse directions then very approximately

$$\overline{v_x^2} = \overline{v_1^2} (\cos\theta + \beta \sin\theta)^2 \quad (2.15)$$

where β is the ratio of $(\overline{v_2^2}/\overline{v_1^2})^{1/2}$.

If we now write l_0 for a typical length scale in the turbulence and v_0 for a typical velocity in the

turbulence in a moving frame then a relation must exist between ω_0 , v_0 and l_0 such that

$$\frac{\omega_0 l_0}{v_0} = A \quad (2.16)$$

The function A , is the characteristic Strouhal number in the turbulence and can, for our purposes, be assumed to be a constant throughout the flow.

With these relations we can find $\underline{P}_{xx}(\underline{y};\underline{k};\omega)$ throughout the flow and perform the volume integration as required in Equation (2.5). The integration is simplified if the function $C(M,\theta)$ and ω_0 are both assumed to be functions only of the axial distance along the jet; that is, we assume that M is a mean representative convection speed of the bulk of the turbulence and ω_0 is the characteristic frequency of the turbulence in the center of the mixing zone at any station along the jet. Hence, from Equation (2.5) we find

$$\begin{aligned} \underline{P}(\underline{x};\underline{y}) &\sim \frac{Y^3 d \alpha^2}{32 a_0^3 x^2} \int_0^\infty dy_1 (\cos\theta + \beta \sin\theta)^4 E(y_1) \\ &\cdot \frac{l_0^3(y_1) v_0^4(y_1) \rho_0^2(y_1)^2}{\omega_0^4(y_1)} \\ &\cdot \frac{b(y_1)}{l_0} \exp\left\{-\frac{Y^2}{4\omega_0^2} C\right\} \quad (2.17) \end{aligned}$$

where

$$E(y_1) = \iint \frac{dy_2 dy_3}{\pi d b(y_1)} \left[\frac{l_1}{l_0}\right]^3 \frac{v_1^4}{v_0^4} \left[\frac{\rho}{\rho_0}\right]^2$$

$b(y_1)$ is a reference width of the mixing zone, $l_2 = l_3$ and $l_2/l_1 = \alpha$, a constant, d , is the jet diameter and ρ_0 is an appropriate reference density in each region of the jet. The non-dimensional quantity E will vary slowly along the flow but for our purpose may be assumed to have constant values in each of the mixing regions of the jet within and downstream of the potential core.

The form of the spectral density is made clear if the two regions specified above are treated separately in the integration over y_1 . Thus, on using Equation (2.16) and specifying appropriate variations of l_0 , v_0 and ρ_0 with y we find, on changing the variable of integration from y_1 to s , where $s = \omega_0/\omega_1$ and ω_1 is the value of ω_0 at the end of the potential core which is located at the station $y_1 = L$, that the integral from 0 to L is of the form

$$\int_1^\infty \frac{ds}{s^m} \exp(-\Gamma/s^2)$$

while the integral from L to ∞ in the far jet is

$$\int_0^1 \frac{ds}{s^n} \exp\{-\Gamma/s^2\}$$

where

$$\Gamma = \frac{y^2}{k_0^2} C(M, \theta)$$

and m and n . The values of m and n reflect the variations of v etc. with y . In Equation (2.17) the value of θ is the angle of the wave number vector in the turbulence, which will be different from that in the external sound field whenever the model is extended to include the effects of refraction. The two angles are coupled as a result of the convection Mach number, frequency, and speed of sound ratio between the flow inside the jet and in the ambient air outside. Since the value of Γ can be taken as constant, say Γ_0 , according to our assumptions, from 0 to L , and noting

$$\Gamma_0 = \frac{S^2 C_0}{4} \left/ \left(\frac{\omega_1 d}{V_j} \right)^2 \right. \quad (2.18)$$

where the jet circular frequency Strouhal number $S = \omega d/V_j$, and C_0 is some average value of C , we find the following approximate asymptotic forms to the above integrals for low and high values of the Strouhal number. Thus, for

$$\Gamma_0 \gg 1 \quad \tilde{B}(x; \gamma) \sim \frac{1}{C_0^2 S^2}$$

and

$$\Gamma_0 \ll 1 \quad \tilde{B}(x; \gamma) \sim \frac{S^2}{C_0}$$

showing that the convective amplification at low frequencies is much reduced as compared with higher frequencies. Other results which can easily be deduced are that the peak Strouhal number

$$S_m \sim 1/\sqrt{C_0}$$

and that at the Mach wave emission angle $M \cos \theta = 1$, S_m decreases with Mach number at sufficiently large values of M . In this latter case $\gamma_m d/a_\infty$ is constant.

The mean value of the square of the far-field density, obtained from Equation (2.17),

$$B(x, \theta) \sim M_j^8 / x^2 C_0^{5/2} \quad (2.19)$$

is a result previously given by Ffowcs Williams⁽⁴⁾ and Ribner⁽⁶⁾. It is also found that approximately half the total value of $B(x, \theta)$ is generated within the initial mixing region and the remaining half is generated downstream of the potential core.

The spectrum at high frequencies can be adjusted

for refraction effects, as stated above, by the use of ray theory. If the mean value of density in the early part of the mixing region is ρ_1 , say, then the relation between θ and θ^* (where θ is now the angle of the wave number vector in the external sound field) is

$$\cos \theta^* = \left| \frac{\cos \theta}{1 - M \cos \theta} \right| \sqrt{\frac{\rho_\infty}{\rho_1}} \quad (2.20)$$

The cut-off angle for high frequency radiation is then found for $\theta^* = 0$ and is given by

$$\cos \theta_c = \frac{1}{M + \sqrt{\rho_\infty/\rho_1}} \quad (2.21)$$

Most of these results are not inconsistent with experimental data and demonstrate the deep understanding that can be found from a systematic study of Lighthill's theory of aerodynamic noise. However, the simple results obtained above and supported by experimental data of Lush⁽¹⁵⁾ and others, indicate that the interaction between the wave motion generated by the turbulence and the flow itself is complex and cannot adequately be described by ray theory except in the asymptotic case of very high frequencies. It is for this reason that the study described in Section 1-2.4 is undertaken in order to display a more adequate representation of the flow field than can be obtained on the basis of a simple convective quadrupole source model.

1-2.3 The Generalized Wave Equation for the Inner Flow

In Lighthill's acoustic analogy the sources of sound strength and their distribution reflect not only the turbulent generation terms but also the wave-flow interaction processes, which include refraction and scattering. Lighthill's formulation is therefore of importance when these interaction effects are negligible, since then the source function is determined from a specification of the turbulence with these interaction effects absent. When interaction effects require investigation it is necessary to separately describe the flow field (inner region) from the radiation or far-field (outer region).

In Appendix 1-2A the flow equations are analyzed for a slowly diverging mean flow field representative of a jet mixing region, and a generalized inhomogeneous convective wave equation is derived for $r \equiv 1/\gamma \ln p$ and its fluctuating part r' . This equation can be written symbolically as

$$L\{r'\} = \Lambda \quad (3.1)$$

where Λ is the source function, which contains all terms not linearly dependent on r' , and $L\{\}$ is a linear operator on r' having variable coefficients which are functions of the mean flow field and are assumed to be known. Now in a turbulent flow r' can be regarded as a random function of space and time centered on local conditions in the flow. If we denote this fixed location at \underline{x} , then r' will be a random function of x_1, x_3 , and t such that

$$r' \equiv r'(x_1, x_3, t; x_2; \underline{x}) \quad (3.2)$$

Normally we will refer to the position \underline{x} as the axial station x_1 . For a pseudo-two dimensional mixing region we may Fourier decompose r' with respect to x_2 and t in terms of the real wave number k_2 and the real frequency ω . Hence, we write

$$r' = \int e^{i\omega t} e^{ik_2 x_2} \tilde{r}'(x_1, k_2; \omega, x_2; \underline{x}) d\omega \quad (3.3)$$

which is a Fourier-Stieltjes integral of a generalized kind with $d\tilde{r}'$, the Fourier coefficient of r' not in general of bounded variation. For the case of a slowly diverging mean flow, such as the mixing region of a jet, we may choose

$$\underline{x} = \frac{1}{2} (x_1' + x_2')$$

and

$$x_2 = x_2' - x_1'$$

Then on the assumption that derivatives of r' with respect to \underline{x} are small compared with the difference coordinate x_2 and noting that the mean flow variables are functions of \underline{x} only and are dominated by their variations in the x_2 direction, we find that the Equation (3.1) for r' is unchanged provided all its space differentiations are in terms of x_2 , having its origin at the chosen station \underline{x} . In effect these assumptions are equivalent to replacing the real diverging flow by a localized parallel flow at each station \underline{x} . The mean flow properties in each parallel flow are those appropriate to the station \underline{x} . This stepwise parallel flow approximation to the diverging flow can be improved by the use of the WKBJ method or alternatively by making use of the similarity properties of the mean flow. However, irrespective of the method employed it is the wave motion crossing each station \underline{x} that must be under consideration. Thus, we will introduce the Fourier transform on r' in respect of the difference coordinate x_2 in terms of the real wave number component k_2 , so that from Equation (3.3)

$$r' = \int e^{i(\omega t + k_1 x_1 + k_2 x_2)} \tilde{r}' d\omega \quad (3.4)$$

where k_1, k_2 are functions of the station \underline{x} in the aerodynamic flow. Thus, from Equation (3.1) the fundamental characteristic equation can be derived and for either two-dimensional or axisymmetrical flow we find (see Appendix 1-2A)

$$\frac{d^2 \zeta}{dx_2^2} + \zeta q(x_2) = h(x_2) \quad (3.5)$$

where ζ is a modified Fourier coefficient related to $d\tilde{r}'$, $q(x_2)$ is a flow function dependent on the mean velocity and the mean temperature and their gradients as well as the frequency ω and the wave number vector \underline{k} . Typical mean velocity and $q(x_2)$ profiles for a two-dimensional jet are shown in Figure 1; the velocity profile in the mixing region is based on the error function. $h(x_2)$ is a modified Fourier coefficient of the 'source' function Λ in Equation (3.1). Equation (3.5), which is the well-known diffraction equation, is fundamental to the problem of noise generation in turbulent flows. At high frequencies it reduces to the characteristic equation of ray acoustics. Equation (3.5) is valid for all frequencies and wave numbers although

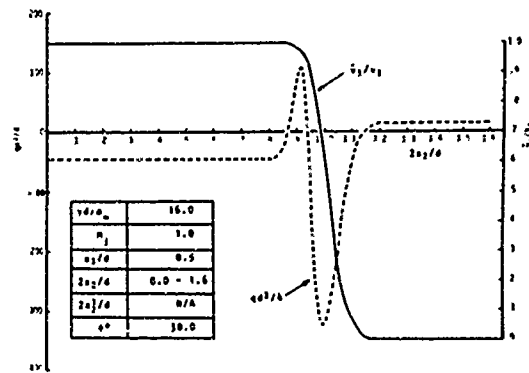


Figure 1. Jet Mean Velocity Profile, \bar{v}_1/V_j , at Axial Station, X_1 , One-Half Jet "Diameter", d , from Nozzle; Typical q Coefficient Profile at Same Axial Station for Observer Angle, θ , of 30° and a Reduced Frequency, yd/a_0 , of 16.

clearly it is dependent on the validity of the assumptions in respect of the flow model corresponding to a slowly diverging mean flow. The equation, in its homogeneous form, has been subjected to careful investigation in many branches of mathematical physics. For a mechanical system of one degree of freedom

$$q(x_2) = \frac{2m(E - V)}{\hbar^2}$$

where m , E and V are respectively the mass, total energy and potential energy and $\hbar = h/2\pi$, where h is Planck's constant. For general values of $q(x_2)$ the equation is not explicitly solvable. (16)

The solution of Equation (3.5) depends on the position and number of the transition points or zeros of $q(x_2)$. In any general analytic solution it is necessary to find the continuous solution across the transition points and this can be achieved by following the method described by Langer. (16) The solution is found in terms of Bessel functions of order $1/3$ or in terms of Airy functions. Details of this solution were given recently by Pao (17) and earlier by Lilley (18). Here we will consider some recent numerical solutions.

It is interesting to note, before considering the numerical results, that the properties of the solution of this diffraction equation are not destroyed when the mean flow is replaced by a vortex sheet model in which the mean velocity and mean temperature fields are constant, but different, on both sides of the vortex sheet. This latter model is sometimes referred to as the 'plug' or 'slug' flow model. In such a model the properties of the mixing region are contracted into the thin vortex sheet where the finite gradients in mean velocity and temperature are replaced by infinite gradients. Naturally although the solution of the vortex sheet model is qualitatively similar to that of the complete diffraction equation nevertheless certain important characteristics of the wave interaction with the flow are only found when the equation is solved for the finite mixing region dimensions and the finite gradients for the mean flow field. For example, the far-field sound pressure due to a

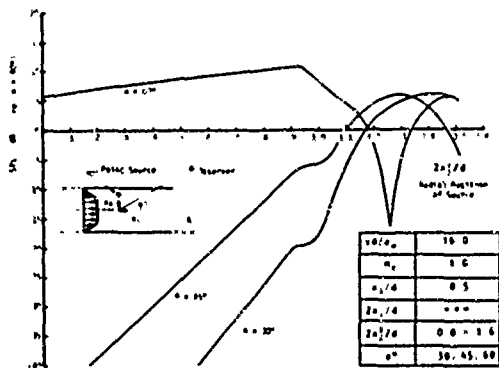


Figure 2. Far-Field SPL as a Function of Source Radial Position for Three Observer Angles

monopole point source in a jet can be critically dependent on the radial position of the source within the mixing region, as illustrated in Figure 2; in these examples both the source and observer are "above" the jet center-line. The far-field sound pressure at the same angle but "below" the center-line would be much smaller; because the Fourier coefficient, $\tilde{d}\omega$, decays exponentially in regions where $q(x_2)$ is negative, as shown in Figure 3. This is also the reason for the low far-field sound pressure levels (SPL) in Figure 2 when the source is separated from the observer by negative $q(x_2)$ regions: taking the case $\theta = 30^\circ$ the regions where $q(x)$ is negative are, from Figure 1, $0 \leq 2x_2/d \leq .87$ and $.94 \leq 2x_2/d \leq 1.15$. When both regions lie between the source and observer, the far-field SPL decreases in direct proportion to the path length through the jet because $q(x_2)$ is constant in the first region: this effect is clear in Figure 2. When the source and observer are separated by the second region alone, the SPL (for $\alpha = 30^\circ$) is still 20 dB below the free-field level (10 dB in Figure 2) and this is partly due to attenuation through this narrow second region. However, the free-field SPL's do not result if the source is placed outside the jet flow: reflections from the jet flow cause a simple interference pattern in the far-field. In Figure 2 a pressure minimum in the far-field occurs at $\theta = 60^\circ$ when the source is at $2x_1/d = 1.25$ and maxima occur at $\theta = 45^\circ$ for $2x_2/d = 1.3$ and at $\theta = 30^\circ$ for $2x_2/d = 1.4$.

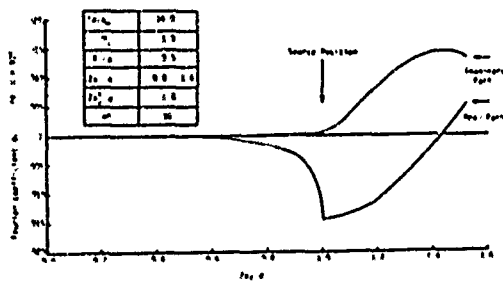


Figure 3. Variation of Fourier Coefficient, $\tilde{d}\omega$ (re: $\theta = 90^\circ$), with "Radius"; Source at $x_1 = d/2$.

In the vortex sheet model the diffraction equation can be conveniently replaced by convective wave equations with constant coefficients on each side of the vortex sheet and the solutions for the pressure on each side are matched, together with satisfying the vortex sheet displacement boundary condition. Some far-field directivity patterns of a monopole point source located on the centerline of a two-dimensional sonic 'plug' jet flow are shown in Figure 4 for frequencies which span the usual jet noise frequency range: clearly there are very significant changes in far-field directivity with frequency. Of particular importance is the loss in intensity of the high frequency radiation in directions close to the jet axis in the downstream direction, a result clearly demonstrated in the experimental results of Lush⁽¹⁵⁾ and others. This result has of course been known for some time and is generally referred to as the refraction effect in the high frequency limit.

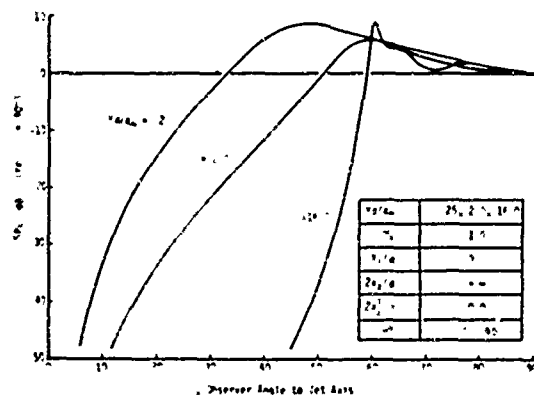


Figure 4. Far-Field SPL Directivity of Source Located on Centerline of a "Plug" Jet Flow at Three Frequencies

Some solutions to the diffraction equation in the form of far-field SPL directivity patterns are compared with 'plug' flow solutions in Figures 5 and 6; for axial stations at and close to the jet nozzle there is almost complete agreement between the two solutions and low and high frequencies. However, there are substantial differences at both frequencies when the axial station is at the end of the potential core (shown by the dashed line).

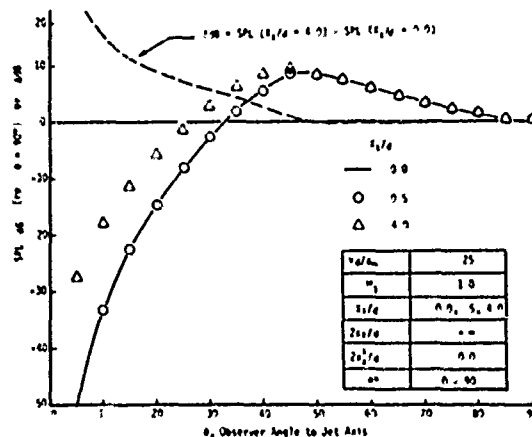


Figure 5. Variation of Far-Field SPL Directivity with Axial Station for Source on Jet Centerline: $\gamma d/a_\infty = .25$

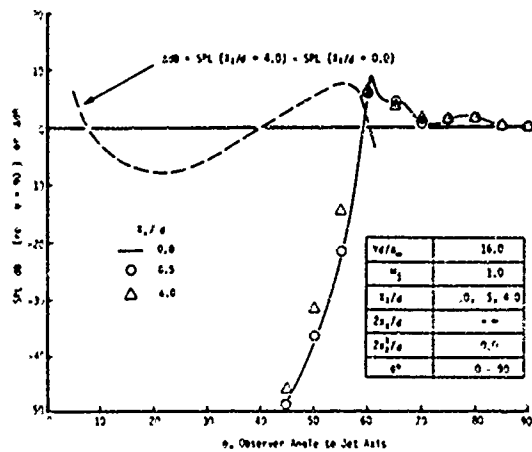


Figure 6. Variation of Far-Field SPL Directivity with Axial Station for Source on Jet Centerline: $\gamma d/a_0 = 16.0$

In order to obtain experimental verification of solutions to the diffraction equation, we must consider the circular jet and eventually, jets of other cross-sections. Diffraction equation solutions for a circular jet will be presented elsewhere, but the good qualitative agreement between measured directivity patterns in Figure 7 and those calculated with a circular 'plug' jet flow model in Figure 8 indicates that adequate experimental verification will soon be forthcoming.

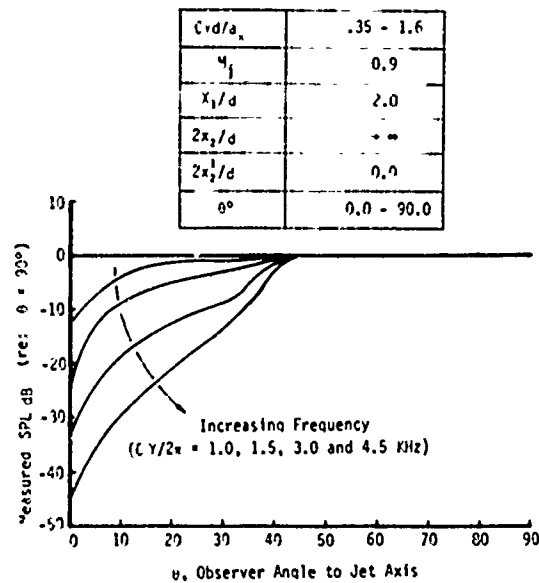


Figure 7. Measured Far-Field SPL Directivities of a Source on a Jet Centerline ($d = 3/4''$) Taken From MacGregor et al (27)

$$C = [(1 - M_c \cos \theta)^2 + \alpha^2 M_c^2]^{1/2};$$

$$M_c = 0.5 M_j; \alpha = .55$$

$C\gamma d/a_0$.35 - 1.6
M_j	0.9
x_1/d	0.0
$2x_2/d$	∞
$2x_2^1/d$	0.0
θ°	0.0 - 90.0

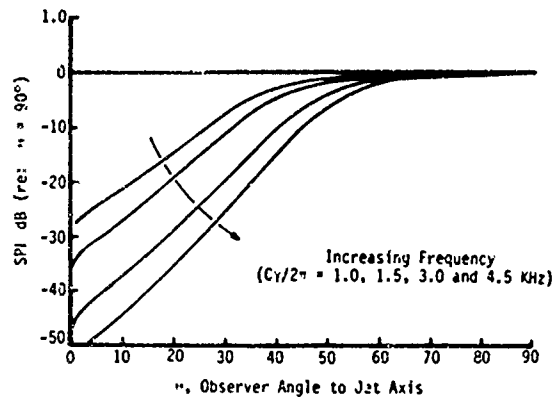


Figure 8. Far-Field SPL Directivities of a Source on the Centerline of a Circular 'Plug' Jet Flow (That is, Axial Station at Nozzle) for Comparison with MacGregor's (27) Measurements in Figure 7.

$$C = [(1 - M_c \cos \theta)^2 + \alpha^2 M_c^2]^{1/2};$$

$$M_c = 0.5 M_j; \alpha = 0.55$$

As shown in Appendix 1-2A, the solution for the Fourier coefficient $d\bar{w}$ depends on the source function Fourier coefficient and its distribution across the mixing region. The solution can then be turned into the wave-number/frequency spectrum function of the far-field pressure for each axial station of the mixing region and the results summed over the entire jet. The detailed results and their comparison with experiment will be left to a later paper.

However, before leaving this section we refer to the fact that here we have specifically chosen real frequencies and real wave-number components. Our justification for this is that in this section we are dealing with a turbulent source function, which is represented by a summation of harmonic waves which do not suffer amplification or damping. We thus have replaced any problem relating to discrete events in the flow which might indeed be present in the real flow, especially in the larger scale structure, by an equivalent continuous structure for the turbulent flow. The further explanation of our model will be left to the next section.

1-2.4 The Wave-Model of a Turbulent Mixing Region

The generation of noise from the turbulent mixing of a jet has been shown to depend critically on the flow structure and the interaction of the wave motion generated by the flow and the flow itself.

Experimental data^{(10), (11)} on the mean flow and the turbulence properties have only recently reached a state of sophistication such that it is now fairly clear to deduce that a large-scale organized structure exists in what is usually referred to as a high Reynolds number turbulent jet flow. The early work of Townsend⁽¹⁹⁾ also predicted a large-scale equilibrium structure for the turbulence which passed through cycles of growth and decay. However, it is not yet clear that this large-scale equilibrium structure is of similar form to the organized structure found by Crow and Champagne⁽¹⁰⁾ and Lau, Fuchs and Fisher⁽¹¹⁾ and how far the latter structure is a function of the break-up of a pseudo laminar flow near the jet exit into distorted vortex ring-like structures, which become more and more disorganized as they convect downstream.

Attacks on the theoretical problem of turbulent shear flows are thwart with difficulties. Nevertheless on the crude but simple and plausible assumption that the large-scale turbulent structure possess little energy, it is possible to derive linear equations describing their structure and motion. If further the flow variables are Fourier decomposed in terms of wave-number and frequency it is easily demonstrated that the equation to solve is the inhomogeneous Orr-Sommerfeld equation. Thus in the mixing region flow the large-scale structure will be dominated by the spatially unstable modes, which are the eigenvalues of the Orr-Sommerfeld equation.

We can now conjecture a series of events in sequence. As soon as the mean flow is disturbed at any station in a jet mixing region the most unstable mode will appear and dominate the flow. It commences to grow in magnitude, at an initial growth rate governed by linear theory, while being convected downstream. However, as is evident from experimental observation, it cannot grow indefinitely. Its interaction with the background turbulence will lead to damping. The mode is also propagating in a region of diverging flow whose mean characteristics are changing which will result in distortion and damping of the mode. For example, there is no linear growth of the axisymmetric mode downstream of the potential core⁽²⁹⁾. In addition, the growth itself will generate non-linear inertial and damping effects which in turn damp the mode growth. It is important to notice that if only the effects of background turbulence and flow divergence are considered, then the limiting amplitude of the mode is entirely dependent on the initial disturbance amplitude, see Figure 12, a phenomenon not verified by experiment.⁽¹⁰⁾ Clearly the non-linear self-limiting process must be taken into account. On this basis it is reasonable to conjecture that an amplitude limiting situation governs the mean square intensity of the turbulence. In this state the turbulence acts as a series of marginally stable waves as suggested, in a different connection, by Landahl⁽²⁰⁾. Thus, all that may be deduced from the eigenvalues of the Orr-Sommerfeld equation is the initial growth rate of the amplifying modes. The inclusion of important non-linear effects and flow divergence require further treatment to predict the growth of the mode towards its amplitude limiting state and ultimate decay.⁽²¹⁾

The linear perturbation theory for both two and three-dimensional jets, leading to solutions of equations analogous to the Orr-Sommerfeld equation, can be developed for both incompressible and compressible flow. Vortical, sound and entropy modes all occur in the compressible flow problem. The vortical modes, which were referred to above as the unstable modes, possess phase speeds which are comparable with the mean flow speeds in the jet. The sound modes, having phase speeds equal to the local speed of sound, are thought to be damped and are hence of relatively minor importance in determining the turbulent jet flow structure which is essentially unchanged from subsonic to supersonic jet velocities. When the mean flow speeds are supersonic the picture is somewhat confused since the vortical modes may now have supersonic phase speeds. The work of Tam⁽²²⁾ refers to this latter case and demonstrates the form of the amplifying mode wave fronts propagating downstream with supersonic phase speeds and forming weak moving shock fronts in the inner region of the flow external to the jet.

If we consider the case of subsonic mean flow, we find that at each station of the jet downstream of the jet exit an amplifying wave is set up which is distorted and damped by non-linear interactions and flow divergence effects. The major amplifying effects occur in the region upstream of the potential core since the local growth rates are related to the local width and jet centerline velocity. However, we have noted earlier that the linear perturbation solutions only describe the initial growth of a mode. The spatial behavior of the mode as it propagates downstream is governed by both the amplitude determined by non-linear considerations and the local wave number determined from linear theory. The typical streamwise disturbance behavior, including only effects of flow divergence, is given by Ling and Reynolds.⁽³⁰⁾ It is clear that there will be a wave number spectrum associated with this downstream behavior. This wave number spectrum will contain components with supersonic phase speeds, so that non-linear vortical modes cause acoustic radiation. It is also to be expected that, at the same time as this wave number spreading is occurring, a frequency spreading will also occur.⁽²³⁾ The randomized onset of the amplified wave and its subsequent development may be regarded as forming a large-scale structure in the turbulent motion and is the means by which energy is fed into the turbulence from the mean motion. The subsequent transfer of turbulent energy in different directions and its diffusion and final dissipation may be assumed to follow the usual Kolmogoroff cascade processes. However, the precise form of these processes does not seem to us to be of importance in the mechanism of sound generation and its ultimate radiation from the turbulent layer. We may also note that our theory has not taken account of intermittency since we have assumed the turbulent structure is evolving continuously.

In finding the most unstable (vortical) mode from the eigen solution of the Orr-Sommerfeld equation we assume that the background turbulence is of sufficiently small scale compared with the large-scale amplifying mode that its effect on that mode's development can be expressed in terms of an eddy viscosity supplanting the kinematic viscosity of the fluid. Therefore the effective Reynolds number of the turbulent flow is of $O(100)$ compared with a

value of 10^5 or greater when based on the kinematic viscosity. Typical curves of constant amplification for both two-dimensional and axisymmetrical flow ($n=0$) are shown in Figures 9 and 10, respectively. In Figure 11 is shown the Reynolds stress distribution corresponding to the inviscid $n=1$ mode for a circular jet. In Figure 12 the amplification and attenuation is shown for the axisymmetric mode $n=1$ when flow divergence effects are included. The eigen functions corresponding to the most unstable mode in a two-dimensional mixing region are shown in Figure 13 to reproduce the essential characteristics of the measured distribution of the Reynolds stress. Corresponding calculations for an elliptic jet have recently been given by Crighton(24).

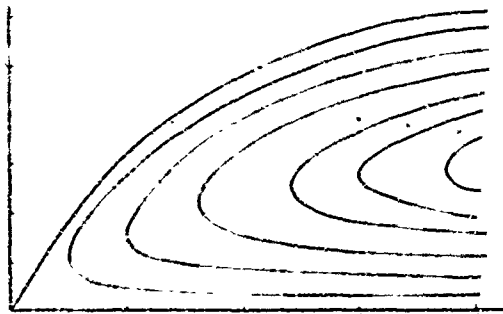


Figure 9. Curves of Constant Amplification Factor for Two-Dimensional Shear Layer.

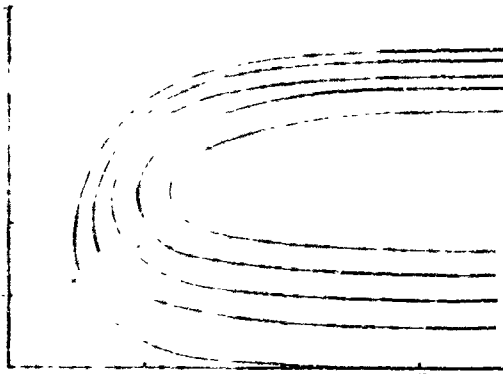


Figure 10. Curves of Constant Amplification Factor for Axisymmetric Jet at $y_1/d = 2.29$, $n = 0$.

These results give confidence that some of the essential features of the large scale motion in the turbulent mixing region of jets can be predicted. The connection through the detailed connection with some of the observable features needs further investigation and clarification. However, our overall picture is that of an order(1), stable, large scale motion set up in the turbulent mixing region which at any station has characteristics fixed by the frequency of the most unstable eigen mode at that station and the wave number spectrum associated with the downstream propagation of that frequency mode. It is the marginally stable local large scale structure which justifies the use of real wave numbers and real frequencies in the analysis used in Section 1-2.3 and

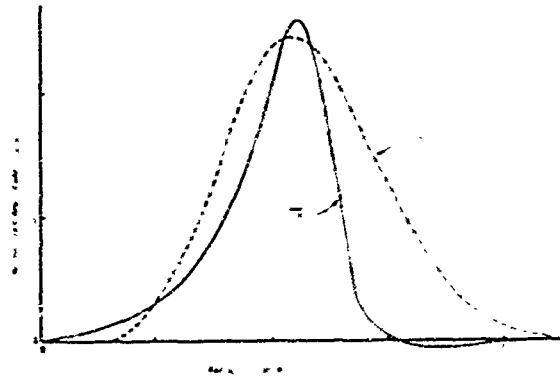


Figure 11. Distribution of $\overline{v_1 v_2}$ for Maximum Spatial Amplification. Axisymmetric Jet, $y_1/d = 2.29$. Disturbance Mode Number = 1 (Most Highly Amplifying).

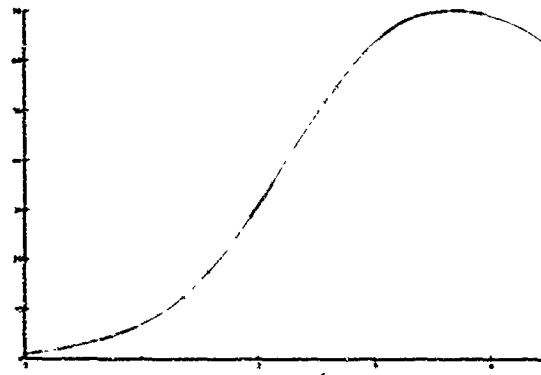


Figure 12. Growth of Disturbance Amplitude with Downstream Distance Due to Flow Divergence. Mode Number = 1. $u_1/d = 1.4$.

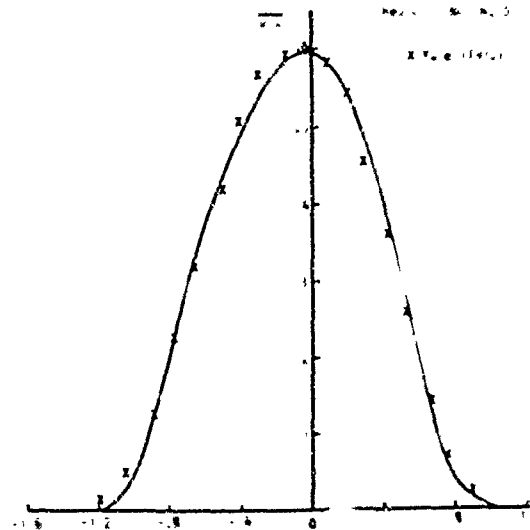


Figure 13. Distribution of $-\overline{v_1 v_2}$ for Maximum Spatial Amplification. Two Dimensional Shear Layer, Velocity Ratio 0.61.

... effects
 ... structure of
 ... possible
 ... function
 ... and from the
 ... to be used is
 ... preferably
 ... the general-
 ... 1-2.3. The
 ... input to
 ... position
 ... spectrum
 ... and the re-
 ... forms used in
 ... through this
 ... by the
 ... and that
 ... time-
 ... from

... global features
 ... that can be
 ... known
 ... to be very
 ... many
 ... and measured.
 ... applying the
 ... between
 ... motion generated
 ... distortion in
 ... conveniently
 ... and recourse to a
 ... necessary. The
 ... are given and

... essential to
 ... the convected
 ... function, re-
 ... noise generated,
 ... consistent
 ... structure
 ... region can be
 ... the stability of
 ... its mean flow
 ... not yet com-
 ... development of a
 ... generation of noise
 ... described.

... density at
 ... factor
 ... pressure and
 ... Fourier
 ...

- ρ_0 etc. reference scales of turbulence
 - M Mach number (\bar{v}_1/a_0)
 - P space-time covariance
 - p pressure
 - $q(\lambda_2)$ flow function
 - Q heat flux vector
 - r $1/\gamma \ln p$
 - s entropy
 - t time
 - T temperature
 - T_{ij} Lighthill's stress tensor
 - v velocity
 - V_c convection speed
 - V_j jet exit velocity
 - x position of observer, space vector
 - y position of source, space vector
 - Δ space separation in fixed coordinates
 - ξ space separation in moving coordinates
 - γ radian frequency; ratio of specific heats C_p/C_v in Appendix A
 - ζ source function
 - ρ density
 - θ angle to jet axis (positive downstream)
 - τ_{ij} viscous stress tensor
 - τ time difference, also retarded time difference
 - ψ dissipation function and wave number/frequency spectrum function
 - Ψ wave number/frequency spectrum function
 - ω_0 reference moving frame frequency in turbulence
 - ω moving frame radian frequency; radian frequency in Appendices A and B
 - ζ modified Fourier coefficient
- bar denotes a mean quantity
 prime denotes a fluctuating variable (except where specified)

References

1. Lighthill, M. J., On sound generated aerodynamically, I General theory. Proc. Roy. Soc. A211 p. 564-578, 1952.
2. Lighthill, M. J., On sound generated aerodynamically, II Turbulence as a source of sound. Proc. Roy. Soc. A222, p. 1-32, 1954.
3. Curle, S. N., The influence of solid boundaries on aerodynamic sound. Proc. Roy. Soc. A231, p. 505, 1955.
4. Ffowcs Williams, J. E., The noise of turbulence travelling at high speed, Phil. Trans. Roy. Soc. A255, p. 469-503, 1963.

5. Ribner, H. S., On the strength of noise sources along a jet. *J. Acous. Soc. Am.* V30, p. 876, 1958.
6. Ribner, H. S., The generation of sound in turbulent jets. *Advances in Applied Mech.* V. 8, p. 103, 1964.
7. Lilley, G. M., On the noise from air jets. *ARC 20 20376*, 1958.
8. Ribner, H. S., and Lee, H. K., Direct correlation of noise and flow of a jet. *J. Acous. Soc. Am.*, V. 52, p. 128, 1972.
9. Doak, P. E., Review of aerodynamic noise theories. *J. Sound Vib.*, V. 25, p. 185, 1972.
10. Crow, S. C. and Champagne, F. M., Grdery structure in jet turbulence. *J. Fluid Mech.* V. 48, p. 547, 1971.
11. Lau, J. C., Fuchs, H. V., and Fisher, F. M., A study of pressure and velocity fluctuations associated with jet flows. *Univ. of Southampton ISVR Rep. 28*, 1970.
12. Laufer, J., Kaplan, R. E., and Chu, W. T., On the generation of jet noise. *AGARD Meeting on Noise Mechanisms, Brussels*, 1973.
13. Lilley, G. M., On the noise from jets. *ACARD Meeting on Noise Mechanisms, Brussels*, 1973.
14. Csanady, G. T., The effect of mean velocity variations on jet noise. *J. Fluid Mech.*, V.26, p. 183, 1966.
15. Lush, P. A., Measurements of subsonic jet noise and comparison with theory. *J. Fluid Mech.*, V.46, p. 477, 1971.
16. Langer, R. E., On the connection formulas and the solutions of the wave equation. *Phy. Rev.* V. 51, p. 669, 1937.
17. Pao, S. P., Aerodynamic noise emission from turbulent shear layers. (To be published), 1973.
18. Lilley, G. M., A review of pressure fluctuations in turbulent shear layers. *Arch. Mech. Stos (2)* V. 16, p. 302, 1964.
19. Townsend, A. A., The structure of turbulent shear flow. *C.U.P.*, 1956.
20. Landahl, M. T., A wave-guide model of turbulent shear flow. *J. Fluid Mech.*, V. 29, p. 441, 1967.
21. Morris, P. J., The structure of turbulent shear flow. *Univ. of Southampton Ph.D. Thesis*, 1971.
22. Tam, C. K. W., Directional acoustic radiation from a supersonic jet generated by a shear layer instability. *J. Fluid Mech.*, V. 46, p. 757, 1971.
23. Stewartson, K., and Stuart, J. T., A non-linear instability theory for a wave system in Poiseuille flow. *J. Fluid Mech.*, V. 48, p. 529, 1971.
24. Crighton, D. G., Instability of an elliptic jet. *J. Fluid Mech.*, V. 59, p. 665, 1973.
25. Phillips, O. M., On the generation of sound by supersonic turbulent shear layers. *J. Fluid Mech.*, V. 9, p. 1, 1960.
26. Lighthill, M. J., The Bakerian Lecture, Sound generated aerodynamically. *Proc. Roy. Soc. A.267*, p. 147, 1961.
27. MacGregor, G. R., et al, "Basic" jet noise patterns after deletion of convection and refraction effects: experiment vs. theory. *J. Sound Vib.*, V. 27, pp. 437-454, 1973.
28. Yule, A., On the mixing of two parallel streams. Part II. *Univ. of Manchester, Ph.D. Thesis*, 1970.
29. Batchelor, F. K., and Gill, A. E., Analysis of the Stability of Axisymmetric Jets. *J. Fluid Mech.*, V. 14, p. 529, 1962.
30. Ling, C. H., and Reynolds, W. C., 'Non-parallel flow corrections for the stability of shear flows.' *J. Fluid Mech.*, V. 59, p. 571, 1973.

APPENDIX 1-2A

The Convected Wave Equation

The convected wave equation is derived by performing a number of operations on the conservation equations of mass, momentum, and energy and the equation of state. The gas is assumed to be perfect. It is convenient to consider as an alternative to the conservation of energy, the equation of entropy production.

Using a standard notation these equations may be written in the following form:

$$\text{Mass} \quad \frac{D\rho}{Dt} + \rho \nabla \cdot \underline{v} = 0 \quad (\text{A.1})$$

$$\text{Momentum} \quad \rho \frac{D\underline{v}}{Dt} + \nabla \cdot \underline{p} = \nabla \cdot \underline{\tau} \quad (\text{A.2})$$

$$\text{Entropy} \quad T \frac{Ds}{Dt} = \rho \frac{Dh}{Dt} - \frac{Dp}{Dt} = \nabla \cdot \underline{q} + \phi \quad (\text{A.3})$$

$$\text{State} \quad p = \frac{\gamma-1}{\gamma} \rho h \quad (\text{A.4})$$

where p , ρ , h , s are the pressure, density specific enthalpy and entropy respectively. γ is the ratio of specific heats, \underline{v} is the velocity, \underline{q} is the heat flux vector, $\underline{\tau}$ is the viscous stress tensor and ϕ is the dissipation function. These equations represent the necessary six equations for the six unknowns, p , ρ , h and \underline{v} .

On eliminating ρ and h between Equations (A.1), (A.3), and (A.4), we find

$$\frac{Dp}{Dt} + \gamma p \nabla \cdot \underline{v} = \rho a^2 \frac{D}{Dt} s/c_p \quad (\text{A.5})$$

where $a^2 = (\gamma-1)h$ is the local speed of sound

squared, and C_p is the specific heat at constant pressure. On combining the divergence of Equation (A.2) with D/Dt of Equation (A.5), we find

$$\begin{aligned} & \frac{\partial^2 p}{\partial t^2} + 2\bar{v} \cdot \nabla \frac{\partial p}{\partial t} + (\bar{v} \bar{v} - a^2 \underline{I}): \nabla \nabla p - a^2 \nabla \rho \cdot \nabla s / C_p \\ & = \rho a^2 \nabla \underline{v}: \nabla \underline{v}^+ + \frac{1}{\rho} \left(\frac{D\rho}{Dt} \right)^2 + \gamma p \frac{\partial^2 s / C_p}{\partial t^2} - \\ & - a^2 (\nabla \cdot \underline{v}) \cdot \nabla s / C_p - a^2 \nabla \cdot (\nabla \cdot \underline{v}) \end{aligned} \quad (A.6)$$

where $\nabla \underline{v}^+$ is the transpose of $\nabla \underline{v}$, \underline{I} is the idem factor and the usual notation for the double multiplication of dyads is employed. This equation is exact and has been the starting point of many unsteady flow problems. In many aerodynamic noise investigations the terms involving viscous and entropy terms have usually been neglected with a priori justification. In such an approximation

$$\begin{aligned} & \frac{\partial^2 p}{\partial t^2} - a^2 \nabla^2 p + \frac{\nabla \rho \cdot \nabla p}{\rho} - \frac{1}{\rho} \left(\frac{D\rho}{Dt} \right)^2 \\ & = \rho a^2 (\nabla \underline{v}: \nabla \underline{v}^+) \end{aligned} \quad (A.7)$$

and can be rearranged to form an inhomogeneous equation in p , in which the right-hand side contains non-linear terms in p and terms not linearly dependent on p . Such an equation was derived by Phillips(25) and forms the basis of his theory of aerodynamic noise for flows having supersonic convection speeds.

However, in all turbulent flow problems it is not immediately obvious that the terms involving entropy changes are negligible compared with the remaining terms in Equation (A.6). Apart from the heat conduction term, entropy production arises from the finite value of the dissipation function and in a turbulent flow the overall dissipation of turbulent energy is balanced by the rate of production of turbulent energy from the main flow. It follows that the terms in entropy are not negligible compared with, say, $\rho a^2 (\nabla \underline{v}: \nabla \underline{v}^+)$ and must therefore be retained.

If we return to Equation (A.6) and eliminate s using Equation (A.3) then we find after some lengthy algebra that

$$\begin{aligned} & \frac{\partial^2 p}{\partial t^2} + (\gamma+1) \bar{v} \cdot \nabla \frac{\partial p}{\partial t} + (\gamma \bar{v} \bar{v} - \underline{I} a^2): \nabla \nabla p - \\ & - a^2 \nabla \rho \cdot \nabla (\ln h) - (\gamma-1) \frac{\partial \rho}{\partial t} \frac{D}{Dt} (\ln h) \\ & = \rho a^2 (\nabla \underline{v}: \nabla \underline{v}^+) - \frac{\gamma-1}{2} \rho \frac{\partial^2 v^2}{\partial t^2} + \\ & + \rho a^2 \left\{ \left(\frac{1}{\gamma} \frac{\partial \ln p}{\partial t} + \bar{v} \cdot \nabla \ln p \right) \frac{D \ln p}{Dt} - \left(\frac{D \ln h}{Dt} \right)^2 \right\} \end{aligned} \quad (A.8)$$

where the terms involving divergences of the heat conduction and viscous terms have been excluded for convenience in writing down the equation. Equation (A.8) is a more appropriate equation to use in problems of aerodynamic noise generation than say,

Equation (A.7), although it is not convenient to proceed without first eliminating ρa^2 from the right-hand side.

If we choose a new variable

$$r \equiv \frac{1}{\gamma} \ln p$$

then the equation for r corresponding to Equation (A.8) is

$$\begin{aligned} & \frac{\partial^2 r}{\partial t^2} + (\gamma+1) \bar{v} \cdot \nabla \frac{\partial r}{\partial t} + (\gamma \bar{v} \bar{v} - \underline{I} a^2): \nabla \nabla r - \\ & - a^2 \nabla \ln h \cdot \nabla r - (\gamma-1) \frac{\partial r}{\partial t} \frac{D \ln h}{Dt} \\ & = \nabla \underline{v}: \nabla \underline{v}^+ - \frac{\gamma-1}{2a^2} \frac{\partial^2 v^2}{\partial t^2} - \left(\frac{D \ln h}{Dt} \right)^2 + \gamma a^2 \nabla r \cdot \nabla r \end{aligned} \quad (A.9)$$

where again for convenience the terms involving viscous and heat conduction terms have not been written out. It would appear that Equation (A.9) is a convenient starting point for problems of aerodynamic noise generation. It should be emphasized, however, that if viscous and heat conduction terms are to be ignored in a problem of aerodynamic noise generation from a turbulent flow then the governing equations from which Equation (A.9) has been derived are as follows:

$$\gamma \frac{Dr}{Dt} + \nabla \cdot \underline{v} = \frac{D \ln h}{Dt} \quad (A.10)$$

which is the combined equation of state and continuity,

$$\frac{Dv}{Dt} + a^2 \nabla r = 0 \quad (A.11)$$

the equation of motion, and

$$\frac{Dh_s}{Dt} = a^2 \frac{\partial r}{\partial t} \quad (A.12)$$

which is the total energy equation, where $h_s \equiv h + 1/2 v^2$ is the specific stagnation enthalpy.

In applications of Equation (A.9) to jet flows we can assume that $\nabla \bar{r} = 0$, where \bar{r} is the time mean of r . Thus, on retaining only linear terms in r' , the fluctuating part of r , on the left-hand side of Equation (A.9) we find

$$\begin{aligned} & \frac{\partial^2 r'}{\partial t^2} + (\gamma+1) \bar{v} \cdot \nabla \frac{\partial r'}{\partial t} + (\gamma \bar{v} \bar{v} - (\gamma-1) \bar{h} \underline{I}): \nabla \nabla r' - \\ & - (\gamma-1) \nabla \bar{h} \cdot \nabla r' - 2 \nabla \bar{v} : \nabla \underline{v}'^+ \\ & = \text{'non-linear' terms.} \end{aligned} \quad (A.13)$$

where we have assumed additionally that $D \ln h / Dt = 0$ and the right-hand side contains terms which in many applications will be found to have the same order of magnitude as $(\nabla \underline{v}': \nabla \underline{v}'^+)$ or less. However, in hot jet flows at low speeds, for instance, this is not necessarily the case and additional terms will then appear on the left-hand

side of Equation (A.13). This will also be the case in flows of high Mach number. In all these cases the additional terms can easily be found from Equation (A.9).

Further simplifications are possible on the assumption that the jet is slowly diverging so that the mean velocity field can be represented by $\bar{v} \equiv (\bar{v}_1, 0, 0)$, where \bar{v}_1 is a strong function of the coordinate transverse to the flow, say x_2 , and is a slowly varying function of x_1 , the coordinate in the direction of flow. We thus use the boundary layer approximation that

$$\frac{\partial \bar{v}_1}{\partial x_2} \gg \frac{\partial \bar{v}_1}{\partial x_1}$$

Similarly we assume that for the mean enthalpy distribution, noting that $(\gamma-1)h = a^2$,

$$\frac{\partial \bar{h}}{\partial x_2} \gg \frac{\partial \bar{h}}{\partial x_1}$$

With these additional approximations Equation (A.13) reduces to

$$\begin{aligned} & \frac{\partial^2 r'}{\partial t^2} + (\gamma+1) \bar{v}_1 \frac{\partial^2 r'}{\partial \partial x_1} + \gamma \bar{v}_1^2 \frac{\partial^2 r'}{\partial x_1^2} - \bar{a}^2 \nabla^2 r' \\ & - (\gamma-1) \frac{\partial \bar{h}}{\partial x_2} \frac{\partial r'}{\partial x_2} - 2 \frac{\partial \bar{v}_1}{\partial x_2} \frac{\partial v_2'}{\partial x_1} \quad (A.14) \\ & = \text{'non-linear' terms.} \end{aligned}$$

In Equation (A.14) we have assumed that the non-linear terms include the terms involving the stagnation enthalpy fluctuations. When these terms cannot be so regarded, noting for instance the relation between the stagnation enthalpy fluctuations and the fluctuations in pressure given by Equation (A.12), then additional terms must be included in the left hand side of Equation (A.14). We see therefore that though the form given for Equation (A.14) is not unique it can be regarded as suitable for many practical applications.

In deriving Equations (A.9) or (A.13) or (A.14) as an equation for the fluctuations in r , some knowledge of the mean and fluctuating flow fields must be assumed. If for instance it is assumed that both the mean and fluctuating velocity and enthalpy fields are known, in the absence of the fluctuating field generated by the r' fluctuations, then provided the latter are small, we can assume that in Equations (A.10), (A.11) and (A.12) all terms other than those involving the derivatives of r' are known. This indeed is the only justification for the use of an equation of the type given by Equation (A.14). Thus in Equation (A.14) it can be taken that

$$\frac{\partial \bar{v}_1}{\partial x_2} \frac{\partial v_2'}{\partial x_1}$$

† A possible modification to Equation (A.14) to include the practical case mentioned above would be to replace $\partial \bar{h} / \partial x_2$ by $\partial \bar{h}_s / \partial x_2$ on the left-hand side.

is a known quantity and should be regarded as a 'source' term to be included with other 'source' terms on the right-hand side of the equation. This was indeed the basis for the theory of Phillips(25) referred to above, and has more recently been used by Lilley(18) and Pao(17). Nevertheless since v_2' and r' are linearly dependent, as given by Equation (A.11), it is necessary to eliminate the term in $\partial v_2' / \partial x_1$ so that finally the right hand side of Equation (A.14) contains only terms which are either not linearly dependent on r' or are of an order of magnitude negligible compared with other terms retained in the equation.

From Equation (A.11) we find that

$$\frac{\partial v_2'}{\partial t} + \bar{v}_1 \frac{\partial v_2'}{\partial x_1} + \bar{a}^2 \frac{\partial r'}{\partial x_2} = \text{non-linear terms} \quad (A.15)$$

and so we can eliminate $\partial v_2' / \partial x_1$ from Equation (A.14), by operating on it with the operator D/Dt v_2' . The resulting equation, which is third-order in r' , is

$$\begin{aligned} & \frac{\partial^3 r'}{\partial t^3} + (\gamma+2) \bar{v}_1 \frac{\partial^3 r'}{\partial t^2 \partial x_1} + \left\{ (2\gamma+1) \bar{v}_1 - \bar{a}^2 \right\} \frac{\partial^3 r'}{\partial t \partial x_1^2} \\ & - \bar{a}^2 \frac{\partial^3 r'}{\partial t \partial x_2^2} + (\gamma \bar{v}_1^3 - \bar{v}_1 \bar{a}^2) \frac{\partial^3 r'}{\partial x_1^3} - \\ & - \bar{a}^2 \bar{v}_1 \frac{\partial^3 r'}{\partial x_1 \partial x_2^2} - (\gamma-1) \frac{\partial \bar{h}}{\partial x_2} \frac{\partial^2 r'}{\partial t \partial x_2} - \bar{a}^2 \frac{\partial^3 r'}{\partial t \partial x_2^2} - \\ & + \left\{ 2\bar{a}^2 \frac{\partial \bar{v}_1}{\partial x_2} - (\gamma-1) \bar{v}_1 \frac{\partial \bar{h}}{\partial x_2} \right\} \frac{\partial^2 r'}{\partial x_1 \partial x_2} - \bar{a}^2 \bar{v}_1 \frac{\partial^3 r'}{\partial x_1 \partial x_2^2} \\ & = \Lambda(x, t) \quad (A.16) \end{aligned}$$

where Λ contains only terms not linearly dependent on r' plus terms involving enthalpy and stagnation enthalpy fluctuations.

This form of the generalized convective wave equation reduces to the simpler form

$$\begin{aligned} & \frac{\bar{D}^3 r'}{\bar{D}t^3} - \frac{\bar{D}}{\bar{D}t} \text{div}(\bar{a}^2 \nabla r') + \\ & + 2\bar{a} \frac{\partial \bar{v}_1}{\partial x_2} \frac{\partial^2 r'}{\partial x_1 \partial x_2} = \Lambda'(x, t) \quad (A.17) \end{aligned}$$

where Λ' contains only non-linear terms, when γ , the ratio of the specific heats, tends to unity. For this special case the stagnation enthalpy fluctuations in the convective frame must vanish. Equation (A.17) is also found when the entropy production terms are neglected completely. A similar equation was previously given by Landahl(20) in his work on turbulent pressure fluctuations in boundary layer flows.

Equation (A.17) shows that whereas the first two terms are just $\partial/\partial t$ of the convected wave equation in an inhomogeneous medium, the third term is the result of the interaction between the disturbance (the fluctuations in r) and the mean flow field arising from fluctuations in the source term Λ^1 .

Now in the derivation of Equations (A.16) or (A.17) the assumption has been made that the mean flow field is slowly diverging. Hence locally at any station $x_1 = X_1$ along the jet we can Fourier decompose the fluctuations in r^1 in terms of frequency ω and real wave number components k_1 and k_2 by application of the Fourier transformation

$$r^1 = \int \exp \left[i\omega t + k \cdot x \right] d\tilde{\omega}^1(x_2; \omega, k; X) \quad (A.18)$$

where $k \equiv (k_1, k_2)$ and $d\tilde{\omega}^1$ is the Fourier coefficient which is not in general of total bounded fluctuation. In place of $d\tilde{\omega}^1$ it is convenient to employ a modified Fourier coefficient ζ given by

$$\zeta = \frac{\tilde{\omega}^1}{a_\infty} \frac{\omega}{(\omega + \bar{v}_1 k_1)} d\tilde{\omega}^1 \quad (A.19)$$

where a_∞ is the constant speed of sound in the uniform medium outside the flow. In terms of ζ the Fourier transformation of Equation (A.17) reduces to the characteristic equation

$$\frac{d^2 \zeta}{dx_2^2} + q(x_2) \zeta = h \quad (A.20)$$

where

$$q = \left\{ \frac{\omega'^2}{\bar{a}} - k^2 + \frac{\bar{v}_1'^2 k_1}{\omega'} - \frac{2k_1^2 \bar{v}_1'^2}{\omega'^2} - \frac{\bar{a}'}{\bar{a}} - \frac{2\bar{a}' \bar{v}_1' k_1}{\bar{a} \omega'} \right\}$$

$$h = \frac{i \omega d \gamma}{\bar{a} a_\infty \omega'^2}$$

$$\omega' = \omega + \bar{v}_1 k_1$$

and $d\gamma$ is the Fourier coefficient of the 'source' function. ω' is the moving frame frequency and primes on \bar{a} and \bar{v}_1 denote differentiations with respect to x_2 . The Fourier coefficient ζ is a function of x_2, ω, k_1, k_2 and X .

We see that Equation (A.20) is the standard diffraction equation of inhomogeneous type. For a given frequency ω and wave number vector k the mean velocity and temperature fields determine the function q , and will therefore be referred to as the flow function.

A similar characteristic equation is found for an axisymmetrical flow field. In this case the transverse coordinate x_2 is the flow radius. The relations for ζ , which we write as $\zeta, (3)$ are now changed as well as those for h and q . We find, however, that

$$-(3)'' + q(3) \zeta(3) = h(3) \quad (A.21)$$

The solution of Equations (A.20) or (A.21) cannot be obtained analytically and resort is made to either approximate analytic solutions or numerical solutions. In either case the equation to be solved is

$$\zeta'' + q \zeta = \delta(x_2 - x_2^1) \quad (A.22)$$

where δ is the delta-function and x_2^1 is the 'source' location. If the solution so obtained is

$$\zeta = \zeta(x_2; x_2^1)$$

for given values of ω and k and distributions of \bar{v}_1 and \bar{a} then the solution for any source function distribution is

$$\zeta(x_2) = \int_{-\infty}^{\infty} h(x_2^1) g(x_2; x_2^1) dx_2^1 \quad (A.23)$$

The corresponding value for the wave-number/frequency spectrum function of the function r^1 is

$$\Psi(x_2; k, X) = \left| \frac{d\tilde{\omega}^1 d\tilde{\omega}^2}{dk_1 d\omega} \right|_{dk_1, d\omega \rightarrow 0}$$

$$= \frac{\omega'(x_2)^2}{\bar{a}(x_2)^2} \int_{-\infty}^{\infty} dx_2^1 \frac{\bar{a}(x_2^1)}{\omega'(x_2^1)} \int_{-\infty}^{\infty} dx_2^{1*} \frac{\bar{a}(x_2^{1*})}{\omega'(x_2^{1*})}$$

$$\cdot \phi(x_2^1; x_2^{1*}; k, \omega) g(x_2; x_2^1) g^*(x_2; x_2^{1*}) \quad (A.24)$$

where

$$\phi(x_2^1; x_2^{1*}; k, \omega) = \left| \frac{d\gamma d\gamma^*}{dk_1 d\omega} \right|_{dk_1, \omega \rightarrow 0}$$

is the wave number/frequency spectrum function of the source function Λ , and $*$ denotes the complex conjugate.

Throughout this Appendix the coordinates used have been fixed coordinates and hence the spectrum functions ϕ and Ψ are also evaluated in a fixed frame. Since ϕ must be specified as representing the known flow field, in general it will be determined with respect to a moving frame of reference and finally transformed to its corresponding value in a fixed set of coordinates.

In concluding this Appendix on the generalized convection equation for r , it is stressed that throughout it is assumed that the flow field can be determined at any station as the sum of a time mean value plus a fluctuating value, which is locally a random function of space and time. In the case of a turbulent jet flow where most of the flow is turbulently intermittent and whose large-scale

structure is known from experiment to be quasi-ordered it is clear that our flow model used in the theoretical analysis is grossly over-simplified. However, in this respect our model is no more simplified than in the related treatments of Lighthill(26), Ffowcs Williams(4), Phillips(25), Ribner(6) and Pao(17).

APPENDIX 1-2B

The Wave-Number-Frequency Spectrum Function
In Fixed and Moving Coordinates

The solution of aerodynamic noise problems requires the specification of a space-time covariance in turbulent flow. In general this function must be obtained from experiment. It can be specified in terms of a fixed set of coordinates or equivalently in a moving frame of reference for which the velocity is that of the mean convective velocity of the turbulence. Thus, the space-time covariance for the source function associated with, say, vortical and non-isentropic modes in the turbulence connected with the local mean speed and expressed in moving coordinates, but evaluated at a fixed station \underline{x} would have a form

$$P(x_2; \tau; \underline{\delta}; \underline{x}) = P(x_2; \underline{x}) \cdot \exp \left\{ -\bar{\delta}_1^2 - \bar{\delta}_3^2 - \bar{\tau}^2 \right\} \quad (B.1)$$

where $\delta_1, \delta_3,$ and τ are the space and time separations in moving coordinates and $\bar{\delta}_1 = \delta_1/l_1;$
 $\bar{\delta}_3 = \delta_3/l_3; \bar{\tau} = \omega_0 \tau$ where l_1, l_3, ω_0 are reference length scales and a reference frequency respectively.

If $\underline{\Delta}$ is the space separation vector in fixed coordinates

$$\underline{\delta} = \underline{\Delta} - \underline{a}_0 \underline{M} \tau \quad (B.2)$$

where $\underline{a}_0 \underline{M} \equiv (V_c, 0, 0),$ and then the space-time covariance in a fixed frame is given by

$$P(\tau, \underline{\delta}) \equiv P(\tau, \underline{\Delta}) - P(x_2; \underline{x}).$$

$$\cdot \exp \left\{ -\bar{\Delta}_1^2 - \bar{\Delta}_3^2 - \bar{\tau}^2 (1 + V_c^2/l_1^2 \omega_0^2) + 2V_c \tau \bar{\Delta}_1/l_1^2 \right\} \quad (B.3)$$

The spectral density of $P(\tau, \underline{\Delta})$ is for $\omega_0 l_1/V_c \ll 1,$

$$\frac{P(\omega, \underline{\Delta})}{P(x_2; \underline{x})} = \exp \left\{ -\frac{i\omega \Delta_1}{V_c} \right\} \exp \left\{ -\frac{\bar{\omega}^2 \bar{\Delta}_1^2 - \bar{\Delta}_3^2 - \bar{\omega}^2}{2\sqrt{\pi} V_c/l_1} \right\} \quad (B.4)$$

where $\bar{\omega}_0 = \omega_0 l_1/V_c$ and $\bar{\omega} = \omega l_1/V_c,$ a result quite different in structure to Equation (B.1). The fixed frame result has a form of a slowly damped wave function which is often interpreted as representing the near-frozen pattern of turbulent motion in a given frequency band. The reference frequency in the moving frame is ω_0 whereas in the fixed frame it is $V_c/l_1.$ Although the space-time covariance in moving coordinates can be transformed to fixed coordinates with comparative ease the reverse is not true. These simple results can easily be generalized to other forms of space-time covariance functions.

Of particular importance is the result given by Equation (B.4) showing that the effective scale length in fixed coordinates in the stream direction is $V_c/\omega_0,$ and not, as usually incorporated in the fixed frame covariance, $l_1.$

1-3. ON THE RESPECTIVE ROLES OF HELMHOLTZ-TYPE INSTABILITIES AND ACOUSTIC PROPAGATION IN JET NOISE GENERATION AND RADIATION

PHILIP E. DRISK
University of Southampton, England

1-3.1 Introduction

In the 19th century, Helmholtz, Kelvin and Rayleigh established that sheared flows of a viscous, heat conducting fluid could, in certain circumstances, exhibit unstable tendencies. For example, if the fluid in the neighborhood of a point in a previously undisturbed, steady, laminar shear layer were to be subjected to a small impulsive disturbance, then the layer downstream of the region of disturbance would subsequently go into oscillations of increasing amplitude. These oscillatory, "unstable" tendencies of the layer are convective, in the sense that, if checked, the amplitude of oscillation would increase, both with distance downstream of the region of disturbance and with time. In other words, the amplitude of unstable oscillation is, as it were, zero for $t-x/V_c < 0$ and thereafter increases monotonically, and often very rapidly, with $t-x/V_c$. Here x is distance downstream from the point of disturbance, t is time subsequent to the time of disturbance and V_c is a convection velocity, which is usually of the order of the average velocity in the x -direction of the fluid in the layer (the average across the layer, that is).

In subsequent studies of the behavior of sheared flows, including those of the present day, this concept of "Helmholtz instability" has been of great consequence. In particular, it has been of central importance in developing understanding of the transition from laminar to turbulent flow of a free shear layer. A problem in this category is that of the development of the mean and turbulent flow characteristics of subsonic and supersonic jets.

In real fluid flows, of course, in which unstable tendencies of the Helmholtz type have been identified and observed, unbounded growth of the oscillations does not occur. The amplitude of oscillation reaches a maximum, almost always after a relatively very short time, and then subsequently decays. In the case of jet flows it has been argued, and/or suggested, that viscosity and heat conduction, flow divergence, non-linear interactions and acoustic radiation may all, either individually or collectively, play some part in the limitation and decay of any such oscillations.

Present experimental and theoretical evidence on the turbulent and mean flow structure of jets, and on the sound fields radiated by them, rather strongly suggests that the process of the growth, limitation and decay of such Helmholtz-type oscillations, in real fluids, may be very closely connected with the process of sound radiation by a turbulent jet. The basic evidence for such a belief is both simple and convincing. First, the region in which Helmholtz-type "instabilities" could be dominant flow components, and be largely instrumental in the dynamical process of converting the jet structure from, effectively, a "plug" flow profile at the jet exit to, eventually, a fully developed turbulent jet, is that extending some ten diameters or so downstream from the exit: that is, the region in-

cluding the potential core and the conically annularly spreading "turbulent" mixing region surrounding it. Second, the region of the jet flow from which the majority of the radiated sound field appears to emanate is precisely the same region. Hence, the process of sound generation must be at the least, a by-product of, if not actually intrinsic to, the process of the development of the mixing region from a thin annular layer at the jet exit into a fully developed turbulent jet flow downstream from the end of the potential core.

It follows at once from this that the detailed nature of this flow development must be relevant to the sound generation process, and *vice versa*. All that remains in question is that of exactly which details of the flow development are mutually relevant.

Self-evidently, since the complete problem is that of determining the flow field both inside and outside the jet (i.e., the nominally "turbulent mixing flow" field inside and the nominally "acoustic" field outside), this remaining question can also be approached either from inside or outside. In the nature of things, one must expect acousticians to prefer the "outside" approach and fluid dynamicists the "inside" one. Similarly, when studies from two such different starting points are undertaken, one cannot expect results which are automatically and instantly in forms displaying the desired mutual relevance.

It is not surprising, therefore, that from recent studies of the two types an apparently fundamental problem of reconciling results and methods has emerged. What is surprising is that this problem of reconciliation is not just an academic one but that it has turned out to be crucial to achieving a common, basic, physical understanding of the processes involved.

In its essentials, the problem of reconciliation can be described in the following terms. From the "Helmholtz instability" approach (i.e., the "inside" approach), present experimental and theoretical evidence suggests that the "acoustic part" of the field, both inside and outside the jet, can be regarded simply as an intrinsic part, locally, of the turbulent mixing flow field. Hence, for example, a *separate* physical identification of (or theoretical calculation of) this "acoustic part" of the field is neither necessary nor permissible. From the "acoustic" (i.e., "outside") approach, however, present experimental and theoretical evidence equally strongly suggests that there is a separately identifiable "acoustic" field both inside and outside the jet, which is a sum of contributions from all regions of the jet in which turbulent mixing is taking place. Thus, this acoustic field is a *collective* property of the whole jet flow rather than just a *local* property determined primarily by local details of the turbulent mixing. Hence, *separate* identification of the "acoustic part" of the field (or theoretical calculation of it from a reasonably

accurate model of the entire region of turbulent mixing flow) is not only permissible but desirable (and, in practice, for reasons to be explained later, it may be necessary).

From this description of the reconciliation problem two key questions can be formulated. (i) Are the two approaches really, and not just apparently, producing mutually contradictory concepts and results, and is one or the other therefore valid? (ii) If both approaches are fundamentally valid, how can the "acoustic" field be determined as part of the "turbulence mixing" flow or, alternatively, how can the aspects of the "turbulent mixing" flow that do determine the "acoustic" field be evaluated so that "separate" determination of the "acoustic" field from them is permissible?

The answer to the first question is that the two approaches are not mutually contradictory in any way and that neither is invalid. Justification for this statement, in the form of a proof of the validity of the "acoustic" approach solution, is given in Appendix 1-3A. Physical clarification and discussion of the situation is given in the next section, in which also answers to the second question are proposed.

1-3.2 Discussion

1-3.2.1 The Helmholtz "Instability" Approach

The apparent difficulties referred to in question (i) of the reconciliation problem arise primarily from physical misinterpretation of the physical significance, and applicability to real fluid flows, of the familiar Helmholtz instability motion of *linear* type, which is mathematically unbounded in space and time. As pressure, density and velocity fluctuations in real fluid flows are bounded, no mechanical function of unbounded behavior can be permitted to represent real flow fluctuations. The theoretical consequences of this necessary restriction on the solutions of whatever equations are used to provide a mathematical model of the flow field are, fairly rigorously, derived and stated in Appendix 1-3A. (These results will be used in the remainder of this discussion, translated into physically descriptive terms, without any further proof of their validity, as this obviously would be unnecessary and redundant.)

Thus, *real* Helmholtz-type "instability" motion is not "unstable" at all. Instead, real Helmholtz-type instability motion is an oscillation that, beginning near the jet exit, grows initially with fair rapidity, as it is convected down the jet mixing region, and then with almost equal rapidity becomes limited in amplitude and decays away. The longest time scale for the growth-decay lifetime of such a disturbance is of the order of the transit time of a fluid particle in going from the jet exit to the end of the potential core. The longest length scales are of the order of the jet diameter. Non-dimensional frequencies (Strouhal numbers) characteristic of the larger, and initially more rapidly growing, disturbances are of order unity (based on jet exit diameter and velocity).

In high speed jet flows there is as yet no experimental evidence available which can be said to constitute direct and conclusive identification of the existence and/or characteristics of this type of

motion. The circumstantial evidence, both experimental and theoretical, however, is considerable, and it is generally agreed that the developing turbulent mixing region of a jet is dominated by some kind of superposition and/or interactions of motions of this type. The lack of direct experimental evidence can be ascribed to the usual well known experimental difficulties of making and interpreting observations of fairly random, convected fluctuations in high speed flows.

Experiment is not alone in being unable, as yet, to produce more than approximate descriptions of the character of the turbulent mixing region motion. When one attempts to go beyond a linearized theory of the Helmholtz-type motion, to obtain the physically necessary amplitude limitation, decay and non-linear interactions of the Helmholtz-type motions, mathematical difficulties arise, and again it must be said at present that results as detailed as one would like are as yet unobtainable. However, by use of the methods developed by Morris and Lilley (1,2), a working model of *real fluid* Helmholtz-type motions can be obtained. In this model, reasonably accurate growth-limitation-decay amplitude envelopes can be obtained for the range of the representative Helmholtz-type motions that can be expected to dominate the mixing region motion. Also, the spatial distribution (both axial, radial and circumferential), the convection velocity, the phase or group velocity, and the frequency power spectral density of each of these "wave-packets" can be obtained. Some phase information on the fluctuations in the packets is obtainable, but not complete information. Further, the model includes non-linear interaction effects among the several quasi-linear Helmholtz "instability" modes only to the extent of providing, approximately, the limitation-decay portion of the amplitude envelope for each quasi-linear mode.

There is little doubt that this amplitude-limited Helmholtz-type "instability" model is fully capable of providing a very good representation of the *measurable*, locally dominant features of the mean and fluctuating flow in a jet turbulent mixing region. Indeed, one would expect that the results may well be, if anything, *more* accurate and detailed in a number of respects than those which can be measured by any present, or presently envisaged, measurement techniques.

However, there must be grave doubts as to whether the results from the model in its present stage of development can be *directly* extended into regions outside the jet to provide an adequately representation of the radiated acoustic field. The reason for these doubts is that the fluctuating motion inside the mixing region, which the model *can* represent with considerable accuracy, is very much dominated by convected wave-packets of *subsonic* phase velocities (except, of course, when the jet speed is so high that the "eddy convection velocity" itself becomes supersonic — i.e., the jet speed is of the order of twice the speed of sound). It is well known, however, that *only* the components of the fluctuating motion in the mixing region that have *supersonic* phase velocities, will produce any radiated acoustic field at all. Such components, in the amplitude-limited, Helmholtz-type "instability" representation of the mixing region, will arise almost entirely from the non-linear interaction processes among the quasi-linear Helmholtz-type modes and, as has been explained, the model presently incorporates such effects only in an approxi-

mate way, primarily to provide the amplitude limitation and decay. In particular, the supersonic phase speed components can be expected to be somewhat sensitive to the phase information in the wave-packet fluctuations and, as has been mentioned, this information is not completely included in the model.

(It has been suggested, incidentally, that flow divergence effects may assist in the active coupling of the mixing region flow field to the external acoustic field, but from the standpoint of a connected wave equation analysis of the acoustic radiation problem it appears that this is not at all an effective enough form of active coupling.)

Of course, if either theoretical or experimental techniques were available to provide a sufficiently detailed and accurate description of *both* the supersonic *and* subsonic phase velocity components of the mixing region fluctuations, direct extension of the mixing region flow outward to accurately include the entire radiated acoustic field would certainly be possible. Any correct model of the mixing region flow fluctuations, such as that of Morris, must, of course, include correct boundary conditions at large distances from the flow (i.e., acoustic radiation conditions). Thus, in principle, any such model can be extended directly to include an acoustic radiated field. It is only because of the present imperfect state of knowledge and limited available computational techniques that there can be little confidence in the accuracy of such a directly extended result at present, despite the fact that the model *can* be very confidently expected to give a highly accurate and detailed description of the directly measurable properties of the mixing region itself.

This situation, of course, arises directly as a consequence of the principle, first enunciated by Lighthill(3) and recognized by him as the cornerstone of aerodynamic noise theory: namely, that acoustic radiation in general is very much a by-product of practically no significance to the total fluctuating power, of a jet flow.

Thus the present, and immediately foreseeable situation is that development of the Helmholtz-type "instability" approach can be expected to provide better and better descriptions of the mixing region flow, but not yet by itself, directly, better (or even perhaps adequate) descriptions of the radiated acoustic field.

It is patently clear that in such a situation, any "separate", exact descriptions of the dependence of the acoustic field on the *entire* mixing region flow field which may be available must be employed to, at the least, provide whatever information is available on the *collective* (as distinct from *direct*) mutual dependence.

It is also a presently valid inference that even if the Helmholtz-type "instability" approach could be so refined as to become capable of direct extension to include the radiated acoustic field, the dominance of the mixing region flow field by disturbance of subsonic phase velocities is so great that the *collective* "acoustic" approach would still be necessary to provide the information on inherent cancellation effects, etc. (such as given intrinsically by Lighthill's quadrupole form of the source distribution, e.g.) which will be required for any calculation of the acoustic radiation field to be done in practice, rather than just in principle.

In this context the Helmholtz-type "instability" approach can be regarded, in the language of the method of matched asymptotic expansions, as being used, as it were, to provide the "inner expansion" of the complete flow field, with the "acoustic" approach providing the "outer expansion". Methods of matching the two "expansions", which are valid in principle, include both that of using the "inner" field as an acoustic source distribution from which the "outer" radiated acoustic field can be calculated and that of actually matching the two "expansions" over some convenient outer boundary of the jet. (Use of this simile for descriptive purposes should not be taken to imply that either approach is intrinsically capable of giving correct answers in only one or the other of the two, "inner" and "outer", regions. In principle, of course, both methods are perfectly valid for both regions.)

1-3.2.2 The "Acoustic" Approach

In Appendix 1-3A it is proved that the "acoustic" approach, in which, say, the fluctuating pressure is represented everywhere as a superposition of "acoustic" waves, arising from either "equivalent" or "true" sources representing the exact, "non-acoustic" motions of the fluid, provides a *complete* and *unique* representation of the fluctuating pressure *everywhere*, both inside and outside the jet. The representation is unique in the sense that, although the functional form of the representation may equally well be expressed in other forms (i.e., for example, in terms of Bessel functions instead of sines and cosines, etc.), any other valid equivalent functional form must give the same pressure as a function of space and time. In the context here, the field variable thus represented could equally well be the fluctuating part of the logarithm of the pressure, or the acoustic momentum potential, etc. Also, the "acoustic" waves thus being superposed to make up the total representation are understood, broadly speaking, to be nearly locally adiabatic pressure disturbances in the form of elementary wave trains or wave-packets, each travelling at a phase speed of approximately the speed of sound relative to the locally moving fluid. (This broad interpretation of the superposed elements as "acoustic" waves must not, of course, be taken too literally, or out of context. For example, Lighthill's exact formulation of his "equation of aerodynamic sound" requires one to conceive of thermal diffusion of density at constant pressure as a process made up as a superposition of acoustic waves (!), and is nonetheless an *exact* representation.)

It is also similarly proved in Appendix 1-3A that although the "acoustic" approach, in the special case of domains of *infinitely small extent* in both space and time, *may* yield not only an "acoustic"-type solution but also an additional solution of the linear Helmholtz instability type, this additional solution is *definitely not* a solution of the full equations concerned in the general, non-linear problem (but only, naturally enough, of certain linearized limiting forms of these equations. It is of course, obvious from the most elementary considerations that an unbounded function cannot be permitted at all, strictly speaking, as a solution to any mathematical model of a physical problem where boundedness is required from physical considerations (and especially not when a perfectly good, complete and unique bounded solution is available [!])). Equally, of course, it is obvious that solutions of

the *linear* Helmholtz instability type have physical significance in relation to real problems only insofar as they are used to describe the *initial* growth tendencies of a disturbance; even then, of course, such solutions are only approximate — they are exact only, as it were, at zero time (or amplitude).

As another academic point in the same vein, it is worth commenting (but only because a curious interpretation of the results to be mentioned has been put forward, apparently seriously, on a number of occasions) on the fact that the linear Helmholtz-type instability solutions are required, along with an "acoustic" solution, to provide complete solutions satisfying "causality" for certain linearized (and also otherwise idealized) theoretical problems. Such mathematically correct results are, strictly speaking, of no generalizable relevance to real fluid motion, either in practice or in theory, because the linearized problem itself represents real fluid motion only for zero time (and/or amplitude). Also, the use of the word "causality" in connection with such problems can be misleading. It is a trivial matter to verify that in such linearized solutions that the "acoustic" part of the solution and the linear Helmholtz instability part each *independently* satisfy the causality principle in its usually accepted sense (indeed, its only physically valid and relevant sense): that is, that the cause must precede the effect. Causality, in this valid sense, is, of course, also satisfied by the complete and unique "acoustic" approach solution to the full non-linear problem.

The matters discussed in the preceding two paragraphs are admittedly rather academic in nature. Nevertheless, in relation to real problems the discussion has provided some further insight into how it comes about that the "acoustic" approach solution is complete and unique for realistic formulations of the aerodynamic noise radiation problem, and into how it is that *linear* Helmholtz-type instability solutions have no role to fulfill in this approach, except, if desired, that of approximate solutions for very limited space and time domains (infinitesimal times and amplitudes). However, a valid, real question remains. Granted that the acoustic field outside the jet may indeed have a representation that has the character of a superposition of "acoustic" disturbances, how can the (presumably non-linear) pressure field inside the jet validly have the superficial appearance of such a character and how is such a representation to be reconciled with the amplitude-limited Helmholtz-type instability representation of *subsonically*, rather than *sonically* travelling disturbances?

The answer to the first part of the question is straightforward and is not of much physical significance. The phenomenon of interference makes it possible for very wide classes of functions ("almost any function") to possess a representation as a superposition of waves of apparently "acoustic" (or other) form. Again, the example of Lighthill's "equivalent acoustic waves" representing thermal diffusion is relevant. The only real physical relevance of this otherwise more or less mathematically accidental occurrence, of representation of the pressure field inside the flow in terms of

and hence, in principle, *measurably*.

"acoustic" waves, can be established in aerodynamic noise theories such as those of Lilley⁽²⁾ or Doak^(4,5). In these theories physical reality can be ascribed to the elementary "acoustic" waves as representing, say, the *actual* individual contributions from different regions in the mixing flow to the fluctuations of logarithm of the pressure, as arising from certain well-defined[†] second order non-linear flow interactions (Lilley), or, similarly, the *actual* fluctuating, well-defined[†] acoustic momentum potential field *caused* by fluctuations in the likewise well defined[†] turbulent and thermal fluctuations (Doak).

The more interesting part of the question, for present purposes, and the part that requires answering to complete the conceptual reconciliation of the Helmholtz "instability" approach and the "acoustic" approach, is that of the relationship of the fluctuating pressure field, as calculable, say, in practice from the "acoustic" approach representation, and that similarly calculable from the Helmholtz "instability" approach, for the pressure field both inside and outside the jet.

Here the "acoustic" approach solutions show very definite advantages over the Helmholtz "stability" approach, particularly for the *radiated* acoustic field. The "acoustic" approach representations show that, subject to acoustic scattering effects (including refraction, diffraction and radiation efficiency) explicitly and completely represented to date only in the Lilley and Doak theories, the radiated acoustic field can be determined *primarily* by knowledge *only* of the *solenoidal* and *thermal* components of the jet mixing region and jet core motion, and that in this type of representation the detailed nature of the pressure field inside the jet is of secondary importance [for detailed justification of this point see the cumulative arguments put forward in reference (4)].

Thus, because of the strong tendency towards collective dependence of the fluctuating acoustic (pressure) field, both inside and outside the jet, on contributions from *all* parts of the turbulent mixing region and potential core of the jet, the radiated acoustic field especially, can be fairly accurately estimated on the basis of *minimally* accurate estimations of the *solenoidal* (turbulent) and *thermal* components of the motion in the jet. To obtain reasonably accurate estimations of the fluctuating pressure field, at a point either inside or outside the jet, in other words, it is *not* especially helpful to know the fluctuating pressure field at other points (to the degree of approximation that it *can* be known at present), but it *is* helpful to know the mean and fluctuating *turbulent* (solenoidal) velocity (or momentum potential) fields and the mean and fluctuating *thermal* fields *inside* the jet.

It might be said, by way of descriptive explanation of the situation, that the whole matter is simply a consequence of Bernoulli's equation. Local pressure fluctuations in turbulence are known, from both observation and the theoretical work of Obukhov, Batchelor and Proudman [see, for example, reference (6)], to be proportional to the square of the local turbulent velocity fluctuations. The radiating pressures associated with these local fluctuations are known, both from experiment⁽⁷⁾ and from Lighthill's theory⁽³⁾, for example, to be proportional, because of quadrupole inefficiency, to

the fourth power of the local velocity fluctuations (subject to mitigation by source convection, scattering and radiation efficiency effects). Thus, the contribution of the radiated pressure field, at a point either inside or outside the jet, may well be, generally, of quite a different order to that of the locally determined contribution. As has been argued (4, see p 313) it is presently very much an open question as to whether or not pressure fluctuations inside the jet will be dominated by the local contribution, or by radiated contributions from other parts of the jet, or by neither. Hence, in the present state of knowledge, it is much safer to regard the pressure field inside the jet as possibly made up of both local and radiated contributions.

It is now evident that for the present, at least, descriptions by the Helmholtz-type "instability" approach should be considered to give the best possible descriptions of the turbulent velocity (or momentum) fluctuations inside the jet but that "acoustic" approach descriptions should be considered as giving the best possible descriptions of pressure (or "acoustic") field fluctuations, both inside and outside the jet.

1-3.3 Conclusions

(i) The Helmholtz "instability" approach, in the present state of advancement of techniques and knowledge, is capable of giving the best possible representations of the mean and turbulent velocity and temperature fields inside a jet flow.

(ii) The "acoustic" approach (of Lilley or Doak), in the present state of advancement of techniques and knowledge, is capable of giving the best possible representation of the fluctuating pressure (or momentum potential or particle velocity) fields, both inside and outside the jet, given either experimental knowledge, or theoretical modelling from the Helmholtz "instability" approach of the mean and turbulent velocity fields, and the mean fields, inside the jet.

(iii) The Helmholtz instabilities have no direct relevance either to real jet flows or to the sound radiated from them. They have indirect relevance only insofar as they can be regarded as approximations, for very small times and amplitudes, to the bounded, non-linear Helmholtz-type motion.

References

1. P. J. Morris, 1971, Ph.D. Thesis, University of Southampton, The structure of turbulent shear flow.
2. G. M. Lilley, 1972, The generation and radiation of supersonic jet noise, AFAPL-TR-53, Vol. IV, 2-90, Generation of sound in a mixing region.
3. M. J. Lighthill, 1952, Proceedings of the Royal Society A 211, 564-578, On sound generated aerodynamically: 1. General Theory.
4. P. E. Doak, 1972, J. Sound and Vib, 25, 263-335, Analysis of internally generated sound in continuous materials: 2. A critical review of the conceptual adequacy and physical scope of

existing theories of aerodynamic noise, with special reference to supersonic jet noise.

5. P. E. Doak, 1973, J. Sound and Vib, 28, 527-561, Fundamentals of aerodynamic sound theory and flow duct acoustics.
6. G. K. Batchelor, 1953, The theory of homogeneous turbulence, Cambridge University Press.
7. P. A. Lush and R. H. Burrin, 1972, The generation and radiation of supersonic jet noise, AFAPL-TR-72-53, Vol. V. An experimental investigation of jet noise variation with velocity and temperature.
8. B. J. Tester, 1973, J. Sound and Vib, 28, 217-246, Some aspects of "sound" attenuation in lined ducts containing inviscid mean flows with boundary layers.
9. P. N. Shankar, 1972, J. Sound and Vib, 22, 233-246, Acoustic refraction and attenuation in cylindrical and annular ducts.

APPENDIX 1-3A

A Proof of the Validity of the Acoustic Approach Solutions for Describing Acoustic Field Variables both Outside and Inside a Jet or Other Turbulent Flow Field

In aerodynamic noise theories, the complete "exact" equations of mass density and energy density transport of the fluid are arranged to yield some generalized form of "inhomogeneous acoustic wave equation":

$$L_3 p' = -Q \quad (A.1)$$

where L_3 is a linear partial differential operator with variable coefficients (usually functions of position but in general they also could be functions of time), p' is the (total, "exact") fluctuating pressure (or logarithm of the pressure, or momentum potential) and Q is a non-linear function of the pressure, mass density and fluid velocities (or of some other suitable set of primary dependent field variables).

For applications to far field acoustic radiation from disturbed flow regions embedded in an infinite extent of fluid which tends to a state of rest at very large distances from the disturbed region, the operator L_3 is selected so that outside the disturbed fluid it tends to proportionality to the small amplitude acoustic wave equation operator, i.e.

$$L_3 \rightarrow A (C_\infty^2 \nabla^2 / \partial x_i^2 - \partial^2 / \partial t^2),$$

where A is a constant (or a trivial space or time differentiation), C_∞ is the speed of sound in the fluid at large distances from the disturbed region, the x_i are the Cartesian position coordinates, and t is time. It is clear that in such situations the necessary and sufficient physical boundary condition for equation (A.1) as $|x_i| \rightarrow \infty$ is the usual acoustic radiation condition.

In this context, the exact problem of fluid

motion posed by equation (A.1) can be put as follows. Given the coefficients of the operator L_a and the source function Q as bounded functions of position and time, find p' as a bounded function of position and time that satisfies equation (A.1) everywhere in space-time and satisfies acoustic radiation conditions as $|x_i| \rightarrow \infty$. (For the purpose here, it is not necessary to explicitly consider situations in which the fluid has boundaries either inside or outside the source region. Such boundaries, if present, could in any case be represented simply by equivalent, bounded surface or image volume source distributions in addition to Q .)

Boundedness is, of course, an essential condition to impose on p' if p' is indeed to represent a physically realizable quantity. By imposing the condition, and by assuming that L_a and Q are bounded, one is, in effect, making the assumption (which is in fact the only assumption made in this proof) that the complete transport equations of the fluid actually possess a set of bounded solutions for the dependent field variables (pressure, density velocities). If the transport equations do not possess a bounded solution, it is clear that they must be an unsuitable mathematical model for physical phenomena that are bounded.

Formally, because equation (A.1), with L_a and Q known, can be regarded as an inhomogeneous linear partial differential equation, its solution can be expressed as

$$p' = \int G(x_i, t; y_i, \tau) Q(y_i, \tau) dy_i d\tau \quad (A.2)$$

where G is a suitable Green's function (space-time impulse response function), obtained from

$$L_a G = -\delta(x_i - y_i) \delta(t - \tau), \quad (A.3)$$

where $\delta(\)$ is the Dirac delta function. (Of course, in the general case L_a may not be self-adjoint, etc., and so certain adjustments would be necessary in the notation of equations (A.2) and (A.3), but their essential form would be unaffected.)

Now it is possible in some circumstances for G , as the solution of the impulse response problem (A.3), to appear to contain an unbounded part. In particular, when L_a is the Landahl operator (as used, for example, in Lilley's convected inhomogeneous wave equation for aerodynamic noise theory) G as obtained from equation (A.3) is known in at least one well-documented case (see reference [8]) to appear to have two parts: a bounded, "acoustic" part, G_a , say, and a part displaying Helmholtz-type instability behavior, G_H . Thus, in such a case equation (A.2) would appear to yield, with $G = G_a + G_H$,

$$p' = p_a' + p_H',$$

where p_a' is bounded for all space and time but p_H' is not. (Also, p_H' may not satisfy the radiation conditions.)

Formal application of the Green function approach in this manner may thus lead, when unstable solutions of the linearized equation

$$L_a p' = 0$$

exist, to an *unbounded* solution in a situation where a bounded solution is required. Because of the requirement of boundedness; therefore, there is no alternative but to reject the entire solution containing any such unbounded part, should it be obtained, and to ask if any bounded solution can be obtained.

In some particular cases where L_a is the Landahl operator, it has been argued by Shankar(9), on the basis of certain general considerations and computer tests, that the set of acoustic function solutions alone of the homogeneous form of equation (A.1), the Helmholtz instability solutions being excluded, is "in all probability complete!" If this is the case, it follows that the acoustic part

$$p' = p_a' = \int G_a Q dy_i d\tau \quad (A.4)$$

is, by itself, a particular solution of

$$L_a p' = -Q.$$

Furthermore, in the shear layer cases investigated by Howe and by Tester(8), in which an unbounded part of the Green function, G_H , has been found, it is a trivial matter to prove that the acoustic solution by itself is in fact a particular solution of

$$L_a p' = -Q.$$

(The proof for these cases amounts simply to the observation that in the source region, where $Q \neq 0$, in these problems p_H' is always zero, so that

$$L_a p_H' = 0$$

everywhere in the fluid and hence p_H' is a purely complementary function, not in any way essential to any particular integral.)

The discussion of the general problem can now, on the basis of these observations, be conducted in respect to the two possible cases: (i) G_a by itself is a particular solution of

$$L_a G_a = -\delta(x_i - y_i) \delta(t - \tau)$$

(or, alternatively, the bounded solutions of

$$L_a p' = 0$$

form a complete set of functions); (ii) all particular solutions, $G_a + G_H$ contain an unbounded part.

Case (i): G_a is a particular solution. Let the desired, bounded solution of equation (A.1) be written as

$$p' = p_a' + p_c',$$

where

$$p_a' = \int G_a Q dy_i d\tau;$$

p_a' is then a particular integral of

$$L_a p' = -Q.$$

Hence

$$L_a p_c' = 0.$$

Case (ii): All particular solutions, $G_a + G_H$, contain an unbounded part.

The complete solution then must be of the form

$$p' = \int (G_a Q + G_H Q) dy_i d\tau.$$

The part

$$\int G_a Q dy_i d\tau$$

satisfies the boundedness and radiation conditions but the part

$$\int G_H Q dy_i d\tau$$

satisfies neither. If this part contains a component essential to the particular integral it cannot normally be removed by addition of any physically acceptable complementary function. Hence, no solution satisfying the prescribed boundedness and radiation conditions exists. The fundamental mathematical model then cannot be valid for the physical situation envisaged. (If, by virtue of some kind of pathological circumstances, it should be possible to

remove both the particular integral and complementary function parts of

$$\int G_H Q dy_i d\tau$$

by addition of some further complementary function, then one would simply return to the result of Case (i):

$$p' = \int G_a Q dy_i d\tau.$$

Conclusion: Insofar as the complete, "exact" equations of fluid motion are believed to be valid models for real fluids, and insofar as all observations of aerodynamic noise phenomena to date confirm that boundedness, and acoustic radiation conditions at large distances, are always characteristic of the flows concerned, it follows that all "acoustic" operators such as the Landahl operators must have complete sets of acoustic functions among their homogeneous solutions so that the bounded acoustic solution by itself is a particular integral of equation (A.1). To establish the mathematical sufficiency of the acoustic solution in any particular case, it is sufficient to establish that the acoustic part of the Green function alone is a particular integral of

$$L_a G_a = -\delta(x_i - y_i) \delta(t - \tau),$$

or that the acoustic solutions of

$$L_a p' = 0$$

form a complete set.

Brian J. Tester and Robert H. Burri
Lockheed-Georgia Company
Marietta, Georgia

Abstract

Sound generated by velocity fluctuations in a turbulent jet interacts with the mean flow field along its propagation path through the jet to produce significant changes in the far-field radiation level and directivity. Lilley's equation allows us to evaluate these sound-mean flow interaction effects, that is sound convection, refraction or diffraction, for any given source distribution. To fully illustrate some of these effects and to provide the basis for constructing a complete solution to Lilley's equation, we solve the problem of a stationary point source located in a circular, unidirectional, sheared subsonic jet with a realistic mean velocity profile. Calculated far-field acoustic radiation levels are presented as a function of source location, frequency and jet Mach numbers. Calculated far-field radiation directivity patterns of a modified point source are compared with measurements of the directivity of sound radiated from a probe source placed inside a jet. These are only in qualitative agreement and while questions remain concerning representation of the probe source and the type of solution utilized here, consideration of theoretical results, obtained elsewhere, strongly suggests that a more realistic mean flow model is required. A complete solution to Lilley's equation, for a simplified version of the standard type of turbulence source function statistics, evaluated in the form of difference spectra and found to be in good qualitative agreement with measurement.

1-4.1 Introduction

In recent papers Lilley (1),(2) has described the formulation of a new theoretical jet noise model, as in Lighthill's (3) and Phillip's (4) models it is based on an inhomogeneous wave equation. Lilley's equation, however, describes explicitly the combined effects of both sound convection and refraction, or diffraction, by a unidirectional, sheared jet flow field, and it shows, also, that the sources of sound in such a jet, are, to a good approximation, a non-linear function of the turbulent velocity fluctuations.

The purpose of this paper is to describe one aspect of our progress to date in a theoretical program which has as its goal a detailed evaluation of Lilley's model for a circular, turbulent, high speed jet.

The complete solution to Lilley's equation will be constructed from an appropriate specification of the non-linear source function and solutions to the same equation, but with the source function replaced by that for a point source. A model for the turbulent velocity field is being developed by Morris (5) and results from his model, in conjunction with measured data, will be used, in due course, to determine the source function statistics.

Here we examine point source solutions (section

1-4.5) and solutions for a simplified version of a standard type of turbulence source function which are then compared with measured jet noise difference spectra (section 1-4.8). The point source solutions to Lilley's equation are presented here in some detail to fully illustrate the effects of interactions between sound propagation and a unidirectional sheared jet flow field (convection, refraction or diffraction) on the far-field radiation directivity, which in the absence of flow would be omnidirectional. Point source solutions are also compared with measurements, in the form of measured radiation directivity patterns from the probe jet experiments, since it is clearly desirable that the validity of these solutions be thoroughly explored before proceeding to construct complete solutions to Lilley's equation for realistic source functions (see section 1-4.8).

It is recognized that our present solutions to Lilley's equation are open to criticism because the unstable type of solution is ignored, this point is discussed in the following section.

1-4.2 Discussion

Lilley's equation for pressure fluctuations, p' , in a unidirectional or parallel sheared flow is of the form

$$L(p) = F$$

where L is a partial differential operator and F is a non-linear function of the turbulent velocity fluctuations. Its homogeneous form, $L(p) = 0$, reduces to an ordinary homogeneous differential equation for the Fourier transform of p' which is identical to the equation used to study sound propagation in lined ducts containing parallel sheared flows (6),(7). It can also be recognized as the same equation, in effect, which is used to study the linear stability properties of inviscid, compressible, parallel sheared flows (8) and because of this the application of Lilley's equation to the jet noise problem, as described here, has been seriously questioned by some students of current jet noise theory. Opponents argue, often on the basis of results obtained with vortex sheet or "plug" flow models (9), that two types of solution can be expected from Lilley's equation, which are referred to here as the acoustic solution and the unstable solution. The acoustic solution, as the name implies, is well behaved and decays as the inverse of distance from the jet source distribution in the r -field. The unstable solution, if restricted to real frequencies, may grow exponentially in the downstream direction and unless flow divergence and other mechanisms are taken into account which limit this growth (5), it is impossible to derive a realistic far-field contribution from this solution. The work reported here is concerned only with the acoustic solution. It is naturally desirable to have a working knowledge of the acoustic solution before proceeding to study the unstable solution and also there are possibly regions of the jet where for

... of the present work is to be published in the Journal of Applied Physics.

... of the present work is to be published in the Journal of Applied Physics.

onal sheared, cylindrical jet contains a finite volume of turbulence in which the space-time covariance of the square of the velocity fluctuations, v_i^2 , is known. The mean static pressure, p_0 , is uniform throughout the jet and radiation field; the jet is inviscid and obeys the laws for a perfect gas. The axial mean velocity, \bar{v}_1 , density, temperature and speed of sound, \bar{c} , may vary consistently with radial position inside the jet but are otherwise constant. For this model Lighthill's equation takes the form (if $p'/\rho_0 \ll 1$):

$$L(p') = \frac{\partial^2 p'}{\partial t^2} \quad (3.1)$$

where, in cartesian coordinates

$$L(p') = \frac{1}{\bar{c}^2} \frac{\partial^2 p'}{\partial t^2} - \frac{\partial}{\partial x_i} (\bar{v}_i p') - \frac{d}{dx_i} (\log_e S^2) \frac{\partial}{\partial x_i} (\bar{v}_i p') + 2 \frac{d\bar{v}_i}{dx_i} \frac{\partial^2 p'}{\partial x_i \partial x_i} \quad (3.2)$$

and the non-linear source function is

$$S = \frac{\partial}{\partial t} \left(\frac{\partial v_i^2}{\partial x_j} - \frac{\partial v_j^2}{\partial x_i} \right) - 2\bar{v}_i \frac{d\bar{v}_i}{dx_i} \left(\frac{\partial v_k^2}{\partial x_k} - \frac{\partial v_k^2}{\partial x_k} \right) \quad (3.3)$$

and

$$\frac{\partial}{\partial t} = \frac{\partial}{\partial t} + \bar{v}_1 \frac{\partial}{\partial x_1} \quad (3.4)$$

For the purposes of the present study the second term in the source function, S , is ignored and the velocity fluctuations are assumed to be incompressible, that is,

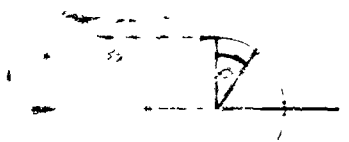
$$\frac{\partial v_i^2}{\partial x_i} = 0$$

so that the source function takes on a familiar form

$$S = \frac{\partial}{\partial t} \left(\frac{\partial^2 (v_i^2 v_j^2 - v_j^2 v_i^2)}{\partial x_i \partial x_j} \right) = \frac{\partial S}{\partial t} \quad (3.5)$$

We shall work in cylindrical coordinates as defined in Figure (1); the differential operator, L , remains the same except x_2 is replaced by the radial coordinate r where it appears explicitly in equation 3.2. The Lighthill source function in cylindrical coordinates, S_c , is the sum of the following terms:

$$\begin{aligned} & \frac{\partial^2 (v_r^2)}{\partial t^2} + \frac{1}{r} \frac{\partial}{\partial r} (v_r v_r) + \frac{1}{r^2} \frac{\partial}{\partial \theta} (v_r v_\theta) \\ & \frac{1}{r} \frac{\partial}{\partial x_1} (v_r v_1) + \frac{1}{r} \frac{\partial}{\partial r} (v_r v_r) + \frac{1}{r} \frac{\partial}{\partial \theta} (v_r v_\theta) \\ & \frac{1}{2\pi r} \frac{\partial}{\partial t} (v_r^2) + \frac{1}{2\pi r} \frac{\partial}{\partial t} (v_\theta^2) + \frac{1}{2\pi r} \frac{\partial}{\partial t} (v_r v_\theta) \end{aligned} \quad (3.6)$$



where C_n is a coefficient obtained from numerical solutions of equation 3.16. The method of numerical solution is described in Appendix 1-4.C and the Fourier inversion in Appendix 1-4.B. In the Fourier inversion it is shown that solutions are required for only specific wavenumbers such that

$$k_1 = \frac{k}{a_0} \cos \mu$$

where μ is the observer angle to the jet axis:

$$\mu = \cos^{-1} \frac{(x_1 - x_1')}{\sqrt{(x_1 - x_1')^2 + r^2}}$$

The frequency, ω , is necessarily restricted to real values in the present analysis and equal to the observed frequency.

The numerical coefficients, C_n , then are functions of the circumferential wavenumbers, n , the observer angle to the jet axis, μ , the frequency or Helmholtz number, $H = kr_0$ (where r_0 is the jet nozzle radius), the radial position of the source, $R' = r'/r_0$, and the non-dimensionalized mean velocity and speed of sound profiles, M_1 , a/a_0 , and their gradients with respect to the radial coordinate, $R = r/r_0$.

It is the presence of the mean velocity and temperature gradient terms in equation 3.16 which distinguishes it from the Fourier transform of Phillips equation (4). There are undoubtedly conditions under which these gradient terms do not significantly affect the solution to equation 3.16, but these have yet to be determined; qualitatively such conditions will be associated with large values of the Helmholtz number, k , based on the width, δ , of the jet shear region. At the opposite extreme, $k \rightarrow 0$, where the gradients based on the scaled radial coordinate, R , are becoming indefinitely large, the solutions are certainly independent of these terms and converge to the analytic solutions for a "top hat" or "plug" mean velocity profile. Thus, Lilley's equation certainly includes the circular "plug" jet model, used, for example, by Mani (13), as a special case. In this limit the C_n coefficients take one of two values, depending on whether the source is inside or outside the "plug" jet:

$$C_n = \frac{2 J_n(\bar{k}_2 r')}{j \bar{E}_n} \exp[jn\pi/2] \quad r' < r_0$$

$$C_n = \frac{2}{j \bar{E}_n} \left\{ \frac{\pi}{2} [\bar{\psi}(\bar{k}_2 r_0) J_n(\bar{k}_2 r_0) \bar{a}_n - \bar{k}_2 r_0 J_n'(\bar{k}_2 r_0) \bar{a}_n'] \right\} \quad r' > r_0$$

where

$$(\bar{k}_2 r_0)^2 = (kr_0)^2 \left(\frac{a}{a_0} \right)^2 (1 - M_1 \cos \theta)^2 - \cos^2 \theta$$

$$\bar{E}_n = -(\bar{k}_2 r_0) H_n^{(2)}(\bar{k}_2 r_0) J_n(\bar{k}_2 r_0) -$$

$$-\bar{k}_2 r_0 H_n(\bar{k}_2 r_0) J_n'(\bar{k}_2 r_0)$$

$$\bar{a}_n = (1 - M_1 \cos \theta)^2 \frac{E}{E_0}$$

$$\bar{a}_n = J_n(\bar{k}_2 r') Y_n(\bar{k}_2 r_0) - J_n(\bar{k}_2 r_0) Y_n(\bar{k}_2 r')$$

$$\bar{b}_n = J_n(\bar{k}_2 r') Y_n'(\bar{k}_2 r_0) - J_n'(\bar{k}_2 r_0) Y_n(\bar{k}_2 r')$$

$$\bar{k}_2 r_0 = kr_0 \sin \theta$$

The zeros of the function E_n determine the position of poles on the complex k_1 plane; one or more of these poles defines the unstable eigenvalues of k_1 and the Fourier inversion should include contributions from these poles to give the unstable solution. This type of solution, as we have already mentioned, is ignored in the present study and in similar work elsewhere (10), (13), but will be studied in future work. It should be emphasized that the utilization of Lilley's equation, with realistic velocity and speed of sound profiles as opposed to the top-hat profile, does not alter the general picture in any way. There will still be an acoustic solution and one or more unstable solutions, both of which will be modified by real profile effects. But, both types of solution can be recognized and obtained independently by numerical methods (at least for jet Mach numbers less than two).

The acoustic Green's function solution to Lilley's equation, equation 3.19, will be utilized in sections 1-4.4 and 1-4.5 to form solutions for particular source distributions.

1-4.4 On Theoretical Models of the Probe-Jet Experiment

In a recent paper by MacGregor *et al* (14) results are presented from an experimental configuration which we now attempt to represent with an approximate, theoretical model. The experiment consisted of a source of sound, introduced through a 1/16" i.d. hypodermic tube, placed inside a jet, two diameters downstream of the jet nozzle on the jet axis. With the aid of an instrument which "behaves somewhat like a correlator" (14), the acoustic radiation level, in the far-field, at the source frequency was effectively extracted from the jet noise signal. The radiation level directivity, relative to the level at 90° to the jet is presented by MacGregor *et al* (14) for two jet exit Mach numbers, 0.5 and 0.9, and for four Doppler shifted frequencies, 1, 1.5, 3.0 and 4.5 KHz. This extraction process, that is the exclusion of acoustic signals at all other frequencies, means that our acoustic component of the Green's function, which only includes the effects of stable linear transmission of sound through the jet shear layer, may provide a valid theoretical description of directivity patterns measured in this way.

where $v_1^2 = v_1'^2 - v_1''^2$
 $v_1 r v_r = v_1' r v_r' - v_1'' r v_r''$, etc.

In the Lighthill model the inhomogeneous wave equation is solved by means of the Green's function, $g(\underline{x}, t/\underline{x}', t')$, which is the acoustic pressure at (\underline{x}, t) due to a pulse at time t' from a point source at \underline{x}' ; in the absence of boundaries, it is simply

$$g(\underline{x}, t/\underline{x}', t') = \frac{\delta(t - t' - |\underline{x} - \underline{x}'|/a_0)}{4\pi |\underline{x} - \underline{x}'|} \quad 3.7$$

The acoustic pressure, p' , due to an arbitrary source distribution, S_p , is then

$$p'(\underline{x}, t) = \int_{-\infty}^{+\infty} \int_V g(\underline{x}, t/\underline{x}', t') S_p(\underline{x}', t') d\underline{x}' dt' \quad 3.8$$

or

$$p'(\underline{x}, t) = \int_V \frac{S_p(\underline{x}', t - |\underline{x} - \underline{x}'|/a_0)}{4\pi |\underline{x} - \underline{x}'|} d\underline{x}'. \quad 3.9$$

In the present model we do not attempt to find $g(\underline{x}, t/\underline{x}', t')$ since we are mainly interested in the spectral density of the acoustic pressure and therefore the Fourier coefficient $p'(\underline{x}, \omega)$ where

$$p'(\underline{x}, \omega) = \int_{-\infty}^{+\infty} p'(\underline{x}, t) \exp[j\omega t] dt \quad 3.10$$

The Fourier transform of equation 3.8 is

$$p'(\underline{x}, \omega) = \int_{-\infty}^{+\infty} \int_V g(\underline{x}, \omega/\underline{x}', t') S_p(\underline{x}', t') d\underline{x}' dt' \quad 3.11$$

and thus we require $g(\underline{x}, \omega/\underline{x}', t')$ the (complex) Fourier coefficient of the acoustic pressure at the observation point \underline{x} due to a pulse at time t' emitted from a point source at the point \underline{x}' .

To summarize, we solve Lilley's inhomogeneous wave equation

$$L(p') = \frac{\partial}{\partial t} \left\{ \rho_0 \frac{a_0^2}{\partial^2} \cdot S_c \right\} \quad 3.12$$

by assuming the existence of the Green's function $g(\underline{x}, t/\underline{x}', t')$, which satisfies,

$$L(g) = \frac{\partial}{\partial t} \{ \delta(\underline{x} - \underline{x}') \delta(t - t') \} \quad 3.13$$

and by finding the solution to this equation for the Green's function Fourier coefficient, $g(\underline{x}, \omega/\underline{x}', t')$. The solution to Lilley's equation for the Fourier coefficient $p'(\underline{x}, \omega)$ is then

$$p'(\underline{x}, \omega) =$$

$$\int_{-\infty}^{+\infty} \int_V \rho_0 \frac{a_0^2}{\partial^2} S_c(\underline{x}', t') g(\underline{x}, \omega/\underline{x}', t') d\underline{x}' dt'. \quad 3.14$$

In cylindrical coordinates the right-hand side of equation 3.13 is

$$\frac{\partial}{\partial t} \left\{ \delta(x_1 - x_1') \frac{\delta(r - r')}{r} \delta(\phi - \phi') \delta(t - t') \right\}. \quad 3.15$$

We now proceed to solve equation 3.13 by taking its Fourier transform with respect to t , x_1 and ϕ ; the circumferential wavenumber is restricted to integer values, n , due to the usual continuity argument. The result is an ordinary differential equation

$$\begin{aligned} & \frac{1}{r} \frac{d}{dr} \left(r \frac{dg}{dr} \right) + \left\{ \frac{d}{dr} \left(\log_e \frac{a_0^2}{\partial^2} \right) \right\} + \\ & + \frac{2 k_1/k}{(1 - M_1 k_1/k)} \frac{dM_1}{dr} \frac{dg}{dr} + g \left[k^2 \left\{ \left(\frac{a_0^2}{\partial^2} \right) (1 - M_1 k_1/k)^2 - \right. \right. \\ & \left. \left. - (k_1/k)^2 \right\} - \frac{n^2}{r^2} \right] = \\ & = - \frac{\delta(r - r')}{r} \exp[-j\omega t' + jk_1 x_1' + jn\phi'] \quad 3.16 \end{aligned}$$

where $k = \omega/a_0$, $M_1 = \bar{v}_1/a_0$ and the dependent variable

$$g \equiv g(k_1, r, n, \omega/x_1', r', \phi', t')$$

$$= \int_{-\infty}^{+\infty} \int_0^{2\pi} g(\underline{x}, \omega/\underline{x}', t') \exp[jk_1 x_1 + jn\phi] dx_1 d\phi. \quad 3.17$$

Once the solution to equation 3.16 is found, the required solution $g(\underline{x}, \omega/\underline{x}', t')$ is obtained by inversion:

$$\begin{aligned} g(\underline{x}, \omega/\underline{x}', t') &= \left(\frac{1}{2\pi} \right)^2 \sum_{n=-\infty}^{+\infty} \left\{ \int g(k_1, r, n, \omega/x_1', t') \right. \\ & \left. \times \exp[-jk_1 x_1] dk_1 \right\} \cdot \exp[-jn\phi] \quad 3.18 \end{aligned}$$

When the inversion with respect to the axial wavenumber, k_1 , is restricted to the far-field solution, as discussed in the previous section, it takes the form (see Appendix 1-4B):

$$\begin{aligned} g(\underline{x}, \omega/\underline{x}', t') &= \frac{\exp[-jk_1 x_1 \cos\theta - jk r \sin\theta]}{4\pi \{ (x_1 - x_1')^2 + r^2 \}} \\ & \times \exp[-j\omega t'] \exp[jk \cos\theta x_1'] \sum_{n=-\infty}^{+\infty} C_n \exp[-jn(\phi - \phi')] \quad 3.19 \end{aligned}$$

It might appear that a theoretical model of this experiment is straightforward: Lilley's equation could be solved with the velocity profile found at two-diameters from the jet nozzle and with an appropriate representation of this experimental "point" source on the right-hand side of that equation. We propose here a slightly different approach based on the argument that the experimental source is surrounded by a thin annular region of disturbed fluid whose mean velocity in the axial direction is zero adjacent to the source. This disturbed fluid, which is the probe boundary layer and wake, will of course spread at a certain rate downstream of the probe but once again we will use a non-diverging, infinite, parallel flow model for this particular region and, further, for simplicity, it will be assigned a 'plug' flow representation. In fact both the probe, and hence the wake diameter will be zero in the present model but, initially equations are formulated for the model shown in Figure 2. Region 1 (the diameter having a limit zero) contains a stationary fluid and a point source representing the probe excitation. Lilley's equation will be utilized in Region 2, which contains the sheared jet flow, together with the radiation condition at its boundary with Region 3 and an inner boundary condition at the interface with Region 1. Region 3 contains the ambient fluid surrounding the jet. Through this model of the source and its immediate surroundings we can deduce the effective source strength to be used on the right-hand side of Lilley's equation.

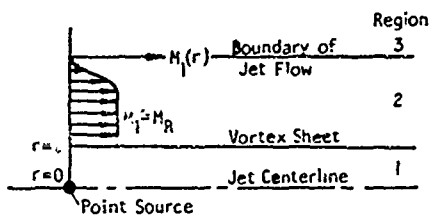


Fig. 2 Parallel Flow Model of Probe-in-Jet Experiment

In Region 1 the Green's function, G_1 , must satisfy

$$\frac{d^2 G_1}{dr^2} + \frac{1}{r} \frac{dG_1}{dr} + k_2^2 G_1 = \frac{\delta(r)}{r} S \quad 4.1$$

where

$$k_2^2 = k^2 - k_1^2$$

$$S = -\exp[-j\omega t] \exp[jk_1 x_1']$$

and the solution is of the form

$$G_1 = A_1 J_0(k_2 r) + \frac{j\pi S}{2} H_0^{(2)}(k_2 r) \quad 4.2$$

In Region 2 the Green's function must satisfy Lilley's equation but in the vicinity of $r = \delta$ where the mean flow is uniform Lilley's equation reduces to

$$\frac{d^2 G_2}{dr^2} + \frac{1}{r} \frac{dG_2}{dr} + K_2^2 G_2 = 0 \quad 4.3$$

$$\text{where } K_2^2 = k^2 \{ (1 - k_1 M_1 / k)^2 - (k_1 / k)^2 \}$$

and the solution is the form

$$G_2 = A_2 J_0(K_2 r) + B_2 Y_0(K_2 r) \quad 4.4$$

but as $K_2 r \rightarrow K_2 \delta \rightarrow 0$ the first term in this solution is negligible compared with the second so that

$$G_2 \approx B_2 Y_0(K_2 r) \quad (K_2 r \rightarrow 0) \quad 4.5$$

Across the vortex sheet of the probe wake "plug" flow the conditions of continuity of pressure and particle displacement are applied

$$G_1 = G_2 \quad 4.6$$

$$\frac{dG_1}{dr} = \frac{1}{(1 - k_1 M_1 / k)^2} \frac{dG_2}{dr} \quad 4.7$$

which with equations 3.2 and 3.5 give in the limit $k\delta \rightarrow 0$

$$B_2 = \frac{j\pi}{2} (1 - k_1 M_1 / k)^2 S = \frac{j\pi}{2} \cdot \psi \cdot S \quad 4.8$$

It follows that the point source of unit strength and the surrounding wake "plug" flow can be replaced by a point source of strength ψ located in a region of uniform flow, that is, in a region, 2, which extends to the jet center-line.

According to this model the far-field pressure is given by (see Appendix 1-4A)

$$p(R_r, \theta, t) = \frac{\exp[-jk_0 R_r]}{4\pi R_r} \exp[j\omega_0 t]$$

$$\times (1 - M_R \cos \theta)^{-2} \left(-\frac{2j}{\pi} \cdot A \right) \quad 4.9$$

where R_r is the distance between the source and observer, θ is the observer angle to the jet axis, M_R is the value of M_1 , the mean flow Mach number, on the jet axis, $\omega_0 = a_0 k_0$ is the source radian frequency and A is, indirectly, the numerical solution to Lilley's equation. If the jet shear layer is also replaced by a vortex sheet then the analytic expression for A is

$$A = \frac{1}{\bar{E}_0} \quad 4.10$$

where

$$\bar{E}_0 = \bar{\psi}(\bar{k}_2 r_0) H_0^{(2)'}(\bar{k}_2 r_0) J_0(\bar{k} r_0) - (\bar{k}_2 r_0) J_0'(\bar{k}_2 r_0) H_0^{(2)}(\bar{k}_2 r_0)$$

$$\bar{\psi} = (1 - M_R \cos \theta)^2$$

$$\bar{k}_2 r = k r_0 \sin \theta$$

$$\bar{k}_2^2 r_0^2 = (k r_0)^2 \{ (1 - M_R \cos \theta)^2 - \cos^2 \theta \}$$

MacGregor's (14) results are reproduced in Figures 3 and 5. (In Figures 3-7 the Doppler shift factor, C , is defined as $C = [(1 - M_R \cos \theta)^2 + \alpha^2 M_R^2]^{1/2}$; $M_R = 0.5 V_j/a_0$; $\alpha = 0.55$.) The corresponding calculated plug flow directivities

$$20 \log_{10} \left| \frac{-2j/\pi}{E_0(k_0 r_0)} (1 - M_R \cos \theta)^2 \right|$$

are shown in Figures 4 and 6. At the condition $M_R = V_j/a_0 = 0.5$ the measured and calculated results, in Figures 3 and 4, are not significantly different for angles greater than 10° (when the observer is either inside, or close to, the local residual jet flow, a parallel flow model cannot be expected to be valid). At the higher jet Mach number, Figures 5 and 6 show that there are clearly substantial differences between measurement and theory over the whole range of frequencies and angles.

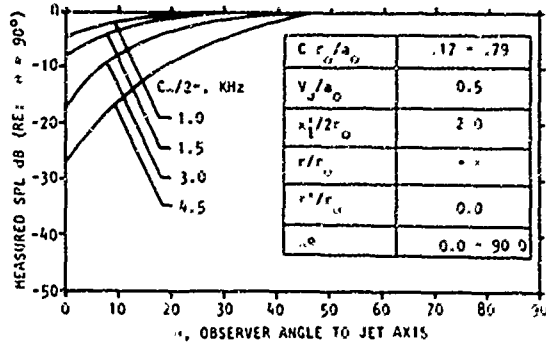


Fig. 3 Measured Far-Field SPL Directivities of a Source on Jet Center-Line ($r_0 = 3/8''$) Taken from MacGregor's (14) ($V_j/a_0 = 0.5$)

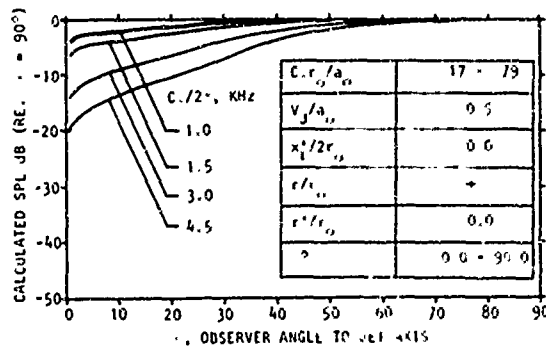


Fig. 4 Calculated Far-Field SPL Directivities of a Source on the Center-Line of a Circular "Plug" Jet Flow (That is, Axial Station at Nozzle) for Comparison with MacGregor's (14) Measurements Shown in Fig. 3 ($V_j/a_0 = 0.5$)

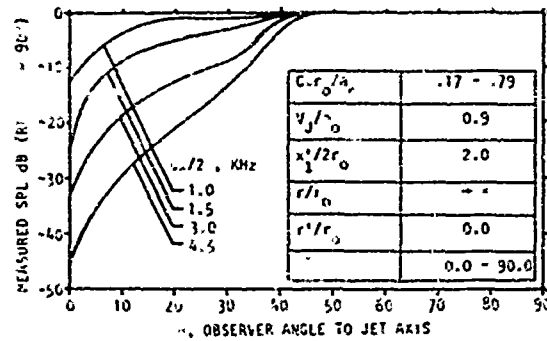


Fig. 5 Measured Far-Field SPL Directivities of a Source on Jet Center-Line ($r_0 = 3/8''$) Taken from MacGregor's (14) ($V_j/a_0 = 0.9$)

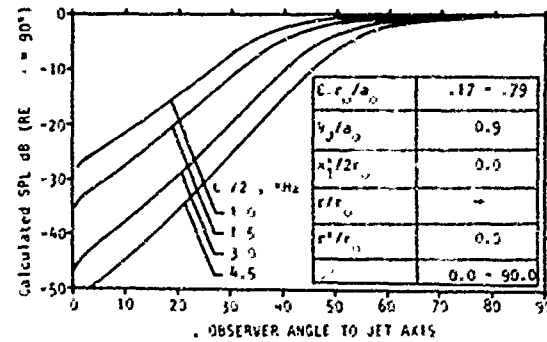


Fig. 6 Calculated Far-Field SPL Directivities of a Source on the Center-Line of a Circular "Plug" Jet Flow (That is, Axial Station at Nozzle) for Comparison with MacGregor's (14) Measurements Shown in Fig. 5 ($V_j/a_0 = 0.9$)

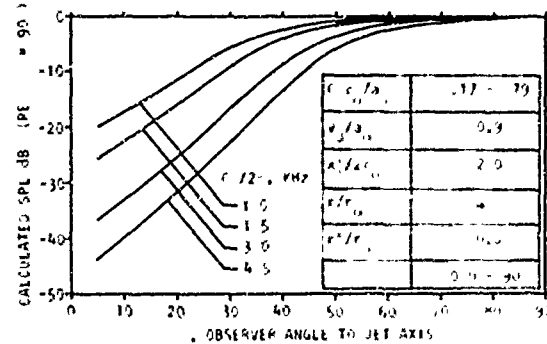


Fig. 7 Lilley Equation Solutions: Far-Field SPL Directivities of a Source on the Center-Line of a Circular Sheared Jet Flow for Comparison with MacGregor's (14) Measurements Shown in Fig. 5 ($V_j/a_0 = 0.9$)

The directivities of solutions to Lilley's equation are shown in Figure 7 for the condition $M_R = 0.9$; for the lower Mach number (0.5) the results are almost identical to those for a plug flow profile. The $M_R = 0.9$ solutions have been obtained using a velocity profile which is a good approximation to that found in a convergent nozzle jet two diameters downstream of the nozzle — the location of the probe termination in MacGregor's experiment. There are now less but still substantial differences between these Lilley equation solutions

and MacGregor's measurements and we now consider the possible reasons for this.

We have already stressed that to obtain the present results we have ignored the existence of unstable modes and the effects of diverging flow. We will also consider the possibility that the modeling of the probe source is in question. The effect of unstable modes is outside the scope of this report but we can consider the effects of diverging flow by reference to the work of Schubert (15) and Mungur (16). We fix the absolute Helmholtz number at $k_0 r_0 = .53$, consider three jet Mach numbers, 0.3, 0.5 and 0.9, and use Grande's (17) experimental results in which conditions are virtually identical to those in MacGregor's work but here, in the directivity patterns, the frequency is held constant (rather than the Doppler shifted frequency). Both Schubert (15) and Mungur (16) take diverging flow into account, with certain approximations, but Mungur's (16) results, shown in Figures 8-10, are in better agreement with experiment (Grande's (17) measurements in this case) than Schubert's are with his own measurements (15). Although the Lilley equation solutions are not particularly different from both Grande's measurements and Mungur's results at the conditions $M_j = 0.3$ and 0.5 (outside the 0-10° sector) there are substantial differences at the highest Mach number. In Figure 10 the plug flow model results are also shown; Lilley equation solutions yield an improvement over those for the plug flow model but the characteristic shape of the measured directivity pattern, it appears, cannot be reproduced with either parallel flow model. A diverging flow model does give the correct shape as well as excellent absolute levels and we are therefore forced to conclude, tentatively at least, that an accurate prediction of sound-mean flow interaction effects requires some form of diverging jet flow model.

Unfortunately, this conclusion can only be regarded as tentative, not only because of the neglect of the unstable modes but because of some new experimental results recently reported by Ingard (18). The strong implication in these results is that the injection of sound into a mean flow through a boundary layer may not be correctly modelled by the assumption that the particle displacement is constant through that boundary layer. Further, the results indicate that continuity of particle velocity, while not explicitly justified by Ingard (18), should be used instead. While the experimental configuration (a rigid walled flow duct) is

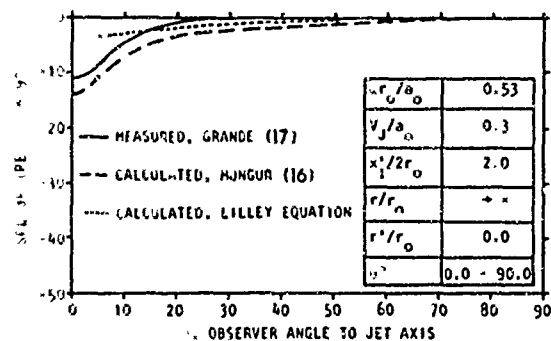


Fig. 8 Comparison of Theoretical Point Source Directivities with Grande's (17) Measurements ($V_j/a_0 = 0.3$)

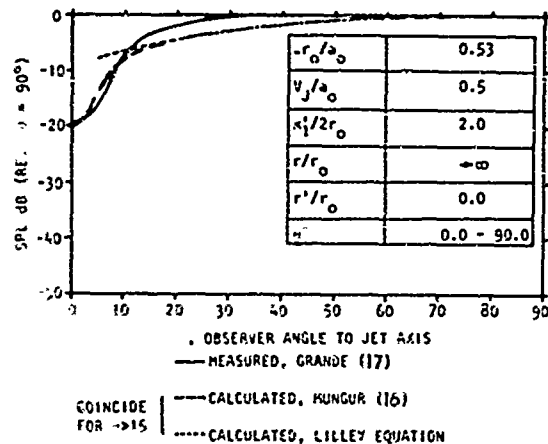


Fig. 9 Comparison of Theoretical Point Source Directivities with Grande's (17) Measurements ($V_j/a_0 = 0.5$)

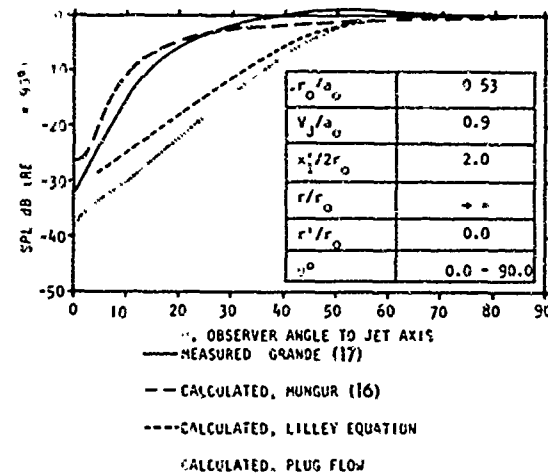


Fig. 10 Comparison of Theoretical Point Source Directivities with Grande's (17) Measurements ($V_j/a_0 = 0.9$)

different from that of the probe-jet experiment, it is of interest to modify our source model accordingly and to compute the new directivity patterns, at least for the "plug" jet flow profile. The results for comparison with MacGregor's (14) measurements are shown in Figure 11 and although the appearance of a peak in the calculated results is not consistent with measurement it may be more than coincidence that there is good agreement for the two higher frequencies, outside the 0-10° sector.

In spite of these results and our other areas of doubt, Mungur's impressive predictions have persuaded us that either his model, or perhaps a similar model still based on a locally parallel flow representation, should be used in our future work.

In the next section solutions to Lilley's equation will be used to construct a crude jet noise model and particular emphasis will be placed on the dependence of these solutions on source location and Helmholtz number. In the light of the above comparisons with experiment we should consider the

trends exhibited by the solutions to be only qualitatively correct.

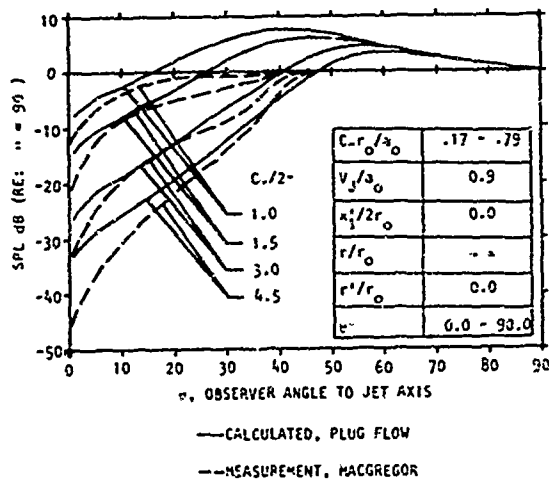


Fig. 11 Comparison of Plug Flow "Constant Particle Velocity Source" Directivities with MacGregor's (14) Measurements ($V_j/a_0 = 0.9$)

1-4.5 Solutions to Lilley's Equation

Having obtained the Green's function solution to Lilley's equation (in the far-field) as a function of frequency, source position, \underline{x}' , and the time at which the source emits a pulse, t' , the far-field pressure, $p(\underline{x}, \omega)$, due to a source distribution (in cylindrical coordinates)

$$\frac{a_0^2}{\partial^2(x_2)} S_c(\underline{x}, t)$$

is

$$p(\underline{x}, \omega) = \iiint_{-\infty}^{+\infty} \left(\frac{a_0^2}{\partial^2(r')} S_c(\underline{x}', t') \right) \times g(\underline{x}, \omega/\underline{x}', t') d\underline{x}' dt' \quad 5.1$$

where

$$\underline{x}' \equiv (x_1', r', \phi')$$

$$d\underline{x}' \equiv r' dr' d\phi' dx_1'$$

The form of S_c is given by equation 3.6 and the Green's function is, from equation 3.19,

$$g(x_1, r, \phi, \omega/x_1', r', \phi', t') =$$

$$= \frac{\exp[-jkx_1 \cos\theta - jkr \sin\theta]}{4\pi((x-x_1')^2 + r^2)} \exp[-j\omega t']$$

$$\exp[jk \cos\theta \cdot x_1'] \cdot \sum_{n=-\infty}^{\infty} C_n \exp[-jn(\phi-\phi')] \quad 5.2$$

where

$$C_n(r') = \frac{2 A_n(r')}{j^n} \exp[jn\pi/2]$$

$$A_{-n} = \exp[-n\pi i] A_n$$

and $A_n(r') = A(k \cos\theta, r', n)$ is a numerical solution to Lilley's equation. The components of the source distribution consist of first and second derivatives, with respect to x_1, r and ϕ , of the velocity products $v_1 v_1, v_1 v_r$, etc., but these can be removed, as in Lighthill's analysis, by partial integration. (From this point on we restrict the analysis to isothermal jet flows). An example of this manipulation is as follows; the leading term in S_c is

$$\rho_0 \frac{v_1^2}{\partial x_1'^2}$$

and the radiated pressure due to this component is

$$p(\underline{x}, \omega) = \iiint_{-\infty}^{+\infty} \rho_0 \frac{\partial^2 v_1^2}{\partial x_1'^2} g(\underline{x}, \omega/\underline{x}', t') d\underline{x}' dt'$$

which, after partial integration, is

$$p(\underline{x}, \omega) = \iiint_{-\infty}^{+\infty} \rho_0 v_1^2 \frac{\partial^2 g}{\partial x_1'^2}(\underline{x}, \omega/\underline{x}', t') d\underline{x}' dt'$$

This is an exact result as long as $\partial^2/\partial x_1'^2$ and v_1^2 vanish at $x_1' \rightarrow \pm \infty$. We now use the usual approximation, valid in the far-field, that terms like

$$\frac{\partial}{\partial x_1'} \left[\frac{1}{((x_1 - x_1')^2 + r^2)^{3/2}} \right] = \frac{\cos\theta}{R r^2}$$

(where $R^2 = (x_1 - x_1')^2 + r^2$)

$$\text{and } \frac{\partial}{\partial x_1'} (\cos\theta) = \frac{-\sin^2\theta}{R}$$

which appear in,

$$\frac{\partial}{\partial x_1'} \{ \exp[jk \cos\theta x_1'] \} = [jk \cos\theta$$

$$+ j k x_1' \frac{\partial}{\partial x_1'} \cos\theta] \exp[jk \cos\theta x_1']$$

can be neglected; so that for this example,

$$p(\underline{x}, \omega) \approx \iiint_{-\infty}^{+\infty} g(\underline{x}, \omega/\underline{x}', t') (-k^2 \cos^2\theta) \rho_0 v_1^2 d\underline{x}' dt'$$

Repeating these steps with all the components of S_c we obtain:

$$p(\underline{x}, \omega) = - \frac{\exp[-jk\bar{R}_r]}{4\pi\bar{R}_r} \cdot k^2 \iiint_{-\infty}^{+\infty} \Omega(x'_1, r', \phi') \phi(\rho_0 v_1 v_j, \Omega, \cos\bar{\theta}) \exp[-j\omega t'] r' dr' d\phi' dX'_1 dt' \quad 5.3$$

where

$$\begin{aligned} \bar{R}_r^2 &= (x_1 - \bar{x}'_1)^2 + r^2 \\ \cos\bar{\theta} &= (x_1 - \bar{x}'_1)/\bar{R}_r \\ X'_1 &= x'_1 - \bar{x}'_1 \end{aligned}$$

$$\Omega(x'_1, r', \phi') = \exp[jk\cos\bar{\theta}X'_1] \sum_{n=-\infty}^{\infty} C_n(r') \exp[-jn(\phi-\phi')] \quad 5.4$$

and

$$\begin{aligned} \phi(\rho_0 v_1 v_j, \Omega, \cos\bar{\theta}) &= \\ \rho_0 [v_1^2 \cos^2\bar{\theta} + v_1 v_2 \frac{j\cos\bar{\theta}}{\Omega} \frac{\partial\Omega}{\partial(kr')} + v_1 v_3 \frac{j\cos\bar{\theta}}{(kr')\Omega} \frac{\partial\Omega}{\partial\phi'} & \\ + v_2 v_1 \frac{j\cos\bar{\theta}}{\Omega} \frac{\partial\Omega}{\partial(kr')} + \frac{v_2^2}{\Omega} \frac{\partial^2\Omega}{\partial(kr')^2} & \\ + v_2 v_3 \{ \frac{1}{(kr')\Omega} \frac{\partial^2\Omega}{\partial(kr')\partial\phi'} - \frac{1}{(kr')^2\Omega} \frac{\partial\Omega}{\partial\phi'} \} & \\ + v_3 v_1 \frac{j\cos\bar{\theta}}{(kr')\Omega} \frac{\partial\Omega}{\partial\phi'} + v_3 v_2 \{ \frac{1}{(kr')\Omega} \frac{\partial^2\Omega}{\partial(kr')\partial\phi'} & \\ - \frac{1}{(kr')^2} \frac{\partial\Omega}{\partial\phi'} \} + v_3^2 \{ \frac{1}{(kr')^2\Omega} \frac{\partial^2\Omega}{\partial\phi'^2} & \\ + \frac{1}{(kr')\Omega} \frac{\partial\Omega}{\partial(kr')} \} & \end{aligned} \quad 5.5$$

Note that average values have been assigned to $\theta(\bar{\theta})$ and $R_r(\bar{R}_r)$, corresponding to an average value of $x'_1(\bar{x}'_1)$ since the variation of θ and R_r with x'_1 has been neglected in the above steps; \bar{x}'_1 is chosen in such a way as to minimize the errors incurred in these approximations.

In view of the apparent complexity of the expression for $p(\underline{x}, \omega)$ given in equation 5.3, it is of interest to consider the simplified expressions for the functions which appear in that equation when interactions between sound propagation and the mean flow field are ignored. This is a necessary exercise in any case; for we need to calculate the radiation in the direction normal to the jet flow, which is unaffected by flow effects (in isothermal jets), in order to compare this theory with experi-

mental results (which are normalized by the radiation level at 90° to the jet axis). The functions (for no interactions) become

$$\begin{aligned} \Omega(x'_1, r', \phi') &= \\ &= \exp[jk\cos\bar{\theta} X'_1 + jkr'\sin\bar{\theta}\cos(\phi-\phi')] \end{aligned} \quad 5.6$$

$$\phi(\rho_0 v_1 v_j, \Omega, \cos\bar{\theta}) = \rho_0 v_R^2 \quad 5.7$$

where

$$v_R = v_1 \cos\bar{\theta} + v_r \sin\bar{\theta} \cos(\phi-\phi') + v_\phi \sin\bar{\theta} \sin(\phi-\phi')$$

is the turbulent velocity component in the direction of the observer. We now proceed to obtain explicit expressions for $P(\underline{x}, \omega)$ the spectral density of $p(\underline{x}, \omega)$ and for this purpose equation (5.6) is rewritten as

$$\begin{aligned} \Omega(x'_1, r', \phi') &= \\ &= \exp[jk\cos\bar{\theta}X'_1] \sum_{n=-\infty}^{\infty} \exp[jn\pi/2] J_n(kr'\sin\bar{\theta}) \\ &\quad \times \exp[-jn(\phi-\phi')]. \\ P(\underline{x}, \omega) &= \frac{\rho_0^2 k^4}{16\pi^2 \bar{R}_r^2} \iiint_{-\infty}^{+\infty} \exp[jk\cos\bar{\theta}(X'-X'')] \\ &\quad \times \sum_{n=-\infty}^{\infty} \exp[jn\pi/2] J_n(kr'\sin\bar{\theta}) \exp[-jn(\phi-\phi')] \\ &\quad \times \sum_{m=-\infty}^{\infty} \exp[-jm\pi/2] J_m(kr''\sin\bar{\theta}) \exp[+jm(\phi-\phi'')] \\ &\quad \times \exp[-j\omega\tau] \cdot V_R^4(x'_1, x''_1, r', r'', \phi', \phi'', \tau) \\ &\quad \times r' dr' d\phi' dX'_1 dt' r'' dr'' d\phi'' dX''_1 dt'' \end{aligned} \quad 5.8$$

where

$$\begin{aligned} V_R^4 &= \text{Limit}_{T \rightarrow \infty} \frac{1}{2T} \int_T^T v_R^2(x'_1, r', \phi', \tau+t'') \\ &\quad \times v_R^2(x''_1, r'', \phi'', t'') dt'' \end{aligned} \quad 5.9$$

$$P(\underline{x}, \omega) = \text{Limit}_{T \rightarrow \infty} \frac{p(\underline{x}, \omega) p^*(\underline{x}, \omega)}{2T}$$

For simplicity we will assume that the source distribution is confined to a narrow annular region

such that its r dependence can be represented approximately by a delta function; then the integrations with respect to r' and r'' can be discarded to give

$$P(\underline{x}, \omega/r') = \frac{\rho_0^2 k^4}{16\pi^2 \bar{R}_r^2} \iiint_{-\infty}^{+\infty} \exp[jk \cos \bar{\theta} (X_1' - X_1'')] \times \left(\sum_{n,m} \exp[j\pi/2(m-n)] J_n(kr' \sin \bar{\theta}) J_m(kr' \sin \bar{\theta}) \right) \times \exp[j\phi(m-n) \exp(j(n\phi' - m\phi''))] \exp[-j\omega\tau] \times V_R^4(X_1', X_1'', r', \phi', \phi'', \tau) d\phi' dX_1' d\tau d\phi'' dX_1'' \quad 5.10$$

To carry out the ϕ'' and X_1'' integrations we make the usual assumption that V_R^4 can be expressed in the form

$$V_R^4 = V^4 S_1(X_1'') S_2(r') S_3(\phi'') S(X_1' - X_1'', \phi' - \phi'', \tau) \quad 5.11$$

but in the present analysis we make the realistic assumption that the V_R^4 is independent of ϕ'' for zero separation $\phi' - \phi'' = 0$, that is $S_3(\phi'') = 1$. With the transformations

$$\begin{aligned} X_1' - X_1'' &= \Delta_1 & dX_1' &= d\Delta_1 \\ \phi' - \phi'' &= \Delta_3 & d\phi' &= d\Delta_3 \\ m - n &= \ell \end{aligned}$$

equation 5.10 becomes

$$P(\underline{x}, \omega/r') = \frac{\rho_0^2 k^4 V^4 S_2(r')}{16\pi^2 \bar{R}_r^2} \iiint_{-\infty}^{+\infty} \exp[jk \Delta_1 \cos \bar{\theta}] \times \exp[-j\omega\tau] \left(\sum_{n,\ell} \exp[j\ell\pi/2] J_n(kr' \sin \bar{\theta}) \right) \times J_{n+\ell}(kr' \sin \bar{\theta}) \exp[j\ell\phi] \times \exp[jn\Delta_3] \exp[-j\ell\phi''] S_1(X_1') S(\Delta_1, \alpha, \tau) \times d\Delta_1 d\Delta_3 d\tau d\phi'' dX_1'' \quad 5.12$$

The integration with respect to ϕ'' is non-zero only when $\ell = 0$ so that $P(\underline{x}, \omega/r')$ is independent of ϕ and

$$P(\underline{x}, \omega/r') = \frac{\rho_0^2 k^4 V^4 S_2(r')}{8\pi \bar{R}_r^2} I_1 \iiint_{-\infty}^{+\infty} \exp[jk \Delta_1 \cos \bar{\theta}]$$

$$\times \exp[-j\omega\tau] \sum_n J_n^2(kr' \sin \bar{\theta}) \exp[jn\Delta_3] S(\Delta_1, \alpha, \tau) d\Delta_1 d\Delta_3 d\tau \quad 5.13$$

where

$$I_1 = \int_{-\infty}^{+\infty} S_1(X_1'') dX_1''$$

which can be calculated, numerically if necessary, independently of the other integrals.

To perform the remaining three integrations, we again make the usual assumption for the form of S and the functional dependence on Δ_1, Δ_3, τ :

$$S(\Delta_1, \Delta_3, \tau) = \exp\{-\delta_1^2/x^2 - \omega^2 \tau^2\} S_3(\Delta_3) \quad 5.14$$

where $\delta_1 = \Delta_1 - a_0 M_C \tau$ and where $S_3(\Delta_3)$ will be specified later. Equation 5.13 is then of the form

$$P(\underline{x}, \omega/r') = F_1 \cdot F_2 \iiint_{-\infty}^{+\infty} \exp[-\tau^2(\omega_0^2 + V_c^2/\ell_1^2)] \times \exp[-j\omega\tau(1 + 2jV_c \Delta_1/\omega \ell_1^2)] \exp[jk \Delta_1 \cos \bar{\theta}] d\tau d\Delta_1 \quad 5.15$$

where

$$F_1 = \frac{\rho_0^2 k^4 V^4 S_2(r')}{8\pi \bar{R}_r^2} I_1 \quad 5.16$$

$$F_2 = \sum_n J_n^2(kr' \sin \bar{\theta}) \int_0^{2\pi} S_3(\Delta_3) \exp[jn\Delta_3] d\Delta_3 \quad 5.17$$

The integration with respect to τ is of the form

$$\int_{-\infty}^{+\infty} e^{-a\tau^2} e^{-jb\tau} d\tau = \left(\frac{\pi}{a}\right)^{1/2} e^{-b^2/4a} \quad 5.18$$

where

$$a = \omega_0^2 + V_c^2/\ell_1^2$$

$$b = \omega(1 + 2jV_c \Delta_1/\omega \ell_1^2)$$

so that

$$P(\underline{x}, \omega/r') = F_1 \cdot F_2 \left(\frac{\pi}{\omega_0^2 + V_c^2/\ell_1^2}\right)^{1/2} \exp\left[\frac{-\omega^2}{4(\omega_0^2 + V_c^2/\ell_1^2)}\right] \int_{-\infty}^{+\infty} \exp\left[-\frac{\Delta_1^2}{x^2} \left(\frac{\omega_0^2}{\omega_0^2 + V_c^2/\ell_1^2}\right)\right]$$

$$\exp \left[-j \Delta_1 \left(\frac{V_c \omega / k_1^2}{\omega^2 + V_c^2 / k_1^2} - k \cos \bar{\theta} \right) \right] d\Delta_1 \quad 5.19$$

which again is of the same form as equation 5.18 and after some manipulation we get

$$P(\underline{x}, \omega / r^1) = F_1 \cdot F_2 \frac{-k_1}{\omega_0} \exp \left[\frac{-\omega^2}{4\omega_0^2} (1 - M_c \cos \bar{\theta})^2 \right] + \left(\frac{\omega_0 k_1 \cos \bar{\theta}}{a_0} \right)^2 \quad 5.20$$

Now consider the integral in equation 5.17 with

$$S_1(\Delta_1) = \exp \left[-\Delta_1^2 / \lambda_1^2 \right]$$

If the correlation length λ_1 is sufficiently small ($\ll 2\pi$), then to a good approximation the upper limit can be extended to infinity

$$\int_0^{2\pi} \exp \left[-\Delta_1^2 / \lambda_1^2 \right] \exp \{ j n \Delta_1 \} d\Delta_1 \\ = \int_0^{2\pi} \exp \left[-\Delta_1^2 / \lambda_1^2 \right] \exp \{ j n \Delta_1 \} d\Delta_1 \\ = \sqrt{\pi} \lambda_1 \int_{-\infty}^{\infty} \frac{\exp \left[-\Delta_1^2 / \lambda_1^2 \right]}{\sqrt{\pi} \lambda_1} \exp \{ j n \Delta_1 \} d\Delta_1$$

and in the limit $\lambda_1 \rightarrow 0$ the integral is simply $\sqrt{\pi} \lambda_1 / 2$ for all values of n . Thus, equation 5.17 becomes

$$F = \frac{\sqrt{\pi} \lambda_1}{2} \sum_n J_n^2(kr^1 \sin \bar{\theta}) = \frac{\sqrt{\pi} \lambda_1}{2} \quad 5.21$$

that is, it is independent of source position, kr^1 , and angle of observation $\bar{\theta}$.

The final expression for $P(\underline{x}, \omega / r^1)$ is

$$P(\underline{x}, \omega / r^1) = \frac{\omega_0^2 k^4 V^4 S_2(r^1) I_1}{8\pi \bar{R}_r^2} \left(\frac{\omega_0 k_1 \cos \bar{\theta}}{2\omega_0} \right)^{3/2} \\ \times \exp \left[\frac{-\omega^2}{4\omega_0^2} \left\{ (1 - M_c \cos \bar{\theta})^2 + \left(\frac{\omega_0 k_1 \cos \bar{\theta}}{a_0} \right)^2 \right\} \right] \quad 5.22$$

Although we will not be concerned with the intensity, $I(\underline{x}/r^1)$, where

$$I_0 a_0 I(\underline{x}/r^1) = \int_0^{\infty} P(\underline{x}, \omega / r^1) d\omega \quad 5.23$$

in the present work, for completeness we note that the integration can be carried out without recourse to numerical methods (in the absence of sound-mean flow interactions); the integral is of the form

$$\int_0^{\infty} \omega^{2n} e^{-\alpha^2 \omega^2} d\omega = \\ = (-1)^n \Gamma \left(\frac{1}{2} \right) 2^{-n-1} \alpha^{-(2n+1)} D_{2n}(0) \quad 5.24$$

where D_n is the parabolic cylinder function. With $n=2$, $D_4(0) = 3$ and

$$I = \frac{1}{2} \left\{ (1 - M_c \cos \bar{\theta})^2 + \left(\frac{\omega_0 k_1 \cos \bar{\theta}}{a_0} \right)^2 \right\}^{-1/2}$$

we get

$$\frac{3}{2} \frac{2^{-2-1} 2^{-2-1} \alpha^{-(2 \cdot 2 + 1)}}{\left\{ (1 - M_c \cos \bar{\theta})^2 + \left(\frac{\omega_0 k_1 \cos \bar{\theta}}{a_0} \right)^2 \right\}^{-1/2}}$$

so that

$$I(\underline{x}/r^1) = \frac{3\pi}{4\bar{R}_r} \frac{S(r^1) I_1 (r^1 \lambda_1) \omega_0^4 V^4 a_0^{-3/2}}{\left\{ (1 - M_c \cos \bar{\theta})^2 + \left(\frac{\omega_0 k_1 \cos \bar{\theta}}{a_0} \right)^2 \right\}^{1/2}} \quad 5.25$$

This expression for the intensity is identical in form to the expression first obtained by Ffowcs Williams (19), but it should be emphasized we have not employed a moving source analysis. As Lilley has pointed out, provided the same source space-time covariance function, $S(\Delta_1, \Delta_2, \tau)$ is used, the present stationary source analysis and any correctly performed moving source analysis must give the same result.

The spectral density result forms the basis for the presentation of experimental data in the form of difference spectra. With

$$\omega_s = \omega \left\{ (1 - M_c \cos \bar{\theta})^2 + \left(\frac{\omega_0 k_1 \cos \bar{\theta}}{a_0} \right)^2 \right\}^{1/2}$$

equation 5.22 becomes

$$P(\underline{x}, \omega / r^1) = \frac{\omega_0^2 V^4 S_2(r^1) I_1}{8\pi \bar{R}_r^2 a_0^4} \left(\frac{\omega_0 k_1 \cos \bar{\theta}}{2\omega_0} \right)^{3/2} \times \\ \frac{\omega_s^4}{\left\{ (1 - M_c \cos \bar{\theta})^2 + \left(\frac{\omega_0 k_1 \cos \bar{\theta}}{a_0} \right)^2 \right\}^2} \cdot \exp \left\{ \frac{-\omega_s^2}{4\omega_0^2} \right\} \quad 5.26$$

To allow for the fact that experimental spectrum measurements are in bandwidths proportional to frequency, we consider the quantity, $\omega P(\underline{x}, \omega/r')$ where

$$\omega P(\underline{x}, \omega/r') = \frac{1}{\{(1-M_c \cos \bar{\theta})^2 + (\frac{\omega_0 k_1}{a_0} \cos \bar{\theta})^2\}^{5/2}} \quad 5.27$$

and where we have retained only the $\bar{\theta}$ dependent form. This is the predicted directivity factor provided ω_s is held constant. In the rear arc ($\bar{\theta} < 90^\circ$) this means referring to increasing observed frequencies with decreasing $\bar{\theta}$. The difference spectra are defined as the difference between the measured sound pressure levels and the levels predicted by equation 5.27.

We now repeat the analysis (given above) with at least some sound-mean flow interactions included. In the present study we neglect flow effects in the function ψ which, in the absence of flow, is

$$\psi = \rho_0 v_R^2$$

and is otherwise given by equation 5.5. We then have

$$p(\underline{x}, \omega/r') = - \frac{\exp[-jkR_r]}{4\pi R_r} k^2 \iiint_{-\infty}^{+\infty} \rho_0 \tilde{v}_R^2 \Omega(X_1', r', \phi') \exp[-j\omega t'] d\phi' dX_1' dt' \quad 5.3a$$

where

$$\rho_0 \tilde{v}_R^2 = \rho_0 \tilde{v}_R^2(X_1', r', \phi', t') = \psi$$

is assumed to be independent of sound-mean flow interaction effects and, it will be assumed, has the same space-time covariance. The function Ω is defined in equation 5.4; it has the same form as in the zero flow case, but with the Bessel function $J_n(kr' \sin \bar{\theta})$ replaced by a function $C_n(r')$ which is only known numerically and is a function of frequency and the jet mean flow parameters as well as the point source position r' and n . The dependence of Ω on X_1' and ϕ' is otherwise the same as before up to the point where the relation

$$\sum_{n=-\infty}^{\infty} J_n^2(kr' \sin \bar{\theta}) = 1$$

is used. In the present case the expression

$$\sum_{n=-\infty}^{\infty} C_n(r') C_n^*(r')$$

cannot be further simplified and must be evaluated numerically. The final expression for the frequency weighted spectral density is thus

$$\omega P(\underline{x}, \omega/r') = \frac{\rho_0 \tilde{v}_R^2 S_2(r') I_1}{8\pi^2 R_r^2 a_0^4} \left\{ \frac{\omega_s^2}{2\omega_0} \right\} \frac{\omega_s^5}{\{(1-M_c \cos \bar{\theta})^2 + (\frac{\omega_0 k_1}{a_0} \cos \bar{\theta})^2\}^{5/2}} \times \exp\left\{-\frac{\omega_s^2}{4\omega_0^2}\right\} \sum_{n=-\infty}^{\infty} C_n(r') C_n^*(r') \quad 5.26a$$

We now present some results which show how the coefficient $C_n(r')$ depends on the Helmholtz number kr_0 , the radial position of the source r'/r_0 , the mode number n , the jet exit Mach number $M_R = V_J/a_0$ and the mean velocity profile, represented by the distance from the nozzle where such a profile is found in a real diverging jet. Temperature effects are excluded and mean velocity profiles are confined to those which would be found in the mixing region, that is up to approximately four diameters from the jet nozzle. Finally, with some further assumptions we will calculate the sum

$$\sum_{n=0}^N C_n(r') C_n^*(r')$$

and compare this with the difference spectra obtained from experimental results.

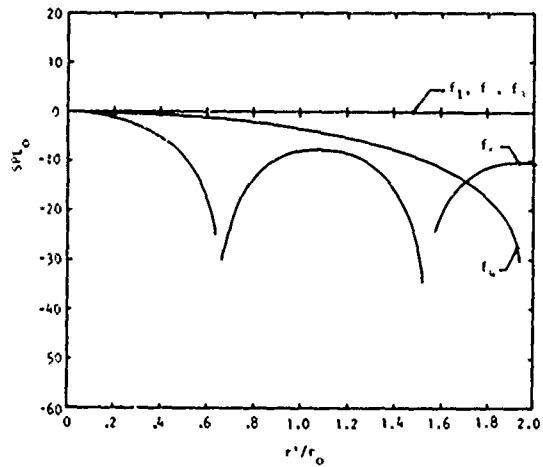
In the following results we evaluate $10 \log_{10}(C_n C_n^*) \equiv \text{SPL}_n$ at five selected Helmholtz numbers denoted by f_i , $i = 1, 5$, where

	kr_0	fd/a_0
f_1	.09426	.03
f_2	.3142	.1
f_3	.9426	.3
f_4	3.142	1.0
f_5	9.426	3.0

These span the frequencies of interest in our model jet experiments. In Figures 12-18 we keep the observer angle to the jet axis constant at 22.5° and show results for the ($n=0$) axisymmetric mode; Figures 19-25 are at the same conditions but for ($n=1$) the first circumferential mode. All these figures are plots of SPL_n versus the radial position of the source, r'/r , at the five selected Helmholtz numbers. Figure 12 is for the trivial case of no flow, showing that, except at the two highest frequencies, the radiation level (which is proportional to SPL_n) is independent of the radial position of the source. In Figure 13 the conditions are the same except the Mach number is 0.32 with a "top-hat" or "plug" profile (that is, corresponding approximately to the profile at the jet nozzle). At low frequencies radiation due to sources anywhere inside the jet are increased whereas at high frequencies

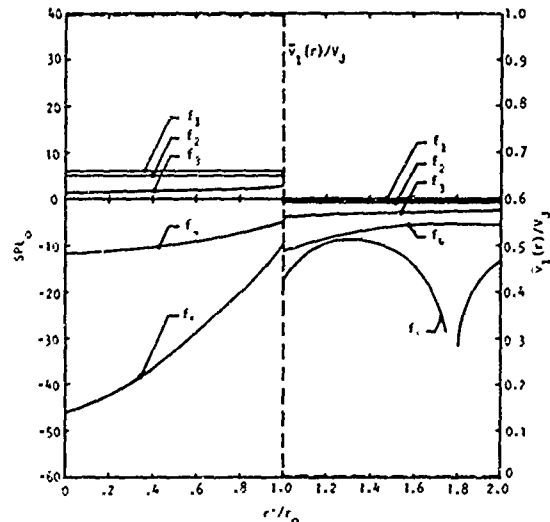
particularly for sources near the axis there is a substantial reduction or attenuation in radiation levels. The discontinuity in level when the source is on the "lip-line", $r' = r_0$ is due to the discontinuity in the mean velocity profile at the same point: the source is either inside or outside the mean flow. When we use a velocity profile like that at the end of the mixing region, that is a continuous mean velocity profile, the solutions to Lilley's equation for SPL_n are well behaved, as shown, in Figure 14; the "low frequency lift" and the high frequency attenuation characteristics of the "plug" flow solutions remain although quantitatively there are large differences between the two solutions. Figures 13 and 14 illustrate one of the many advantages offered by Lilley's equation; the radiation can be calculated in a realistic way for source distributions within the jet shear layer. The use of "plug" flow models inevitably leads to an unrealistic discontinuity in radiation levels unless the source distribution is arbitrarily confined to regions either inside or outside the jet. At higher Mach numbers Figures 15 and 16 ($M_R = 0.71$) and Figures 17 and 18 ($M_R = 1.0$) show that the "low frequency lift" and the high frequency attenuation levels continue to diverge unless the source is located in the outer regions of the jet where resulting radiation levels are relatively insensitive to frequency.

In Figures 19-25 the results are repeated for the $n=1$ mode; the "low frequency lift" is far less apparent but the high frequency attenuation effect is clearly visible and is very similar to the $n=0$ mode's behavior at the highest frequency.



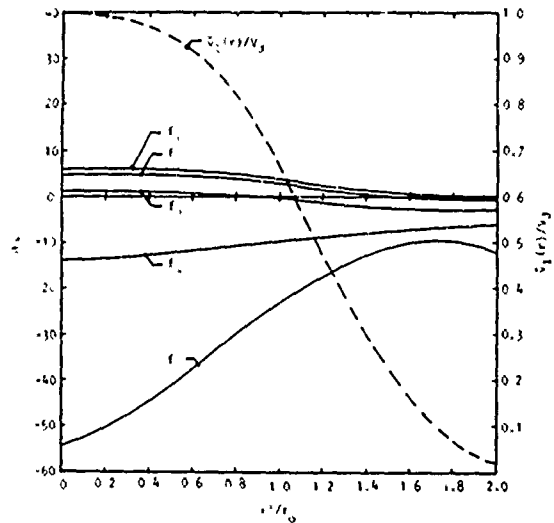
$-r_0/a_0$.094 - 9.4
M_R	0.0
$x_1/2r_0$	0.0
r/r_0	-
r'/r_0	0 - 2
ω^0	22.5
n	0

Fig. 12 Variation of SPL_0 with Radial Position of Source: $M_R = 0.0$, $n = 0$



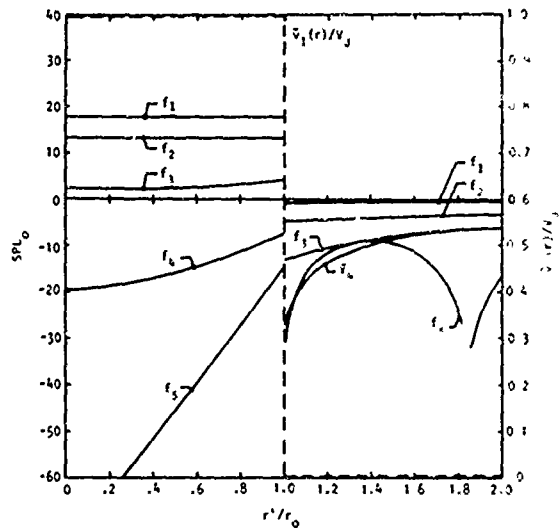
$-r_0/a_0$.094 - 9.4
M_R	0.32
$x_1/2r_0$	0.0
r/r_0	-
r'/r_0	0 - 2
ω^0	22.5
n	0

Fig. 13 Variation of SPL_0 with Radial Position of Source: $M_R = .32$, $n = 0$



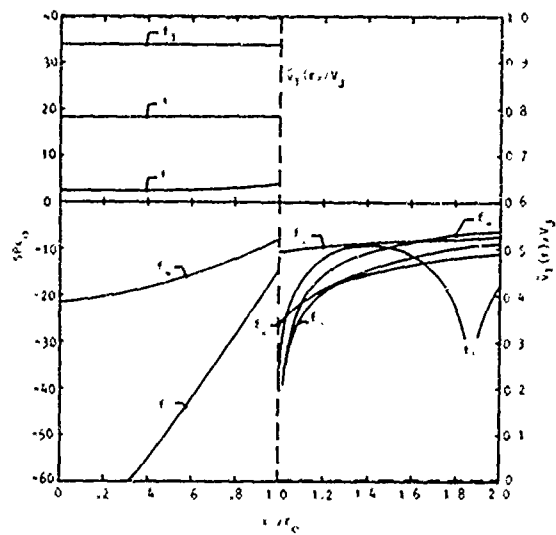
$-r_0/a_0$.094 - 9.4
M_R	0.32
$x_1/2r_0$	0
r/r_0	-
r'/r_0	0 - 2
ω^0	22.5
n	0

Fig. 14 Variation of SPL_0 with Radial Position of Source: $M_R = 0.32$, $n = 0$



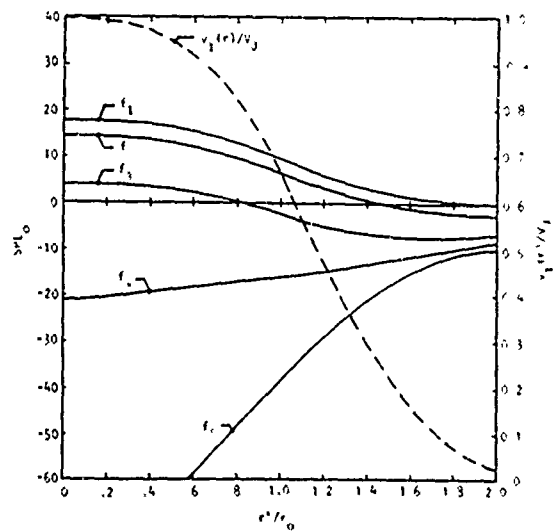
r_0/a_0	.094 - 9.4
M_R	0.71
$\lambda_1/2r_0$	0.0
r/r_0	-
r'/r_0	0 - 2
-	22.5
n	0

Fig. 15 Variation of SPL_0 with Radial Position of Source: $M_R = .71$, $n = 0$



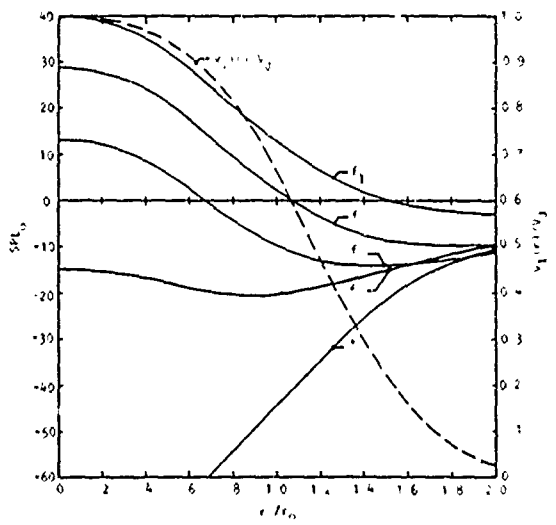
r_0/a_0	.094 - 9.4
M_R	1.0
$\lambda_1/2r_0$	4
r/r_0	-
r'/r_0	0 - 2
-	22.5
n	0

Fig. 17 Variation of SPL_0 with Radial Position of Source: $M_R = 1.0$, $n = 0$



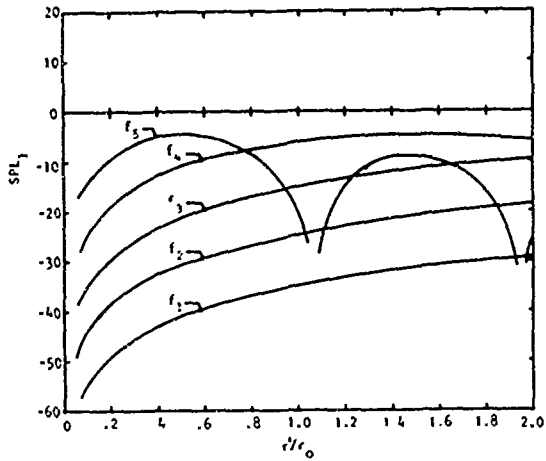
r_0/a_0	.094 - 9.4
M_R	0.71
$\lambda_1/2r_0$	4
r/r_0	-
r'/r_0	0 - 2
-	22.5
n	0

Fig. 16 Variation of SPL_0 with Radial of Source: $M_R = .71$, $n = 0$



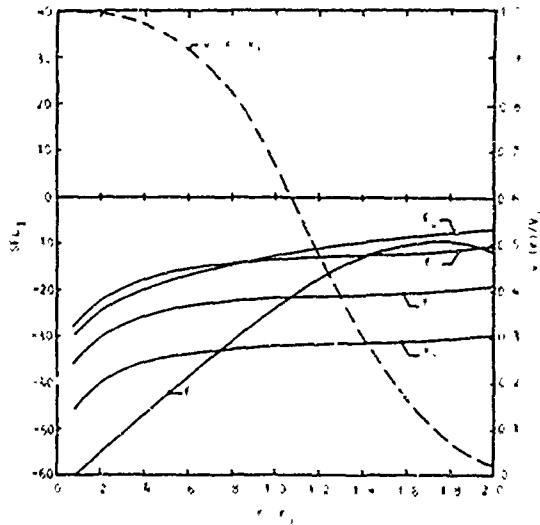
r_0/a_0	.094 - 9.4
M_R	1.0
$\lambda_1/2r_0$	4
r/r_0	-
r'/r_0	0 - 2
-	22.5
n	0

Fig. 18 Variation of SPL_0 with Radial Position of Source: $M_R = 1.0$, $n = 0$



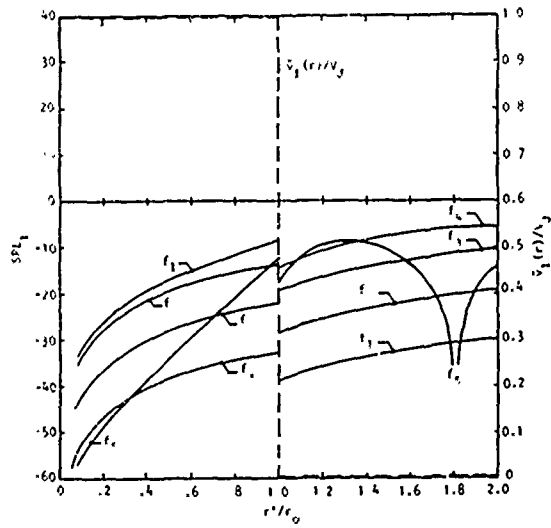
r'_0/a_0	.094 - 9.4
M_R	0.0
$x'_1/2r_0$	0.0
r/r_0	∞
r'/r_0	0 - 2
ω^0	22.5
n	1

Fig. 19 Variation of SPL_1 with Radial Position of Source: $M_R = 0, n = 1$



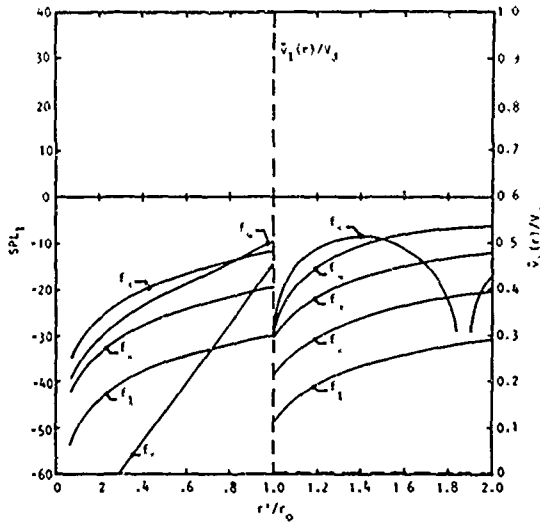
r'_0/a_0	.094 - 9.4
M_R	0.32
$x'_1/2r_0$	0
r/r_0	∞
r'/r_0	0 - 2
ω^0	22.5
n	1

Fig. 21 Variation of SPL_1 with Radial Position of Source: $M_R = .32, n = 1$



r'_0/a_0	.094 - 9.4
M_R	0.32
$x'_1/2r_0$	0.0
r/r_0	∞
r'/r_0	0 - 2
ω^0	22.5
n	1

Fig. 20 Variation of SPL_1 with Radial Position of Source: $M_R = .32, n = 1$



r'_0/a_0	.094 - 9.4
M_R	0.71
$x'_1/2r_0$	0.0
r/r_0	∞
r'/r_0	0 - 2
ω^0	22.5
n	1

Fig. 22 Variation of SPL_1 with Radial Position of Source: $M_R = .71, n = 1$

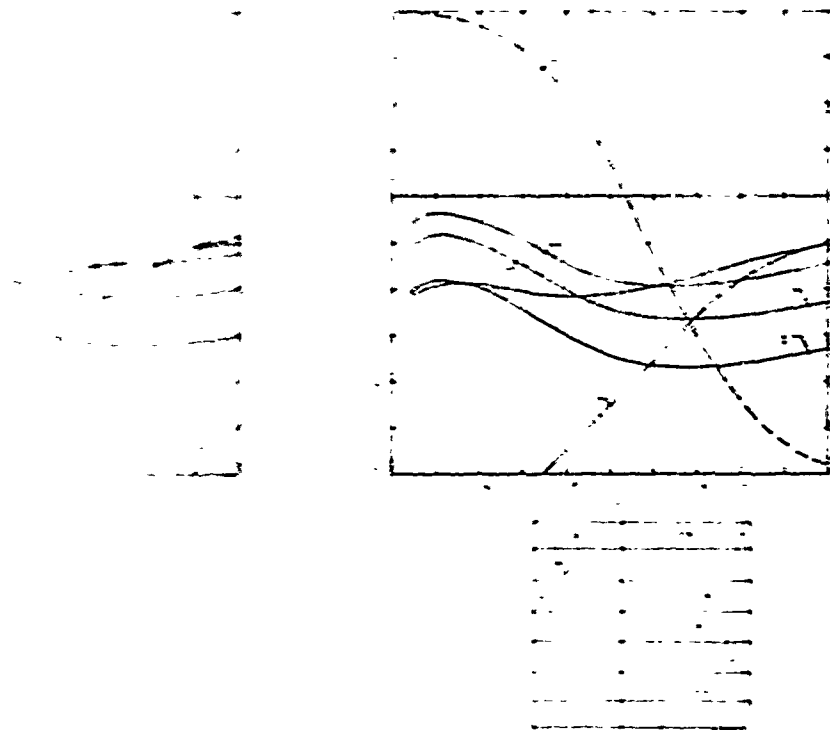


Fig. 26 Variation of SPL_n with Radial Position of Sources $M_0 = 1, n = 1$

To illustrate the behavior of SPL_n with the observer angle θ and higher circumferential mode orders, n , we fix the radial source position at the "lip-line," r'/r_0 , and the jet Mach number at unity. We suggest that the strongest source components in the mixing region of a real jet will be located at r' near the lip-line, we are, of course, ignoring the other regions of the jet downstream of the potential core where the more important low frequency sources are thought to exist. Thus, in comparing the following results with experimental trends, we cannot expect agreement at low frequencies. In Figure 26 SPL_n is shown as a function of frequency for five observer angles. Since the source is located off the jet axis, the "low frequency lift" is not so large — up to 12 dB at the smallest angle. At high frequencies the radiation at all angles is reduced but this trend is modified when we consider the total radiation due to all mode orders. In Figures 27-29 SPL_n for mode numbers 1, 2 and 3 is shown for the same conditions as in Figure 26; we can now observe the trends predicted by Michalke (20) that, at low frequencies ($kr_0 < 1$), the non-axisymmetric modes cannot radiate but as the frequency is increased each mode becomes "cut-on" and gives rise to higher levels than the axisymmetric mode ($n=0$).

We have not attempted to carry out extensive comparisons with experimental results since we have considered completely realistic source distributions. Also, it is clear that we must obtain more agreement with, for example, the probe-interferometric patterns before proceeding to compare the radiation from any detailed source distribution with experimental results.

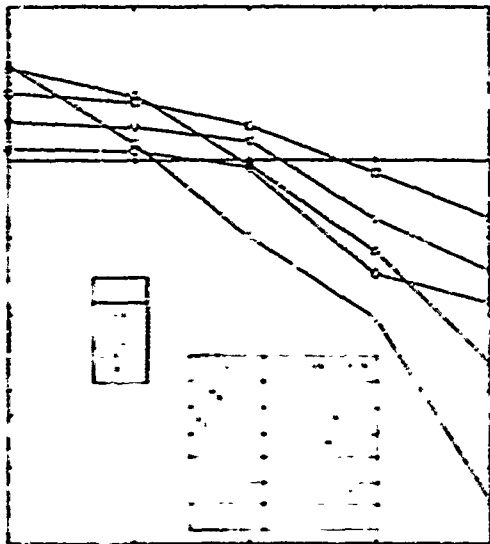


Fig. 26 Variation of SPL_D with Frequency: $n = 0$

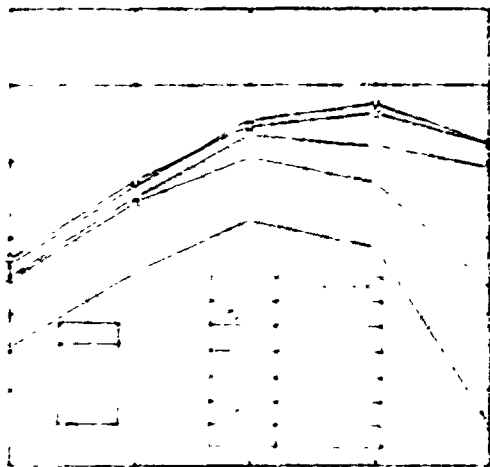


Fig. 27 Variation of SPL_D with Frequency: $n = 1$

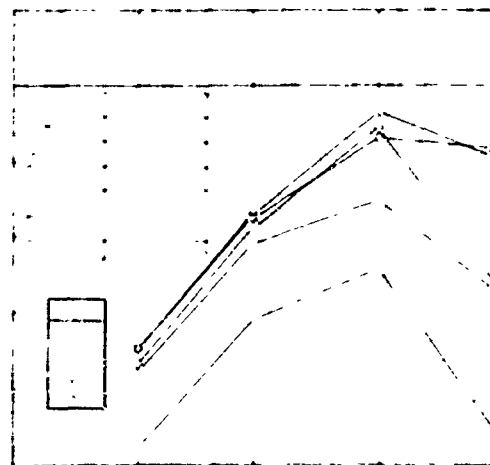


Fig. 28 Variation of SPL_D with Frequency: $n = 2$

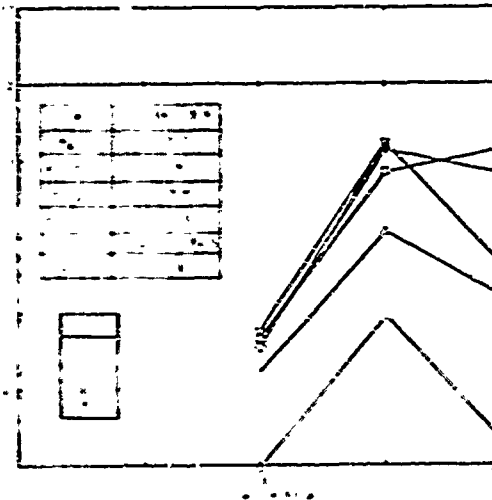


Fig. 29 Variation of SPL_D with Frequency: $n = 3$

However, it is worth comparing our results with measurements on a limited basis for an assumed form of the source distribution which leads to the expression for spectral density given by equation 5.26a. This expression is identical to that given by equation 5.26, where sound mean flow interactions have been ignored, except for the factor

$$\sum_{n=-\infty}^{\infty} C_n(r') C_n^*(r')$$

This infinite sum, over all mode numbers, is equal to unity for zero mean flow but when the C_n coefficients are numerical solutions to Lilley's equation, we can only evaluate this sum numerically and include as many terms as are necessary for convergence. The table below shows the highest value of n required to obtain convergence in the zero flow case for each angle/frequency combination. These numbers appear to be a good indication of those required to evaluate the sum at finite Mach numbers.

kr_0/r	82.5	67.5	52.5	37.5	22.5
0.09426	0	0	0	0	0
0.3142	1	1	1	1	0
0.9426	2	2	1	1	1
3.142	4	4	3	2	1
9.426	11	10	9	7	5

We associate the sum

$$SPL_D = 10 \log_{10} \left(\sum_n C_n(r') C_n^*(r') \right)$$

with the non-zero difference spectra; that is, the model which ignores interactions between sound propagation and the mean flow gives an expression (equation 5.26) which predicts a certain dependence on the observer angle θ . This dependence is assumed to be correct and is subtracted from the

measured directivity to yield the so-called difference spectra. If the model was correct, the difference spectra levels would collapse on the 0 dB line. An example of their actual behavior for $M_R = 1$ taken from reference (21) is shown in Figure 30. Our evaluation of the sound-mean flow interaction effects for direct comparison with Figure 30 are shown in Figure 31 (with $r' = r_0$, that is a point source radial distribution centered on the lip-line). The agreement is not good at low frequencies, as we might have expected; at high frequencies and small angles the predicted trends are correct while at larger angles the calculated spectrum levels are too high. Nevertheless, we feel that this comparison is fairly encouraging when we reflect upon the number of assumptions used to obtain these theoretical difference spectra. Both the general low frequency behavior and the high frequency-large angle discrepancies may be radically improved once (i) effects of the diverging jet flow are more adequately modeled, (ii) other problem areas mentioned are satisfactorily resolved and (iii) a more accurate source function distribution is used.

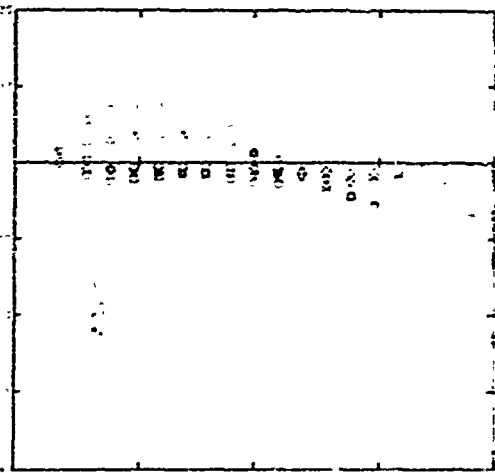


Fig. 30 Measured Difference Spectra: $M_R = 1.0$

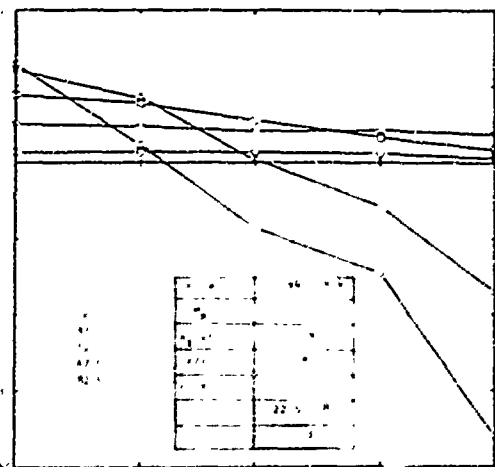


Fig. 31 Theoretical Difference Spectra

*Some of the infrequently used symbols defined in the text have been omitted.

1-4.6 Conclusions and Future Work

1. The homogeneous form of Lilley's equation is recognized to be the same as the equation which is used to investigate the stability of inviscid, compressible sheared flows. Thus, two types of solution can be obtained: the "acoustic solution" and the "unstable solution". Unstable solutions are being studied in our theoretical program to provide information for a model of the source function in Lilley's equation and are described elsewhere. The "acoustic solution" is the subject of this report.

2. Acoustic solutions to Lilley's equation can be constructed from an appropriate specification of the source function and point source or Green's function solutions.

3. The influence of sound-mean flow interaction effects on the radiation level and directivity of point source solutions has been evaluated in some detail for subsonic parallel jet flows with realistic mean velocity profiles.

4. The directivity of modified point solutions are only in qualitative agreement with measurement and while questions remain concerning representation of the experimental source and the type of solution utilized here, consideration of theoretical results, obtained elsewhere, strongly suggests that a more realistic mean flow model is required.

5. A complete solution to Lilley's equation for a simplified version of the standard type of source function is evaluated in the form of difference spectra which are found to be in good qualitative agreement with measurement.

Future work will concentrate on the role of unstable solutions from the acoustic viewpoint, the development of a more realistic mean flow model and the evaluation of solutions to Lilley's equation for source functions based on a combination of turbulence measurements and the theoretical model currently under development.

1-4.7 Acknowledgements

The work described in this report was sponsored by Air Force Contract F33615-73-C-2032, which is jointly funded by the Air Force Aero Propulsion Laboratory and the U. S. Department of Transportation. The contract is administered by the AFAPL and the Technical Monitor is Paul Shahady.

The authors are grateful to Lockheed's Contract Program Manager, Harry E. Plumblee, for many useful discussions, and to Prof. G. M. Lilley for his encouragement and technical guidance.

List of Symbols*

$\bar{a}(r), a_0$	speed of sound inside and outside jet
b, c	constants in analytic representation of mean velocity profile
C_n	numerical solution to Lilley's equation

E_n	dispersion relationship in "plug" flow model	v_R	fluctuating velocity in direction of observer
g, G	Green's functions	$\underline{x} = (x_1, x_2, x_3)$	position vector in cartesian coordinates
H	Helmholtz number	$\underline{x} = (x_1, r, \phi)$	position vector in cylindrical coordinates
$H_0^{(2)}$	Bessel function of the third kind or Hankel function	$\underline{x} = (R, \theta, \phi)$	position vector in spherical coordinates
H_n	Hermite polynomial	Y_n	Bessel function of the second kind
I	sound intensity	α	polar coordinate angle in complex R plane
j	$\sqrt{-1}$	β	admittance parameter
J_n	Bessel function of the first kind	γ	ratio of specific heats - assumed constant
$k = \omega/a_0$	free space wavenumber	Δ_1, Δ_3	separation coordinates in x_1, x_3 directions
k_z	axial wavenumber	$\delta(\)$	Dirac delta function
k_r, k_θ	radial (r) wavenumber inside and outside jet	ϵ	probe radius
l_1, l_3	source function correlation lengths in x_1, x_3 coordinates	ϵ_1	separation coordinate in x_1 direction in moving frame
∇	partial differential operator of Lilley's equation	ϵ_n	$\epsilon_0 = 1; \epsilon_n = 2, n > 0$
m	circumferential mode number	ζ	Lilley transform variable
$M_1 = \bar{v}_1(r)/a_0$	mean axial Mach number	η	similarity variable in mean velocity profile functions
$M_R = V_J/a_0$	mean axial Mach number at jet nozzle and in potential core	Λ	source function in Lilley's equation
M_c	eddy convection Mach number	ξ	displacement parameter in r direction
n	circumferential mode number	ξ_d	displacement in r direction
p', p	fluctuating pressure	$\rho(r), \rho_0$	mean density inside and outside jet
P_0	mean pressure - assumed constant	σ	polar coordinate radius in complex R plane
P	spectral density of p	τ	time separation variable
q	coefficient in Lilley's transformed equation	χ	variable used in mean velocity profile functions
r_0	jet nozzle radius	ω	radian frequency
$R = r/r_0$	nondimensionalized radial coordinate	ω_0	probe excitation frequency in section 1-4.4
R_c	radial position of critical point	ω_0	frequency constant of source function in section 1-4.5
S_p, S_c	Lighthill's source function in cartesian and cylindrical coordinates		
t	time		
$v_i', i=1,2,3$	fluctuating velocity components in cartesian coordinate directions $x_i, i=1,2,3$		
$\bar{v}_1 = \bar{v}_1(r)$	mean axial velocity		
V_J	mean axial velocity at jet nozzle and in potential core		

References

1. G. M. Lilley, H. E. Plumblee, W. C. Strahle, S. Y. Ruo and P. E. Doak, 1972. T. R. AFAPL-TR-72-53-Vol. IV. Theory of turbulence generated jet noise, noise radiation from upstream sources and combustion noise.

2. G. M. Lilley, P. J. Morris and E. J. Tester, 1973. AIAA Paper No. 73-987. On the theory of jet noise and its application.
3. M. J. Lighthill, 1952. Proc. Roy. Soc. A211, pp. 564-578. On sound generated aerodynamically. I - general theory.
4. O. M. Phillips, 1960. J. Fluid Mech., 9, pp. 1-28. On the generation of sound by supersonic turbulent shear layers.
5. P. J. Morris, 1974. AIAA Paper No. 74-1. A model for the structure of jet turbulence as a source of noise
6. D. C. Pridmore-Brown, 1958. J. Fluid Mech. 4, pp. 393-406. Sound propagation in a fluid flowing through an attenuating duct.
7. P. Mungur and H. E. Plumblee, 1969, NASA SP-207. Basic Aerodynamic Noise Research, pp. 305-327. Propagation and attenuation of sound in a soft-walled annular duct containing a sheared flow.
8. L. Lees and C. C. Lin, 1946. NACA T.N. 1115. Investigation of the stability of the laminar boundary layer in a compressible fluid.
9. M. S. Howe, 1970. J. Fluid Mech. 43, pp. 353-367. Transmission of an acoustic pulse through a plane vortex sheet.
10. G. Moretti and S. Slutsky, 1959. AFOSR TN-59-1310. The noise field of a subsonic jet.
11. S. Slutsky and J. Tamagno, 1961. AFOSR TN 1935. Sound field distribution about a jet.
12. S. Slutsky, 1962. AFOSR 2455. Acoustic field of a cylindrical jet due to a distribution of random sources or quadrupoles.
13. R. Mani, 1972. J. Sound Vib. 25, pp. 337-347. A moving source problem relevant to jet noise.
14. G. R. MacGregor, H. S. Ribner and H. Lam, 1973. J. Sound Vib. 27(4), pp. 437-454. "Basic" jet noise patterns after deletion of convection and refraction effects: experiment vs. theory.
15. L. K. Schubert, 1972. J.A.S.A. 51, pp. 447-463. Numerical study of sound refraction by a jet flow, II. Wave acoustics.
16. P. M. Mungur, H. E. Plumblee and P. E. Doak. Submitted to J. Sound Vib. On the influence of jet flow on sound radiation.
17. E. Grande, 1967, NASA CR-840. Refraction of sound by jet flow and jet temperature, II.
18. U. Ingard, V. K. Singhal and A. G. Galitsis, 1973. Proceedings of the Interagency Symposium on University Research in Transportation Noise, Stanford University, Stanford, California, Vol. II. Studies of duct liners and the interactions of sound and flow in ducts.
19. J. E. Ffowcs Williams, 1963. Phil. Trans. Roy. Soc. A. 255, pp. 469-503. The noise from turbulence convected at high speed.
20. A. Michalke, 1972. Z. Flugwiss 20, pp. 229-237. An expansion scheme for the noise from circular jets.
21. P. A. Lush and R. H. Burrin, 1972. T.R. AFAPL-TR-72-53-Vol. V. An experimental investigation of jet noise variation with velocity and temperature.
22. L. M. Brekhovskikh, 1960. Waves in layered media. Academic Press.
23. J. W. Miles, 1962. J. Fluid Mech. 13, p. 427. A note on the inviscid Orr-Sommerfeld equation.
24. M. J. Fisher, 1973. Private Communication.
25. H. Schlichting, 1960. Boundary layer theory. McGraw-Hill.
26. M. Abramowitz and I. A. Stegun, 1966. Handbook of mathematical functions. National Bureau of Standards, Applied Mathematical Series.

APPENDIX 1-4A

Plug Flow Model

The Green's functions in region 1 (see Figure 2) must satisfy the equation

$$\frac{d^2 G}{dr^2} + \frac{1}{r} \frac{dG}{dr} + k_2^2 G = \frac{s(r)}{r} \quad \text{A.1}$$

where

$$k_2^2 = k^2 - k_1^2 \quad \text{A.2}$$

$$s = -\exp[-j\omega t'] \exp[jk_1 x_1']$$

The Green's function in region 2 must satisfy the equation

$$\frac{d^2 G}{dr^2} + \frac{1}{r} \frac{dG}{dr} + K_2^2 G = 0 \quad \text{A.3}$$

where

$$K_2^2 = (k - k_1 M_1)^2 - k_1^2 \quad \text{A.4}$$

The Green's function in region 3 must satisfy the equation

$$\frac{d^2 g}{dr^2} + \frac{1}{r} \frac{dg}{dr} + k_2^2 g = 0 \quad \text{A.5}$$

where

$$k_2^2 = k^2 - k_1^2 \quad \text{A.6}$$

The required solution to equation A.1 in region 1 is

$$G_1 = A_1 J_0(k_2 r) + S \cdot \frac{j\pi}{2} H_0^{(2)}(k_2 r) \quad \text{A.7}$$

The required solution to equation A.3 in region 2 is

$$G_2 = A_2 J_0(k_2 r) + B_2 Y_0(k_2 r) \quad A.8$$

The required solution to equation A.5 in region 3 is

$$g_3 = A_3 H_0^{(2)}(k_2 r) \quad A.9$$

The unknown coefficients A_r, B_r ($r = 1, 2, 3$) are determined by the conditions of continuity of pressure and particle displacement across the vortex sheets at their mean positions $r = \delta$ and $r = r_0$.

The continuity of pressure at $r = \delta, r_0$ gives

$$\begin{aligned} A_1 J_0(k_2 \delta) + \frac{jS\pi}{2} H_0^{(2)}(k_2 \delta) \\ = A_2 J_0(k_2 \delta) + B_2 Y_0(k_2 \delta) \end{aligned} \quad A.10$$

$$A_2 J_0(k_2 r_0) + B_2 Y_0(k_2 r_0) = A_3 H_0^{(2)}(k_2 r_0) \quad A.11$$

and the continuity of particle displacement at $r = \delta, r_0$ gives

$$\begin{aligned} k_2 \{ A_1 J_0'(k_2 \delta) + \frac{jS\pi}{2} H_0^{(2)'}(k_2 \delta) \} \\ = (1 - k_1 M_1 / k)^{-1} k_2 \{ A_2 J_0'(k_2 \delta) \\ + B_2 Y_0'(k_2 \delta) \} \end{aligned} \quad A.12$$

$$\begin{aligned} \{ (1 - k_1 M_1 / k)^{-1} k_2 \{ A_2 J_0'(k_2 r_0) + B_2 Y_0'(k_2 r_0) \} \\ = k_2 A_3 H_0^{(2)'}(k_2 r_0) \end{aligned} \quad A.13$$

From equations A.10 - A.13 the solution for A_3 is, in the limit $k\delta \rightarrow 0$,

$$A_3 = \frac{\psi S}{E_0} \quad A.14$$

where

$$\begin{aligned} E_0 = \psi k_2 r_0 H_0^{(2)'}(k_2 r_0) J_0(k_2 r_0) \\ - k_2 r_0 J_0'(k_2 r_0) H_0^{(2)}(k_2 r_0) \end{aligned} \quad A.15$$

$$\psi = (1 - k_1 M_1 / k)^2. \quad A.16$$

The required Green's function is then obtained by performing the two Fourier inversions (the latter being trivial as $n = 0$):

$$\begin{aligned} g_3(x_1, r, n, \omega/x_1', 0, 0, t') = \\ \frac{1}{2\pi} \int_{-\infty}^{+\infty} A_3 H_0^{(2)}(k_2 r) \exp[-jk_1 x_1] dk_1 \end{aligned} \quad A.17$$

$$g_3(x_1, r, \phi, \omega/x_1', 0, 0, t') =$$

$$\frac{1}{2\pi} g_3(x_1, r, n, \omega/x_1', 0, 0, t'). \quad A.18$$

and from Appendix 1-4B the far-field approximations, $kR_r \rightarrow \infty$, to equation A.18 for the acoustic component of g_3 is

$$\begin{aligned} g_3(R_r, \theta, \phi, \omega/x_1', 0, 0, t') = \\ \frac{\exp[-jkR_r]}{4\pi R_r} \exp[-j\omega t'] \frac{(-2j/\pi)}{E_0} \bar{\psi} \end{aligned} \quad A.19$$

where

$$\begin{aligned} R_r^2 &= (x_1 - x_1')^2 + r^2 \\ \bar{\psi} &= (1 - M_1 \cos\theta)^2 \\ \bar{E}_0 &= \bar{\psi} \bar{k}_2 r_0 H_0^{(2)'}(\bar{k}_2 r_0) J_0(\bar{k}_2 r_0) \\ &\quad - \bar{k}_2 r_0 J_0'(\bar{k}_2 r_0) H_0^{(2)}(\bar{k}_2 r_0) \\ \bar{k}_2 r_0 &= kr_0 \sin\theta \\ \bar{k}_2^2 r_0^2 &= (kr_0)^2 \{ (1 - M_1 \cos\theta)^2 - \cos^2\theta \}. \end{aligned}$$

in principle the Green's function $g_3(t/t')$ may be obtained from equation A.19 with

$$g_3(t/t') = \frac{1}{2\pi} \int_{-\infty}^{+\infty} g_3(\omega/t') \exp[j\omega t'] d\omega \quad A.20$$

but this is not actually evaluated since we only require the far-field pressure, $p(t)$, due to the source time dependence, $f(t) = \exp[j\omega_0 t]$, rather than $\delta(t-t')$, and with

$$p(t) = \int_{-\infty}^{+\infty} g_3(t/t') f(t') dt'$$

we obtain, formally,

$$p(R_r, \theta, \phi, t) = \frac{\exp[-jk_0 R_r]}{4\pi R_r} \exp[j\omega_0 t] \frac{(-2j/\pi)}{\bar{E}_0(k_0 r_0)} \bar{\psi} \quad A.21$$

or, as to be expected, the function \bar{E}_0 is to be evaluated with $kr_0 = k_0 r_0$ where $k_0 = \omega_0/a_0$. For $\theta = 90^\circ$ that function takes the value $-2j/\pi$ and $\bar{\psi} = 1$ so that

$$\frac{p(0)}{p(90^\circ)} = \frac{-2j/\pi}{\bar{E}_0(k_0 r_0)} \cdot \bar{\psi} \quad A.22$$

APPENDIX I-4B

Fourier Inversion by
the Method of Steepest Descents

The inversion integral is of the form:

$$I = \frac{1}{2\pi} \int_{-\infty}^{+\infty} a(k_1) H_n^{(2)}(k_2 r) \exp[-jk_1(x_1 - x_1')] dk_1 \quad B.1$$

$$\text{where } (k_2 r_0)^2 = (kr_0)^2 \{1 - (k_1/k)^2\} \quad B.2$$

This integral can be evaluated approximately in the limit $kr_r \rightarrow +\infty$, where

$$R_r^2 = r^2 + (x_1 - x_1')^2 \quad B.3$$

It will also be assumed here that the argument of the Hankel function $k_2 r$ is sufficiently large such that the function can be replaced by its asymptotic representation:

$$H_n^{(2)}(z) \approx \sqrt{\frac{2}{\pi z}} \exp[-j(z - \frac{n\pi}{2} - \frac{1}{4}\pi)] \quad B.4$$

This approximation is made to simplify the analysis; however, a more detailed analysis [see for example, Moretti and Slutsky(10)], does not require this approximation and there is no restriction on the value of $k_2 r$, except, indirectly, as stated above, that $kr_r \rightarrow +\infty$.

With equation B.4, equation B.1 becomes

$$I = \frac{1}{2\pi} \int_{-\infty}^{+\infty} a(k_1) \sqrt{\frac{2}{\pi k_2 r}} \exp[-jk_2 r - jk_1(x_1 - x_1')] \exp[j(\frac{n\pi}{2} + \frac{\pi}{4})] dk_1 \quad B.5$$

By using spherical coordinates, (R_r, θ, ϕ) , (see Figure B.1),

$$\begin{aligned} x_1 - x_1' &= R_r \cos\theta \\ r &= R_r \sin\theta \end{aligned}$$

(where θ is the observer angle to the jet axis) equation B.5 is obtained in the required form:

$$I = \frac{1}{2\pi} \int_{-\infty}^{+\infty} a_3(k_1) \sqrt{\frac{2}{\pi k R_r \sin\theta}} \exp[kR_r(-j\frac{k_1}{k} \cos\theta - j\frac{k_2}{k} \sin\theta)] \exp[j(\frac{n\pi}{2} + \frac{\pi}{4})] dk_1 \quad B.6$$

that is

$$I = \int_c \exp[kR_r f(k_1)] F(k_1) dk_1 \quad B.7$$

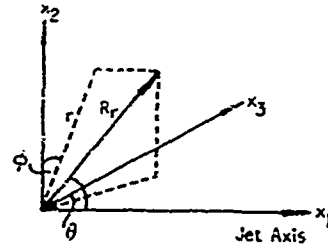


Fig. B.1 Spherical Coordinate System

where

$$f(k_1) = -j(k_1/k) \cos\theta - j(k_2/k) \sin\theta$$

$$F(k_1) = \frac{1}{2\pi} a(k_1) \sqrt{\frac{2}{\pi k_2 R_r \sin\theta}} \cdot \exp[j(\frac{n\pi}{2} + \frac{\pi}{4})]$$

Equation B.6 is in a standard form which can be evaluated approximately in the limit $kr_r \rightarrow +\infty$ [see for example, Brekhovskikh(22), p. 245]:

$$I \approx \exp[kR_r f(\bar{k}_1)] \sqrt{\frac{\pi}{R_r}} \{1 + \frac{1}{4R_r} \psi'' + \dots\} \quad B.8$$

where \bar{k}_1 is a solution to the equation

$$\frac{df}{dk_1} = 0 \quad B.9$$

and

$$\psi = \left\{ \frac{-2}{f''(\bar{k}_1)} \right\}^{\frac{1}{2}} F(\bar{k}_1) \quad B.10$$

The required solution to equation B.9 is

$$k_1 = k \cos\theta \quad B.11$$

and

$$f''(\bar{k}_1) = \frac{j}{k^2 \sin^2\theta} \quad B.12$$

$$f(\bar{k}_1) = -j$$

so that equation B.8 becomes

$$I = \exp[-jkR_r] \sqrt{\frac{\pi}{kR_r}} \left\{ \frac{-2k^2 \sin^2\theta}{j} \right\}^{\frac{1}{2}} F(k_1 = k \cos\theta)$$

or

$$I = \exp[-jkR_r] \left\{ \frac{-2\pi k^2 \sin^2\theta}{jkR_r} \cdot \frac{2}{kR_r \sin^2\theta} \right\}^{\frac{1}{2}}$$

$$\frac{a(k \cos\theta)}{2\pi} \exp[j(\frac{n\pi}{2} + \frac{\pi}{4})]$$

or

$$I = \exp[-jkR_r] \frac{1}{4\pi R_r} \cdot a(k\cos\theta) \exp[j \frac{n\pi}{2}] \quad \text{B.13}$$

A useful check for equation B.13 is the simple case of a point source located at $r' = 0$ in free space: then

$$a_3 = -\frac{j}{4} \exp[-j\omega t']; \quad n = 0$$

and

$$I = \frac{\exp[-jkR_r]}{4\pi R_r} \exp[-j\omega t'] .$$

APPENDIX 1-4C

Lilley's Equations: Method of Solution

1-4C.1 Lilley's Equation for the Circular Jet: Method of Solution of Fourier Transformed Equation

The Fourier transform of Lilley's equation in cylindrical coordinates for the Green's function, G , is

$$\frac{1}{r} \frac{d}{dr} \left(r \frac{dG}{dr} \right) + \left[\frac{d}{dr} \left\{ \log_e \left(\frac{\bar{a}^2}{a_0^2} \right) \right\} + \frac{2k_1/k}{(1-M_1 k_1/k)} \frac{dM_1}{dr} \right] \frac{dG}{dr} + G \left[k^2 \left\{ \left(\frac{a_0}{\bar{a}} \right)^2 (1-M_1 k_1/k)^2 - (k_1/k)^2 \right\} - \frac{n^2}{r^2} \right] = \frac{\delta(r-r')}{r} \quad \text{C.1.1}$$

where $G \equiv G(k_1, r, n, \omega/x_1, r', \phi', t')$ and where the source strength factor $S = -\exp[-j\omega t + jk_1 x_1 + jn\phi']$ for simplicity has been suppressed. The jet and its surrounding medium are divided into three basic regions (see Figure C.1).

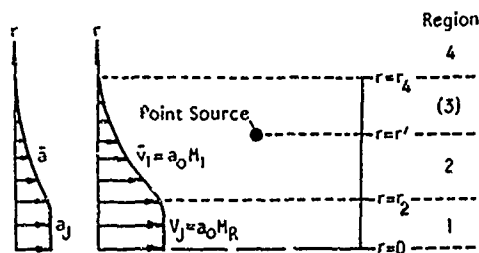


Fig. C.1 Cylindrical Jet Regions: (1) Uniform Flow, (2) Sheared Flow (and "Below" Point Source), (3) "Above" Point Source, (4) No Mean Flow

Region 4 ($r_4 \leq r \leq \infty$): A homogeneous fluid at rest (speed of sound a_0) containing no sources or boundaries.

Region 3 ($r_2 \leq r \leq r_4$): A fluid with a mean velocity, $a_0 M_1$, and speed of sound, \bar{a} , which vary with r and which may contain a point source at $r = r'$ (that is, the jet mixing region).

Region 1 ($0 \leq r \leq r_2$): A homogeneous fluid with a uniform mean velocity, V_j , and a uniform speed of sound, a_j , which may contain a source at $r = r'$ (that is, the potential core).

In region 4 equation C.1.1 reduces to ($\bar{a} = a_0$, $M_1 = dM_1/dr = 0$)

$$\frac{d^2 g_4}{dr^2} + \frac{1}{r} \frac{dg_4}{dr} + \left(k_2^2 - \frac{n^2}{r^2} \right) g_4 = 0 \quad \text{C.1.2}$$

where

$$k_2^2 = k^2 - k_1^2$$

(and where the notation g is used for the Green's function in region 4). The solution to equation C.1.2 is of the form

$$g_4 = A_4 H_n^{(2)}(k_2 r) + B_4 H_n^{(1)}(k_2 r)$$

but B_4 must be zero to satisfy the radiation condition, so

$$g_4 = A_4 H_n^{(2)}(k_2 r) \quad \text{C.1.3}$$

where A_4 is yet to be determined.

In region 1 equation C.1.1 reduces to ($d\bar{a}/dr = dM_1/dr = 0$).

$$\frac{d^2 G_1}{dr^2} + \frac{1}{r} \frac{dG_1}{dr} + \left(k_2^2 - \frac{n^2}{r^2} \right) G_1 = 0 \quad \text{C.1.4}$$

the right hand side being zero because we have chosen the source position $r = r'$ to lie in region 2. (The necessary modifications to the present analysis for the case when the source does lie inside region 1 are given at the end of this section.)

The solution to equation C.1.4 is of the form

$$G_1 = A_1 J_n(k_2 r) + B_1 Y_n(k_2 r)$$

where

$$k_2^2 = k^2 \left\{ \left(\frac{a_0}{\bar{a}} \right)^2 (1 - M_1 k_1/k)^2 - (k_1/k)^2 \right\}$$

but B_1 must be zero as G_1 must be finite on the axis ($r = 0$), so

$$G_1 = A_1 J_n(k_2 r) \quad \text{C.1.5}$$

In region 2, the Green's function, G_2 , must satisfy equation C.1.1 which, in general, can be only solved numerically.

We now consider how the solutions in the three regions are matched together to provide numerical values of the coefficients A_n and A_1 ; the coefficient A_n will determine the required Green's function in the far-field, after one of the Fourier inversions has been performed.

The first step is to introduce a variable, ξ , which is proportional to the particle displacement, ξ_d , where

$$\xi = r \frac{dG}{dr} \frac{1}{\left(\frac{a_0}{a}\right)^2 (1 - M_1 k_1/k)^2} = r \frac{dG}{dr} \cdot \frac{1}{P} \quad \text{C.1.6}$$

$$P = \left(\frac{a_0}{a}\right)^2 (1 - M_1 k_1/k)^2$$

and

$$\xi = \xi_d \cdot kr(a_0/a)$$

From the "plug" flow models it is known that, ξ_d , the particle displacement will be nearly constant through thin shear layers, as will the pressure, G , and therefore these are probably the most suitable dependent variables for the type of numerical integration scheme described below. At present, however, we find it more convenient to use the variable ξ rather than ξ_d ; its variation through thin shear layers will clearly be very similar as the variations in kr will be small.

With equation C.1.6, equation C.1.1 reduces to

$$\frac{d\xi}{dr} = G(Q) + \frac{\delta(r-r')}{P} \quad \text{C.1.7}$$

and rewriting equation C.1.6

$$\frac{dG}{dr} = \xi \left\{ \frac{P}{r} \right\} \quad \text{C.1.8}$$

where

$$Q = -\frac{r}{P} \left(k^2(P - k_1^2/k^2) - \frac{n^2}{r^2} \right)$$

we obtain a pair of coupled first order differential equations, C.1.7 and C.1.8, in the dependent variables G and ξ . These are the equations which are actually solved numerically, as described in section 1-4C.4, but one further step is required in order to illustrate the principle by which solutions in each region are matched. An admittance parameter, β , is introduced, where

$$\beta = \frac{\xi}{G}$$

and equations C.1.7 and C.1.8 are combined to give a Riccati equation†

$$\frac{d\beta}{dr} + \beta \left\{ \frac{P}{r} \right\} + Q = \frac{\delta(r-r')}{P \cdot G} \quad \text{C.1.9}$$

a first order, non-linear differential equation. We now divide region 2 into regions 2 and 3 where region 3 is $r' + \epsilon \leq r \leq r_4$ and region 2 is $r_2 \leq r \leq r' - \epsilon$, that is neither region now contains the point source which is assumed to exist in the region $r' - \epsilon \leq r \leq r' + \epsilon$ such that

$$\int_{r'-\epsilon}^{r'+\epsilon} \delta(r-r') f(r) dr = f(r') \quad \text{C.1.10}$$

Consider now region 3 ($r' + \epsilon \leq r \leq r_4$) and the solution $\beta_3(r)$ to equation C.1.9; an initial value of β_3 at $r = r_4$ would, with numerical integration of equation C.1.9, yield a (unique) value of β_3 at $r = r' + \epsilon$. Similarly an initial value of β_2 at $r = r_2$ would yield a value of β_2 at $r = r' - \epsilon$. Analytic integration of equation C.1.9 across the source position gives, in the limit as $\epsilon \rightarrow 0$, the condition that

$$\beta_3(r') - \beta_2(r') = \frac{1}{P(r')G(r')}$$

or

$$G(r') = \frac{1}{\{\beta_3(r') - \beta_2(r')\} P(r')} \quad \text{C.1.11}$$

[where $G(r') = G_3(r') = G_2(r')$].

The values of $\beta_3(r_4)$ and $\beta_2(r_2)$ are obtained from equations C.1.3 and C.1.5. For $r \geq r_4$:

$$\beta_3 = \beta_4 = \frac{r_4}{G_4} = r \frac{dg_4}{dr} \cdot \frac{1}{P} = (k_2 r) \frac{H_n^{(2)'}(k_2 r)}{H_n(k_2 r)} \cdot \frac{1}{P(r)}$$

or

$$\beta_3(r_4) = (k_2 r_4) \frac{H_n^{(2)'}(k_2 r_4)}{H_n(k_2 r_4)} \quad \text{C.1.12}$$

[as $P(r) = 1$, $r \geq r_4$, by definition] and for $r \leq r_2$

$$\beta_2 = \beta_1 = \frac{r_2}{G_1} = r \frac{dG_1}{dr} \cdot \frac{1}{P} = (k_2 r) \frac{J_n'(k_2 r)}{J_n(k_2 r)} \cdot \frac{1}{P(r)}$$

or

$$\beta_2(r_2) = (k_2 r_2) \frac{J_n'(k_2 r_2)}{J_n(k_2 r_2)} \frac{1}{\left(\frac{a_0}{a}\right)^2 (1 - M_1 k_1/k)^2} \quad \text{C.1.13}$$

In principle the coupled equations may be integrated numerically outward from $r = r'$ to $r = r_4$ and from $r = r'$ to $r = r_2$ with the starting value $G(r')$ given by equation C.1.11 and with

†This equation was derived independently of a similar equation obtained by Miles(23) for the simpler case of two-dimensional incompressible flows.

$$\xi_3(r') = \beta_3(r') G(r') \quad \text{C.1.14}$$

and the "outward" integration and

$$\xi_2(r') = \beta_2(r') G(r') \quad \text{C.1.15}$$

for the "inward" integration. Thus, absolute values of G and ξ would be obtained at $r = r_4$ and $r = r_2$ which immediately determines the unknown coefficients A_4 and A_1 ; in particular:

$$A_4 = \frac{g_4(r_4)}{H_n^{(2)}(k_2 r)} = \frac{G(r_4)}{H_n^{(2)}(k_2 r)} \quad \text{C.1.16}$$

In practice we do not solve the Riccati equation C.1.9 but instead integrate the coupled equations C.1.7, C.1.8 with $G(r_4)$ and $G(r_2)$ set equal to unity to obtain 'guessed' values $G_3(r')$ and $G_2(r')$ and true values $\beta_3(r')$, $\beta_2(r')$. Equation C.1.11 is then used to calculate the true value of $G(r')$ and the amplitude A_4 is then still given by equation C.1.16 but with

$$G(r_4) = \frac{G(r')}{G_3(r')} \quad \text{C.1.17}$$

Detailed aspects of the numerical integration of equations C.1.7 and C.1.8 are given in section C.4.

We now consider the case when the source is located inside region 1 which, since r_2 may be assigned an arbitrarily small value, amounts to the case when the source is on the jet axis. From the jet noise radiation point of view this special case may not be particularly relevant when considering the potential core region since the noise sources on the jet axis are presumably insignificant, if not non-existent. However, we will eventually consider other regions of the jet flow and, perhaps of more importance, we wish to model experiments where a controlled source of sound is placed inside the jet flow on the center-line, in order to compare the measured far-field acoustic radiation from the controlled source with solutions to Lilley's equation.

The modifications to the above equations for this special case are as follows. The Green's function in region 1, G_1 , does not have to be finite at $r = 0$ and is zero for $n \neq 0$, so that $B_1 \neq 0$ and it can be shown that G_1 is of the form

$$G_1 = A_1 J_0(K_2 r) + \frac{j\pi}{2} H_0^{(2)}(K_2 r) \quad \text{C.1.5a}$$

or as $K_2 r \rightarrow 0$.

$$G_1 \rightarrow \frac{\pi}{2} \cdot Y_0(K_2 r)$$

Equations C.1.6 - C.1.8 still apply, as does the radiation boundary condition given by equation C.1.12; also the first integration pass from $r = r_4$ to $r = r_2$ is carried out to obtain $G_3(r_2)$. But now we simply need to match $G_3(r_2)$ with G_1 , defined above, and hence

$$G(r_4) = \frac{G_1(r_2)}{G_3(r_2)} \quad \text{C.1.17a}$$

which with equation C.1.16 (and $n = 0$) gives the required value of A_4 .

1-4C.2 Fourier Inversions of the Solution Outside the Jet and Source Region (Region 4)

As described in the previous section, the solution in region 4 (outside the jet flow and source region) can be obtained from the solutions to the Lilley equation inside the jet flow and source regions, and the radiation condition, and is of the form

$$g = A H_n^{(-)}(k_2 r) \quad r \geq r_4 \quad \text{C.2.1}$$

where the coefficient A is a function of the source position, frequency, jet flow parameters (all these parameters are suitably normalized in section C.1.4) wavenumber, n , and the normalized axial wavenumber k_1/k . To obtain g as a function of the space coordinates (x_1, ϕ) the Fourier inversions must be performed:

$$g(x_1, r, n, \omega/x_1, r', \phi', t') = \frac{1}{2\pi} \int_{-\infty}^{+\infty} g \exp[-jk_1 x_1] dk_1$$

$$= \int_{-\infty}^{+\infty} A(k_1, n) H_n^{(2)}(k_2 r) \exp[-jk_1 x_1] dk_1 \quad \text{C.2.3}$$

$$g(x_1, r, \phi, \omega/x_1, r', \phi', t')$$

$$= \frac{1}{2\pi} \sum_{n=0}^{\infty} c_n g(x_1, r, n, \omega/x_1, r', \phi', t') \cos n(\phi - \phi')$$

$$\text{where } c_0 = 1 \quad c_n = 2, n > 0 \quad \text{C.2.4}$$

The coefficient A is determined with a source function

$$\frac{\delta(r-r')}{r}$$

that is, the source strength, S , is suppressed but can now be re-introduced so that

$$g(x_1, r, n, \omega/x_1, r', \phi', t') = \frac{1}{2\pi} \exp[-j\omega t' + jn\phi']$$

$$\times \int_{-\infty}^{+\infty} -A(k_1, n) H_n^{(2)}(k_2 r') \exp[-jk_1(x_1 - x_1')] dk_1 \quad \text{C.2.5}$$

It is the following step which is the center of any significant criticism of the present work, for, as in the "plug" flow models (discussed in the main text) the integrand in equation C.2.5 has one or more poles which represent the unstable jet modes. In principle there are two components which result

from this Fourier inversion and these will be simply referred to here as the acoustic solution and the unstable solution. The acoustic solution is obtained from the method of steepest descents, as described in Appendix 1-4B, whereas the unstable solution results from the residue evaluation of the integral along the contour enclosing one or more poles in the complex k_1 plane. In the present work the unstable solution is deliberately suppressed for the reasons discussed in the main text.

Thus, the acoustic solution, is, from Appendix B

$$g(R_r, \theta, n, \omega/x', r', \phi', t') = - \exp[-j\omega t' + jn\phi']$$

$$\exp[-jkR_r] \frac{j}{\pi R_r} A(k\cos\theta, n) \exp[jn\pi/2]$$

and

$$g(R_r, \theta, \phi, \omega/x'_1, r'_1, \phi'_1, t'_1) = \frac{\exp[-jkR_{r_1}]}{4\pi R_{r_1}} \exp[-j\omega t'_1]$$

$$\times \sum_{n=0}^{\infty} \epsilon_n \{-2j \frac{A}{\pi} (k\cos\theta, n) e^{jn\pi/2}\} \cos n(\phi - \phi'_1).$$

It can be seen that, for this acoustic solution, the coefficient A is only required for a specific value of ' k_1 ' (= $k\cos\theta$); that is, when the equations with appropriate boundary conditions are solved numerically, ' k_1 ' need only take the above value in those equations. In addition 'n' need only take positive values. The equations with this specific value of ' k_1 ' are given in section 1-4C.4.

1-4C.3 Alternative Form of Lilley's Equation: 'q' Coefficient Definitions

In reference (1) Lilley transformed his equation into the form

$$\frac{d^2 \zeta_1}{dr^2} + q_1 \zeta_1 = h_1 \quad C.3.1$$

as a first step toward obtaining approximate analytic solutions and to aid interpretation of the behavior of the solution both inside and outside the jet. The alternative form is given here again because a minor simplification can be made to the one given in reference (1) and because we wish to compare it with another alternative form which may be preferable or even necessary in the present coordinate system. Lilley transformed equation C.1.1 with (in the present notation)

$$\zeta_1 = \frac{r^{\frac{1}{2}}}{\left(\frac{a_0}{a}\right) (1-k_1 M_1/k)} G = \phi G \quad C.3.2$$

into the form shown above (C.3.1) with

$$q_1 = k^2 \left\{ \left(\frac{a_0}{a}\right)^2 (1-M_1 k_1/k)^2 - (k_1/k)^2 \right\}$$

$$- \frac{n^2}{r^2} - \frac{\phi''}{\phi}$$

$$C.3.3 \quad + G \left[(kr_0)^2 \left(\frac{a_0}{a}\right)^2 (1-M_1 \cos\theta)^2 - \cos^2\theta \right] - \frac{n}{R^2} = 0 \quad C.4.1$$

and

$$h_1 = \frac{\delta(r-r')}{r^{\frac{1}{2}} \left(\frac{a_0}{a}\right) (1-k_1 M_1/k)} \quad C.3.4$$

where

$$\frac{\phi''}{\phi} = \left\{ \frac{1}{r} + \frac{2 k_1 M_1'/k}{(1-k_1 M_1/k)} \right\} \left\{ \log_e \left(\frac{a}{a_0}\right)^2 \right\}' + \frac{k_1 M_1'/k}{(1-k_1 M_1/k)} + \left\{ \frac{\bar{a}''}{\bar{a}} + \frac{k_1 M_1''/k}{(1-k_1 M_1/k)} \right\} - \frac{1}{4r^2} \quad C.3.5$$

Fisher(24) has pointed out that the coefficient, q_1 , defined by equation C.3.3, must inevitably be negative on and near the axis due to the terms $-(n^2 + 1/4)/r^2$. When all the other terms add up to a positive quantity in this region a zero or transition point will exist near the jet axis. It is suggested here that a zero or transition point of q_1 , due to this feature of q_1 , may not have any mathematical or physical significance because the transformed equation should be in a form appropriate to the coordinate system on which it is based. Such an equation can be obtained by using the transformation

$$\zeta_2 = \frac{G}{\left(\frac{a_0}{a}\right) (1-k_1 M_1/k)} \quad C.3.6$$

to give

$$\frac{d^2 \zeta_2}{dr^2} + \frac{1}{r} \frac{d\zeta_2}{dr} + \left\{ q_2 - \frac{n^2}{r^2} \right\} \zeta_2 = \frac{\delta(r-r')}{\left(\frac{a_0}{a}\right) (1-k_1 M_1/k)} \quad C.3.7$$

where

$$q_2 = k^2 \left\{ \left(\frac{a_0}{a}\right)^2 (1-k_1 M_1/k)^2 - (k_1/k)^2 \right\} - \left\{ \frac{1}{r} + \frac{2k_1 M_1'/k}{(1-k_1 M_1/k)} \right\} \left\{ \log_e \left(\frac{a}{a_0}\right)^2 \right\}' + \frac{k_1 M_1'/k}{(1-k_1 M_1/k)} - \left\{ \frac{\bar{a}''}{\bar{a}} + \frac{k_1 M_1''/k}{(1-k_1 M_1/k)} \right\}. \quad C.3.8$$

Note that the $1/r$ term is multiplied by gradients of mean velocity and temperature which must vanish as $r \rightarrow 0$ (at least in the context of axisymmetric mean flows).

1-4C.4 Numerical Solution of Lilley's Equation: Computational Details

We solve Lilley's differential equation

$$\frac{1}{R} \frac{d}{dR} \left\{ R \frac{dG}{dR} \right\} + \left\{ \frac{d}{dR} \left\{ \log_e \left(\frac{\bar{a}^2}{a_0^2}\right) \right\} + \frac{2\cos\theta}{(1-M_1 \cos\theta)} \frac{dM_1}{dR} \right\} \frac{dG}{dR} \frac{dG}{dR}$$

$$+ G \left[(kr_0)^2 \left(\frac{a_0}{a}\right)^2 (1-M_1 \cos\theta)^2 - \cos^2\theta \right] - \frac{n}{R^2} = 0 \quad C.4.1$$

in the form of two coupled, first order, ordinary differential equations (see section I-4C.1 for derivation)

$$\frac{dG}{dR} = \{0\}G + \left\{\frac{P}{R}\right\}\xi \quad C.4.2$$

$$\frac{d\xi}{dR} = \{Q\}G + \{0\}\xi \quad C.4.3$$

where

$$R = r/r_0 \quad C.4.4$$

$$P(R) = \left(\frac{a_0}{\bar{a}(R)}\right)^2 (1-M_1(R)\cos\theta)^2 \quad C.4.5$$

$$Q(R) = -\frac{1}{P(R)} \{R(kr_0)^2 \{P(R) - \cos^2\theta\} - \frac{n^2}{R}\} \quad C.4.6$$

Note that although the mean velocity gradient $a_0 dM_1/dR$ and the temperature gradient, $d/dR(\log_e(\bar{a}^2/a_0^2))$, appear in the original Lilley equation, these are absent in the coefficients of the coupled first order equations and one only has to specify M_1 and \bar{a} as a function of R . This is a rather useful feature especially when measured values for $M_1(R)$ and $\bar{a}(R)$ are to be used, for, while these can usually be measured fairly accurately, estimated values of their gradients and higher derivatives almost inevitably contain relatively large errors. Of course, this does not mean that solutions for the dependent variables are necessarily independent of flow gradients (although in the limit of vanishing shear layer thickness they in fact are): in general the solution must depend on the variation of the coefficient P and Q with R and hence the flow gradients and higher derivatives.

Equations C.4.2 and C.4.3 are integrated numerically from the outer boundary at $R = R_4$

$$G = 1.0; \quad \xi = (k_2 r_0 R_4) \frac{H_n^{(2)}(\bar{k}_2 r_0 R_4)}{H_n^{(2)}(\bar{k}_2 r_0 R_4)} \quad C.4.7$$

where $\bar{k}_2 r = kr_0 \sin\theta$ to the point $R = R_2$ (see Figure C.1). This upper bound of the numerical integration, $R = R_2$ appears to be unnecessary as the method of solution outlined in section C.1 requires the upper bound to be $R = R_1$, that is the source location. However, we will require the source location to be varied in the range $R_2 \leq R_1 \leq R_4$ and hence we include all possible locations by choosing this upper bound. The results from this first integration pass are stored and the same equations are integrated again, starting at $R = R_2$ with

$$G = 1.0; \quad \xi = \frac{(\bar{k}_2 r_0 R_2) J_n^{(1)}(\bar{k}_2 r_0 R_2)}{J_n(\bar{k}_2 r_0 R_2) P(R_2)} \quad C.4.8$$

up to the point $R = R_4$ (instead of $R = R_1$, again for the same reason). We note that

$$P(R_2) = (a_0/a_j)^2 (1-M_R \cos\theta)^2 \quad C.4.9$$

and

$$\bar{k}_2 r_0 = (kr_0)^2 \left(\frac{a_0}{a_j}\right)^2 (1-M_R \cos\theta)^2 - \cos^2\theta \quad C.4.10$$

as, for convenience, R_2 is chosen to be virtually on the jet axis so that $\bar{a} = a_j$, $M_1 = M_R$. (This is only true, of course, for the potential core region, to which the present analysis is restricted.)

We now consider a particular source position and, if necessary with elementary interpolation, obtain from the stored values of G and ξ the value $G(R')$ and the values $\beta_3(R')$, $\beta_3(R')$ ($\beta = \xi/G$).

Then $G(R')$ is calculated from

$$G(R') = \frac{1}{\{\beta_3(R') - \beta_2(R')\}P(R')} \quad C.4.11$$

and the required coefficient A from

$$A_k = \frac{G(R')}{G_1(R') H_n^{(2)}(\bar{k}_2 r_0 R_k)} \quad C.4.12$$

As an aid to the interpretation of solution behavior the coefficient q_2 is computed in the form:

$$q_2 r_0 = (kr_0)^2 \left(\frac{a_0}{a}\right)^2 (1-M_1 \cos\theta)^2 - \cos^2\theta \\ - \left\{\frac{1}{R} + \frac{2M_1 \cos\theta}{(1-M_1 \cos\theta)}\right\} \left\{\log_e \left(\frac{\bar{a}}{a_0}\right)^2\right\} + \frac{M_1 \cos\theta}{(1-M_1 \cos\theta)} \\ - \left\{\frac{\bar{a}''}{\bar{a}} + \frac{M_1' \cos\theta}{(1-M_1 \cos\theta)}\right\} \quad C.4.13$$

The numerical integration is performed by an IBM routine, HPCL, which utilizes the Hamming's modified predictor-corrector method and which chooses and changes the integration step size based on an estimate of the local truncation error. In its original form the local truncation error was calculated as an absolute value so that the variables had to be carefully scaled; now the routine has been modified so that the error is calculated on a relative basis and no scaling is necessary. This type of routine is particularly useful in detecting regions where unusually small step sizes are required due to rapid variations in the dependent variable. Conversely it will use large step sizes where the variation is small, for example, at low frequencies.

As long as the factor $(1-M_1 \cos\theta)$ remains positive, the computational procedure described above is straightforward; but when there exists a point, R_c , along the integration path such that

$$1 - M_1(R_c) \cos\theta = 0 \quad C.4.14$$

the step size chosen by the integration routine decreases indefinitely as this point is approached. This behavior is caused by the appearance of a singularity in the differential equations: the above factor appears in the denominator of the coefficient Q , raised to the second power. This singularity at the so-called critical point, R_c , is well known in stability analysis (8) and it is now well established that the correct treatment of this problem is to deform the path of integration into the complex R plane so that it passes around the critical point and hence the coefficients and the solution remain finite and well behaved. The inte-

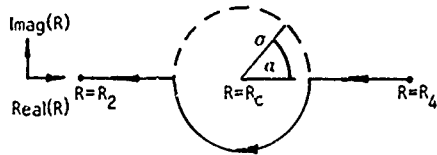


Fig. C.2 Integration Contour in the Complex R Plane

gration path chosen is shown in Figure C.2; in the present notation the integration path must pass below the critical point (8), that is, α must vary between 0 and π . The contour is chosen to be a semi-circle of radius σ . On this contour the complex coordinate R is related to α by

$$R = R_c + \sigma e^{i\alpha} \quad C.4.15$$

and the differential operators are related by

$$\frac{d}{dR} = \frac{1}{i\sigma e^{i\alpha}} \cdot \frac{d}{d\alpha} \quad C.4.16$$

so that equations C.4.2 and C.4.3 are transformed to

$$\frac{dG}{d\alpha} = [0]G + [i\sigma e^{i\alpha} \frac{P}{(R_c + \sigma e^{i\alpha})}] \xi \quad C.4.17$$

$$\frac{d\xi}{d\alpha} = [i\sigma e^{i\alpha} Q]G + [0] \xi \quad C.4.18$$

where

$$P(\sigma, \alpha) = \left\{ \frac{a_0}{\bar{a}(\sigma, \alpha)} \right\}^2 (1 - M_1(\sigma, \alpha) \cos \theta)^2 \quad C.4.19$$

$$Q(\sigma, \alpha) = - \frac{1}{P(\sigma, \alpha)} \left\{ (R_c + \sigma e^{i\alpha}) (kr_0)^2 \right. \\ \left. \times [P(\sigma, \alpha) - \cos^2 \theta] - \frac{n^2}{R_c + \sigma e^{i\alpha}} \right\} \quad C.4.20$$

The Mach number, $M_1(\sigma, \alpha)$, and speed of sound, \bar{a} are expressed in the complex plane as a Taylor series expansion about the point $R = R_c$:

$$M_1(R) = M_1(\sigma, \alpha) = M_1(R_c) + M_1'(R_c) \frac{(R - R_c)}{1!} \\ + M_1''(R_c) \frac{(R - R_c)^2}{2!} + \dots$$

or

$$M_1(\sigma, \alpha) = M_1(R_c) + M_1'(R_c) \frac{(\sigma e^{i\alpha})}{1!} \\ + M_1''(R_c) \frac{(\sigma e^{i\alpha})^2}{2!} + \dots \quad C.4.21$$

and

$$\frac{\bar{a}}{a_0} = \frac{\bar{a}}{a_0}(R_c) + \left(\frac{\bar{a}}{a_0} \right)' \left(\frac{e^{i\alpha}}{1!} \right) + \left(\frac{\bar{a}}{a_0} \right)'' \left(\frac{e^{i\alpha}}{2!} \right) + \dots \quad C.4.22$$

The critical point R_c is determined by solving by iteration the equation

$$1 - M_1(R_c) \cos \theta = 0 \quad C.4.23$$

The velocity and speed of sound profiles used in these equations are described in the following section.

1-4C.5 Mean Velocity Profiles

The velocity profile used in reference (1),

$$\frac{\bar{v}_1(R)}{V_J} = \exp[-\chi^2] \quad C.5.1$$

where

$$\chi = \frac{r + c}{b}$$

and

$$\chi = \frac{R - 1}{(x_1^2/r_0)}$$

$$b = 0.145 \quad c = 0.104$$

had to be discarded because its second derivative is non-zero at $\chi = 0$ where the shear layer merges with the potential core. This causes the second derivative of \bar{v}_1 and hence the 'q coefficient' (see section 1-4C.3) to be discontinuous at this point and often resulted in excessive step size subdivision in numerical integration; it would also probably cause difficulties in the representation of M (and \bar{a}) in the complex plane (see section 1-4C.4). The expressions for the first and second derivatives are:

$$\frac{\bar{v}_1'(R)}{V_J} = \frac{-2\chi}{bx_1^2/r_0} \exp[-\chi^2] \quad C.5.2$$

$$\frac{\bar{v}_1''(R)}{V_J} = \frac{(-2 + 4\chi^2)}{(bx_1^2/r_0)^2} \exp[-\chi^2] \quad C.5.3$$

The magnitude of the discontinuity at $\chi = 0$ is

$$\frac{-2}{(bx_1^2/r_0)^2}$$

and is inversely proportional to the square of the normalized distance from the nozzle.

Other velocity profiles, such as the hyperbolic tangent profile, were used in the early stages of this work but eventually the error function profile given by Schlichting⁽²⁵⁾ was adopted. This is of the form

$$\frac{\bar{v}_1(R)}{V_J} = \frac{1}{2} \{1 - \text{erf}[X]\}$$

C.5.4

which is the value used to obtain the results presented in this paper.

The erf function is evaluated using a rational approximation [(26), p. 299]

where

$$X = \frac{\eta + c}{b}$$

$$\eta = \frac{R-1}{(x_1^2/r_0)}$$

and [from Schlichting (25)]

$$b = 1/13.5.$$

The constant c defines the point at which

$$\frac{\bar{v}_1}{V_J} = 0.5;$$

in recent calculations the value of c used was

$$c = -.016$$

but work is in hand to provide values of b and c which will give improved agreement with measured velocity profiles. Currently comparisons with measured profiles such as those shown in Figures C.3a and b indicate that b = 1/13.5 should remain the same but a better value of c is

$$c = -.022$$

$$\text{erf}(X) =$$

$$1 - \frac{1}{[1 + a_1X + a_2X^2 + a_3X^3 + a_4X^4]^4 + \dots} \quad \text{C.5.5}$$

$$|c(X)| \leq 5 \times 10^{-4} \quad \text{C.5.5}$$

where

$$a_1 = .278393 \quad a_2 = .230389$$

$$a_3 = .000972 \quad a_4 = .078108$$

Derivatives of \bar{v}_1 , for integration in the complex R plane (see section 1-4C.4), are evaluated using the exact expression

$$\frac{d^{n+1}}{dR^{n+1}} \left(\frac{\bar{v}_1(R)}{V_J} \right) = \frac{1}{2} \cdot \left(\frac{1}{bx_1^2/r_0} \right)^{n+1} (-1)^{n+1} \left(\frac{2}{i\pi} \right) \times H_n(X) \exp[-X^2] \quad (n \geq 0) \quad \text{C.5.6}$$

where H_n is the Hermite polynomial of order n.

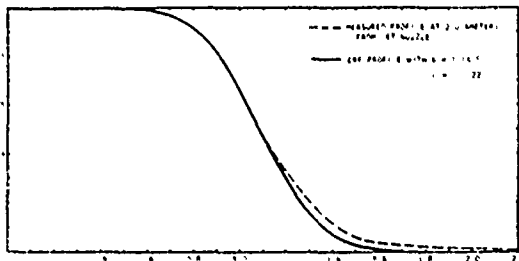


Fig. C.3a Comparison of Measured Mean Velocity Profiles with Erf Profile Used for Lilley Equation Solutions: At 2 Diameters

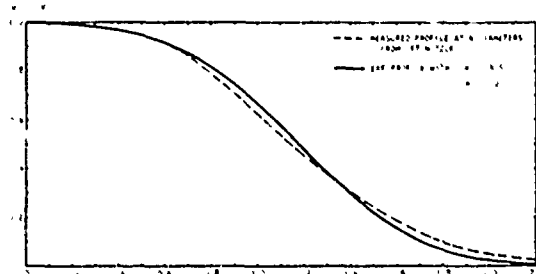


Fig. C.3b Comparison of Measured Mean Velocity Profiles with Erf Profile Used for Lilley Equation Solutions: At 4 Diameters

1-5 A MODEL FOR THE STRUCTURE OF JET TURBULENCE AS A SOURCE OF NOISE

Philip J. Morris
Lockheed-Georgia Company
Marietta, Georgia

Abstract

A model for the organized turbulent structure of a jet which describes the acoustic sources is presented. The noise radiation may be calculated using Lilley's equation with the source terms provided by the turbulence model. The organized turbulent structure is described as the sum of the least stable fluctuations of each azimuthal mode number at any axial location. These modes are obtained using techniques analogous to those of stability theory. Non-linearity leading to amplitude limiting of the modes is described. The effect of the background turbulence is accounted for by a turbulent eddy viscosity. The downstream behavior of single frequency organized motions is described. Results are presented for an axisymmetric jet.

1-5.1 Introduction

The aim of this paper is to describe the large-scale noise-producing turbulent structure of an axisymmetric jet. The work represents the continuation and expansion of earlier ideas on the structure of turbulence in a two-dimensional shear layer⁽¹⁾.

The existence and importance of a large-scale organized structure in turbulent flows has only recently been justified by experimental results⁽²⁾, ⁽³⁾. This is mainly due to the degree of sophistication in the experimental techniques that are required. However, the postulation of such a structure is not new. The early work of Townsend⁽⁴⁾ predicted a large-scale equilibrium structure for the turbulence. The relationship between this structure and the organized motion detected by Crow and Champagne⁽²⁾ and Lau, Fuchs and Fisher⁽³⁾ is not yet clear.

Evidence that a large-scale organized motion is important in the noise generated by turbulence has also been obtained. The work of Mollo-Christensen⁽⁵⁾ indicated that turbulence 'may be more regular than we think it is'. Laufer, Kaplan and Chu⁽⁶⁾ also concluded that 'the large-scale structures are the primary sources of noise'. Bishop, Ffowcs Williams and Smith⁽⁷⁾ were drawn to similar conclusions and proposed a model for the large sound-producing eddy structure which in many ways parallels the model to be presented here.

Considerable attention has also been paid recently to the similarity between the large-scale ordered motions in a high Reynolds number turbulent flow and the instabilities of a laminar flow. The transition from laminar to turbulent flow is dominated by certain wave-like modes which grow very rapidly before reaching a limiting amplitude and decaying.⁽⁸⁾ The appearance of harmonics of these dominant waves also occurs. Occasional small eddies or 'bursts' of turbulent fluid are detected. All these phenomena have been determined analytically or numerically by various theories of hydrodynamic stability. The results indicate that the transition process is dominated by the most unstable

or most highly amplifying mode. All the features of this transition process have their equivalents in turbulent flow. The existence of a large-scale wave-like motion has been observed and 'bursting' of turbulence is readily visible in jet flows. This is to be expected since there is a close correspondence between the stability equations and the disturbance equations for the turbulent flow.

The work by Tam⁽⁹⁻¹¹⁾ on the noise from supersonic jets has made use of these ideas. Tam chose to only consider a single frequency for the large-scale noise producing structure. This model is essentially different from the work to be presented here which is not so restrictive.

The paper first describes the model for the turbulence in general terms. Secondly, the equations for the model are derived and their solutions given. A few comparisons between the results for the turbulence model and experimentally obtained data will be made. A more complete comparison will be left until later when results are available from an experimental program paralleling this work. A method by which the noise radiated by the large-scale structure can be calculated has been covered by Lilley, Morris and Tester⁽¹²⁾, and this work will not be repeated here. Further discussion of this aspect of the work will be given by Tester⁽¹³⁾.

1-5.2 The Turbulence Model

In this section a model for the large-scale, noise producing, structure of an axisymmetric incompressible jet will be presented. The corresponding mathematical formulation will be given later.

The velocity and pressure in the jet are separated into three parts⁽¹⁴⁾. The first being the time averaged component, the second a time dependent organized fluctuation and the third representing the background disorganized turbulence. This background turbulence is accounted for by the use of a turbulent eddy viscosity. This has the effect of reducing the effective Reynolds number of the flow which has a stabilizing effect on the organized motion. Crow⁽¹⁵⁾ has considered how a body of fine-scale turbulence may be regarded as a continuous viscoelastic medium. The relationship between the time averaged disorganized turbulence shear stresses and the rate of strain of the mean motion is also represented in terms of an eddy viscosity.

If the equations for the organized motion are Fourier decomposed and linearized and the mean flow is assumed to be locally parallel, the fluctuations are seen to satisfy the homogeneous stability equations. Hence, the structure of the organized motion is seen to be dominated by the spatially unstable modes which are eigensolutions to the stability equations. It was noted earlier that in the transition from laminar to turbulent flow the motion was dominated by that solution of the stability equations which receives the highest amplification. The inclusion of an eddy viscosity has meant that the organized fluctuations exist within an equivalent low

Reynolds number flow. Thus, it is a plausible assumption of the turbulence model that the structure of the jet at any axial location is dominated by the most preferred mode or the most highly amplifying fluctuation at that location. It is this mode which extracts energy at the fastest rate from the mean motion.

The amplification rates observed in free shear flows are very large and the organized fluctuation quickly reaches a level where the assumptions of linear theory are no longer valid. Under these circumstances it is the divergence and changing character of the mean flow and a self amplitude limiting process which prevents the continued growth of the fluctuation amplitude. The downstream amplitude of the organized motion and its effect on the mean flow is determined by the solutions to a set of integral equations (16), (17), which are non-linear in the fluctuations. These products of turbulent velocities and pressures are approximated by the products of the eigensolutions to the stability equations assuming that the flow is locally parallel. In this manner account may be taken of the effects of flow divergence in the integral equations. Ling and Reynolds (18), however, have shown that a non-parallel flow correction to the amplification factor for a two-dimensional jet is only required for a Reynolds number of less than 20.

However, any Fourier component of the organized motion will propagate downstream and pass through regions where it is amplifying, neutral and decaying. It is only at that location where it is most amplifying that it dominates the flow structure. It is clear that at any location the turbulent structure is not dominated by the component having the greatest magnitude but rather by the mode having the greatest amplification. For example, a frequency component of the organized motion which is most amplifying at the end of the potential core will not reach its maximum amplitude until further downstream. The local amplitude of any frequency component may be obtained by considering the local growth rate, given by solution of the stability equations assuming locally parallel flow, as a function of downstream distance, noting that the mean flow structure has been pre-determined by considering its interaction with the most amplifying mode at any axial location.

The model may now be summarized. It is hypothesized that the large-scale organized motions within the shear flow dominate the flow structure. The large scale motions are given by the locally most amplifying disturbances in the flow. The disorganized background turbulence is of smaller scale and may be connected with a turbulent eddy viscosity which reduces the effective Reynolds number of the flow. The downstream growth of the organized large scale motion is distorted and damped by non-linear interactions and flow divergence effects. The axial variation in amplitude of any single frequency component is given by the local amplification or decay rate from linear theory. It is the axial variation in amplitude which enables a particular frequency component, whose phase velocity given by linear theory may be subsonic, to radiate acoustically. Associated with the typical streamwise behavior of growth and decay of a disturbance will be a wave number spectrum. This spectrum will contain components with supersonic phase speeds, so that non-linear vortical modes cause acoustic radiation.

In the next section the integral equations governing the downstream development of the jet are derived.

1-5.3 Integral Equations

The downstream development of the mean flow and the large-scale fluctuations is governed by a set of integral equations. The mean momentum, mean mechanical energy and fluctuation energy integral equations are derived in Appendix 1-5A

In order to simplify the analysis and make interpretation of the integral equations easier, certain assumptions may be made. It is assumed that terms involving differences of squares of turbulent velocity components, such as $(\bar{u}^2 - \bar{v}^2)$ are small. Further, the turbulence production is assumed to be dominated by the integral term,

$$\int_0^{\infty} \bar{u}\bar{v} \frac{\bar{u}}{r} r dr \quad 3.1$$

These assumptions are valid if the axial rate of change of the mean flow width is small but are not valid for very low wave number fluctuations.

With these two experimentally justifiable assumptions the three integral equations reduce to,

$$\frac{d}{dx} \int_0^{\infty} \bar{u}^2 r dr = 0 \quad 3.2$$

$$\begin{aligned} \frac{d}{dx} \int_0^{\infty} \bar{u}^3 r dr &= 2 \int_0^{\infty} \bar{u}\bar{v} \frac{\partial \bar{u}}{\partial r} r dr \\ &- 2(v + \bar{v}_T) \int_0^{\infty} \left(\frac{\partial \bar{u}}{\partial r}\right)^2 r dr \end{aligned} \quad 3.3$$

$$\begin{aligned} \frac{d}{dx} \int_0^{\infty} \left(\bar{u}(\bar{v}^2 - \bar{w}^2) + \bar{u}^3 + \bar{u}\bar{v}^2 + \bar{u}\bar{w}^2 + 2\bar{u}\bar{\phi} \right) r dr \\ = -2 \int_0^{\infty} \bar{u}\bar{v} \frac{\partial \bar{u}}{\partial r} r dr - 2(v + \bar{v}_T) \int_0^{\infty} \phi dr \end{aligned} \quad 3.4$$

where ϕ represents the viscous dissipation terms defined in Appendix 1-5A.

Equation 3.2 which states that the momentum flux across the jet is constant at any downstream station is directly integrable and leads to,

$$\int_0^{\infty} \bar{u}^2 r dr = \frac{\bar{u}_0^2}{2} r_0^2 \quad 3.5$$

where r_0 is the jet exit radius. Nondimensionalizing equations 3.5, 3.3 and 3.4 with respect to the jet exit velocity and radius gives:

$$\int_0^{\infty} \bar{u}^{*2} r^* dr^* = \frac{1}{2} \quad 3.6$$

$$\frac{d}{dx} \int_0^x \bar{u}^2 r^2 dr = 2 \int_0^x \bar{u} \frac{\partial \bar{u}}{\partial x} r^2 dr - 2 \left(\frac{1}{R} + \frac{1}{R_T} \right) \int_0^x \frac{\partial \bar{u}}{\partial r} r^2 dr \quad 3.7$$

$$\frac{d}{dx} \int_0^x (\bar{u}^2 + \overline{u^2} + \overline{v^2} + \overline{w^2}) + \overline{u^3} + \overline{u^2 v} + \overline{u v^2} + 2\overline{u^2 p} r^2 dr = -2 \int_0^x \bar{u} \frac{\partial \bar{u}}{\partial x} r^2 dr - 2 \left(\frac{1}{R} + \frac{1}{R_T} \right) \int_0^x \frac{\partial \bar{u}}{\partial r} r^2 dr \quad 3.8$$

where

$$R = \frac{\bar{u}_j r_0}{j}, \quad \bar{R}_T = \frac{\bar{u}_j r_0}{v_T}, \quad R_T = \frac{\bar{u}_j r_0}{v_T} \quad 3.9$$

and nondimensional quantities are denoted by stars.

Inspection of equations 3.7 and 3.8 reveals how the mechanical energy of the mean flow is balanced by the production of turbulence and effective viscous dissipation while the fluctuation gains energy from the mean flow and is dissipated by viscosity and the viscous action of the background turbulence.

1-5.4 Shape Assumption for the Mean Flow and Fluctuations

Ko *et al* (17) demonstrated that the unknowns that exist in the integral equations may be approximated by a few shape parameters. The same approach will be adopted here.

A sketch of the coordinate system used to characterize the mean velocity is the same as that used by Tam (11) and is sketched in figure 1.

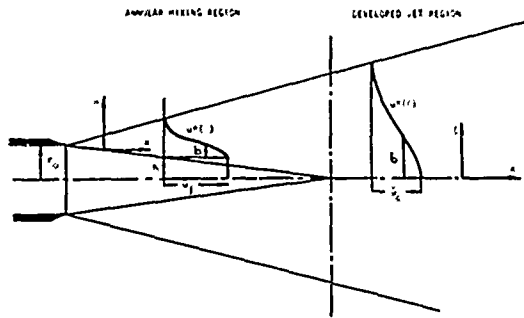


Fig. 1 Sketch of Coordinate System for Jet

It is convenient to divide the jet into two regions: the first being the annular mixing region which exists from the jet exit to the end of the potential core and the second being the developed jet region downstream of the potential core. The mean velocity takes the form,

$$\begin{aligned} \bar{u}/\bar{u}_c &= \bar{u} = 1 & r < h & \quad x < x_c \\ \bar{u} &= U(\eta) & r \geq h & \quad x < x_c \\ \bar{u}/\bar{u}_c &= U(\eta) & & \quad x \geq x_c \end{aligned} \quad 4.1$$

where $\eta = r-h/b$, h is the radius of the potential core, x_c is the length of the potential core and b is the momentum thickness of the jet defined by,

$$b = \int_0^x \bar{u} \cdot (1 - \bar{u}) dr \quad 4.2$$

$\xi = r/b$ and \bar{u}_c is the center-line velocity of the jet. The mean velocity shape function is shown in figure 2. It has been compared with the results of a jet mean flow prediction program which is accurate for the subsonic, unheated jet. Also shown for reference is the mean velocity shape function used by Tam (11) for a supersonic jet. The use of these coordinate systems for describing the mean flow is very convenient, however, close to the jet exit deviations from measured velocity profiles are discernable.

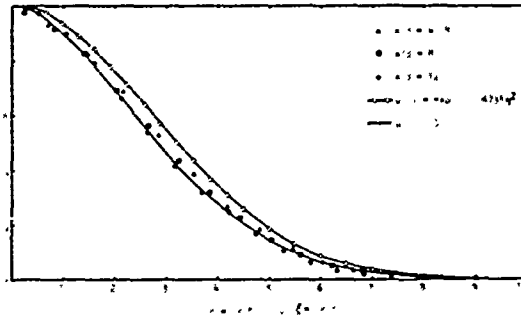


Fig. 2 Mean Velocity Profiles and Mean Velocity Shape Function

Changing the independent variables in equations 3.6, 3.7 and 3.8 to x , η and ξ leads to

i) in the annular mixing region,

$$(h^2-1) + 2h^2 b^2 \beta_1 + 2b^2 \beta_2 = 0 \quad 4.3$$

$$\begin{aligned} & \frac{d}{dx} (h^2 + h^2 b^2 \beta_3 + b^2 \beta_4) \\ & = 2b^2 \beta_4 - 2 \left(\frac{1}{R} + \frac{1}{R_T} \right) \left\{ \frac{h^2}{b^2} \beta_5 + \beta_6 \right\} \end{aligned} \quad 4.4$$

$$\begin{aligned} & \frac{d}{dx} (b^2 (1_1 + 1_2 + 21_3)) \\ & = -2i^2 \beta_4 - 2 \left(\frac{1}{R} + \frac{1}{R_T} \right) \{ 1_5 + 1_6 \} \end{aligned} \quad 4.5$$

and (ii) in the developed jet region,

$$\bar{u}_c^{*2} b^{*2} \gamma_2 = \frac{1}{2} \quad 4.6$$

$$\frac{d}{dx^*} \{ \bar{u}_c^{*3} b^{*2} \gamma_4 \} \\ = 2 \bar{u}_c^{*2} b^{*2} I_4 - 2 \left(\frac{1}{R} + \frac{1}{R_T} \right) \bar{u}_c^{*2} \gamma_6 \quad 4.7$$

$$\frac{d}{dx^*} \{ \bar{u}_c^{*3} b^{*2} \gamma_4 \} \\ = -2 \bar{u}_c^{*2} b^{*2} I_4 - 2 \left(\frac{1}{R} + \frac{1}{R_T} \right) \bar{u}_c^{*2} \gamma_6 \quad 4.8$$

where the α 's and γ 's are integral functions of the mean flow and the I 's are integral functions of the fluctuations. These are defined in Appendix 1-5C. In these definitions the independent variables η and ξ , defined above, are both used for convenience. All velocities in the integrands are referred to the local center-line velocity.

Once the fluctuation integral terms in these equations have been defined, they present a simultaneous system of differential equations which may be solved for b^* and h^* or \bar{u}_c^{*2} as functions of x^* .

The organized turbulent fluctuations are described in terms of the eigensolutions of the Fourier transformed fluctuation continuity and momentum equations. The Fourier transform of any velocity or pressure fluctuation is defined such that

$$e^{in\tau} \hat{q}(r; k, n, \omega) \\ = \frac{1}{4\pi^2} \int_{-\infty}^{\infty} \int_{-\infty}^{\infty} e^{i(\omega t - kx)} \cdot \hat{q}(r; x, \phi, t) dx dt \quad 4.9$$

The continuity and momentum equations for the Fourier transforms of the organized motion are,

$$ik\hat{u} + \hat{v}' + \frac{\hat{v}}{r} + \frac{in}{r} \hat{w} = 0 \quad 4.10$$

$$ik(\bar{u} - c)\hat{u} + U'\hat{v} + ik\hat{p} \\ = (v + \bar{v}_T) \{ \hat{u}' + \frac{\hat{u}}{r} - (k^2 + \frac{n^2}{r^2}) \hat{u} \} \quad 4.11$$

$$ik(\bar{u} - c)\hat{v} + \hat{p}' \\ = (v + \bar{v}_T) \{ \hat{v}' + \frac{\hat{v}}{r} - (k^2 + \frac{n^2+1}{r^2}) \hat{v} - \frac{2in}{r^2} \hat{w} \} \quad 4.12$$

$$ik(\bar{u} - c)\hat{w} + \frac{in}{r} \hat{p} \\ = (v + \bar{v}_T) \{ \hat{w}' + \frac{\hat{w}}{r} - (k^2 + \frac{n^2+1}{r^2}) \hat{w} + \frac{2in}{r^2} \hat{v} \} \quad 4.13$$

The boundary conditions are:

$$\left. \begin{aligned} \hat{v}(0) = \hat{w}(0) = 0 & \quad n \neq 1 \\ \hat{v}(0) = -i\hat{w}(0) & \quad n = 1 \\ u(0) \text{ and } \hat{p}(0) \text{ finite} & \quad n = 0 \\ \hat{u}(0) = \hat{p}(0) = 0 & \quad n \neq 0 \\ \hat{u}(r), \hat{v}(r), \hat{w}(r), \hat{p}(r) \rightarrow 0 & \text{ as } r \rightarrow 0 \end{aligned} \right\} \quad 4.14$$

where k is the wave number, ω the real frequency, $c = \omega/k$ and \bar{v}_T is the turbulent eddy viscosity relating the time dependent random shear stresses with the rate of strain of the organized disturbance.

In the annular mixing region of the jet the equations are nondimensionalized with respect to the jet exit velocity and the local momentum thickness. Downstream of the potential core the reference velocity used is the jet center-line velocity.

The eigensolutions are found using the method of solution described in Appendix 1-5B

The assumptions that led to the mean momentum integral equation being written in the form of equation 3.6 have enabled the potential core radius h^* and the jet center-line velocity \bar{u}_c^{*2} to be directly related to the local momentum thickness b^* . Thus, the integrals of the fluctuations may be written

$$I_i = |A|^2 k_i (b^*)^i \quad i = 1, 2, \dots, 6. \quad 4.15$$

The turbulent diffusion integral I_2 involves triple products of the fluctuations and thus becomes zero.

The integrals are normalized such that

$$k_1 + 2k_3 = 1, \quad 4.16$$

so that

$$|A|^2 = \int_0^{\infty} \{ \bar{u}(\bar{u}^{*2} + \bar{v}^{*2} + \bar{w}^{*2}) + 2\bar{u}\bar{p}^* \} r dr \quad 4.17$$

The total fluctuation mechanical energy flux, E_F , is given by

$$E_F = \frac{\rho}{2} \int_0^{\infty} \{ \bar{u}(\bar{u}^2 + \bar{v}^2 + \bar{w}^2) + \frac{2\bar{u}\bar{p}}{\rho} \} r dr \quad 4.18$$

Then, in the annular mixing region,

$$E_F = \frac{1}{2} |A|^2 b^{*2} \bar{u}_j^3, \quad 4.19$$

and in the developed jet region,

$$E_F = \frac{1}{2} |A|^2 b^{*2} \bar{u}_c^{*3} \bar{u}_j^3. \quad 4.20$$

In terms of E_F the mean mechanical energy and fluctuation energy equations may be written,

$$f(h^*, b^*) \frac{db^*}{dx^*} = 4 \frac{E_F}{b^*} k_u - 2 \left\{ \frac{1}{R^*} + \frac{1}{R_T^*} \right\} (h^* \beta_5 + b^* \beta_6) \quad 4.21$$

$$\frac{b^*}{E_F} \frac{dE_F}{dx^*} = -2k_u - 2 \left\{ \frac{1}{R^*} + \frac{1}{R_T^*} \right\} (k_5 + k_f) \quad 4.22$$

in the annular mixing region, where

$$f(h^*, b^*) = \frac{h^{*2}(\beta_3 - \beta_1) + 2h^*b^*(\beta_4 - \beta_2) + 2b^{*2}(\beta_1\beta_4 - \beta_2\beta_3)}{(h^* + b^*\beta_1)} \quad 4.23$$

and

$$Y_4 \frac{db^*}{dx^*} = -8Y_2 \frac{E_F}{b^*} k_u + 2 \left\{ \frac{1}{R^*} + \frac{1}{R_T^*} \right\} r_c \quad 4.24$$

$$\frac{b^*}{E_F} \frac{dE_F}{dx^*} = -2k_u - 2 \left\{ \frac{1}{R^*} + \frac{1}{R_T^*} \right\} (k_5 + k_f) \quad 4.25$$

in the developed jet region, where,

$$\left. \begin{aligned} R^* &= \frac{\bar{u}_j b}{v} & \text{and} & & R_T^* &= \frac{\bar{u}_j b}{v_T} & x < x_c \\ R^* &= \frac{\bar{u}_c b}{v} & \text{and} & & R_T^* &= \frac{\bar{u}_c b}{v_T} & x \geq x_c \end{aligned} \right\} \quad 4.26$$

Equations 4.21, 4.22, 4.24 and 4.25 may be solved to determine the axial variation of b^* , E_F and h^* or \bar{u}_c^* . These results are given in the next section.

1-5.5 Results and Discussion

Before calculations can be made the values of the eddy viscosities $\bar{\nu}_T$ and $\bar{\nu}_T'$ need to be specified. Tam(11) has argued that since the effects of viscosity on the organized motion are confined to a thin critical layer whose dimension is much smaller than b^* , the value of $\bar{\nu}_T$ will be an order of magnitude smaller than $\bar{\nu}_T'$. However, the thickness of the critical layer is a function of the viscosity, increasing with decreasing viscosity. Also, as will be seen below, the wave length of the most amplifying mode is only of the order of four times the local physical width of the jet. Thus, the eddy viscosity coefficients are chosen to be equal. The same hypothesis was used by Reynolds and Hussain(14). In physical terms it states that, since the large scale and the mean flow structure of the jet are of a similar scale, then the action of the background shear stresses in the form of a viscosity will be of the same order of magnitude on each. The notation $\bar{\nu}_T$ is used to represent both coefficients of eddy viscosity and in the two jet

regions they are

$$\left. \begin{aligned} \bar{\nu}_T &= K b^* \bar{u}_j r_c & x < x_c \\ \bar{\nu}_T &= K b^* \bar{u}_c r_c & x \geq x_c \end{aligned} \right\} \quad 5.1$$

The value of K is taken to be .02. This corresponds to the value used by Tam(11) and is approximately equal to the values given in Schlichting(23) for the two dimensional and axisymmetric jet. It can then be seen that the local turbulent Reynolds number, R_T^* , defined in equation 4.26, is constant throughout the jet.

With this definition of eddy viscosity the solutions to equations 4.10 to 4.13 with boundary conditions 4.14 may be found. The viscous solutions for all values of n have not been obtained but a qualitative comparison between their amplification factors may be obtained by considering the inviscid solutions. The amplification factor $-\alpha_1$ as a function of frequency is shown in figure 3. Clearly, the order of modes from most unstable to more stable is $n = 1, 0, 2$. This is in agreement with the results for axisymmetric pipe flow by Garg and Rouleau(19), who also continued this sequence to higher mode numbers. The results of Batchelor and Gill(21) for linear temporal stability show that for a plug flow the amplification for all modes is equal at high wave numbers and for a bell-shaped profile, characteristic of the developed jet, only the $n = 1$ mode is amplifying in the inviscid limit. These results are confirmed by the present viscous analysis. The amplification factor as a function of frequency for the $n = 0$ mode is shown in figure 4 and for the $n = 1$ mode in figure 5. As the jet width increases, the $n = 1$ mode becomes increasingly more amplifying relative to the $n = 0$ mode. However, for small jet widths the $n = 0$ mode and $n = 1$ mode have similar maximum amplification rates. This is shown in figure 6. The detailed radial variation of the mean velocity profile governs the relative magnitudes of the modes. The phase velocities defined by $c_r = \omega/\alpha_r$, where α_r is the real part of the wave number, are shown in figure 7 for both $n = 0$ and 1 modes for two jet momentum thicknesses. The value of $b^* = .4128$ corresponds to the momentum thickness at the end of the potential core, since $\beta_2 = 2.93408$. The phase velocity of the $n = 1$ mode increases with increasing frequency. This relationship is characteristic of the fully developed axisymmetric jet [e.g. Wagnanski and Fiedler(22)]. It is in the fully developed region of the jet that only the $n = 1$ mode is amplifying. The $n = 0$ mode has a phase velocity which decreases with increasing frequency. It is interesting to note that the results of Crow and Champagne(2) indicate a different phase-velocity/frequency relationship for the axisymmetric mode. However, their results were for a plug flow jet velocity profile and inviscid flow whereas the $n = 0$ mode was growing in a jet flow whose mean flow characteristics were becoming more smooth as a function of axial distance. The inclusion of viscous effects would have reduced their overestimate of the amplification rate and the use of realistic velocity profiles would have improved the phase velocity agreement for spatial amplification. Thus, their conclusion that temporal instability theory is more valid by comparison with experimental results is open to question.

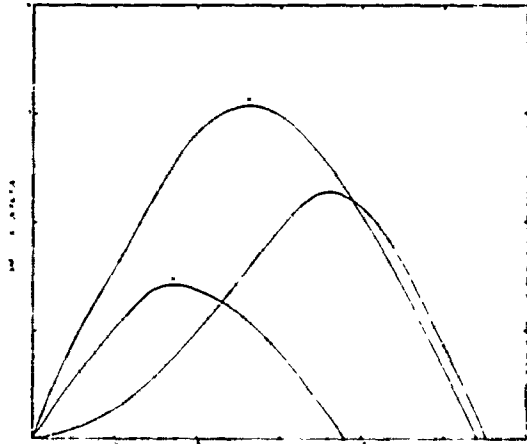


Fig. 3 Inviscid Amplification Curves for First Three Azimuthal Mode Numbers

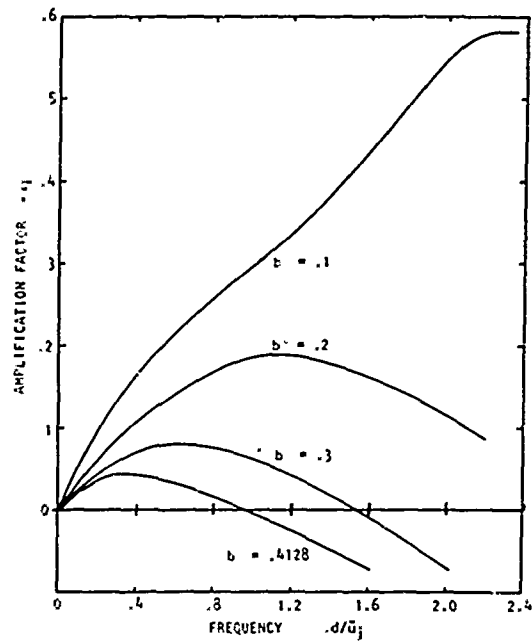


Fig. 5 Amplification of $n = 1$ Mode as a Function of Frequency at Various Downstream Locations

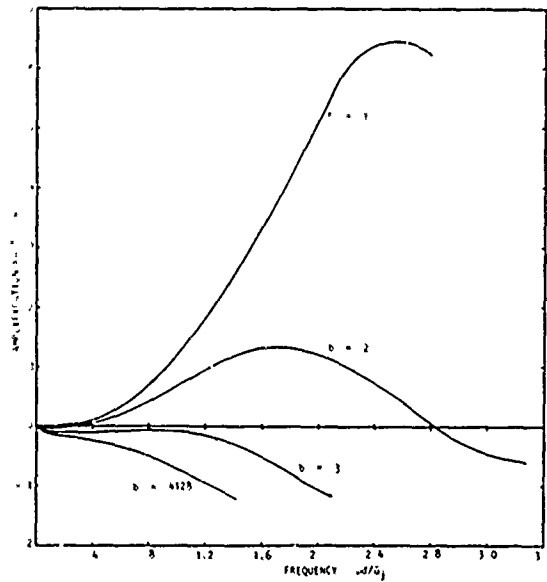


Fig. 4 Amplification Factor for $n = 0$ as a Function of Frequency at Several Downstream Locations

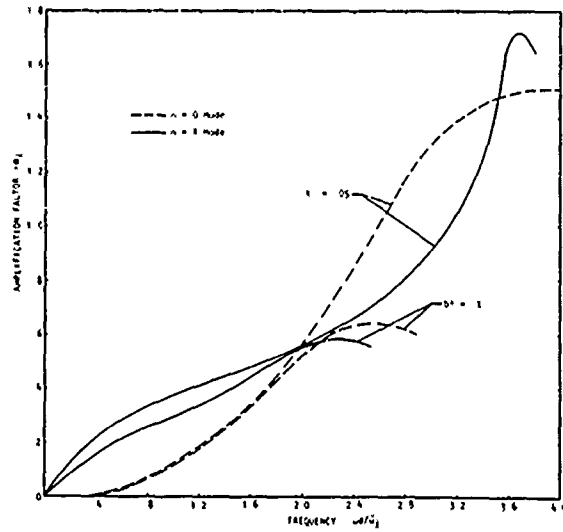


Fig. 6 Comparison of Amplification of $n = 0$ and $n = 1$ Modes for $b^* = .05$ and $b^* = .1$

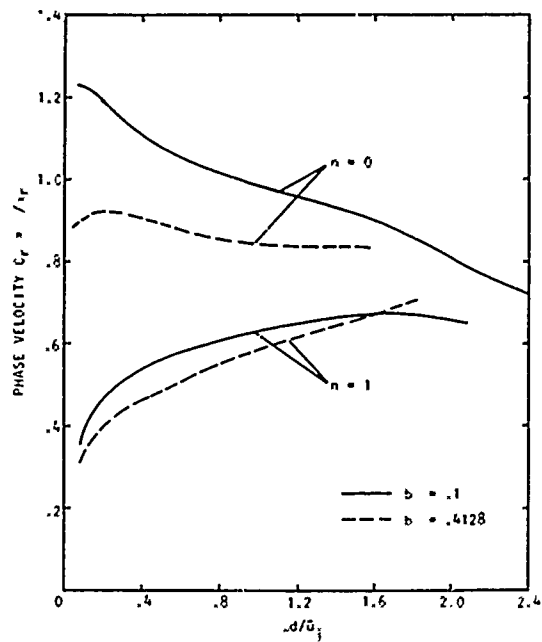


Fig. 7 Phase Velocity as a Function of Frequency and Two Momentum Thicknesses

The eigenfunctions $u^*(r)$ for the most amplifying $n = 0$ and $n = 1$ modes are shown in figures 8 and 9, respectively. The $n = 0$ mode is normalized such that $u^*(0) = 1$ and the $n = 1$ mode is normalized such that $v^*(0) = 1$. The corresponding radial velocity fluctuation eigenfunctions are shown for the $n = 0$ and $n = 1$ mode in figures 10 and 11, respectively.

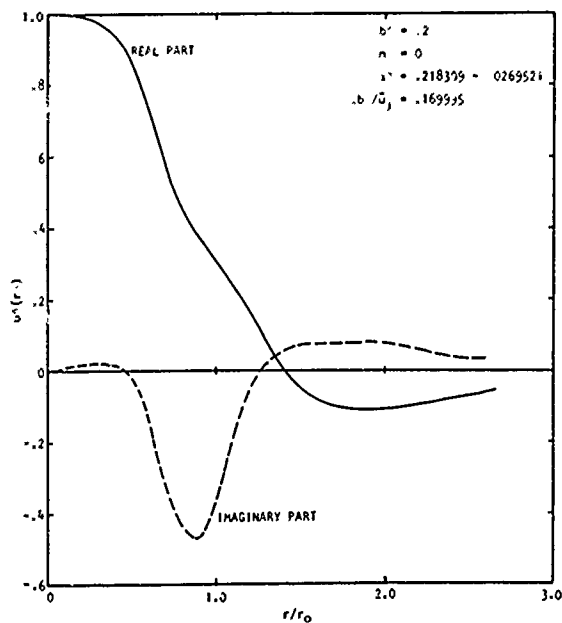


Fig. 8 $u^*(r^*)$ for Most Amplifying $n = 0$ Mode for $b^* = .2$

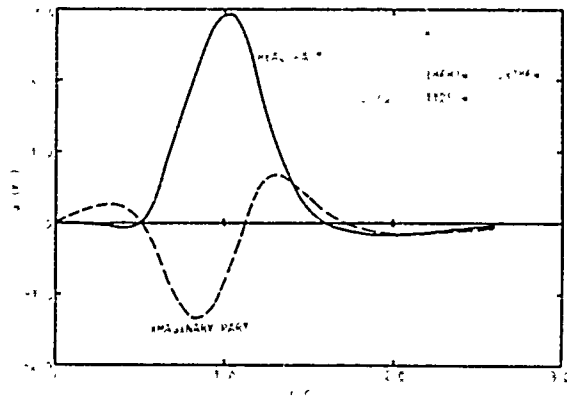


Fig. 9 $u^*(r^*)$ for Most Amplifying $n = 1$ Mode for $b^* = .2$

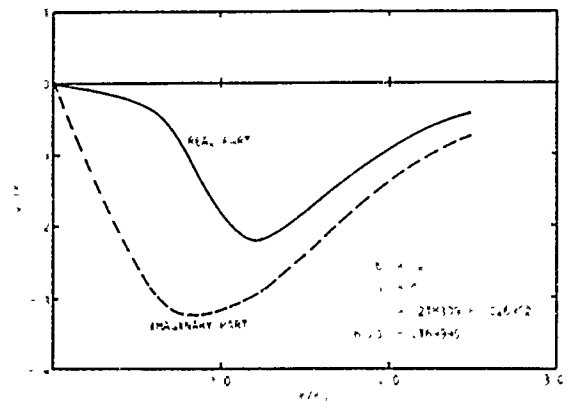


Fig. 10 $v^*(r^*)$ for Most Amplifying $n = 0$ Mode at $b^* = .2$

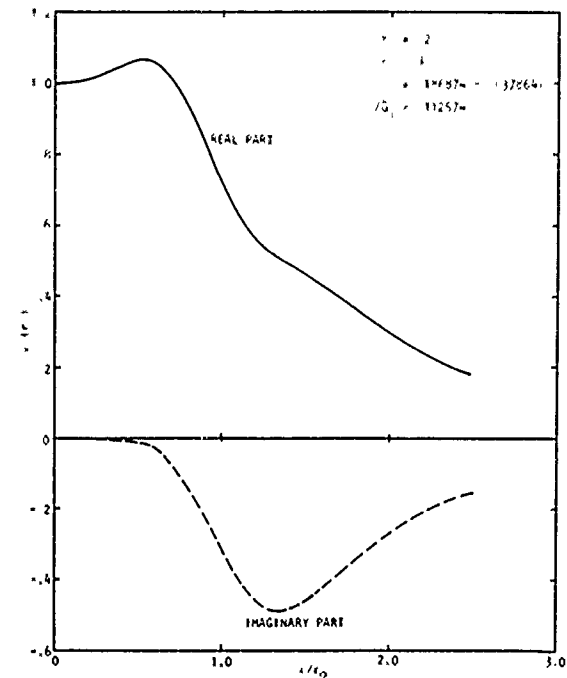


Fig. 11 $v^*(r^*)$ for Most Amplifying $n = 1$ Mode at $b^* = .2$

In order to determine the axial behavior of the organized motion as well as the growth of the jet, it is necessary to specify which eigenfunctions are appropriate at each axial location. In the work of Ko *et al.* (17) the problem of transition in an incompressible wake considering finite amplitude disturbances was studied. In this case it was appropriate to look at the development of a mode with a frequency corresponding to the measured frequency of the fundamental mode. Tam (11) also chose to look at a single frequency to represent the noise-producing, large-scale, turbulent structure of a supersonic jet. However, the spectrum of turbulence does not consist of a single frequency but a continuous spectrum whose peak varies with axial location.

It has already been noted that in stability theory the mode which dominates is that receiving the highest amplification. It has also been argued that the mode within the turbulence which locally dominates the flow structure is that which is locally most amplifying as it is this mode which extracts energy at the greatest rate from the mean flow. Thus, it is clear that at each axial location the integrals to be used to determine the downstream behavior of the turbulent energy and the growth of the mean flow, are those given by the eigenfunctions of the most amplifying mode. However in the axisymmetric jet there is a most amplifying or least damped solution corresponding to each azimuthal mode number. The amplification factor for all these modes is of a similar magnitude close to the jet exit. It is only away from the jet exit that the $n = 1$ mode is the only amplifying mode.

The overall organized structure can only be fully accounted for by considering all these modes. If only the $n = 1$ mode is used, the rate at which energy is transferred from the mean flow to the organized motion will be too great. Although the other modes have gained energy from the mean flow in the region near the jet exit they will be losing this energy back to the mean flow and by viscous dissipation as they propagate downstream.

The mean mechanical and fluctuation energy equations are written,

$$f(h^*, b^*) \frac{db^*}{dx^*} = \frac{4}{b^*} \sum_{i=0}^m E_{F_i} k_{i_1} - 2 \left\{ \frac{1}{R^*} + \frac{1}{R_T^*} \right\} (h^* \gamma_5 + b^* \gamma_6) \quad 5.2$$

$$b^* \frac{d}{dx^*} \left\{ \sum_{i=0}^m E_{F_i} \right\} = -2 \sum_{i=0}^m \left\{ (k_{i_1} + \frac{1}{R^*} + \frac{1}{R_T^*}) (k_{5_i} + k_{6_i}) \right\} E_{F_i} \quad 5.3$$

$$\gamma_4 \frac{db^*}{dx^*} = -8 \frac{\gamma_2}{\bar{u}_c^*} \sum_{i=0}^m E_{F_i} k_{i_1} + 2 \left\{ \frac{1}{R^*} + \frac{1}{R_T^*} \right\} \gamma_6 \quad 5.4$$

$$b^* \frac{d}{dx^*} \left\{ \sum_{i=0}^m E_{F_i} \right\} = -2 \sum_{i=0}^m \left\{ (k_{i_1} + \frac{1}{R^*} + \frac{1}{R_T^*}) (k_{5_i} + k_{6_i}) \right\} E_{F_i} \quad 5.5$$

The fluctuation energy equation 5.3 and 5.5 take an identical form in the annular mixing region and the developed region of the jet. However, the reference velocity used in the evaluation of the integral terms is the jet exit velocity in the annular mixing region and the jet center-line velocity in the developed jet.

It will be assumed that the growth of each mode satisfies equation 5.3 and 5.5 independently.

The fluctuation energy equation must give the same amplification factor as the eigenvalue solution, that is,

$$b^* \frac{d}{dx^*} E_{F_i} = -2 \alpha_i^* \quad 5.6$$

For example with $R_T^* = 50.$, $R^* = 2.15332 \times 10^5$ at $b^* = .2$, $\alpha_1^* = .174533$ for $n = 1$

$$k_4 = .05402$$

$$k_5 = 1.144$$

$$k_6 = .08733,$$

equation 5.3 then gives $b^* dE_F/dx^* = .058716$, which agrees closely with the eigenvalue $\alpha^* = .2771248 - .0293371i$.

Having established the validity of the solutions, equations 5.2 to 5.4 will be solved. The calculations are made for only the $n = 0$ and $n = 1$ modes. This is expected to increase the rate at which the jet center-line velocity decays and the jet spreads.

The frequency for maximum amplification as a function of the jet momentum thickness b^* is shown in figure 12 for the $n = 0$ and $n = 1$ modes. Near the end of the potential core the least damped ($n = 0$) mode is at zero frequency, however, the frequency used in the calculations was chosen to coincide with the peak in the amplification curves in the damped region. The Strouhal number at the end of the potential core, that is $b^* = .4128$, is .385 for the $n = 0$ mode and .35 for the $n = 1$ mode. Figure 13 shows the amplification factor as a function of jet momentum thickness for the $n = 0$ and $n = 1$ modes. The $n = 0$ mode is seen to be damped for $b^* > .29$ whereas the $n = 1$ mode is always amplifying.

The downstream growth of E_{F_i} for the $n = 0$ and 1 modes are shown in figures 14 and 15 respectively for various equal initial amplitudes of the two modes. Examination of equation 5.3 and 5.5 reveals that the value of E_{F_i} tends to a constant as b^* becomes very large. The corresponding center-line velocity profiles are shown in figure 16. The best agreement is seen to be obtained with initial values of E_{F_0} and E_{F_1} equal to 1×10^{-5} . As noted

earlier, by considering only the first two azimuthal mode numbers, the rate at which energy is lost by the mean flow, which is reflected in the center-line velocity decay, is too high. This is shown in figure 17 where the decay of \bar{u}_c^* is calculated, assuming only the $n = 0$ mode or the $n = 1$ mode is present. The $n = 0$ mode does not cause sufficient energy loss by the mean flow whereas the $n = 1$ mode alone causes too great a loss of mean flow energy.

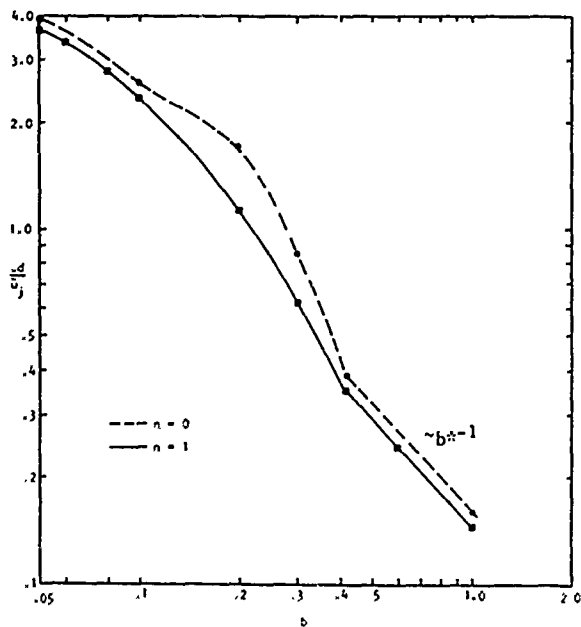


Fig. 12 Most Amplifying Frequencies for $n = 0$ and 1 Modes as a Function of Momentum Thickness

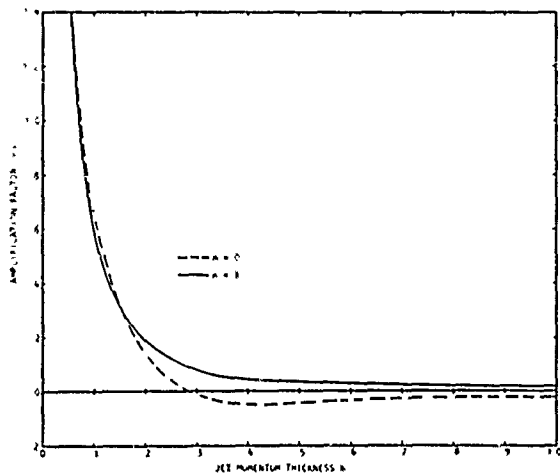


Fig. 13 Amplification Rate for the Least Stable $n = 0$ and $n = 1$ Modes

The effect of the initial ratio of E_{F_0} to E_{F_1} is shown in figure 18. Increasing the $n = 0$ mode initial value decreases the center-line velocity decay but moves the end of the potential core downstream. The following calculations will be made with initial values of E_{F_0} and E_{F_1} equal to 1×10^{-5} . Their relative amplitudes are shown in figure 19.

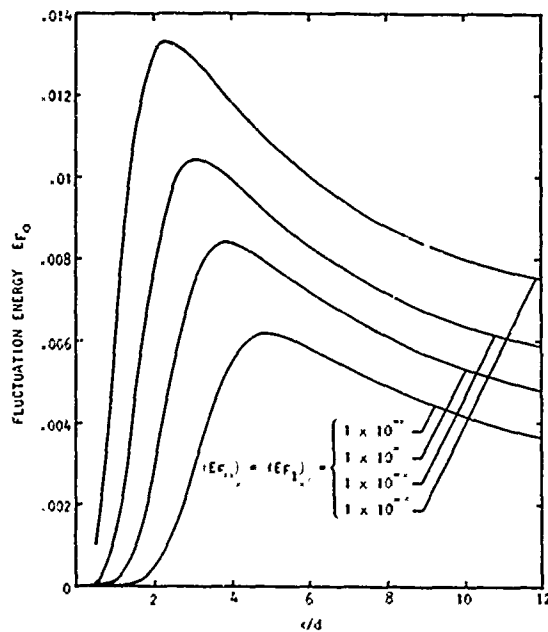


Fig. 14 Fluctuation Energy in $n = 0$ Mode for Various Initial Conditions

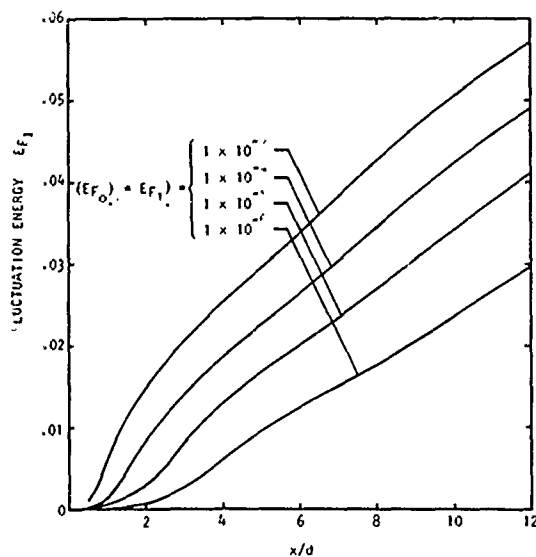


Fig. 15 Fluctuation Energy in $n = 1$ Mode for Various Initial Conditions

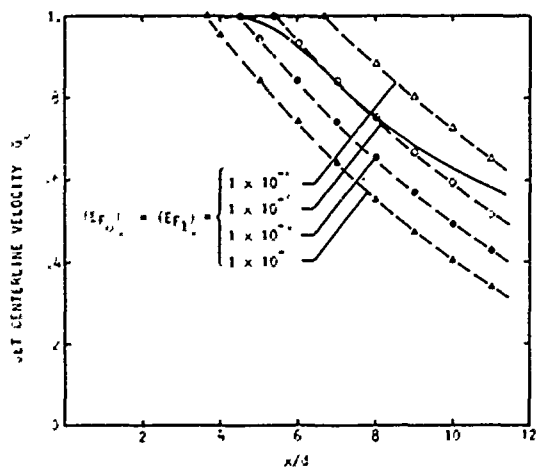


Fig. 16 Effect of Initial Energy Amplitude or Jet Center-Line Velocity

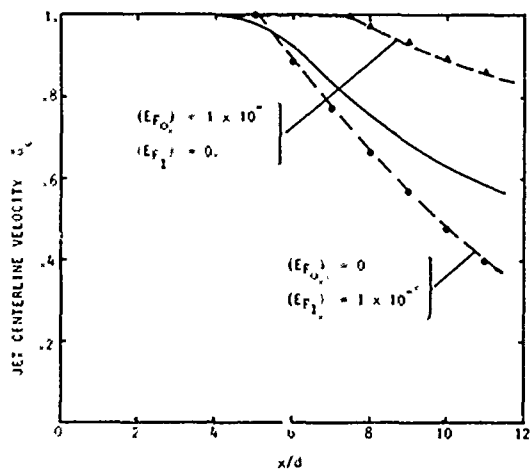


Fig. 17 Effect of Single Mode Number on Jet Center-Line Velocity

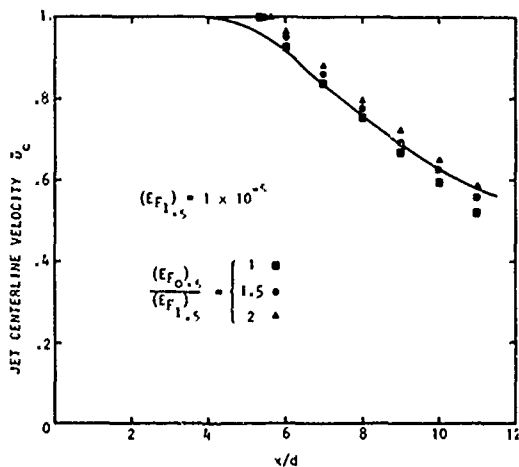


Fig. 18 Effect of Rates of Initial Mode Energy Amplitudes on Jet Center-Line Velocity

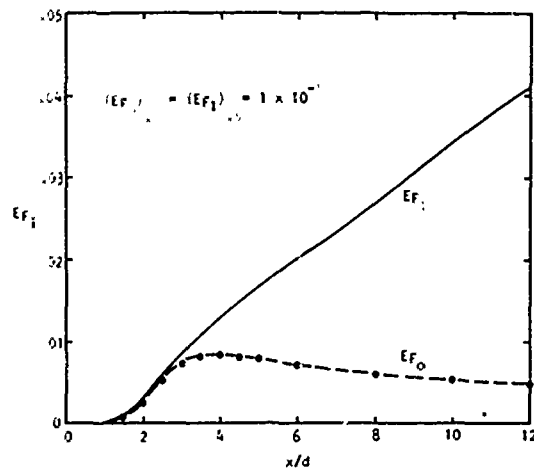


Fig. 19 Relative Magnitudes of $n = 0$ and $n = 1$ Modes

Examination of equation 5.4 reveals that for db^*/dx^* to asymptotically approach a constant in the developed jet region,

$$\sum_{i=0}^m E_{F_i} k h_i$$

must be proportional to \bar{u}_c^* or else be zero. If only the $n = 1$ mode is considered, then E_{F_1} tends to a constant since the mode's amplification is approaching zero as the jet momentum thickness increases. Thus, the asymptotic behavior of E_F must be determined by the sum of several azimuthal modes. However, it is also probable that for long wavelength motions the transfer of energy from the mean flow to the fluctuation does not obey a simple linear relationship and the sub-harmonics and harmonics of the fluctuation contribute to further amplitude limitation of the mode.

Ko *et al.*⁽¹⁷⁾ have correctly noted that a more realistic indication of the amplitude of the turbulent fluctuations is given by an energy density rather than a total energy calculation. Defining

$$E_T = \frac{\rho}{2} \int_0^{\infty} \{ \overline{u^2} + \overline{v^2} + \overline{w^2} \} + 2 \frac{\overline{u \partial p}}{\rho} \} \epsilon d\epsilon \quad 5.7$$

this gives

$$E_T = \frac{E_F}{D^2} = \frac{|A|^2}{2} \frac{1}{u_j^3} \quad x < x_c \quad 5.8$$

$$= \frac{|A|^2}{2} \frac{1}{\bar{u}_c^3} \frac{1}{u_j^3} \quad x \geq x_c$$

The magnitude of E_{T_0} and E_{T_1} for initial values of E_F of 1×10^{-5} are plotted in figure 20. Both modes are seen to peak at approximately $2\frac{1}{2}$ diameters downstream of the jet exit.

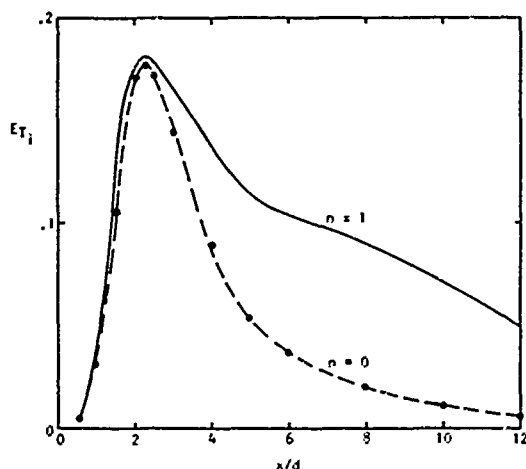


Fig. 20 Energy Density as a Function of Axial Location

With this information on the relative magnitudes of the turbulent fluctuations the mean square turbulent velocity distributions in the jet may be obtained. The radial distributions of mean square, axial velocity fluctuations, $\overline{u^{*2}}$, radial velocity fluctuations, $\overline{v^{*2}}$, azimuthal velocity fluctuations, $\overline{w^{*2}}$, and $\overline{u^*v^*}$ at $x/d = 2.75$ are shown in figures 21, 22, 23 and 24, respectively. The same distributions downstream of the potential core at $x/d = 8$ are shown in figures 25, 26, 27, and 28. The distributions are all normalized such that $v^*(0) = \text{unity}$ for the $n = 0$ mode. In the annular mixing region the axial velocity fluctuation is dominated by the $n = 0$ mode in the potential core region. However, it is to be remembered that no account has been made of the intermittent character of the real turbulent flow. In the model the organized motion is assumed to be evolving continuously and uniformly along the mixing region of the jet. The $n = 0$ mode need not possess an azimuthal velocity fluctuation, since this fluctuation satisfies a completely independent differential equation. The $\overline{u^*v^*}$ distribution, which for incompressible flow, is proportional to the Reynolds stress exhibits similar characteristics for the $n = 0$ and $n = 1$ modes in the annular mixing region and is dominated by the $n = 1$ mode in the developed region of the jet.

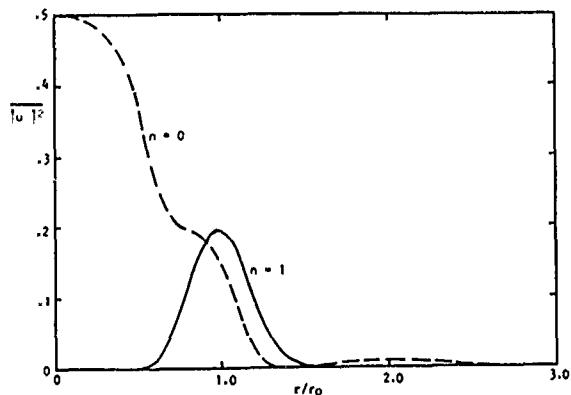


Fig. 21 Radial Distributions of Mean Square Axial Velocity Fluctuations, $x/d = 2.75$

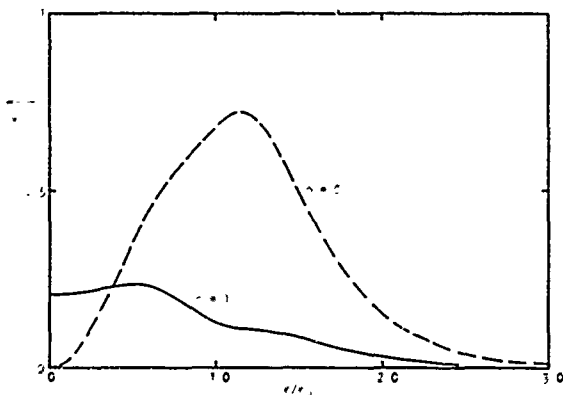


Fig. 22 Radial Distribution of Mean Square Radial Velocity Fluctuation; $x/d = 2.75$

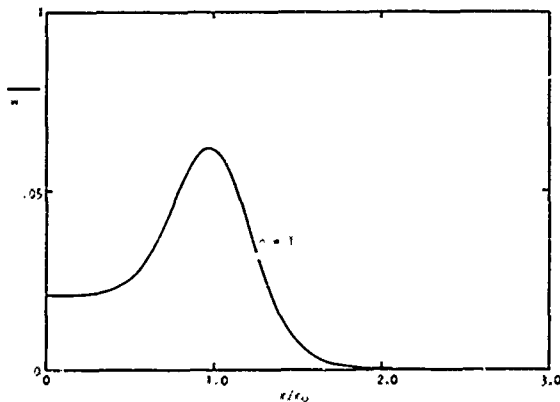


Fig. 23 Radial Distribution of Mean Square Azimuthal Velocity Fluctuations; $x/d = 2.75$

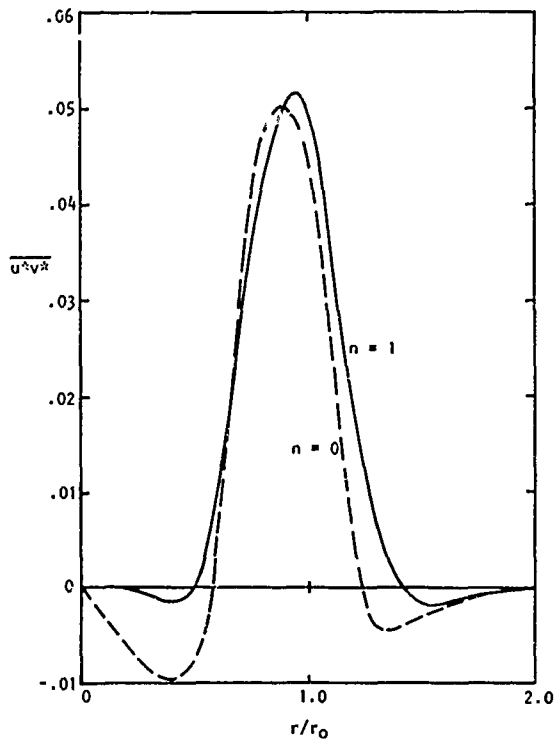


Fig. 24 Radial Distribution of $\overline{u^*v^*}$; $x/d = 2.75$

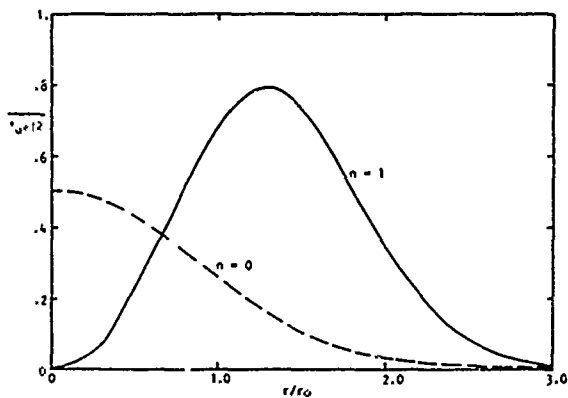


Fig. 25 Radial Distribution of Mean Square Axial Velocity Fluctuations; $x/d = 8$

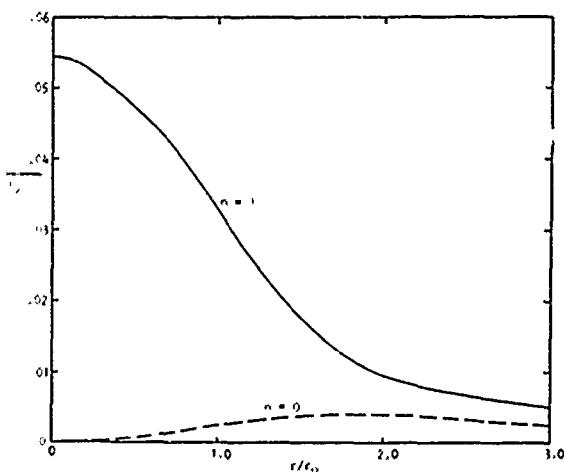


Fig. 26 Radial Distributions of Mean Square Radial Velocity Fluctuations; $x/d = 8$

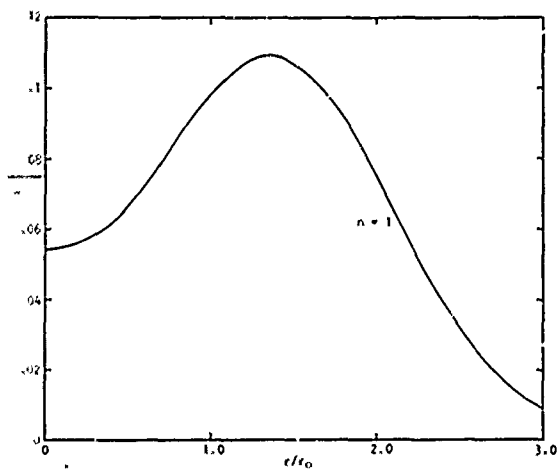


Fig. 27 Radial Distribution of Mean Square Azimuthal Velocity Fluctuation; $x/d = 8$

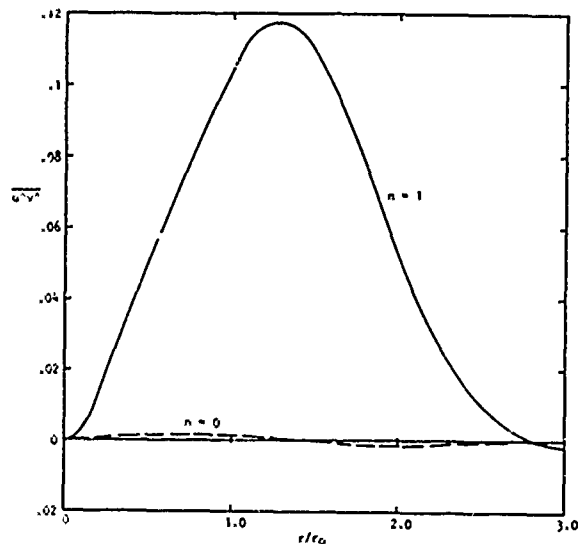


Fig. 28 Radial Distribution of $\overline{u^2 v^2}$; $x/d = 8$

The axial growth and decay of single real frequency velocity fluctuations may be determined by solution of equations 5.3 and 5.5 or equation 5.6, with the axial dependence of b^* already determined by the most amplifying modes. The value of α_j for several frequencies as a function of axial position is shown in figure 29. The downstream behavior of a number of different frequency components for the $n = 1$ mode, for a given equal initial amplitude of 1×10^{-5} , is shown in figure 30. The higher frequency components grow very rapidly to a peak before decaying at a similar rate, whereas the lower frequency components peak further downstream. The downstream distance at which a particular frequency component peaks is given in the table below.

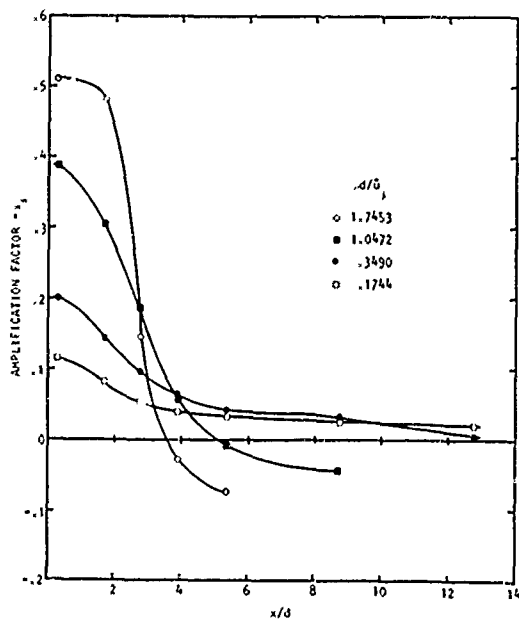


Fig. 29 Amplification Factor for Several Frequencies as a Function of Axial Position, $n = 1$

$\omega d/\bar{u}_j$	x/d Peak
1.7453	3.5
1.0472	5.3
.3490	13.75
.1744	18.8C

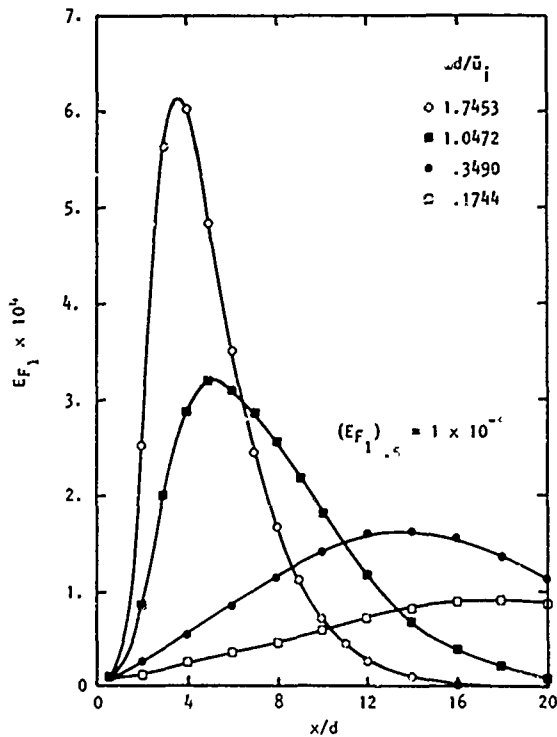


Fig. 30 Integrated Fluctuation Energy Flux for Single Frequency Components as a Function of Axial Location, $n = 1$

The relative magnitude of these frequency components may be determined since the magnitude of each is known at the axial location where that frequency component was most amplifying. The relative magnitudes of the frequency components computed in this manner for the $n = 1$ mode are shown in figure 31.

Since the magnitude of EF_1 tends to a constant far downstream in the developed region of the jet, the peak amplitudes of lower frequency components will eventually decrease with decreasing frequency.

1-5.6 Summary

A model has been presented for the organized large scale structure of an axisymmetric incompressible jet. The structure is described locally by a sum of the least stable modes for each azimuthal mode number. The downstream growth of the mean flow dimensions, jet center-line velocity decay and turbulent energy are found by solution of the integral forms of the momentum and energy equations for the mean flow and the fluctuations. The mean velocity profile is characterized by a shape function and a

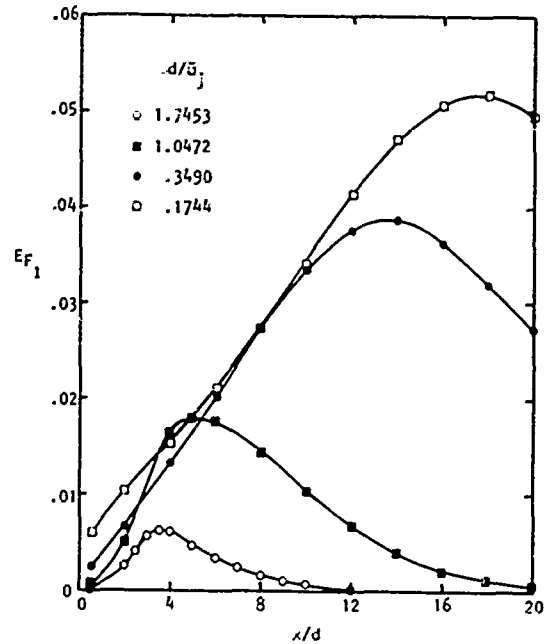


Fig. 31 Relative Amplitudes of Integrated Fluctuation Energy Flux for Single Frequency Components, $n = 1$

coordinate system depending on the jet momentum thickness and the potential core width in the annular mixing region of the jet, and the jet center-line velocity in the developed region of the jet. The integrated energy flux associated with the first helical azimuthal mode, $n = 1$, is shown to increase at a gradually decreasing rate with axial distance whereas the energy flux of all other modes decreases with axial distance. The amplitude of the organized fluctuations, which is characterized in terms of an energy density, is shown to reach a peak in the annular mixing region of the jet before decaying. The downstream growth and decay of single frequency components is found by determining the local amplification rate as a function of downstream distance with the scale of the mean flow predetermined by the most amplifying mode analysis. The relative magnitudes of the single frequency components are calculated using the amplitudes of the components when they are most amplifying, which are calculated in the determination of the overall structure. The location of the peak magnitude of high frequency components occurs close to the jet exit and increasingly lower frequency components have their peaks further downstream.

Future work includes:

- (1) extensive comparison with measurements currently being obtained using a laser velocimeter,
- (2) calculation of radiated noise using both an extension of Lighthill's theory of aerodynamic noise, Lilley *et al.*(12), and solutions of Lilley's equation with the source wavenumber/frequency spectrum determined from the present work,
- (3) extension of the work to include compressible flow. Results are already being analyzed for a two-dimensional compressible shear layer, and

(4) examination of the rôle of harmonics of the fundamental mode in the distribution of energy from the mean flow to the organized motion.

1-5.7 Acknowledgements

The author wishes to acknowledge the many helpful discussions held with Prof. G. M. Lilley and his continual interest in this work.

The work was sponsored by Air Force Contract F33615-73-C-2032, which is jointly funded by the Air Force Aero Propulsion Laboratory and the U. S. Department of Transportation. The contract is administered by the AFAPL and the Technical Monitor is Paul Shahady. The Contract Program Manager for Lockheed is Harry E. Plumblee.

Notation

b	jet momentum thickness
c_r	phase velocity
d	jet diameter
E_F	integrated fluctuation energy flux
E_T	integrated fluctuation energy density flux
h	radius of potential core
I_i	integral functions of fluctuations
k	wave number
n	azimuthal mode number
P, p	pressure
r	radial coordinate
R	Reynolds number
R_T	turbulent Reynolds number
r_0	jet radius
U, u	axial velocity
u_j	jet exit velocity
u_c	jet center-line velocity
V, v	radial velocity
\dot{w} , w	azimuthal velocity
x	axial coordinate
α	non-dimensional wave number
β_i	integrals of mean flow profile in annular mixing region
γ_i	integrals of mean flow profile in developed jet region
n	diverging coordinate in annular mixing region
v	kinematic viscosity

ν_T	kinematic eddy viscosity
ω	radian frequency
ξ	diverging coordinate in developed jet region
bar	denotes a time averaged quantity
tilde	denotes a fluctuation associated with the organized motion
prime	denotes a fluctuation associated with random motion
asterisk	denotes a non-dimensional quantity

References

- Morris, P. J., The structure of turbulent shear flow. Univ. of Southampton, Ph.D. Thesis, 1971.
- Crow, S. C. and Champagne, F. M., Orderly structure in jet turbulence, J. Fluid Mech. V. 48. p. 547, 1971.
- Lau, J. C., Fuchs, H. V. and Fisher, M. J., A study of pressure and velocity fluctuations associated with jet flows. Univ. of Southampton, ISVR Rep. 28, 1970.
- Townsend, A. A., The structure of turbulent shear flow. C.U.P., 1956.
- Hollo-Christensen, E., Jet noise and shear flow instability seen from an experimenter's viewpoint. J. Appl. Mech., V. 89, p. 1, 1967.
- Laufer, J., Kaplan, R. E. and Chu, W. T., Acoustic modelling of the jet noise abatement problem. Proc. of Interagency Symposium on University Research in Transportation Noise, Stanford University, V. 1, 1973.
- Bishop, K. A., Ffowcs Williams, J. E. and Smith, W., On the noise sources of the unexpanded high-speed jet. J. Fluid Mech., V. 50, p. 21, 1971.
- Browand, F. K., An experimental investigation of the instability of an incompressible, separated shear layer. J. Fluid Mech., V. 26, p. 281, 1966.
- Tam, C. K. W., Directional acoustic radiation from a supersonic jet generated by shear layer instability. J. Fluid Mech., V. 46, p. 757, 1971.
- Tam, C. K. W., On the noise of a nearly ideally expanded supersonic jet. J. Fluid Mech. V. 51, p. 69, 1972.
- Tam, C. K. W., Supersonic jet noise generated by large scale disturbances. AIAA Paper No. 73-992, 1973.
- Lilley, G. M., Morris, P. J. and Tester, B. J., On the theory of jet noise and its applications. AIAA Paper No. 73-987, 1973.
- Tester, B. J. and Burrin, R. B., On sound radiation from sources in parallel sheared jet flows. AIAA Paper No. 74-57, 1974.

14. Reynolds, W. C. and Hussain, A. K. M. F., The mechanics of an organized wave in turbulent shear flow. Part 3. Theoretical models and comparisons with experiments. *J. Fluid Mech.* V. 54, p. 263, 1972.
15. Crow, S. C., Viscoelastic properties of fine-grained incompressible turbulence. *J. Fluid Mech.* V. 33, p. 1, 1968.
16. Stuart, J. T., On the non-linear mechanics of wave disturbances in stable and unstable parallel flows. Part 1, *J. Fluid Mech.* V. 9, p. 353, 1960.
17. Ko, D. R-S., Kubota, T. and Lees, L., Finite disturbance effect on the stability of a laminar incompressible wake behind a flat plate. *J. Fluid Mech.* V. 40, p. 315, 1970.
18. Ling, C-H., and Reynolds, W. C., Non-parallel flow corrections for the stability of shear flows. *J. Fluid Mech.*, V. 59, p. 571, 1973.
19. Garg, V. K. and Rouleau, W. T., Linear spatial stability of pipe Poiseuille flow. *J. Fluid Mech.* V. 54, p. 113, 1972.
20. Garg, V. K., Spatial stability of pipe Poiseuille flow to infinitesimal disturbances. Carnegie-Mellon Univ., Pittsburgh, Ph.D. Thesis, 1971.
21. Batchelor, G. K. and Gill, A. E., Analysis of the stability of axisymmetric jets. *J. Fluid Mech.*, V. 14, p. 529, 1962.
22. Wagnanski, I. and Fiedler, H., Some measurements in the self-preserving jet. *J. Fluid Mech.* V. 38, p. 577, 1969.
23. Schlichting, H., *Boundary Layer Theory*. McGraw-Hill, New York, 1960.
24. Michalke, A. and Schade, H., Zur Stabilität von freien Grenzschichten. *Ingenieur-Archiv*, V. 33, p. 1, 1963.
25. Gill, A. E., On the behavior of small disturbances to Poiseuille flow in a circular pipe. *J. Fluid Mech.* V. 21, p. 145, 1965.
26. Bellman, R. E. and Kalaba, R. E., *Quasi-linearization and non-linear boundary value problems*. Elsevier, New York, 1965.
27. Betchov, R. and Criminale, W. O., *Stability of parallel flows*. Academic Press, New York, 1967.

APPENDIX 1-5A

INTEGRAL EQUATIONS FOR AN AXISYMMETRIC JET

Making use of the equation of continuity, the equations of motion in cylindrical coordinates may be written

$$\frac{\partial U}{\partial t} + \frac{\partial U^2}{\partial x} + \frac{1}{r} \frac{\partial UV}{\partial r} + \frac{1}{r} \frac{\partial UW}{\partial \phi} = -\frac{1}{\rho} \frac{\partial P}{\partial x} + \nu \nabla^2[U], \quad A.1$$

$$\begin{aligned} \frac{\partial V}{\partial t} + \frac{\partial UV}{\partial x} + \frac{1}{r} \frac{\partial V^2}{\partial r} + \frac{1}{r} \frac{\partial VW}{\partial \phi} - \frac{W^2}{r} = -\frac{1}{\rho} \frac{\partial P}{\partial r} + \\ + \nu \nabla^2[V] - \frac{V}{r^2} - \frac{2}{r^2} \frac{\partial W}{\partial \phi} \end{aligned} \quad A.2$$

$$\begin{aligned} \text{and } \frac{\partial W}{\partial t} + \frac{\partial UW}{\partial x} + \frac{1}{r} \frac{\partial VW}{\partial r} + \frac{1}{r} \frac{\partial W^2}{\partial \phi} + \frac{VW}{r} = \\ -\frac{1}{\rho r} \frac{\partial P}{\partial \phi} + \nu \nabla^2[W] - \frac{W}{r^2} - \frac{2}{r^2} \frac{\partial V}{\partial \phi}, \end{aligned} \quad A.3$$

where U, V and W are the velocity components in the x, r and ϕ directions respectively and

$$\nabla^2 \equiv \left\{ \frac{\partial^2}{\partial r^2} + \frac{1}{r} \frac{\partial}{\partial r} + \frac{\partial^2}{\partial x^2} + \frac{1}{r^2} \frac{\partial^2}{\partial \phi^2} \right\}.$$

The velocity and pressure are separated into three parts:

- (i) the mean value denoted by an overbar,
- (ii) the component associated with the organized motion denoted by a tilde and
- (iii) the component associated with the disorganized, random motion denoted by a prime.

On substituting into the equations of motion, phase averaging, averaging over time and introducing an eddy viscosity to describe the influence of the background random motion on the mean flow we obtain:

$$\begin{aligned} \frac{\partial (\bar{u}^2 + \bar{u}'^2)}{\partial x} + \frac{1}{r} \frac{\partial (\bar{v}\bar{u} + \bar{v}'\bar{u}')}{\partial r} + \frac{1}{r} \frac{\partial (\bar{w}\bar{u} + \bar{w}'\bar{u}')}{\partial \phi} = \\ = -\frac{1}{\rho} \frac{\partial \bar{p}}{\partial x} + (\bar{v} + \bar{v}') \{ \nabla^2 [\bar{u}] \}, \end{aligned} \quad A.4$$

$$\begin{aligned} \frac{\partial (\bar{u}\bar{v} + \bar{u}'\bar{v}')}{\partial x} + \frac{1}{r} \frac{\partial (\bar{v}^2 + \bar{v}'^2)}{\partial r} + \frac{1}{r} \frac{\partial (\bar{w}\bar{v} + \bar{w}'\bar{v}')}{\partial \phi} - \\ - \frac{(\bar{w}^2 + \bar{w}'^2)}{r} = -\frac{1}{\rho} \frac{\partial \bar{p}}{\partial r} + \\ + (\bar{v} + \bar{v}') \{ \nabla^2 [\bar{v}] - \frac{\bar{v}}{r^2} - \frac{2}{r^2} \frac{\partial \bar{w}}{\partial \phi} \} \end{aligned} \quad A.5$$

$$\begin{aligned} \text{and } \frac{\partial (\bar{u}\bar{w} + \bar{u}'\bar{w}')}{\partial x} + \frac{1}{r} \frac{\partial (\bar{v}\bar{w} + \bar{v}'\bar{w}')}{\partial r} + \\ + \frac{1}{r} \frac{\partial (\bar{w}^2 + \bar{w}'^2)}{\partial \phi} + \frac{(\bar{v}\bar{w} + \bar{v}'\bar{w}')}{r} = \\ = -\frac{1}{\rho r} \frac{\partial \bar{p}}{\partial \phi} + (\bar{v} + \bar{v}') \{ \nabla^2 [\bar{w}] - \frac{\bar{w}}{r^2} + \frac{2}{r} \frac{\partial \bar{v}}{\partial \phi} \} \end{aligned} \quad A.6$$

where ν_T is defined by

$$\begin{pmatrix} \langle \bar{u}'^2 \rangle & \langle \bar{u}'v' \rangle & \langle \bar{u}'w' \rangle \\ \langle \bar{u}'v' \rangle & \langle \bar{v}'^2 \rangle & \langle \bar{v}'w' \rangle \\ \langle \bar{u}'w' \rangle & \langle \bar{v}'w' \rangle & \langle \bar{w}'^2 \rangle \end{pmatrix} = -2\bar{\nu}_T$$

$$\times \begin{pmatrix} \frac{\partial \bar{u}}{\partial x} & \frac{1}{2} \left(\frac{\partial \bar{v}}{\partial x} + \frac{\partial \bar{u}}{\partial r} \right) & \frac{1}{2} \left(\frac{1}{r} \frac{\partial \bar{u}}{\partial \phi} + \frac{\partial \bar{w}}{\partial x} \right) \\ \frac{1}{2} \left(\frac{\partial \bar{v}}{\partial x} + \frac{\partial \bar{u}}{\partial r} \right) & \frac{\partial \bar{v}}{\partial r} & \frac{1}{2} \left(r \frac{\partial}{\partial r} \left(\frac{\bar{w}}{r} \right) + \frac{1}{r} \frac{\partial \bar{v}}{\partial \phi} \right) \\ \frac{1}{2} \left(\frac{1}{r} \frac{\partial \bar{u}}{\partial \phi} + \frac{\partial \bar{w}}{\partial x} \right) & \frac{1}{2} \left(r \frac{\partial}{\partial r} \left(\frac{\bar{w}}{r} \right) + \frac{1}{r} \frac{\partial \bar{v}}{\partial \phi} \right) & \frac{1}{r} \frac{\partial \bar{w}}{\partial \theta} + \frac{\bar{v}}{r} \end{pmatrix}$$

This relates the time averaged components of the background shear stresses with the rate of strain of the mean motion. Phase averaging is denoted by $\langle \rangle$ and time averaging by an overbar. Fuller distribution of the definition of phase and time averaging and their corresponding properties are given by Reynolds and Hussain (14). In the light of the results of Reynolds and Hussain, the eddy viscosity has been assumed to be independent of radial position

Use of the boundary layer approximations for an axisymmetric mean flow allows the pressure to be eliminated from equations A.4 and A.5, yielding,

$$\frac{\partial \bar{u}^2}{\partial x} + \frac{1}{r} \frac{\partial \bar{u}\bar{v}}{\partial r} + \frac{\partial (\bar{u}^2 - \bar{v}^2)}{\partial x} + \frac{1}{r} \frac{\partial \bar{u}\bar{v}}{\partial r} - \frac{\partial}{\partial x} \left[r \int \frac{\bar{v}^2 - \bar{w}^2}{\gamma} dy \right] = \frac{(v + \bar{\nu}_T)}{r} \frac{\partial}{\partial r} \left[r \frac{\partial \bar{u}}{\partial r} \right] \quad A.7$$

Integration of equation A.7 across the jet with the assumption of no fluctuations at the edge of the jet gives finally,

$$\frac{d}{dx} \int_0^\infty r (\bar{u}^2 + (\bar{u}^2 - \bar{v}^2)) - \int \frac{(\bar{v}^2 - \bar{w}^2)}{\gamma} dy) dr = 0 \quad A.8$$

The integral equation for the mean mechanical energy is obtained by multiplying equation A.7 throughout by \bar{u} and integrating across the jet, giving,

$$\begin{aligned} \frac{d}{dx} \int_0^\infty r \left(\frac{\bar{u}^3}{2} + \bar{u} (\bar{u}^2 - \bar{v}^2) - \bar{u} \int \frac{(\bar{v}^2 - \bar{w}^2)}{\gamma} dy \right) dr = \\ = \int_0^\infty r \frac{\partial \bar{u}}{\partial x} \{ (\bar{u}^2 - \bar{v}^2) - \int \frac{(\bar{v}^2 - \bar{w}^2)}{\gamma} dy \} dr + \\ + \int_0^\infty r \bar{u}\bar{v} \left(\frac{\partial \bar{u}}{\partial r} \right) dr - (v + \bar{\nu}_T) \int_0^\infty r \left(\frac{\partial \bar{u}}{\partial r} \right)^2 dr \end{aligned} \quad A.9$$

The organized disturbance kinetic energy equation may be obtained by multiplying the x , r and ϕ organized disturbance momentum equations by \bar{u} , \bar{v} and \bar{w} respectively adding. The resulting differential equation when multiplied throughout by r and integrated across the jet is,

$$\begin{aligned} \frac{d}{dx} \int_0^\infty \{ \bar{u} (\bar{u}^2 + \bar{v}^2 + \bar{w}^2) + \bar{u}^3 + \bar{u}\bar{v}^2 + \bar{u}\bar{w}^2 + \frac{2\bar{u}\bar{v}}{\rho} \} r dr = \\ = -2 \int_0^\infty (\bar{u}^2 - \bar{v}^2) \frac{\partial \bar{u}}{\partial x} r dr - 2 \int_0^\infty \bar{u}\bar{v} \frac{\partial \bar{u}}{\partial r} r dr + \\ + 2 \int_0^\infty \bar{v} (\bar{v}^2 - \bar{w}^2) dr - 2(v + \bar{\nu}_T) \int_0^\infty \bar{v} dr, \quad A.10 \end{aligned}$$

where the integrand in the dissipation term is given by,

$$\begin{aligned} \bar{\nu}_T \left\{ \left(\frac{\partial \bar{u}}{\partial x} \right)^2 + \left(\frac{\partial \bar{u}}{\partial r} \right)^2 + \left(\frac{\partial \bar{v}}{\partial x} \right)^2 + \left(\frac{\partial \bar{v}}{\partial r} \right)^2 + \left(\frac{\partial \bar{w}}{\partial x} \right)^2 \right. \\ \left. + \left(\frac{\partial \bar{w}}{\partial r} \right)^2 + \frac{1}{r} \left\{ \bar{v}^2 + \bar{w}^2 + 2\bar{v} \frac{\partial \bar{w}}{\partial \phi} - 2\bar{w} \frac{\partial \bar{v}}{\partial \phi} + \left(\frac{\partial \bar{u}}{\partial \phi} \right)^2 \right. \right. \\ \left. \left. + \left(\frac{\partial \bar{v}}{\partial \phi} \right)^2 + \left(\frac{\partial \bar{w}}{\partial \phi} \right)^2 \right\} \right\}, \quad A.11 \end{aligned}$$

and the eddy viscosity $\bar{\nu}_T$ relates the time dependent part of the random background shear stresses to the rate of strain of the organized motion, such that,

$$\tilde{s}_{ij} = -2 \bar{\nu}_T \tilde{e}_{ij} \quad A.12$$

where $\tilde{s}_{ij} =$

$$\begin{pmatrix} \langle \bar{u}^2 \rangle - \langle \bar{u}^2 \rangle & \langle \bar{u}'v' \rangle - \langle \bar{u}'v' \rangle & \langle \bar{u}'w' \rangle - \langle \bar{u}'w' \rangle \\ \langle \bar{u}'v' \rangle - \langle \bar{u}'v' \rangle & \langle \bar{v}'^2 \rangle - \langle \bar{v}'^2 \rangle & \langle \bar{v}'w' \rangle - \langle \bar{v}'w' \rangle \\ \langle \bar{u}'w' \rangle - \langle \bar{u}'w' \rangle & \langle \bar{v}'w' \rangle - \langle \bar{v}'w' \rangle & \langle \bar{w}'^2 \rangle - \langle \bar{w}'^2 \rangle \end{pmatrix} \quad A.13$$

and $\tilde{e}_{ij} =$

$$\begin{pmatrix} \frac{\partial \bar{u}}{\partial x} & \frac{1}{2} \left(\frac{\partial \bar{v}}{\partial x} + \frac{\partial \bar{u}}{\partial r} \right) & \frac{1}{2} \left(\frac{1}{r} \frac{\partial \bar{u}}{\partial \phi} + \frac{\partial \bar{w}}{\partial x} \right) \\ \frac{1}{2} \left(\frac{\partial \bar{v}}{\partial x} + \frac{\partial \bar{u}}{\partial r} \right) & \frac{\partial \bar{v}}{\partial r} & \frac{1}{2} \left(r \frac{\partial}{\partial r} \left(\frac{\bar{w}}{r} \right) + \frac{1}{r} \frac{\partial \bar{v}}{\partial \phi} \right) \\ \frac{1}{2} \left(\frac{1}{r} \frac{\partial \bar{u}}{\partial \phi} + \frac{\partial \bar{w}}{\partial x} \right) & \frac{1}{2} \left(r \frac{\partial}{\partial r} \left(\frac{\bar{w}}{r} \right) + \frac{1}{r} \frac{\partial \bar{v}}{\partial \phi} \right) & \frac{1}{r} \frac{\partial \bar{w}}{\partial \theta} + \frac{\bar{v}}{r} \end{pmatrix} \quad A.14$$

In the derivation of equation A.10 the value of $\bar{\nu}_T$ has been assumed to be constant across the jet.

THE SOLUTION OF THE STABILITY EQUATIONS IN CYLINDRICAL COORDINATES FOR ARBITRARY DISTURBANCE MODE NUMBER

The study of the stability of axisymmetric flows has not been as extensive as that in problems where the flow is described in a rectangular coordinate system. Michalke and Schade(24) have considered the problem of the inviscid stability of various parabolic piecewise mean velocity profiles to axisymmetric disturbances. Batchelor and Gill(21) analyzed the stability of axisymmetric jets and obtained general results for the inviscid case. The viscous stability of bounded axisymmetric flows as pipe flow has been investigated. Recently, Garg and Rouleau(19) looked at the linear spatial stability of Poiseuille flow using a numerical technique and achieved good agreement with the analytic work of Gill(25).

The analysis below presents a method for the solution of the viscous stability of unbounded axisymmetric flows, such as round jets, to disturbances of arbitrary mode number.

Let us define the Fourier transform of any velocity or pressure fluctuation such that

$$e^{in\tau}\hat{q}(r;\alpha,n,\omega) = \frac{1}{4\pi^2} \int_{-\infty-\infty}^{\infty} \int_{-\infty-\infty}^{\infty} e^{i(\omega t - \alpha x)} \cdot \tilde{q}(r;x,\phi,t) dx dt \quad B.1$$

Then the linearized continuity and momentum equations in terms of the transformed fluctuations are,

$$i\alpha\hat{u} + \frac{\hat{v}}{r} + D\hat{v} + \frac{i n}{r} \hat{w} = 0 \quad B.2$$

$$\left\{ D^2 + \frac{D}{r} - \left[\alpha^2 + \frac{n^2}{r^2} + i\alpha R(\bar{u} - c) \right] \right\} \hat{u} - RD\hat{u} \cdot \hat{v} - i\alpha R\hat{p} = 0 \quad B.3$$

$$\left\{ D^2 + \frac{D}{r} - \left[\alpha^2 + \frac{(n^2+1)}{r^2} + i\alpha R(\bar{u} - c) \right] \right\} \hat{v} - \frac{2in}{r^2} \hat{w} - RD\hat{p} = 0 \quad B.4$$

$$\left\{ D^2 + \frac{D}{r} - \left[\alpha^2 + \frac{(n^2+1)}{r^2} + i\alpha R(\bar{u} - c) \right] \right\} \hat{w} + \frac{2in}{r^2} \hat{v} - \frac{i n}{r} R\hat{p} = 0 \quad B.5$$

where $D \equiv d/dr$, $c = \omega/\alpha$ the phase velocity and the equations have been non-dimensionalized with re-

spect to an appropriate velocity, length and density such that

$$R = \frac{\bar{u}_0 L_0}{\nu}$$

For the case where $n = 0$ the terms involving \hat{w} are decoupled from the equations leaving a fourth order system of differential equations. The analysis below is for the case of $n \neq 0$ since this requires a more complicated technique. A similar method may be used to solve the $n = 0$ case.

The solution to equations B.2 to B.5 may be found for small r using a series expansion for the dependent variables. The same result is obtained as that by Garg(20). The dependent variables are found to have the series form,

$$\hat{f}(r) = r^{n+1} (F_1 + F_2 r^2 + F_3 r^4 + \dots + F_i r^{2(i-1)} + \dots)$$

$$\hat{g}(r) = r^{n-1} (G_1 + G_2 r^2 + G_3 r^4 + \dots + G_i r^{2(i-1)} + \dots)$$

$$\hat{u}(r) = r^n (U_1 + U_2 r^2 + U_3 r^4 + \dots + U_i r^{2(i-1)} + \dots)$$

$$\text{and } \hat{p}(r) = r^n (P_1 + P_2 r^2 + P_3 r^4 + \dots + P_i r^{2(i-1)} + \dots)$$

where $\hat{f}(r) = \hat{v} + i\hat{w}$

and $\hat{g}(r) = \hat{v} - i\hat{w}$

The recurrence for F_i , G_i , U_i and P_i are given by

$$G_{i+1} = \frac{1}{2i} \left\{ R P_i - \frac{1}{2(n+i-1)} \sum_{j=1}^m G_{i+1-j} B_j \right\} \quad B.6$$

$$U_{i+1} = \frac{1}{4i(n+i)} \left\{ i\alpha R P_i - \sum_{j=1}^m U_{i+1-j} B_j + R \left[\sum_{j=2}^m (i-1) (F_{i+1-j} + G_{i+2-j}) C_j \right] \right\} \quad B.7$$

$$P_{i+1} = \frac{1}{R} \left\{ -i\alpha U_{i+1} + \frac{1}{4i} \left[\sum_{j=1}^m F_{i+1-j} B_j + \frac{1}{4(n+1)} \left[\sum_{j=1}^m G_{i+2-j} B_j \right] \right] \right\} \quad B.8$$

and

$$F_{\lambda+1} = \frac{1}{2(n+\lambda+1)} \left\{ R P_{\lambda+1} - \frac{1}{2\lambda} \left[\sum_{i=1}^m F_{\lambda+1-i} B_i \right] \right\} \quad B.9$$

where $B_1 = -\alpha^2 - i\alpha R(C_1 - c)$

and $B_i = -i\alpha R C_i$

and the mean velocity \bar{u} is written in a series such that

$$\bar{u} = C_1 + C_2 r^2 + C_3 r^4 + \dots + C_m r^{2(m-1)}$$

Inspection of these recurrence relationships reveals that the solutions may be written in terms of three coefficients, for example P_1 , U_1 and G_1 .

The solutions to the equations in the region outside the jet where the mean velocity is constant may be obtained in analytic form and are found to be:

$$\hat{u}(r) = B_1 H_n^{(1)}(i\alpha r) + B_3 H_n^{(1)}(i\beta r)$$

$$\hat{v}(r) = -B_1 \frac{i}{\alpha} \frac{d}{dr} \{ H_n^{(1)}(i\alpha r) \} -$$

$$- B_2 \frac{i}{\beta} H_{n+1}^{(1)}(i\beta r) - B_5 \frac{i\alpha}{\beta} \frac{H_n^{(1)}(i\beta r)}{r}$$

$$\hat{w}(r) = B_1 \frac{\alpha}{\beta} \frac{H_n^{(1)}(i\alpha r)}{r} + B_3 \frac{i\alpha}{\beta} H_{n+1}^{(1)}(i\beta r) +$$

$$+ \frac{B_5}{\beta} \frac{d}{dr} \{ H_n^{(1)}(i\beta r) \}$$

$$\hat{p}(r) = B_1 (c - \bar{u}_a) H_n^{(1)}(i\alpha r)$$

where \bar{u}_a is the constant mean velocity around the jet and $\beta = [\alpha^2 + i\alpha R(\bar{u}_a - c)]^{1/2}$. Hankel functions of either the first or second kind are used in equation B.10 so as to satisfy the boundary condition in the outer region,

$$\hat{u}, \hat{v}, \hat{w}, \hat{p} \rightarrow 0 \quad \text{as} \quad r \rightarrow \infty.$$

Equations B.2 to B.5 may be written as six first order differential equations in the dependent variables \hat{u} , \hat{v} , \hat{w} , \hat{p} , $\hat{\chi}$ and $\hat{\psi}$, where

$$\hat{\chi} = \frac{d\hat{u}}{dr} \quad \text{and} \quad \hat{\psi} = \frac{d\hat{w}}{dr}.$$

These six equations are integrated numerically outward from the jet axis using the starting conditions provided by the series solution. In order to maintain the linear independence of the three solutions with coefficients U_1 , P_1 and G_1 a nor-

malization and orthogonalization procedure is performed at each step of the numerical integration. [See Bellman and Kalaba (26) and Betchov and Criminale (27).]

The numerical solution at some radial position in the uniform flow outside the jet will be in the form,

$$\hat{u}(a) = P_1 \hat{u}_1(a) + U_1 \hat{u}_2(a) + G_1 \hat{u}_3(a), \text{ etc.} \quad B.11$$

The six coefficients in equations B.10 and B.11 may be found by elimination of the six dependent variables which leads to

$$\underline{F}(\alpha, \omega, R) \times \begin{bmatrix} B_1 \\ B_3 \\ B_5 \\ U_1 \\ G_1 \\ P_1 \end{bmatrix} = 0 \quad B.12$$

where $\underline{F}(\alpha, \omega, R)$ is a 6 x 6 matrix whose coefficients may be easily found from equations B.10 and B.11.

The eigenvalues are determined by satisfying the condition

$$\det. \underline{F} = 0. \quad B.13$$

The eigenvalues may be located using the method proposed by Garg (20) which was found to work well for this problem.

As an example of the solution, the results for an axisymmetric jet profile at $x/d = 2.29$ is given in figure 32. The results are for the $n = 1$ mode and the first five eigenvalues have been located.

A more complete derivation of the above equations and a study of the viscous spatial stability of several axisymmetric jet profiles will be presented later.

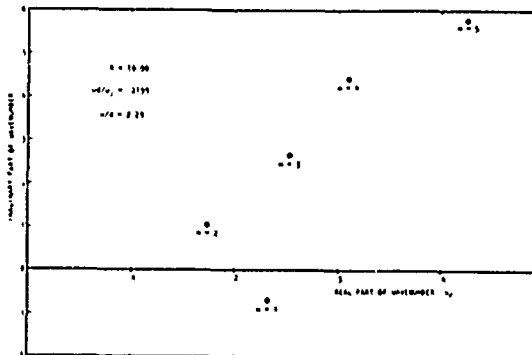


Fig. 32 Location of Eigenvalues for $n = 1$ Mode

APPENDIX 1-5C

DEFINITION OF INTEGRALS IN EQUATIONS 4.3 TO 4.6

$$\beta_1 = \int_0^{\infty} U^{*2}(\eta) d\eta ; \quad \beta_2 = \int_0^{\infty} U^{*2}(\eta) \eta d\eta ;$$

$$\beta_3 = \int_0^{\infty} U^{*3}(\eta) d\eta ; \quad \beta_4 = \int_0^{\infty} U^{*3}(\eta) \eta d\eta ;$$

$$\beta_5 = \int_0^{\infty} \left(\frac{dU^*}{d\eta}\right)^2 d\eta ; \quad \beta_6 = \int_0^{\infty} \left(\frac{dU^*}{d\eta}\right)^2 \eta d\eta ;$$

$$\gamma_2 = \int_0^{\infty} U^{*2}(\xi) \xi d\xi ; \quad \gamma_4 = \int_0^{\infty} U^{*3}(\xi) \xi d\xi ;$$

$$\gamma_6 = \int_0^{\infty} \left(\frac{dU^*}{d\xi}\right)^2 \xi d\xi ;$$

$$I_1 = \int_0^{\infty} U^* (\overline{u^{*2}} + \overline{v^{*2}} + \overline{w^{*2}}) \xi d\xi ;$$

$$I_2 = \int_0^{\infty} (\overline{u^{*3}} + \overline{u^{*2}v^{*2}} + \overline{u^{*2}w^{*2}}) \xi d\xi ;$$

$$I_3 = \int_0^{\infty} \overline{u^{*2}p^{*2}} \xi d\xi ;$$

$$I_4 = \int_0^{\infty} \overline{u^{*2}v^{*2}} \frac{dU^*}{d\xi} \xi d\xi ;$$

$$I_5 = \int_0^{\infty} \left\{ \left(\frac{\partial u^*}{\partial x}\right)^2 + \left(\frac{\partial v^*}{\partial x}\right)^2 + \left(\frac{\partial w^*}{\partial x}\right)^2 + \left(\frac{\partial u^*}{\partial y}\right)^2 + \left(\frac{\partial v^*}{\partial y}\right)^2 + \left(\frac{\partial w^*}{\partial y}\right)^2 \right\} \xi d\xi ;$$

$$\text{and } I_6 = \int_0^{\infty} \frac{1}{\xi} \left\{ \overline{v^{*2}} + \overline{w^{*2}} + 2\overline{v^* \frac{\partial w^*}{\partial \xi}} - 2\overline{w^* \frac{\partial v^*}{\partial \xi}} + \left(\frac{\partial u^*}{\partial \xi}\right)^2 + \left(\frac{\partial v^*}{\partial \xi}\right)^2 + \left(\frac{\partial w^*}{\partial \xi}\right)^2 \right\} d\xi$$

S. S. Kapur and P. J. Morris
Lockheed-Georgia Company
Marietta, Georgia

1-6.1 Introduction

The aim of this work is to extend the model proposed by Morris⁽¹⁾, for the large-scale noise-producing structure of an axisymmetric jet, to include the effects of compressibility. In view of the simplicity afforded by a rectangular coordinate system the first look at compressible flow has been chosen to be a two-dimensional compressible free shear layer.

The basic philosophy behind this model for the turbulence has been discussed in Section 1-5 and further elaboration is not felt to be necessary here. However, in order to properly account for changes in the turbulent structure as, for example, the temperature of the flow increases or the Mach number changes, it is essential to consider the full compressible problem. If the turbulence, as a source of noise, is taken as incompressible, Crow⁽²⁾ has shown that this so-called 'Liepmann approximation' leads to errors in calculation of the radiated noise.

The first stage in the extension of the model to include compressibility is to demonstrate the ability to formulate and solve the relevant differential and integral problems analogous to those of Section 1-5. This has been done and the results are presented below. This exercise has been formulated only to demonstrate the ability to solve compressible flow problems and is the stepping-stone to the problem of the axisymmetric compressible jet flow problem. In view of this, only a limited amount of calculations have been performed and a detailed model of the large-scale structure has not been obtained.

In this study the mean flow is two-dimensional and is assumed to be compressible as well as viscous. Both of these considerations add a degree of complexity to the formulation of the mathematical model. The dependent variables in the problem are the fluctuating components of the velocity, the density, pressure and temperature. To solve these, the internal energy equation and the equation of state have to be considered as well as the momentum equations and the equation of continuity. The viscosity is assumed to be a function of the varying temperature.

In order to determine the structure of the finite amplitude organized disturbances, all flow quantities are separated into three components; a time-averaged component, an organized fluctuation component and a disorganized random component. The effect of this disorganized motion has been represented in this study of organized turbulence through the use of an eddy viscosity and an eddy thermal conductivity. The downstream growth of the shear layer thickness and the amplitude can be described, through an integral formulation of the equations of continuity, momentum and energy in terms of local transverse distribution of fluctuation quantities. This is described in Section 1-6.2. By assuming the flow to be locally parallel, the local transverse distribution of fluctuations can be determined

through an eigenvalue analysis of spatially unstable modes described in 1-6.3. A discussion of numerical results is included in Section 1-6.4.

In the following, the starred quantities refer to dimensional variables whereas non-starred quantities will refer to non-dimensional variables.

1-6.2 Finite Amplitude Effects on Shear Layer Growth

The interaction between mean flow and the finite amplitude disturbances is discussed here, in terms of an integral formulation, where products of the organized fluctuations have been retained. An integral formulation of the type to be described has been used to consider the finite amplitude effects in a laminar compressible wake by Liu and Lees⁽³⁾ and by Ko, Kubota, and Lees⁽⁴⁾ for an incompressible wake. The formulation below for a two-dimensional compressible flow is more general for two reasons. First, the effects of viscosity varying with temperature have not been ignored. Secondly, following Reynolds and Hussain⁽⁵⁾, the total flow quantities have been separated into three parts; viz, mean, organized disturbance and disorganized random disturbance. The effect of the random disturbance has been taken into account by the introduction of an eddy viscosity.

Denoting a flow quantity by q , we define

$$q = \bar{q} + \tilde{q} + q', \quad (2.1)$$

where bar, tilde and prime refer to the mean, the organized disturbance and random disturbance components of the flow. Averaging over a long time interval determines \bar{q} . Then, the phase average $\langle q \rangle$, i.e. the average over a large ensemble of points having the same phase, is

$$\langle q \rangle = \bar{q} + \tilde{q}$$

That is, it is assumed that the phase average of the random motion for a large ensemble is zero. From these definitions, several properties can be easily deduced, for example,

$$\overline{\tilde{q}} = \overline{q'} = \langle q' \rangle = 0$$

For each of the continuity, momentum and energy equations the flow quantities q can be replaced by the form given in equation (2.1). The time average of the equations then provides the corresponding equation for the mean flow. Subtraction of the mean flow equations from the phase averaged equation provides the equation for the organized disturbance.

In order to simplify the model to be presented here, it will be assumed that the temperature of the two streams is equal. It will also be assumed that the mean flow profile may be defined in terms of a shape function whose derivative in the transverse direction is symmetric about the x -axis. It will be seen that the development of the shear layer and the organized fluctuations can be determined by the use

of two integral equations. These are the mean mechanical energy equation and the disturbance kinetic energy equation.

The mean kinetic energy equation is derived by eliminating the pressure term from the mean momentum equations and multiplying the resulting momentum equation by \bar{u} . After application of the appropriate boundary-layer approximations and after non-dimensionalization, we obtain:

$$\begin{aligned} \frac{\partial}{\partial x} \left[\bar{\rho} \frac{1}{2} \bar{u} (\bar{u}^2 - 1) + \bar{\rho} \bar{u} (\bar{u}^2 - \bar{v}^2) + \bar{u} (\bar{\rho} \bar{u}^2 - \bar{\rho} \bar{v}^2) \right] \\ + \frac{\partial}{\partial y} \left[\bar{\rho} \frac{1}{2} \bar{v} (\bar{u}^2 - 1) + \bar{\rho} \bar{u} \bar{u} \bar{v} + \bar{u} \bar{\rho} \bar{u} \bar{v} - \bar{u} T_{12} \right] \\ - \left[\bar{\rho} (\bar{u}^2 - \bar{v}^2) + \bar{\rho} \bar{u}^2 - \bar{\rho} \bar{v}^2 \right] \frac{\partial \bar{u}}{\partial x} \\ - \left[\bar{\rho} \bar{u} \bar{v} + \bar{\rho} \bar{u} \bar{v} - T_{12} \right] \frac{\partial \bar{u}}{\partial y} = 0 \end{aligned} \quad (2.2)$$

where T_{12} is given by,

$$T_{12} = \left(\frac{\mu}{R_0} + \frac{1}{R_T} \right) \frac{\partial \bar{u}}{\partial y} + \frac{1}{R_0} \frac{d\mu}{dt} \bar{T} \left(\frac{\partial \bar{u}}{\partial y} + \frac{\partial \bar{v}}{\partial y} \right) \quad (2.3)$$

Here the kinematic Reynolds number is given by,

$$R_0 = \rho_0 \frac{u_0 d_0}{\mu_0} \quad (2.4)$$

and the turbulent Reynolds number is given by,

$$R_T = \frac{u_0 d_0}{\bar{e}_T} \quad (2.5)$$

where the coefficient of eddy viscosity \bar{e}_T is given by

$$\bar{\rho} \overline{u_i^* u_j^*} = - \bar{e}_T \bar{t}_{ij}^* \quad (2.6)$$

with t_{ij}^* , the rate of strain tensor given by

$$t_{ij}^* = 2 e_{ij}^* + \frac{2}{3} \left(\frac{\mu_0^*}{\mu^*} - 1 \right) e_{kk}^* \delta_{ij}$$

and

$$e_{ij}^* = \frac{1}{2} (\partial u_i^* / \partial x_j^* + \partial u_j^* / \partial x_i^*).$$

μ_0^* is the second coefficient of viscosity and its ratio to μ^* is assumed constant. The eddy viscosity \bar{e}_T in (2.5) describes the effect of background turbulence on the mean flow. Noting the results of Reynolds and Hussain⁽⁵⁾, its value is taken to be independent of the transverse coordinate y as a first approximation.

The time-averaged organized disturbance kinetic energy equation is derived by multiplying the x and y disturbance momentum equations by \bar{u} and \bar{v} respectively and adding. Using the normal boundary layer approximations, the non-dimensionalized form of the

equation can be shown to be,

$$\begin{aligned} \frac{\partial}{\partial x} \left[(\bar{\rho} + \bar{\rho}') (\bar{u} + \bar{u}') \frac{1}{2} (\bar{u}^2 + \bar{v}^2) \right] \\ + \frac{\partial}{\partial y} \left[(\bar{\rho} + \bar{\rho}') (\bar{u} + \bar{u}') \frac{1}{2} (\bar{u}^2 + \bar{v}^2) \right] \\ + \left[\bar{\rho} (\bar{u}^2 - \bar{v}^2) + \bar{\rho} \bar{u}^2 - \bar{\rho} \bar{v}^2 \right] \frac{\partial \bar{u}}{\partial x} \\ + \left[\bar{\rho} \bar{u} \bar{v} + \bar{\rho} \bar{u} \bar{v}' \right] \frac{\partial \bar{u}}{\partial y} = \bar{\phi} - \frac{1}{\gamma_1 M_1^2} \bar{u} \frac{\partial \bar{p}}{\partial x} + \bar{v} \frac{\partial \bar{p}}{\partial y}, \end{aligned} \quad (2.9)$$

where, using summation convention,

$$\bar{\phi} = \bar{u}_i \frac{\partial}{\partial x_j} \bar{T}_{ij}$$

$$T_{ij}^* = (\mu^* + \bar{e}_T) t_{ij}^* \quad (2.10)$$

$$\bar{\rho} \overline{< u_i^* u_j^* >} - \overline{u_i^* u_j^*} = - \bar{e}_T \bar{t}_{ij}^*. \quad (2.11)$$

\bar{e}_T in (2.9) is an equivalent definition of eddy viscosity describing the effect of background turbulence on the organized disturbance. For the reasons discussed in Section 1-5 the values of \bar{e}_T and \bar{e}_T^* are taken to be equal.

The integral form of equation (2.2) and (2.9) can be obtained by eliminating y through integration from the lower edge of the shear layer to the upper edge. The range of integration can, however, be extended from $-\infty$ to $+\infty$ by noting that the integrands vanish outside the disturbed region.

1-6.3 Shape Assumptions for the Organized Motion

In order to evaluate the integrals involving fluctuations in equations (2.2) and (2.9), it is necessary to describe the transverse distributions of the fluctuations.

Following Liu and Lees⁽³⁾, we introduce local 'stretched' coordinates x' and y' given by

$$x' = x/b \quad (3.1)$$

$$y' = \frac{1}{b} \int_y^{\infty} \rho dy$$

The fluctuations are assumed to take the form

$$\begin{aligned} \bar{u} &= \Lambda(x) f(y') \exp(-i\omega't') + \text{conjugate} \\ \bar{v} &= \Lambda(x) \alpha' \phi(y') \exp(-i\omega't') + \text{conjugate} \\ \bar{\rho} &= \Lambda(x) r(y') \exp(-i\omega't') + \text{conjugate} \\ \bar{p} &= \Lambda(x) \pi(y') \exp(-i\omega't') + \text{conjugate} \\ \bar{T} &= \Lambda(x) \zeta(y') \exp(-i\omega't') + \text{conjugate} \end{aligned} \quad (3.2)$$

where $A(x)$ is the amplitude of the disturbance. The primes have been used to indicate that the quantity has been non-dimensionalized with respect to the local thickness b . It is assumed that the local derivative of A with respect to x' is $\alpha' A + O(|A|^2)$.

Substituting these relations in equation (2.2) and (2.9), one can easily obtain

$$\frac{d}{dx} [b I_1 + b |A|^2 I_2] = - I_3 - |A|^2 \left(\frac{db}{dx} I_3 + I_4 + I_4 \right) \quad (3.3)$$

and

$$\frac{d}{dx} [b |A|^2 I_6 + b |A|^2 I_7] = |A|^2 \left(\frac{db}{dx} I_3 + I_4 - I_9 + I_{10} + I_{11} \right) \quad (3.4)$$

where I_K are integrals involving the mean velocity and the shape parameters, given in Appendix 1-6A. These integrals can be evaluated at any downstream distance x , by determining the transverse distributions of the eigenfunctions from the locally parallel flow theory. Thus, after specifying the initial values of the unknown quantities b and $|A|^2$, their downstream growth can be determined by integrating the differential equations (3.3) and (3.4).

The solutions of the equations for the fluctuations are given in the next section.

1-6.4 Eigenvalue Analysis for a Two-Dimensional, Compressible, Turbulent Free-Mixing Layer

The eigenvalue analysis for unstable modes in an incompressible, two-dimensional free-mixing layer has previously been performed by Lessen⁽⁶⁾ and Morris⁽⁷⁾ among others. The extension of this work to compressible, viscous flows has now been carried out. Apart from the mathematical complexities introduced by the compressible and viscous nature of the problem, the major difference between the two analyses is that the single fourth order differential equation for the fluctuating viscous stream function in the incompressible analysis, is replaced for the present problem by three second order ordinary differential equations for the fluctuating axial velocity, pressure and temperature. Using the fact that a three parameter analytic solution can be found on either side of the disturbed region, the eigenvalue problem consists of finding a single parametric family of solutions which will integrate from the solution on the upper side to a solution on the lower side. Again, the effect of the background turbulence on the organized motion has been described using an eddy viscosity and an eddy thermal conductivity coefficient.

The problem to be considered is that of finding eigenvalues for spatially growing two-dimensional modes in a compressible, turbulent free-mixing layer sketched in Figure 1. The equations which describe the fluctuations are the organized disturbance equations for continuity, x , y -momentum

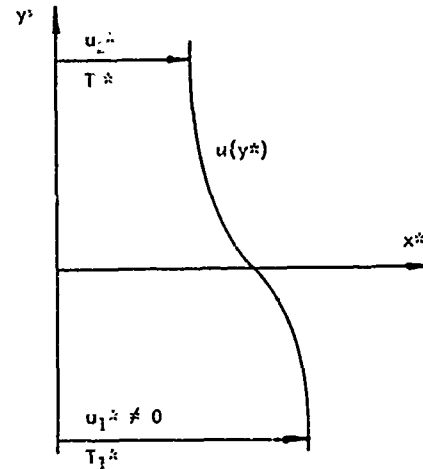


Fig. 1 Coordinate System for Two-Dimensional Shear Layer

equations, internal energy and equation of state. As before, the disturbance equations are derived by subtracting the time-averaged mean equation from the phase averaged equation. The mean flow has been defined in terms of the shape function; i.e., mean velocity is known as a function of position, and the coefficients of viscosity, thermal conductivity and specific heat are described as functions of mean temperature.

The disturbance equations are linearized by assuming that the product of fluctuation quantities is small. Further simplification is introduced by assuming that the mean flow is locally parallel which allows one to ignore the transverse mean velocity components as well as the derivatives, with respect to x , of the mean flow quantities. The fluctuations \tilde{u}^* and \tilde{k}^* in the viscosity and thermal conductivity are approximated as follows,

$$\tilde{u}^* = \frac{d\tilde{u}^*}{dT^*} \tilde{T}^*$$

$$\tilde{k}^* = \frac{d\tilde{k}^*}{dT^*} \tilde{T}^*$$

The eddy viscosity coefficient is introduced as in (2.9). The eddy thermal conductivity coefficient is defined as follows

$$\tilde{\rho}^* (\langle u_1^* T^* \rangle - \overline{u_1^* T^*}) = - k_T \frac{\partial \tilde{T}}{\partial x_1^*}$$

The eddy coefficient ϵ_T and k_T are related to each other by using a turbulent Prandtl number, P_T , defined by

$$P_T = \frac{\epsilon_T C_p^*}{k_T}$$

The 'stretched coordinate' introduced in Section 1-6.3 will be used, that is, the independent vari-

ables x, y are transformed into x', y' by using equation (3.1). The equations are non-dimensionalized with respect to the local shear layer width b .

By introducing the Fourier transforms $r, f, \alpha \phi, \tau$ and ξ of the disturbance quantities $\tilde{\rho}, \tilde{u}, \tilde{v}, \tilde{p}$ and \tilde{T} respectively, we can reduce the partial differential equations of the fluctuations to a set of ordinary differential equations. These equations are given in Appendix 1-6B. Introducing the vector Z of unknowns, as defined below, one can obtain a linear, homogeneous, system of six differential equations

$$Z' = A Z \quad (4.1)$$

where

$$Z = [f, f', \phi, \pi/\gamma_1 M_1^2, \xi, \xi']^T$$

$$A = [a_{ij}], \quad i, j = 1, 6$$

Here, prime denotes differentiation with respect to y' , γ_1 is the ratio of specific heats of the high speed stream, and M_1 is the Mach number of the high speed stream. The coefficients, a_{ij} , are complex expressions involving a single unknown, the parameter c , which is the ratio of real frequency to the complex wave number.

To describe the boundary conditions necessary to solve for Z , equation (4.1) is examined at either side of the shear layer. Since steady state conditions prevail on either side, the matrix A reduces to a constant function of the parameter c . Thus, if λ_i are the eigenvalues of A , the most general solution of (4.1) in the far region is of the form

$$Z = \sum_{i=1}^6 a_i Z_i$$

where $Z_i = w_i e^{\lambda_i y'}$, w_i being the eigenvector corresponding to the eigenvalue λ_i . a_i are arbitrary constants. However, it can be easily determined that the eigenvalues occur as $\pm \lambda_i$ pairs. Thus, depending on the sign of the real part, three of the solutions which do not satisfy the boundary conditions but increase with distance from the shear layer must be discarded. Only three solutions satisfy the boundary conditions on either side. Let Z_1^+, Z_2^+, Z_3^+ and Z_1^-, Z_2^-, Z_3^- be the solutions above and below the mixing layer, respectively.

Because of the homogeneous, linear nature of the differential equation (4.1), it is clear that if Z_1, Z_2, Z_3 are integrated solutions corresponding to initial values Z_1^+, Z_2^+, Z_3^+ , then $a_1 Z_1 + a_2 Z_2 + a_3 Z_3$ is also a solution corresponding to initial condition $a_1 Z_1^+ + a_2 Z_2^+ + a_3 Z_3^+$. Thus, in order to match the boundary conditions at the lower edge, one must have

$$a_1 Z_1 + a_2 Z_2 + a_3 Z_3 = b_1 Z_1^- + b_2 Z_2^- + b_3 Z_3^-$$

In other words, this homogeneous linear 6×6 system must have a non-trivial solution. The values of the parameter c , for which this condition of non-triviality can be met, are the eigenvalues of the

problem. An iterative procedure can now be set up to find the eigenvalues.

1-6.5 Results and Discussion

Before considering the solutions to the integral equations for the development of the shear layer and the growth of the organized fluctuations, we will look at some solutions of the stability equations derived in Section 1-6.4.

The axial behavior of an infinitesimal disturbance in a parallel shear flow is governed by its complex wavenumber, α . For a fluctuation component of frequency ω the change in amplitude as a function of axial distance depends on the imaginary part of its wavenumber. We will consider the problem of a two-dimensional parallel shear layer where the mean velocity profile can be represented by,

$$u(y) = .5 [1 - \tanh(y)] \quad (5.1)$$

and the mean temperature profile takes a similar form. The amplification factor $-\alpha_i$ is shown as a function of frequency for several flow conditions in Figure 2. The inviscid, isothermal incompressible curve gives the greatest amplification. Increasing the Mach number to 1 reduces the maximum amplification rate by 30 per cent. Increasing the high speed stream temperature to 2.54 times that of the ambient air for the same Mach number does not decrease the amplification rate further but shifts the frequency at which maximum amplification is reached to a lower value. It also stabilizes the higher frequencies.

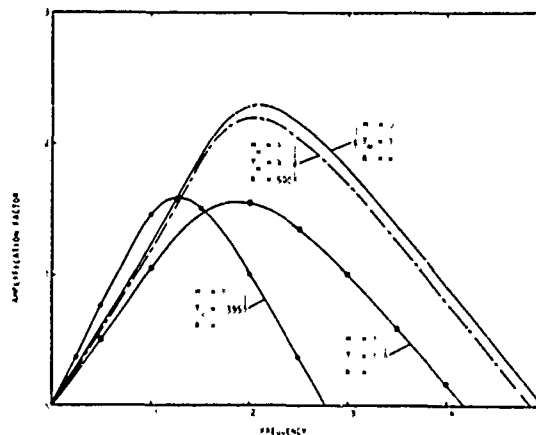


Fig. 2 Curves of Amplification Rate Against Frequency for Compressible 2-D Shear Layer

Let us now look at the results for the finite amplitude organized disturbances. The Mach number of the moving stream is taken to be 0.50883 and both the moving stream and the ambient air have the same temperature. The turbulent Reynolds number defined in the same manner as in Section 1-5 is a constant throughout the flow of value 50. The mean velocity profile is given by

$$u(y') = .5 [1 - \tanh(y')] \quad (5.2)$$

where y' is defined in equation (3.1). The local amplification factor $-\alpha_i'$ is shown as a function of

the local frequency ω' in Figure 3. The maximum amplification occurs for a local frequency of .176 and the neutral mode occurs at a local frequency of 388. Since the local frequency ω' is given by

$$\omega' = \omega b \quad (5.3)$$

a frequency component of fixed frequency ω will pass through growing, neutral and decaying stages as b increases.

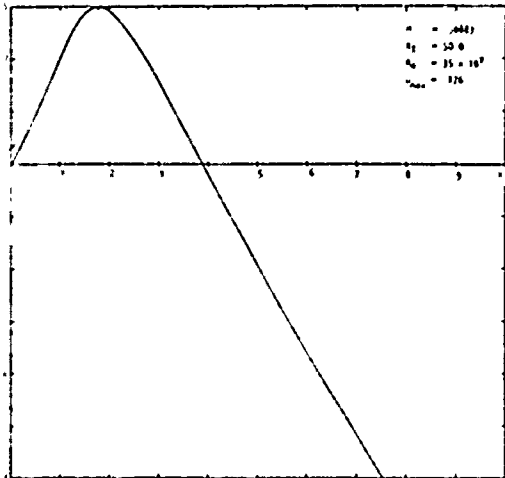


Fig. 3 Local Amplification Rate $-a_i$, as a Function of Local Frequency

In the same manner as for the incompressible problem, the organized motion is considered to be locally dominated by the most highly amplified mode. The transverse distributions of the mean square axial and radial velocity fluctuations and the shear stress parameter \overline{uv} for the most amplifying mode are shown in Figure 4. The phase velocity as a function of frequency is shown in Figure 5. The phase velocity of both the most amplifying mode and the neutral mode is .5.

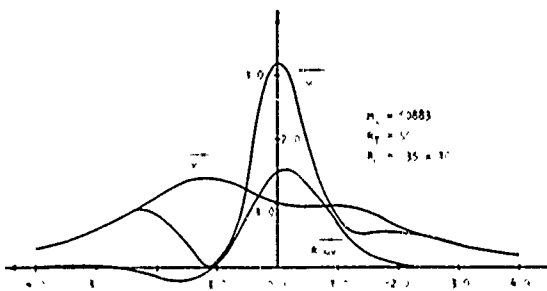


Fig. 4 $\overline{|u'|^2}$, $\overline{|v'|^2}$, \overline{uv} Distributions for Most Amplifying Mode

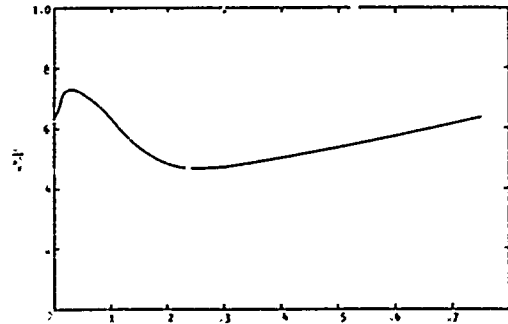


Fig. 5 Phase Velocity as a Function of Frequency

Using the distributions for the most amplifying mode the integrals in equations (3.3) and (3.4) may be evaluated and the development of the shear layer can be found for various initial conditions. The amplitude of the fluctuations as a function of downstream distance is shown in Figure 6 for various initial amplitudes. It can be seen that in spite of a change in initial amplitude of one thousand times the limiting amplitude of the disturbances is the same. The growth of the shear layer width for an initial disturbance amplitude of 1×10^{-6} is shown in Figure 7. After an initial transition region the width increases linearly with axial distance. The location of most amplifying frequencies is shown in Figure 8. The high frequencies dominate at small shear layer widths whereas the lower most amplifying frequencies are inversely proportional to their axial location.

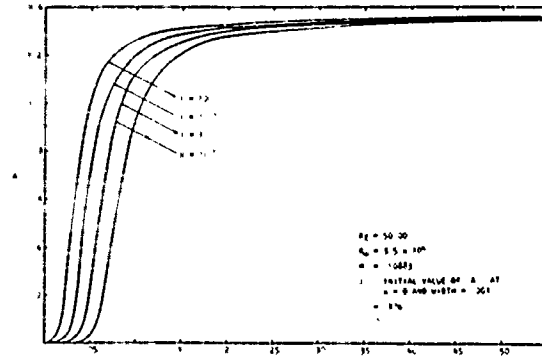


Fig. 6 Growth of Amplitude with Downstream Distance

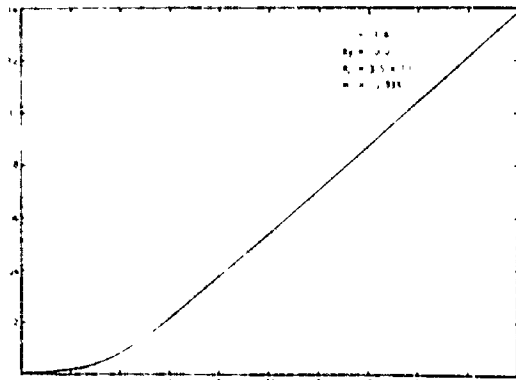


Fig. 7 Growth of Shear Layer Width with Downstream Distance

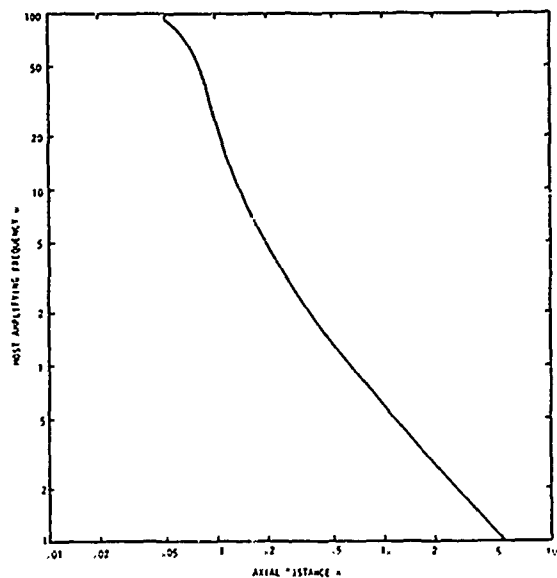


Fig. 8 Most Amplifying Frequencies for Two-Dimensional Disturbances as a Function of Downstream Distance

1-6.6 Conclusions

A differential and integral formulation has been carried out to describe the development of a two-dimensional compressible shear layer. The organized structure at any axial location has been determined from the most amplifying eigensolution to the viscous compressible stability equations.

Future work will

(i) examine the effect of three-dimensional disturbances in the two-dimensional compressible shear layer, and

(ii) extend the compressible flow solutions to an axisymmetric compressible jet.

Notation

$A(x)$	amplitude of organized fluctuation
b	shear layer width
c	eigenvalue, $= \omega/\alpha$
C_p	specified heat at constant pressure
C_v	specific heat at constant volume
f	axial velocity fluctuation shape function
I_j	integral functions of fluctuations
M	Mach number
p	pressure
P_T	turbulent Prandtl number
q	typical dependent variable

\bar{q}	mean value
\bar{q}	organized fluctuation
q'	random fluctuation
r	density fluctuation shape function
R_0	kinematic Reynolds number
R_T	turbulent Reynolds number
T	temperature
u, v	axial and transverse velocities
(x, y)	axial and transverse coordinates
(x', y')	stretched coordinates
α, α'	wavenumber and local wavenumber
$\alpha'\phi$	transverse velocity fluctuation shape function
γ	ratio of specific heats
ϵ_T	coefficient of eddy viscosity
k_T	coefficient of eddy thermal conductivity
ω, ω'	frequency and local frequency
π	pressure fluctuation shape function
ρ	density
ξ	temperature fluctuation shape function

References

- Morris, P. J., A model for the structure of jet turbulence as a source of noise. AIAA Paper 74-1, 1974.
- Crow, S. C., Aerodynamic sound emission as a singular perturbation problem. Studies in Appl. Maths. V. XLIX, p. 21, 1970.
- Liu, J. T. C. and Lees, L., Finite amplitude instability of the compressible laminar wake. Strongly amplified disturbances. Phys. Fluids V. 13, p. 2932, 1970.
- Ko, D. R-S., Kubota, T. and Lees, L., Finite disturbance effect on the stability of a laminar incompressible wake behind a flat plate. J. Fluid Mech. V. 40, p. 315, 1970.
- Reynolds, W. C. and Hussain, A. K. M. F., The mechanics of an organized wave in turbulent shear flow. Part 3. Theoretical models and comparisons with experiments. J. Fluid Mech. V. 54, p. 263, 1972.
- Lessen, M. and Ko, S-H., Viscous instability of an incompressible fluid half-jet flow. Phys. Fluids V.9, p. 1179, 1966.
- Morris, P. J., The structure of turbulent shear flow. Univ. of Southampton, Ph.D. Thesis, 1971.

APPENDIX I-6A

Definition of Integrals in Equations 3.3 and 3.4

$$I_1 = \int_{-\infty}^{\infty} \frac{1}{2} u(u^2 - 1) dy'$$

$$I_2 = \int_{-\infty}^{\infty} u [|f|^2 - |\alpha'\phi|^2] dy'$$

$$I_3 = \int_{-\infty}^{\infty} y' [|f|^2 - |\alpha'\phi|^2] \frac{\partial u}{\partial y'} dy'$$

$$I_4 = - \int_{-\infty}^{\infty} \rho R [f \overline{\alpha'\phi}] \frac{\partial u}{\partial y'} dy'$$

$$I_5 = \int_{-\infty}^{\infty} \left(\frac{\mu}{R_0} + \frac{1}{R_T} \right) \frac{\partial u}{\partial y'} dy'$$

$$I_6 = \int_{-\infty}^{\infty} \frac{1}{2} u [|f|^2 + |\alpha'\phi|^2] dy'$$

$$I_7 = \int_{-\infty}^{\infty} \frac{1}{2\rho} R [r f \overline{\alpha'\phi} + 2 r \bar{f} |\alpha'\phi|^2 + 3 r \bar{f} |f|^2] dy'$$

$$I_9 = \int_{-\infty}^{\infty} \frac{1}{R_0} \frac{du}{dT} R [f' \bar{\xi} - \frac{i}{\rho} \overline{\alpha' \xi} \overline{\alpha'\phi}] dy'$$

$$I_{10} = \int_{-\infty}^{\infty} -\frac{1}{\rho} \left(\frac{\mu}{R_0} + \frac{1}{R_T} \right) \{ k_2 (|\alpha'f|^2 + \rho^2 |\alpha'\phi|^2) + |\alpha'^2 \phi|^2 + \rho^2 |f|^2 + (k_1 + 1) \rho R [i \alpha' f \overline{\alpha'\phi} - i \overline{\alpha' f} \overline{\alpha'\phi}] \} dy'$$

$$I_{11} = - \frac{1}{\gamma_1 M_1^2} \int_{-\infty}^{\infty} R \left[\pi' \overline{\alpha'\phi} + \frac{i \alpha'}{\rho} \pi \bar{f} \right] dy'$$

$$k_1 = \frac{2}{3} \left(\frac{\mu_2^*}{\mu^*} - 1 \right), \quad k_2 = k_1 + 2$$

$$R_0' = b R_0, \quad R_T' = b R_T, \quad \alpha' = b \alpha$$

APPENDIX I-6B

Governing Equations of Motion

1. Continuity

$$i(u - c) r + \rho(\rho\phi' + i f) + \rho\rho'\phi = 0$$

2. x-Momentum Equation

$$i(u - c) \alpha f + \rho \alpha u' \phi = - \frac{i \alpha}{\rho} \frac{\pi}{\gamma_1 M_1^2} + \frac{1}{R_2} \left[- \frac{k_2}{\rho} \alpha^2 f + i(k_1 + 1) \alpha^2 \phi' + \alpha f'' + \rho' f' \right] + \frac{1}{R_0} [(\rho u'' + \rho' u') s + \rho u' s' + (\rho f' + i \alpha^2 \phi) \frac{du}{dT} T']$$

where,

$$s = \frac{du}{dT} \xi$$

$$\frac{1}{R_2} = \frac{\mu}{R_0} + \frac{1}{R_T}$$

$$k_1 = \frac{2}{3} \left(\frac{\mu_2^*}{\mu^*} - 1 \right)$$

$$k_2 = k_1 + 2$$

3. y-Momentum Equation

$$i(u - c) \alpha^2 \phi = - \frac{\pi'}{\gamma_1 M_1^2} + \frac{\alpha}{R_2} [i(k_1 + 1) f - \frac{\alpha^2}{\rho} \phi + k_2 (\rho \phi'' + \rho' \phi')] + \frac{\alpha}{R_0} [i u' s' + \frac{du}{dT} T' (i k_1 f + \rho k_2 \phi')]$$

4. Internal Energy Equation

$$\rho c_v [i(u - c) \xi + \alpha \phi T'] \alpha = \frac{\rho \gamma_1}{\sigma_1 R_0} \left[- \frac{\alpha^2}{\rho} k_t \xi + (\rho k_t \xi' + \rho \frac{dk}{dT} T') \right] - \alpha (\gamma_1 - 1) \rho [i f + \phi'] + \frac{\gamma_1 (\gamma_1 - 1) M_1^2}{R_0} u' [s u' + 2 \mu (\rho f' + i \alpha^2 \phi)]$$

where

$$k_t = k + \frac{\sigma_1 R_0}{\sigma_T \gamma_1 R_T} c_v.$$

σ_T is the turbulent Prandtl number, defined as

$$\sigma_T = \frac{c_T^* C_p^*}{k_T^*},$$

c_T^* and k_T^* being the eddy viscosity and eddy thermal coefficients respectively.

In the above equations, the primes denote the derivatives with respect to y' , as defined in (3.1). Furthermore, all non-dimensionalization has been carried through with respect to the local thickness, b . Thus, the symbols $\alpha_1 R_0$ as used here correspond to the symbols $\alpha_1 R_0'$ in Appendix I-6A. For simplicity, the bars over the mean flow quantities have also been dropped.

1-7 THE MOMENTUM POTENTIAL FIELD DESCRIPTION OF FLUCTUATING FLUID MOTION
AS A BASIS FOR A UNIFIED THEORY OF INTERNALLY GENERATED SOUND

P. E. Doak†‡

Institute of Sound and Vibration Research
University of Southampton
Southampton SO95NH, England

Abstract

A new, concise, exact expression for the scalar momentum potential of a time-stationary, but otherwise arbitrary, fluid flow is derived and discussed. The expression is shown to lead to a generalized analog of the Landahl-Lilley equation, which is presently being used as a basis of studies of local and radiated pressure fluctuations associated with turbulent shear flows.

1-7.1 Introduction

In recent publications(1-4) results of initial investigations of the momentum potential field description of fluctuating fluid motion as a basis for a unified theory of internally generated sound have been reported. In particular, equations describing, to quite a good approximation for many purposes, both the generation and propagation of pressure fluctuations associated with turbulent flows, such as jet flows, have been derived and some of their properties and implications have been investigated and discussed.

In the work reported here, a new expression for these purposes, which is both exact and symbolically much more concise than the previous approximate expressions, has been obtained. Also, this expression leads naturally to an exact, generalized analog of the Landahl-Lilley equation. These expressions provide some new insights into the nature of the local physical processes which result in production of "sound generated aerodynamically" by fluctuating fluid flows.

1-7.2 Momentum Potential Theory:
Basic Definitions

In the momentum potential formulation of problems of fluctuating fluid motion, the linear momentum density, rather than the velocity, is regarded as the primary dependent vector field to be determined in terms of space and time coordinates. It is expressed, by means of Helmholtz's theorem, as a linear superposition of unique solenoidal and irrotational components:

$$\rho v_i(x_k, t) \equiv B_i - \partial\psi/\partial x_i, \quad (1)$$

$$\partial B_i/\partial x_i \equiv 0. \quad (2)$$

Here, ρ is the mass density, v_i the fluid velocity, x_k the Cartesian position coordinates, t the time, and ψ is the scalar momentum potential. B_i is the unique solenoidal component of the linear momentum density and $-\partial\psi/\partial x_i$ is the unique irrotational component (uniqueness of these components, of course, is fully guaranteed only after application of appropriate boundary conditions in each particular situation).

From the mass transport equation, the mass density can be expressed in terms of the scalar momentum potential only, and thus is explicitly independent of the solenoidal momentum field:

$$\partial\rho/\partial t = \partial^2\psi/\partial x_i^2. \quad (3)$$

Also, from the mass transport equation (3) it follows that when the flow is time-stationary (that is when each scalar and vector field variable can be expressed as a sum of a time averaged component and a purely fluctuating component of zero time average), then the time average of the scalar potential is both irrotational and solenoidal: i.e.,

$$\partial^2\bar{\psi}/\partial x_i^2 = 0,$$

where the overbar indicates the time average (or mean). Any vector field that is both irrotational and solenoidal can be expressed in terms of either a scalar potential or a vector potential, both satisfying (in Cartesian coordinates) Laplace's equation. Therefore, it follows that for time-stationary flows, without any loss of generality, the mean value of the scalar momentum can be taken as zero, so that the scalar momentum potential becomes a purely fluctuating quantity, and the mean value of the irrotational momentum component, B_i , then includes all of the mean field that is both solenoidal and irrotational. The mass transport equation thus becomes, for time-stationary flows,

$$\partial\rho'/\partial t = \partial^2\psi'/\partial x_i^2, \quad (4)$$

(the primes indicating purely fluctuating quantities) and the definition of the linear momentum density components, equations (1) and (2), can be rewritten as

†Hawker Siddeley Professor of Acoustics.

‡Consultant, Lockheed-Georgia Company, Aeroacoustics Research and Technology Laboratory, where much of the work reported was carried out during August 1973.

$$\rho v_i(x_k, t) \equiv \bar{B}_i(x_k) + B_i'(x_k, t) - \partial\psi'(x_k, t)/\partial x_i, \quad (5)$$

$$\partial\bar{B}_i/\partial x_i \equiv \partial B_i'/\partial x_i \equiv 0. \quad (6)$$

These results comprise the essential physical and mathematical simplifications, in both concept and analysis, that are introduced by the momentum potential description, especially for time-stationary flows. First, one of the five (scalar) equations specifying the two scalar and one vector dependent fields (say, pressure, entropy and linear momentum density) becomes linear, and involves only the fluctuating quantities [equation (4)]. Second, the vector dependent field can be expressed as a linear combination of three fields: (i) the solenoidal mean field, \bar{B}_i ; (ii) a solenoidal fluctuating field, B_i' , which can meaningfully and unambiguously be called the "vortical" (or, less preferably, the "turbulent") component of the field; (iii) an irrotational fluctuating component, $-\partial\psi'/\partial x_i$, which in turn, if desirable on physical grounds (3), can be expressed as a linear superposition of "acoustic" and "thermal" components.

1-7.3 A Concise, Exact Inhomogeneous Equation for the Scalar Momentum Potential

In previous work (1-3), an equation for the scalar momentum potential was developed which is valid for situations in which the fluctuating thermodynamic quantities are relatively small (i.e. $\rho'/\bar{\rho} \ll 1$ and $p'/\bar{p} \ll 1$, p being the thermodynamic pressure, but all mean quantities and the vortical momentum fluctuations, B_i' , are, a priori, arbitrary). In these previous descriptions all components of the fluctuations -- acoustic, thermal and vortical -- were explicitly identified throughout and their interactions were thus explicitly displayed. The approximate equation previously obtained for the scalar momentum potential is of a generalized convected-wave-equation type, and contains terms explicitly displaying both convective and shear refraction interaction of the scalar potential disturbances with the mean flow and temperature fields.

An exact generalization of this equation can be obtained, as follows. (For convenience and brevity of notation, not all of the interactions among the mean, acoustic, vortical and thermal components of the motion will be explicitly displayed, initially.)

For a Stokesian fluid, the exact equation of linear momentum density transport can be written as (for time-stationary flows)

$$\frac{\partial}{\partial t} (B_i' - \frac{\partial\psi'}{\partial x_i}) + \frac{\partial p}{\partial x_i} + \frac{\partial}{\partial x_j} (\rho v_i v_j - S_{ij}) = 0, \quad (7)$$

where S_{ij} is the viscous stress tensor,

$$S_{ij} \equiv \mu \left(\frac{\partial v_i}{\partial x_j} + \frac{\partial v_j}{\partial x_i} - 2 \frac{\partial v_k}{\partial x_k} \delta_{ij} \right) + \left(\frac{4}{3}\mu + \zeta \right) \frac{\partial v_k}{\partial x_k} \delta_{ij} \quad (8)$$

μ being the coefficient of shear viscosity and ζ that of bulk viscosity, and δ_{ij} is the Kronecker delta ($\delta_{ij} = 0$ when $i \neq j$ and $\delta_{ij} = 1$ when $i = j$).

The irrotational part of equation (7) can be isolated by performance of the vector divergence operation, and the fluctuating part by partial differentiation with respect to time. Performance of these operations yields directly

$$\frac{\partial^2}{\partial x_i^2} \left(\frac{\partial p}{\partial t} - \frac{\partial^2 \psi'}{\partial t^2} \right) + \frac{\partial^2}{\partial x_i \partial x_j} \left\{ v_i \frac{\partial}{\partial t} (\rho v_j) + \rho v_j \frac{\partial v_i}{\partial t} - \frac{\partial S_{ij}}{\partial t} \right\} = 0. \quad (9)$$

By elementary operations, and use of the mass transport equation (4) and the momentum definition (5), the double divergence terms in equation (9) can easily be rearranged as follows:

$$\begin{aligned} \frac{\partial^2}{\partial x_i \partial x_j} \{ \} &= \frac{\partial^2}{\partial x_i \partial x_j} \left\{ v_i \frac{\partial}{\partial t} (\rho v_j) + v_j \frac{\partial}{\partial t} (\rho v_i) \right. \\ &\quad \left. - v_i v_j \frac{\partial \rho}{\partial t} - \frac{\partial S_{ij}}{\partial t} \right\} \\ &= \frac{\partial^2}{\partial x_i \partial x_j} \left\{ 2v_i \frac{\partial}{\partial t} (\rho v_j) - v_i v_j \frac{\partial \rho}{\partial t} - \frac{\partial S_{ij}}{\partial t} \right\} \\ &= - \frac{\partial^2}{\partial x_i \partial x_j} \left\{ 2v_i \frac{\partial \psi'}{\partial t \partial x_j} + v_i v_j \frac{\partial \psi'}{\partial x_k^2} \right\} \\ &\quad + \frac{\partial^2}{\partial x_i \partial x_j} \left(2v_i \frac{\partial B_j}{\partial t} - \frac{\partial S_{ij}}{\partial t} \right). \quad (10) \end{aligned}$$

Finally, provided only an equation of state exists, the pressure time derivative, $\partial p/\partial t$, can always be expressed in terms of the mass density derivative and those of any other appropriate and convenient thermodynamic variables, such as entropy, for example. When the equation of state is that of an ideal gas, an appropriate second thermodynamic variable is the adiabatic variable

$$\sigma \equiv \ln(p/\rho^\gamma), \quad (11)$$

where γ is the ratio of specific heats, $\gamma \equiv C_p/C_v$. The variable σ is obviously closely related to the entropy: variations in σ are in one-to-one correspondence with entropy variations, and vice versa. In terms of ρ and σ , exactly,

$$\frac{\partial p}{\partial t} = c^2 \frac{\partial p}{\partial t} + p \frac{\partial c}{\partial t} = c^2 \frac{\partial^2 \psi'}{\partial x_k^2} + p \frac{\partial c}{\partial t} \quad (12)$$

where c^2 is the instantaneous local speed of sound,

$$c^2 = \gamma p / \rho. \quad (13)$$

Straightforward substitution of expressions (12) and (10) into equation (9) then gives the new, exact equation for the scalar momentum potential:

$$\begin{aligned} & \frac{\partial^2}{\partial x_i^2} \left(c^2 \frac{\partial^2 \psi'}{\partial x_k^2} - \frac{\partial^2 v_i'}{\partial t^2} \right) \\ & - \frac{\partial^2}{\partial x_i \partial x_j} \left(2v_i \frac{\partial^2 \psi'}{\partial t \partial x_j} + v_i v_j \frac{\partial^2 \psi'}{\partial x_k^2} \right) \\ & = - \frac{\partial^2}{\partial x_i \partial x_j} \left(2v_i \frac{\partial B_j}{\partial t} + p \frac{\partial^2 S_{ij}}{\partial t^2} - \frac{\partial S_{ij}}{\partial t} \right). \quad (14) \end{aligned}$$

This exact expression has many very interesting properties in its physical interpretation. Consider first the limiting case of constant mean velocity: i.e., v_i in equation (14) is equal to \bar{V}_i , a constant vector, plus a fluctuating part, v_i' , which is a priori arbitrary. Then equation (14) becomes

$$\begin{aligned} & \frac{\partial^2}{\partial x_i^2} \left(c^2 \frac{\partial^2 \psi'}{\partial x_k^2} \right) - \frac{\bar{D}^2}{Dt^2} \left(\frac{\partial^2 \psi'}{\partial x_k^2} \right) \\ & = - \frac{\partial^2}{\partial x_i \partial x_j} \left(p \frac{\partial^2 S_{ij}}{\partial t^2} - \frac{\partial S_{ij}}{\partial t} + Q'_{ij} \right) \quad (15) \end{aligned}$$

where

$$\bar{D}/Dt \equiv \partial/\partial t + V_i \partial/\partial x_i.$$

In equation (15), the quadrupole fluctuating source strength density tensor, Q'_{ij} , is of quadratic (and higher) order in the fluctuating velocities, v_i' , and/or the mass density fluctuations, ρ' , (or, what is the same thing, quadratic in the mass density fluctuations and/or the fluctuating momentum components, B'_i and $-\partial\psi'/\partial x_i$). The linear term $\partial^2(V_i \partial B_j / \partial t) / \partial x_i \partial x_j$ vanishes because B_j is purely solenoidal. In the absence of mean shear, then, the scalar momentum potential is coupled only quadratically to the vortical momentum fluctuations,

B'_i . (Strictly speaking, the double divergence of the time derivative of the viscous stress tensor, $\partial S_{ij} / \partial t$, on the right side of equation (15), formally throws up some linear coupling terms involving B'_i , but these are usually very small indeed, especially as they depend as well upon gradients of mean mass density and/or the viscosity coefficients.)

Furthermore, in this limiting case of a constant mean velocity, it is clear that equation (15) is simply an inhomogeneous, second order, convected acoustic wave equation for the Laplacian of the scalar momentum potential, $\partial^2 \psi' / \partial x_k^2$, which, by virtue of equation (12) can be replaced by

$$\frac{1}{c^2} \frac{\partial p}{\partial t} - \frac{p}{c^2} \frac{\partial c}{\partial t}.$$

Thus, again exactly, for this limiting case of constant mean flow, equation (15) can be written as

$$\begin{aligned} & \frac{\partial^2}{\partial x_i^2} \left(\frac{\partial p}{\partial t} \right) - \frac{\bar{D}^2}{Dt^2} \left(\frac{1}{c^2} \frac{\partial p}{\partial t} \right) \\ & = - \frac{\partial^2}{\partial x_i \partial x_j} \left(Q'_{ij} - \frac{\partial S_{ij}}{\partial t} \right) - \frac{\bar{D}^2}{Dt^2} \left(\frac{p}{c^2} \frac{\partial c}{\partial t} \right). \quad (16) \end{aligned}$$

Equation (15) thus becomes, in the form of equation (16), an inhomogeneous convected acoustic wave equation for the time derivative of the pressure. The only linear source terms are those arising from irreversible processes (i.e., from S_{ij} and ρ). Further analysis (which will not be described here) readily shows that these simply provide, to first order in the Stokes number [see section 2.1 of reference (2)], the well-known viscous and thermal attenuation of the acoustic pressure waves. The remaining quadratic source terms are dominated by the equivalent quadrupole source strength density tensor Q'_{ij} . The leading terms of this tensor [see equation (14)] are of the form $v_i' \partial B_j / \partial t$, or, when the velocity fluctuations are largely vortical in nature, as in turbulence, $(1/\bar{\rho}) B'_i \partial B'_j / \partial t$.

Apart from the assumption of a constant mean velocity, the results expressed in equations (15) and (16) are exact. No assumptions have been made about the mean or fluctuating behavior of the local instantaneous speed of sound, c^2 (i.e., the temperature), or about the behavior of the adiabatic variable, σ (i.e., the entropy), or about the magnitude of the mean velocity, or about the amplitudes or space-time behavior of any of the fluctuating quantities of primary interest, such as the pressure itself and the velocity fluctuations (i.e. the vortical, "turbulent" fluctuations, B'_i). In this connection, it is interesting to observe that the momentum potential approach yields, for this case of uniform mean velocity, a slightly simpler and more physically satisfying (note, for example, the automatic presence of a quadrupole type of source distribution) description than does Phillips' equation. (See, e.g., section 2.4 of reference (2); further details of the results which can be obtained by comparing equations (14), (15) and (16) with Phillips' equation will not be given here.)

Thus, the pressure fluctuations, in the case of uniform mean flow, but otherwise arbitrary conditions, are, like the scalar momentum potential, only quadratically coupled with (i.e., "driven by") the vortical and/or irrotational momentum (or velocity) fluctuations. Furthermore, this coupling is via a source term of quadrupole type, in a (mean-flow) convected acoustic wave equation.

Again, from the point of view of the physics of the situation, comparison of equation (16) with the Lighthill "acoustic analogy" description of the same situation is instructive. These points will not be pursued further here, however, as much of the ground has already been covered in a previous publication(2). The main conclusion that emerges from such a comparison is simply reinforcement of the need, in the interest of retention of a realistic physical conception of what is actually going on in a moving, turbulent flow, to explicitly display in the theoretical description, as in equation (16), terms that explicitly represent the convection of the pressure disturbances by the mean flow, and the possible contributions to radiated noise by entropy fluctuations.

In sharp contrast to the situation obtaining when the mean flow is uniform, the presence of a mean velocity gradient, in a direction either parallel or transverse to the mean flow direction, results in equation (14) displaying linear coupling of the solenoidal momentum fluctuations with the scalar momentum potential and hence, by inference, with the pressure fluctuations. Of course, if the mean velocity field and the fluctuating solenoidal momentum vector (and the entropy fluctuations, if significant) are known independently, and accurately enough, either from theory or experiment, equation (14) can still then be used, perfectly validly, to calculate the scalar momentum potential, and hence, for example, the near and far field pressure fluctuations associated with a turbulent jet flow, via equation (12). Here it is most interesting to observe that since the linear coupling source term in equation (14) is, exactly,

$$-\frac{\partial}{\partial x_i} \left(2 \frac{\partial \bar{v}_i}{\partial x_j} \frac{\partial B_j}{\partial t} \right),$$

which is a dipole-type source distribution, representing physically a mean shear/vortical fluctuation interaction, it follows that linear coupling of vortical fluctuations to the scalar momentum potential (i.e., "pressure") will only occur importantly in regions where both strong mean shear and strong vortical fluctuations are present. The quadratic coupling, via terms like

$$-\frac{\partial}{\partial x_i} \left(2 \frac{\partial v_i}{\partial x_j} \frac{\partial B_j}{\partial t} \right)$$

(again note that by virtue of the solenoidality of B_j , this term reduces automatically from quadrupole-type source distribution to a dipole-type), which provided the only coupling in the uniform flow case, is, of course, still present as well.

As regards propagation effects of a non-uniform mean flow (as distinct from the generation effects involved in $2\bar{v}_i \partial B_j / \partial t$ on the right side of equation (14)), it is clearly evident that, in the general case, those terms involving the velocity on the left side of equation (14) that are linear in the fluctuations collectively display explicitly all the convection, convective refraction and shear refraction effects on the scalar momentum potential caused by its interaction with the mean flow. Also, of course, the linear term involving \bar{c}^2 on the left side of equation (14), $\bar{c}^2 \partial^2 \psi' / \partial x_k^2$, explicitly represents thermal refraction. Convection, and convective refraction, by the mean flow is explicitly

represented by the terms

$$-2 \bar{v}_i \frac{\partial^2}{\partial x_i \partial t} \left(\frac{\partial^2 \psi'}{\partial x_k^2} \right) - \bar{v}_i \bar{v}_j \frac{\partial^2}{\partial x_i \partial x_j} \left(\frac{\partial^2 \psi'}{\partial x_k^2} \right),$$

pure shear refraction by

$$-2 \frac{\partial \bar{v}_i}{\partial x_j} \frac{\partial}{\partial x_i} \left(\frac{\partial^2 \psi'}{\partial x_j \partial t} \right) - \frac{\partial \bar{v}_i}{\partial x_j} \frac{\partial \bar{v}_j}{\partial x_i} \frac{\partial^2 \psi'}{\partial x_k^2},$$

dilatational "refraction" by terms like

$$-2 \frac{\partial \bar{v}_i}{\partial x_i} \frac{\partial}{\partial t} \left(\frac{\partial^2 \psi'}{\partial x_k^2} \right),$$

and also there are mixed convective-refractive terms like

$$\bar{v}_i \frac{\partial \bar{v}_j}{\partial x_i} \frac{\partial}{\partial x_i} \left(\frac{\partial^2 \psi'}{\partial x_k^2} \right).$$

With only the linear terms on the left side, all the quadratic and higher order terms being represented by an equivalent quadrupole source strength density tensor, M_{ij}^1 , and transferred to the right side (note that each term in M_{ij}^1 , of course, will contain either $\partial^2 \psi' / \partial x_k^2$ or $\partial^2 \psi' / \partial t \partial x_j$ as a factor), equation (14) can be written exactly as

$$\begin{aligned} & \frac{\partial^2}{\partial x_i^2} \left(\bar{c}^2 \frac{\partial^2 \psi'}{\partial x_k^2} - \frac{\partial^2 \psi'}{\partial t^2} \right) \\ & - \frac{\partial^2}{\partial x_i \partial x_j} \left(2 \bar{v}_i \frac{\partial^2 \psi'}{\partial t \partial x_j} + \bar{v}_i \bar{v}_j \frac{\partial^2 \psi'}{\partial x_k^2} \right) \\ & = - \frac{\partial^2}{\partial x_i \partial x_j} \left(2 v_i \frac{\partial B_j}{\partial t} + M_{ij}^1 + \rho \frac{\partial \sigma}{\partial t} \delta_{ij} - \frac{\partial S_{ij}}{\partial t} \right). \quad (17) \end{aligned}$$

Note that, as for the sources in Lighthill's acoustic analogy description, all terms in this equation, and, for that matter, in equation (14), have equivalent "quadrupole source" representations, as double divergences of tensors. Equation (17), incidentally, is not a linearized or otherwise approximated version of the exact equation (14). It is the exact equation simply rewritten in a form such that the left side is linear in the scalar momentum potential (and in all fluctuating quantities generally).

On the computational side, linear partial differential equations with known variable coefficients, of the type of equation (17), can be solved without too much difficulty with the aid of modern analytical and machine-computational techniques. Thus, given knowledge of \bar{c}^2 and \bar{v}_i , say, and sufficiently accurate estimates of the quadrupole type source strength density terms on the right side of equation (17), it is entirely practical to use such an equation for theoretical studies of aerodynamic noise problems and other problems of fluctuating fluid flows.

Finally, although equation (14), the central new result here, is explicitly valid only for an ideal Stokesian fluid, the same procedure can be used, with formally similar results, for studies of time-stationary fluctuations in any continuous medium, provided only that, as in the case here, constitutive relations are available to express fluctuations in the pressure, and in the rest of the stress tensor in the particular medium, in terms of the scalar momentum potential (and other convenient variables, if necessary).

1-7.4 The Generalized Analog of the Landahl-Lilley Equation

It has been pointed out, in the previous section, that the exact scalar momentum potential equation (14) exhibits linear coupling between the scalar momentum potential and the fluctuating solenoidal momentum, whenever the mean flow is either sheared or possesses a gradient in the direction of flow. On the other hand, it is well-known [see, e.g., section 3 of reference (4)] that for the special case of a uni-directional, transversely sheared mean flow, an expression can be derived, the Landahl-Lilley equation, in which the fluctuating pressure (or logarithm of the pressure) exhibits no linear coupling to any other fluctuating quantities.

In previous work [see section 2.3 of reference (3)] it has been proved that, insofar as all linear terms are concerned, the partial time derivative of the Landahl-Lilley equation is equal to the material derivative of the previously obtained approximate version of equation (14) for the scalar momentum potential. It is therefore of interest to re-examine this relationship for the new, exact equation itself.

The comparison can be effected in a very simple manner, which has the advantage of bringing into focus a very close interrelationship between the process of pure shear refraction and the process of linear coupling of the fluctuating pressure (or scalar momentum potential) to other fluctuating variables. The procedure is as follows. When the differentiation with respect to x_j is performed on the first convective-refractive term of equation (14) two terms are obtained:

$$\begin{aligned} & - \frac{\partial^2}{\partial x_i \partial x_j} (2v_i \frac{\partial^2 \psi'}{\partial t \partial x_j}) \\ & = - \frac{\partial}{\partial x_i} (2 \frac{\partial v_i}{\partial x_j} \frac{\partial^2 \psi'}{\partial t \partial x_j}) - \frac{\partial}{\partial x_i} (2 v_i \frac{\partial^3 \psi'}{\partial t \partial x_j^2}). \end{aligned} \quad (18)$$

If the first of these two terms is then transferred to the right side of equation (14), it can be combined with the first term of the right side to give

$$- \frac{\partial}{\partial x_i} [2 \frac{\partial v_i}{\partial x_j} \frac{\partial}{\partial t} (\rho v_j)]. \quad (19)$$

For the case of uni-directional, transversely sheared mean flow, in which the mean mass density may also have a transverse gradient, one has, say,

$$\bar{v}_i = [V_1(x_2), 0, 0],$$

$$\bar{\rho} = \bar{\rho}(x_2).$$

The only linear contribution to expression (19) is then

$$- \frac{\partial}{\partial x_1} [2 \frac{\partial V_1(x_2)}{\partial x_2} \bar{\rho}(x_2) \frac{\partial v_2'}{\partial t}].$$

Operation on this term by the mean flow material derivative, $\bar{D}_1/Dt = \partial/\partial t + V_1(x_2)\partial/\partial x_1$, evidently gives

$$- \frac{\partial}{\partial x_1} [2 \frac{\partial V_1(x_2)}{\partial x_2} \frac{\partial}{\partial t} \{\bar{\rho}(x_2) \frac{D_1 v_2'}{Dt}\}].$$

But from the equations of linear momentum for such a flow,

$$\bar{\rho}(x_2) \frac{D_1 v_2'}{Dt} + \frac{\partial p'}{\partial x_2} - \frac{\partial S_{2k}}{\partial x_k} = 0,$$

to first order. Hence, to first order, and apart from the viscous stress tensor term, the mean flow material derivative of the first term of expression (19), in the case of uni-directional, transversely sheared flow, with mean mass density also varying only in the transverse direction, becomes a pure shear refraction term for pressure, transferable to the left side as

$$- \frac{\partial}{\partial x_i} [2 \frac{\partial v_i}{\partial x_j} \frac{\partial^2 p'}{\partial t \partial x_j}]. \quad (20)$$

It follows from this that the material derivative of equation (14) is a generalized analog of the Landahl-Lilley equation: that is, it will have the same property of exhibiting only quadratic (or higher) order coupling of the pressure (and/or scalar momentum potential) fluctuations to other fluctuating variables in the case of a uni-directional, transversely sheared flow, with only a transverse mean density gradient.

It is a straightforward matter to obtain this equivalent version of the general, exact Landahl-Lilley equation, which is, for comparison [see equations (15), (42) and (45) of reference (2)],

$$\begin{aligned} & \frac{D}{Dt} (c^2 \frac{\partial r}{\partial x_i} - \frac{D^2 r}{Dt^2}) - 2 \frac{\partial v_j}{\partial x_i} \frac{\partial}{\partial x_j} (c^2 \frac{\partial r}{\partial x_i}) \\ & = 2\gamma \frac{\partial v_i}{\partial x_j} \frac{\partial v_j}{\partial x_i} \frac{\partial v_k}{\partial x_i} - \frac{D^3 \sigma}{Dt^3} + \frac{D}{Dt} \frac{\partial}{\partial x_i} (\frac{\gamma}{\rho} \frac{\partial S_{ij}}{\partial x_j}). \end{aligned} \quad (21)$$

The desired analog to equation (21) can be obtained by following the procedure outlined in the two preceding paragraphs. As the algebra is somewhat tedious, it is omitted here. The final result, however, can be expressed in relatively simple terms, as follows.

The time derivative of the equation of linear momentum density transport can be written as

$$\frac{\partial}{\partial x_j} \left[\left(\frac{\partial p}{\partial t} - \frac{\partial^2 \psi'}{\partial t^2} \right) \delta_{ij} - v_i \frac{\partial^2 \psi'}{\partial t \partial x_j} - v_j \frac{\partial^2 \psi'}{\partial t \partial x_i} - v_i v_j \frac{\partial^2 \psi'}{\partial x_k^2} \right]$$

$$= - \left[\frac{\partial^2 B_i}{\partial t^2} + \frac{\partial}{\partial x_j} \left(v_i \frac{\partial B_j}{\partial t} + v_j \frac{\partial B_i}{\partial t} \right) + \frac{\partial^2 S_{ij}}{\partial x_k \partial t} \right] \quad (22)$$

Then, with the definitions

$$\alpha_i \left(\frac{\partial p}{\partial t}, \frac{\partial \psi'}{\partial x_k}; v_k \right) = \text{left side of equation (22)},$$

$$\beta_i (B_k; v_k) \equiv \left[\frac{\partial^2 B_i}{\partial t^2} + \frac{\partial}{\partial x_j} \left(v_i \frac{\partial B_j}{\partial t} + v_j \frac{\partial B_i}{\partial t} \right) \right], \quad (23)$$

the analog of the general Landahl-Lilley equation (21) is, exactly,

$$\left(\frac{D}{Dt} \frac{\partial}{\partial x_i} - 2 \frac{\partial v_k}{\partial x_i} \frac{\partial}{\partial x_k} \right) \alpha_i - \frac{D}{Dt} \frac{\partial^3 S_{ij}}{\partial x_k \partial x_j \partial t}$$

$$= - \left(\frac{D}{Dt} \frac{\partial}{\partial x_i} - 2 \frac{\partial v_k}{\partial x_i} \frac{\partial}{\partial x_k} \right) \beta_i - 2 \frac{\partial v_k}{\partial x_i} \frac{\partial^3 S_{ij}}{\partial x_k \partial x_j \partial t} \quad (24)$$

(The term arising from the viscous stress tensor term in equation (22) has been split because the principal effect of the left side term in the viscous stress tensor in equation (24) is to provide viscous attenuation of acoustic pressure waves via diffusion of momentum, while the corresponding right side term in equation (24) provides terms of a general character like the others on the right side, but which are usually considerably smaller in magnitude.)

The left side terms of equation (24) are clearly all propagation terms in the scalar momentum potential and/or pressure fluctuations. As was noted previously, the pure shear refraction term of equation (18) in the scalar momentum potential will be replaced in the expression, when it is worked out explicitly, by the pure shear refraction term in the pressure, expression (20). Thus, broadly speaking, the left side of equation (24) can be expressed either as a fourth order differential operator acting on the fluctuating pressure, or as a fifth order differential operator acting on the scalar momentum potential. When the fluctuating pressure is used, the equation is obviously a direct analog of the Landahl-Lilley equation for the logarithm of the pressure.

The right side terms of equation (24) are, in an explicit form,

$$\text{right side of equation (23)} = 6 \frac{\partial v_j}{\partial x_k} \frac{\partial v_k}{\partial x_i} \frac{\partial^2 B_i}{\partial x_j \partial t}$$

$$+ 4 \frac{\partial v_k}{\partial x_i} \frac{\partial}{\partial x_k} \left(\frac{\partial v_j}{\partial x_j} \frac{\partial B_i}{\partial t} \right) + 2 \frac{\partial v_j}{\partial x_k} \frac{\partial}{\partial x_i} \left(\frac{\partial v_k}{\partial x_j} \frac{\partial B_i}{\partial t} \right)$$

$$- 2 \frac{\partial}{\partial x_i} \left[\frac{D}{Dt} \left(\frac{v_j}{\partial x_i} \frac{\partial B_i}{\partial t} \right) + \frac{D v_j}{Dt} \frac{\partial}{\partial x_j} \left(\frac{B_i}{\partial t} \right) \right]$$

$$- 2 \frac{\partial v_k}{\partial x_i} \frac{\partial^3 S_{ij}}{\partial x_k \partial x_j \partial t} \quad (25)$$

It can be seen by inspection that all of the terms in equation (24) (apart from the viscous terms, of course) become of quadratic (or higher) order in the solenoidal momentum fluctuations, B_i , and the velocity fluctuations, v_i , when the mean flow is uni-directional, transversely sheared, and has mean mass density variation only in the transverse direction.

These source terms on the right side of equation (24) can be seen from equation (25) to all be explicitly dependent on the solenoidal linear momentum density fluctuations, B_i . It follows that radiated sound fields can only be produced "aerodynamically" when the flow in question has vortical momentum density fluctuations.

For the case of a turbulent mixing region having a uni-directional, transversely sheared mean flow, with zero mean pressure gradient and mean mass density varying only transversely, when all the flow in expression (25) becomes at least quadratic in the fluctuations, one would expect the dominant quadratic terms in equation (25) to be themselves dominated by the solenoidal momentum fluctuations. That is, factors like

$$\frac{\partial v_k'}{\partial x_i} = \frac{\partial}{\partial x_i} \left(\frac{B_k - \partial v'/\partial x_k}{\rho} \right)$$

can be satisfactorily approximated by

$$\frac{\partial v_k'}{\partial x_i} \sim \frac{\partial}{\partial x_i} (B_k' / \bar{\rho}),$$

because, from equation (4), the scalar momentum potential is of the same relative order as the mass density fluctuations.

An interesting consequence of such dominance of the source terms by solenoidal fluctuations (which also has practical uses in analytic and computational work) is that, because of the solenoidality, terms like

$$\frac{\partial v_k'}{\partial x_i} \frac{\partial^2 B_i}{\partial x_j \partial t},$$

say, automatically become expressible as

$$\frac{\partial}{\partial x_i} \left(\frac{B_k'}{\rho} \frac{\partial^2 B_i}{\partial x_j \partial t} \right),$$

and so on.

It is also relevant to note, in equation (25), that the velocity divergences can be replaced by the material derivative of the logarithm of the

mass density, since

$$\frac{1}{\rho} \frac{D\rho}{Dt} + \frac{\partial v_j}{\partial x_j} = 0,$$

and also that the term involving the material acceleration can be expressed in terms of pressure or entropy gradients and viscous stresses, since

$$\frac{Dv_i}{Dt} = -\frac{1}{\rho} \frac{\partial p}{\partial x_i} - \frac{1}{\rho} \frac{\partial S_{ij}}{\partial x_j} = \frac{\partial h}{\partial x_i} - T \frac{\partial S}{\partial x_i} - \frac{1}{\rho} \frac{\partial S_{ij}}{\partial x_j},$$

where h is the enthalpy, T the temperature and S the entropy.

Comparison of equation (24) with the general Landahl-Lilley equation (21) shows that equation (24) is the partial derivative with respect to time of equation (21), rewritten in terms of the fluctuating pressure, instead of the logarithm of the total instantaneous pressure which is used in the Landahl-Lilley equation. Thus, when fluctuating quantities are of interest, the new equation (24) has the advantage of being automatically and explicitly expressed, to the first order, in terms of fluctuating quantities. It also displays explicitly the nature of the fluctuating flow field -- i.e., its irrotational and solenoidal components -- again to first order. In this latter respect it can be made completely explicit by expressing the particle velocity as

$$v_i \equiv \frac{1}{\rho} (\bar{B}_i + B'_i - \partial\psi'/\partial x_i).$$

Like the general Landahl-Lilley equation (21), the new equation (24) is exact and thus is not restricted in its applications to special cases such as that of uni-directional, transversely

sheared mean flow, although the advantage of a quadratic right side will not necessarily be present in general. However, for relatively slowly diverging jet mixing flows, for example, such as those of aircraft engines, it can be easily established by inspection of expression (25) (or from the Landahl-Lilley equation) that quadratic source terms can be expected to continue to dominate, as long as the expansion angle of the jet, in radians, is smaller than the representative turbulence level, $|v'_i|/|\bar{v}_i|$, in the mixing region. Also, of course, the accuracy of the parallel flow model for a slowly diverging flow can easily be increased by the well-known coordinate transformation methods of, say, acoustic horn theory or boundary layer theory.

References

1. P. E. Doak, 1971, Journal of Sound and Vibration 19, 211-225. On the interdependence between acoustic and turbulent fluctuating motions in a moving fluid.
2. P. E. Doak, 1972, Journal of Sound and Vibration 25, 263-335. Analysis of internally generated sound in continuous materials: 2. A critical review of the conceptual adequacy and physical scope of existing theories of aerodynamic noise, with special reference to supersonic jet noise.
3. P. E. Doak, 1973, Journal of Sound and Vibration 26, 91-120. Analysis of internally generated sound in continuous materials: 3. The momentum potential field description of fluctuating fluid motion as a basis for a unified theory of internally generated sound.
4. P. E. Doak, 1973, Journal of Sound and Vibration 28, 527-561. Fundamentals of aerodynamic sound theory and flow duct acoustics.

APPENDIX II

A NEW ANECHOIC FACILITY FOR SUPERSONIC HOT JET NOISE RESEARCH AT LOCKHEED-GEORGIA

R. H. Burrin, P. D. Dean and H. K. Tanna
Lockheed-Georgia Company
Marietta, Georgia

Abstract

The facility described in this paper has been carefully designed accounting for shortcomings of other facilities, being guided by the stringent demands of on-going jet noise research at Lockheed-Georgia. The design goal was the capability of testing 2 in. diameter model jets up to 2000°F stagnation temperature at pressure ratios as high as eight, in a free-field environment, anechoic at all frequencies above 200 Hz.

A comprehensive series of flow visualization and temperature mapping experiments in a one-sixth scale model of the proposed facility, conducted to establish foundations for the unique design features, are described. A test program using a specially designed impedance tube to examine full-scale, four-wedge arrays is discussed, leading to the final selection of an acoustic material and design for the wedges to be used as lining for the new facility to ensure the 200 Hz frequency requirement.

Details of construction of the room and exhaust muffler/collector are given together with a description of the design and fabrication of the air supply system.

Finally, tests conducted to evaluate the performance of the complete facility are discussed in detail. These include (i) exhaust muffler/collector attenuation measurements, (ii) inverse-square law tests to determine the anechoic quality of the room and (iii) a systematic study to establish the lack of any significant internal (or upstream) noise levels for cold as well as hot operation of the facility.

11-1 Introduction

Much confusion about jet noise has arisen in the past as a direct result of inadequate facilities and insufficient knowledge and control of test conditions, in many cases giving rise to completely erroneous conclusions.

The facility described here has been very carefully designed accounting for other facilities' shortcomings and being guided by the stringent demands of on-going jet noise research at Lockheed. The fundamental nature of this research requires a meticulously controlled environment for all tests. This includes not only the quality of the basic acoustic measurements to be made in the anechoic room, involving correct placement of microphones, minimization of air circulation over the microphones which would otherwise affect noise measurements, adequate supply of entrainment air to simulate free-field conditions for the jet, and elimination of adverse temperature gradients affecting sound radiation, but also the precise control of mean flow parameters, which is probably one of the most critical aspects of a jet noise test, since the mean flow pressure and temperature

control the jet efflux velocity.

The following pages outline the design philosophies and steps taken to ensure the best possible facility obtainable, utilizing the existing basic laboratory buildings available in the Lockheed-Georgia Acoustics Research Center, for present and future requirements of fundamental hot jet noise research.

11-2 Facility Planning

The Lockheed-Georgia Company's aeroacoustics laboratory consists of three adjoining rooms: a small 11 x 11 x 17 foot tall anechoic chamber, a 21 x 22 x 28 foot tall reverberation chamber and an instrumentation and control room. In order to conduct the supersonic jet exhaust noise experiments with the required precision, a new facility was needed at Lockheed. It was evident that use of existing buildings would be most desirable from the standpoints of both development time and cost. As a consequence, the existing reverberation room (which had been lined with 6-inch foam slabs to act as a semi-anechoic room in a program of experimental research into the characteristics of duct acoustics) was chosen as the prime candidate for conversion to the new anechoic facility. This new facility was designed to satisfy the following acoustic criteria and physical requirements.

11-2.1 Design Criteria

1. Tests were to be conducted on model jets designed to simulate full-scale jet engine noise throughout the frequency range from 20 Hz to 10 kHz, which is typical of modern jet engines.
2. For the far-field tests, the microphones should be placed in the acoustic as well as the geometric (or interference) far fields of the jet exhaust.
3. Model jet nozzles up to 2 inches in diameter were to be used, which typically is of the order of 1/5 to 1/20 scale.
4. Measurements were to be made over a wide range of jet exit velocities from 400 fps to 3500 fps.
5. Stagnation temperatures of the order of 2000°F were required.
6. Provision should be made to measure the directivity of jet noise both downstream of the nozzle exit plane and in the forward arc.
7. During testing, a continuous and adequate supply of fresh air must flow into the anechoic room to provide both entrainment air for the jet and cooling air to prevent undue heating of the room lining material.

Pages 122, 123 and 124 are blank.

8. Safety required that the material used to line the chamber should have flame retardant characteristics.

11-2.2 Requirements and Decisions

The criteria led to the following requirements and decisions:

1. Assuming a minimum model-to-engine scale of 1:10, the lowest frequency of interest in the model facility would be 200 Hz. In order to ensure that the microphones used to record the sound field would be in the acoustic as well as the geometric (or interference) far-fields of the jet exhaust at all frequencies of interest above 200 Hz, the microphones ideally had to be mounted at least 60 or 70 nozzle diameters from the jet exit (i.e., 10-12 feet for a 2-inch diameter nozzle).

2. The room had to be anechoic at all frequencies above 200 Hz, based on the spectrum of interest from a 2" jet. It was anticipated that this could be achieved by lining all six walls with nominally 18-inch long, polyurethane foam wedges, 9 inches square at the base. The optimum shape and material for these wedges would be evaluated acoustically in a specially constructed impedance tube (see section 11-3). The length of 18 inches was chosen based on the available room dimensions and the required microphone distance from the nozzle exit. It was also essential that the microphones be sufficiently far from the wedge tips to be away from any near-field influence. The 9-inch square base size was chosen for convenience to tie in with the fact that anchor points were available in all walls on three foot centers. The method chosen for mounting the wedges involved gluing an array of 16 wedges onto 3 feet square boards, each board being attached to the wall by a single threaded rod and nut at the center of each board. This system would allow easy replacement in the event of any localized damage during subsequent operation.

3. Another important consideration affecting the final anechoic performance of the room was the design of platforms or equipment required to gain access to instrumentation for calibration and to test installations for modifications. In most facilities of this type platforms or cable floors, etc. are used which provide some degree of unwanted sound reflections. In this particular facility, it was decided to employ a "cherry picker" telescopic crane for access. The room itself has an access door which is located about 11 feet above the concrete floor of the room. The crane could conveniently be placed in one corner of the room with the boom stowed parallel to the floor and side wall when not in use. It had to be of appropriate length when retracted for the required stowage and to have sufficient extended length to reach all points in the room. It had to be totally electrically operated since the possibility of hydraulic fluid leaks would be undesirable in such close proximity of the foam wedges. A further requirement was the provision of crane controls in both the bucket and remotely at the door. The door control was to be used to park the crane in its stowed configuration during testing.

4. During all tests this crane must be completely enclosed by some form of anechoic cover to eliminate unwanted acoustic reflections which would

interfere with the experimental sound field. The cover, like the crane, was also required to be remotely controlled from the access door.

5. The required velocity (and hence SPL) and frequency ranges dictated that microphones with a broad dynamic range and a broad/flat frequency response be used. The 1/2 inch B&K type 4133 free-field microphone has a dynamic range of 32-160 dB, and a flat frequency response from the 20 Hz to 40 kHz. A system based on these microphones was chosen.

6. The existing reverberation room was furnished during construction with a 15-foot long, five-foot square concrete exhaust duct in one outside wall, the center of which was some 16-feet from the floor and offset some 3½ feet from the horizontal centerline of the room. Exactly opposite this duct, provision was made to insert an air supply duct through the front wall from the laboratory control room.

7. This five foot square exhaust duct was to be modified to serve a number of purposes:

- o Provide a means of exhausting air from the room.
- o Provide an anechoic termination for the jet.
- o Provide a means to prevent significant levels of outside noise from entering the room.
- o Provide air for room cooling during heated flow tests.
- o Provide entrainment air for the jet to simulate free-field operation.

8. A unique feature of the exhaust collector/ejector design philosophy was that entrainment air was to be supplied to the jet in quantities dictated by the jet operation conditions themselves. In most facilities extra air required for entrainment is forced into the facility. The main difficulty in these designs is knowing exactly how much air to inject so that a natural free-field entrainment is ensured. In this facility it was planned that the entrainment air would be injected into the room by the operation of the jet itself, thus providing a natural self-generating system. This was to be accomplished with a minimum static pressure drop in the room.

11-3 Impedance Tube Design

In order to evaluate the acoustic performance of selected samples of acoustic flame retardant polyurethane foams, a special impedance tube was required. It was designed to measure the basic acoustic property of acoustic impedance (and normal incidence absorption coefficient) of an array of four wedges. In order to accommodate these wedges, each with a 9-inch by 9-inch base, the impedance tube was designed to have an 18-inch square cross-section.

The lowest frequency for these tests was chosen to be 50 Hz; thus, in order to obtain at least one pressure maximum and minimum in the tube, a length of 15 feet was required. The side walls were constructed from highly polished 5/8-inch thick aluminum plate, thus ensuring that the wall losses would

be negligible for all cases of interest. The end termination plate behind the wedge array was made from 1-inch thick aluminum plate which was fitted with a rubber gasket and clamped to the end of the tube. A loudspeaker was mounted in the opposite end from the test specimens.

The 18-inch square cross-section of the tube places an immediate frequency limitation for the (0,0) mode (plane wave) operation at approximately 370 Hz, since the (0,1) mode cut-on frequency is 374 Hz, (see below).

The 1/2 inch B&K microphone (Type 4133) used was mounted on the longitudinal centerline of the tube and in order to extend the tube frequency range, a four-armed "spider" made from 1/2-inch stainless steel tubing was attached to the grid (see Figure 1). This moved the measuring points from the exact centerline to the quarter points of the duct cross-section. The ends of the tubes were precisely terminated in the same axial plane. In order to move the microphone axially in the impedance tube it was mounted on a "trolley" which could be manually moved along the tube to locate pressure maxima and minima.

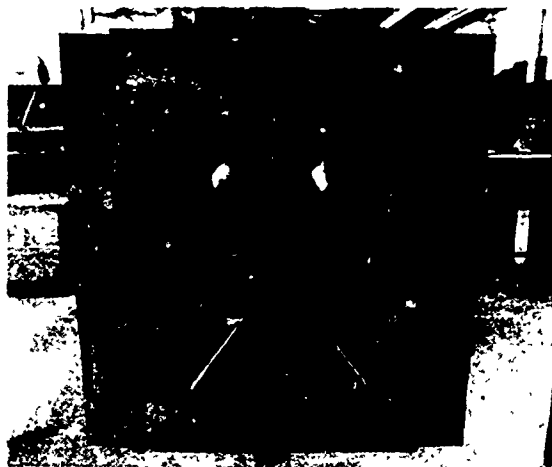


Fig. 1 Microphone "Spider" and Trolley

Thus, this system samples and sums the sound pressure on the quarter points of the tube cross-section diagonals. It is easily shown that, for any higher order mode combination up through the (3,3), the higher order modes cancel (to the accuracy of the spider construction and alignment) and only the plane mode component is measured. However, since this technique relies on the measurement points being on node lines for even modes and cancellation for odd modes, the four point system will not be valid for even modes greater than 2. Higher order mode cancellation systems can be conceived based on greater numbers of microphones.

Theoretically, the mode cut-on frequencies (f_0) can be determined from the following relationship:

$$f_{0(m,n)} = \frac{c_0}{2\pi} \sqrt{\left(\frac{m\pi}{a}\right)^2 + \left(\frac{n\pi}{b}\right)^2}$$

where c_0 is the speed of sound, m and n are the mode orders and a and b are the duct cross dimensions, so that in the present case,

$$f_{0(m,n)} = 374 \sqrt{m^2 + n^2}$$

The mode orders, in ascending frequency, are given in Table I.

TABLE I
CUT-ON FREQUENCIES FOR 18" x 18" DUCT

Mode Order	f_0	Mode Order	f_0	Mode Order	f_0
0,0	0	2,2	1058	1,4	1542
0,1	374	0,3	1122	3,3	1586
1,1	529	1,3	1182	2,4	1673
0,2	748	2,3	1348	0,5	1870
1,2	836	0,4	1496	3,4	1870

The "spider" microphone head eliminates all modal components in order up to $m = 3$ and $n = 3$. The impedance tube results will be valid to an upper frequency limit of only 1490 Hz based on the cut-on frequency of (0,4) mode. This behavior was validated experimentally, prior to proceeding with impedance tests.

11-4 Impedance Tube Wedge Evaluation Tests

Anechoic room wedges have traditionally been evaluated in terms of a normal incidence absorption coefficient as derived from the measured standing wave ratio in an impedance tube. It is recognized however that the absorption coefficient is usually less at other angles of incidence, but this reduction is not very significant until an angle of 60 or 70° is reached.

Thus in the general case the 99% absorption frequency as measured in the impedance tube will be lower than that in a completed anechoic room. However, for this application the nearest walls to the proposed microphone positions will present an angle of incidence not less than 80° or so and thus the normal incidence absorption coefficient should adequately reflect the properties of room walls for the strongest reflected signal situation.

Five different types of polyurethane and polyether foams were selected for testing, the types largely being determined by the manufacturer's ascertains to good acoustic quality. Three of these foams were of the flame retardant variety, the other two being of similar density (but highly flammable) and pore size, thus providing some data for comparison purposes. A wedge configuration consisting of four wedges placed in alternate directions (↑↓) was tested for all samples, with no air gap between the wedges and the tube end termination plate.

The logic of the tests was to attempt to optimize first on the *material composition* and then optimize on the *wedge geometry* while still attempting to remain compatible with the original idea of a wedge height being no greater than 18 inches (as dictated by the aforementioned room volume limitations). Thus, the most promising materials were tested with various air gap depths and wedge dimensions. It should be noted here that the interpretation of the meaning of the word "promising" involves the consideration of cost as well as acoustic performance, as differences of 400% in cost

between similar types were encountered.

Finally, the effect of wedge layout in the impedance tube was investigated, together with the effect of a plywood backing plate on the wedges, which simulated the proposed wedge mounting system in the anechoic room.

The most significant results of these tests are shown in Figures 2 through 6. It can be seen that all but one of the tested materials in Figure 2 exhibited similar absorption characteristics with a pronounced and well defined "knee" denoted loosely as the lower cut-off frequency. One material stands out; the Dunlop DF120 flame retardant foam sample, with its cut-off frequency point markedly lower than the rest. This material was therefore chosen as the most promising acoustically and was used for all subsequent wedge design and mounting investigations.

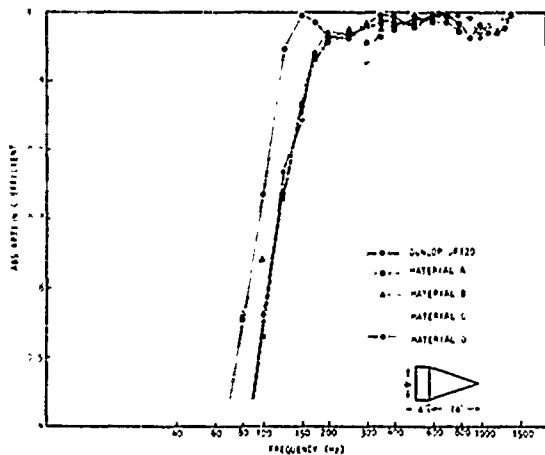


Fig. 2 Comparison of Acoustic Performance of Different Foams Under Consideration for New Anechoic Chamber

The effect of an air gap on wedge performance was then investigated. Figure 3 reveals that while an increasing air gap lowers the frequency of the "knee" point (i.e., increasing the absorption below 100 Hz), an unacceptable decrease in absorption between 100 and 200 Hz occurs; this "valley" increasing in depth as the air gap increased. The 99% absorption value however remained essentially unchanged at a frequency of about 300 to 350 Hz.

In an effort to modify the loss of absorption in the 100 to 200 Hz band, the wedges were shortened by removing 2 inches from each wedge base. The results of this modification as shown in Figure 4 were an increase in the 99% absorption point (of 50 Hz or so) and a 10 to 15% improvement in the 100 to 200 Hz absorption coefficients. This improvement however was not sufficient to meet the targeted minimum absorption in this band of 96% and it was considered that the pursuance of low frequency enhancement by use of an air gap would be fruitless within the current bounds of the geometric constraints of the room.

The question of wedge layout was then investigated and Figure 5 shows conclusively that the three possible wedge layout systems in the impedance tube had negligible effect on the absorption

measurements. The system of alternate horizontal and vertical wedge installation was therefore chosen for its basic aesthetic appeal in conjunction with an unsubstantiated feeling that parallel periodic structures should be avoided from a near field scattering point of view. This aspect could not be tested with such a limited test array.

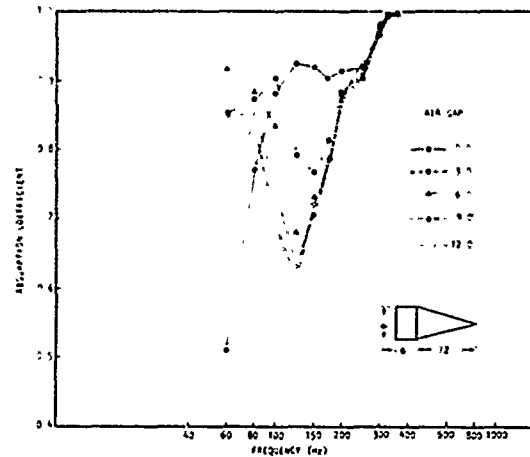


Fig. 3 Effect of Air Gap on 18-Inch Wedge, 6-Inch Base Height, Dunlop DF120 Acoustic Foam

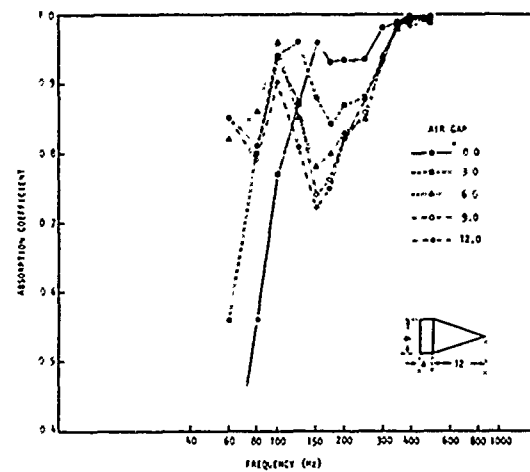


Fig. 4 Effect of Air Gap on 16-Inch Wedge, 4-Inch Base Height, Dunlop DF120 Acoustic Foam

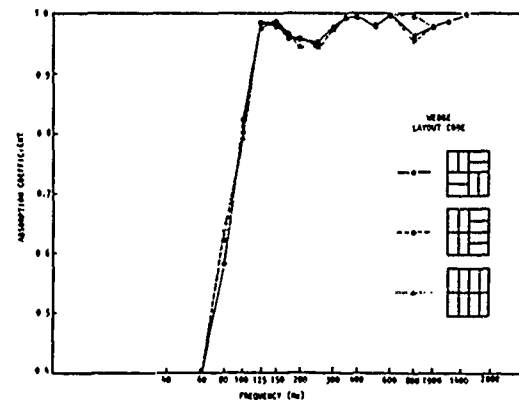


Fig. 5 Effect of Wedge Mounting Layout in Impedance Tube

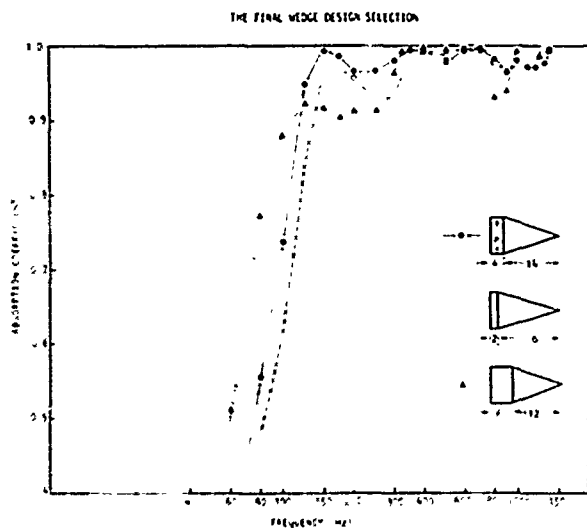


Fig. 6 Effect of Taper Angle Variations on 18-Inch Wedge

The wedge taper angle and base height were the next geometric parameters to be studied. From the earlier tests it was apparent that the 18 inch overall length had to be maintained in order to keep the "knee" roll-off frequencies in the desired region of less than 150 Hz. Thus, modification of the wedge base height was directly related to the taper angle in order to maintain the desired overall length. The three test wedge configurations are shown on Figure 6, with the obvious compromise between high relatively flat absorption with frequency and an acceptably low "knee" roll-off frequency being exhibited by the 4-inch base height wedge layout.

The final test involved the replacement of the aluminum backing plate by a 1/2 inch plywood panel. No significant changes in absorption over the frequency range of test could be discerned and thus this proposed method of mounting the wedges was confirmed to be acceptable.

The primary conclusion reached from all these above tests was that the optimum configuration (for the previously defined constraints of a 9 inch x 9 inch base and an 18 inch overall height) was one having a 4 inch base height with a 14 inch tapered height. In addition, this optimum configuration, fabricated in Dunlop DF120 foam, demonstrated its complete ability to provide the required low frequency performance in the proposed anechoic room application.

11-5 One-Sixth Scale Model of Room

The primary objective of building this model was to aid in the design of the jet ejector such that the wedge thermal and the jet entrainment criteria could be satisfied. In addition, the positioning of the microphones for the proposed acoustic measurements and the best location for the crane in terms of accessibility to microphones and test installations could conveniently be assessed.

The completed model is shown in Figure 7. The rear wall on the left side containing the exhaust duct was made removable for convenience. The plexiglass window in the side was included so that the flow visualization tests could be accomplished using a smoke generator. Another window was included in

the roof. The extension at the left represents the concrete room exhaust duct with the modified exit and intake hardware. In order to make the best use of this existing duct a rectangular concentric tube system was adopted for the exhaust collector. The design philosophy was to use the centrally exhausting jet together with its entrained air, to inject fresh, cool outside air through the outer concentric duct, and diffuse this throughout the room in order to cool the wedges and provide a free-field type entrainment for the jet. Several designs were investigated for the collector intake and for the method by which the injected air could be distributed evenly throughout the room. The final design is shown schematically in Figure 8. This system involves a false wall behind the acoustic wedges creating an air gap between the wedges and the concrete wall. The outside air is drawn in and directed between the two walls (concrete and false) and allowed to diffuse into the room around the periphery of the rear wall. This system was devised to minimize or eliminate a collector lip vortex that existed when intake air was allowed to enter the room from immediately behind the collector.



Fig. 7 One-Sixth Scale Model of Anechoic Room

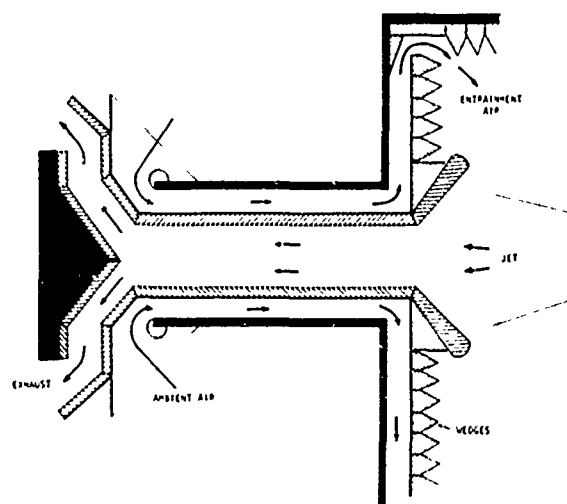


Fig. 8 Schematic of Final Design of Exhaust Collector

11-5.1 Flow Visualization Tests

Flow visualization tests, using a smoke generator probe inserted through the wall of the model, with a model jet operating at various velocities, indicated that the intake air diffused very evenly into the room from around the rear wall periphery at extremely low velocities. Also, the undesirable lip vortex was virtually eliminated, thus minimizing any reflections of hot turbulent air from the collector back into the room.

Although the visual observations of the air flow circulation patterns obtained in the model room were very clear, attempts to photograph the smoke through the plexiglass windows were rather unsuccessful due to surface light reflections and optical imperfections in the windows. The observed air flow patterns are therefore shown schematically in Figure 9.

The figure shows that as soon as the cold intake air leaves the air gap between the walls it diffuses evenly throughout the room and provides essentially free-field type entrainment for the jet.

A smoke generator was also used to investigate performance of the intake end of the system. Figure 10 illustrates that the cold ambient air was being drawn into the outer concentric duct for distribution throughout the room. The absence of any short circuit between the air exhausting through the central duct and the intake duct is demonstrated in Figure 11.

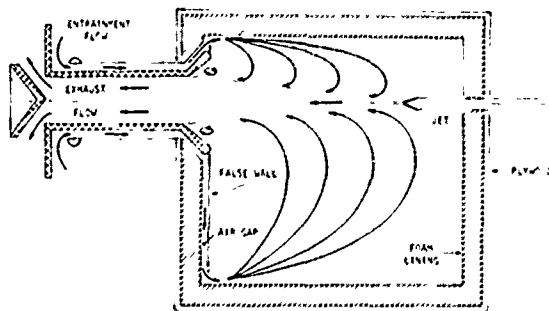


Fig. 9 Air Flow in One-Sixth Scale Model

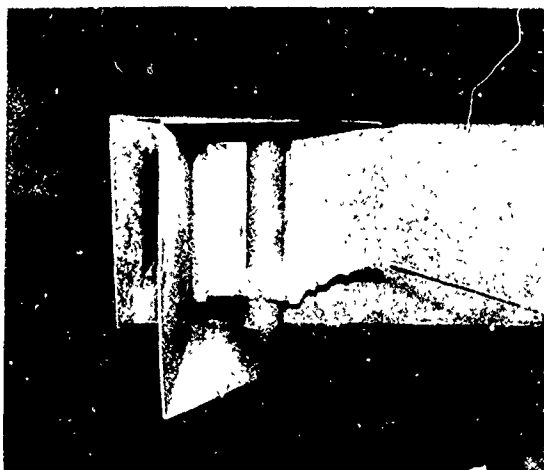


Fig. 10 Smoke Flow into Outer End of Room Air Intake



Fig. 11 Smoke Flow Illustrating Lack of Short Circuit Between Intake and Exhaust

11-5.2 Room Temperature Distribution Tests

A vital requirement of the jet exhaust collector was that it should provide sufficient cooling air for all jet operating conditions so that the room temperature would never reach a level that would exceed the temperature limit of the foam wedges. In addition, the temperature gradients in the room were required to be small enough so that acoustic measurements would not be affected.

In order to investigate these aspects of the collector performance, a one-sixth scale jet of 0.33 in. nozzle diameter was operated at a temperature of 750°F at three pressure ratios. The temperature distribution in the model room was measured using seven thermocouples placed at critical locations inside the room and in the collector, and an eighth thermocouple mounted on a hand-held "wand" was used to measure temperature distributions within and surrounding the jet flow.

The results of the three tests are shown in Figures 12, 13, and 14 where, in addition to the temperature values at various locations, contours of constant temperature are also illustrated. The shaded areas indicate temperature between 75° and 80°F. The temperature of the entrainment air measured in the outer concentric duct was less than 70°F during all tests, with an ambient air temperature of 69°F.

It is interesting to note that, as the pressure ratio was increased while maintaining an essentially constant stagnation temperature of approximately 750°F, the room temperature distribution remained approximately constant. This was due to the fact that as the pressure ratio increased the mass flow through the nozzle of course increased, but the jet static temperature decreased. At the same time, the amount of entrainment air injected through the collector also increased.

The temperature at the collector walls was less than 100°F and the temperature on the foam lining on the wall closest to the jet axis was between 85° and 90°F. Outside the jet flow region the temperature gradients were found to be too small to produce any significant effect on the proposed acoustic measurements.

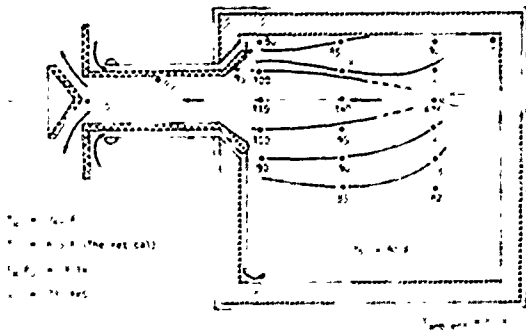


Fig. 12 Model Room Temperature Distribution, Plan View Jet Velocity = 730 fps

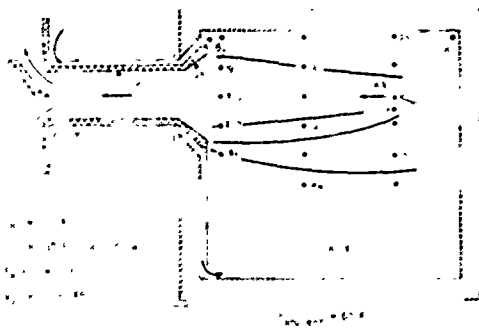


Fig. 13 Model Room Temperature Distribution, Plan View Jet Velocity = 1090 fps

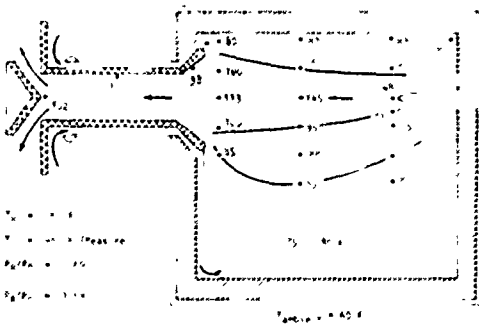


Fig. 14 Model Room Temperature Distribution, Plan View Jet Velocity = 1420 fps

11-6 Construction of the Exhaust Collector

Following the design principles established during the one-sixth scale model tests, a concentric sound attenuating duct system was to be constructed utilizing a 5 foot square, 15 foot long exhaust tunnel in the wall opposite the jet air supply ducting. A square cross-section plywood duct, 4 feet by 4 feet was constructed in situ, being attached to threaded rods mounted in wall anchors and forming, with the concrete duct, a central tube surrounded by a square section annular outer duct 6 inches wide. As indicated earlier, this exhaust duct was also required to act as a muffler to minimize outside noise interference in the interior of the anechoic room and to provide an anechoic termination for the jet. An acoustic lining consisting of 4 inches of polyurethane foam covered by 1 inch of thermal/acoustic insulation (Kaowool) retained

by coarse glass cloth and wire mesh was installed. Figure 15 shows the top and side walls almost complete and the plywood floor installed.

Figure 16 shows the completed exhaust collector as seen from the jet centerline from the opposite wall. The outer edge of the 45° square collector was fitted with a bell mouth fairing made from the same acoustic foam as used for the anechoic wedges.



Fig. 15 Completed Plywood Installation of Exhaust Duct Showing Sides and Top Partially Lined with Acoustic Material

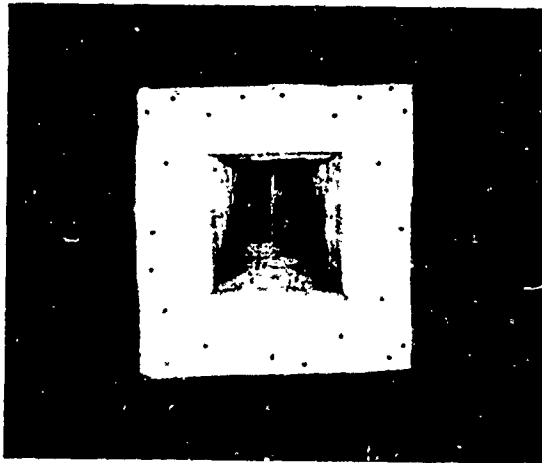


Fig. 16 Completed Exhaust Collector/Muffler

Figure 17 shows the outside construction of the exhaust duct. This is seen to be exactly like the one-sixth scale model. The intake was connected to the outer annulus, all joints being sealed to prevent short circuiting between the exhaust and intake sections. An identical intake/exhaust "wing"

was installed on the opposite side of the concrete tunnel shown, forming a symmetrical system. An anti-insect and bird screen was installed across the intakes.

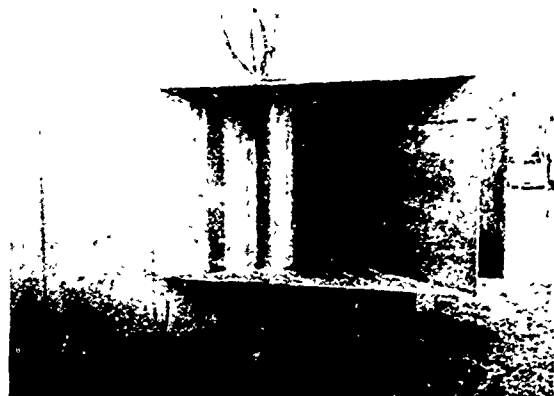


Fig. 17 Details of Collector Exhaust and Intake at Exterior of Building

11-7 Anechoic Room Construction

A number of preliminary tasks were required to be accomplished prior to installation of the room lining:

1. An overhead monorail crane installation was removed.
2. Light fittings were suspended from the ceiling, electrical outlets extended from all four walls and the sprinkler system was modified to position the heads below the level at which the ceiling wedges would be mounted.
3. A false wall on which to mount the wedge boards was installed to enclose existing air supply ducts and valves.

The first major task was to install the "cherry picker" crane. Its optimum location was determined by making a one-sixth scale cardboard replica to be placed in the room model. Installed in the chosen position, with the bucket removed, it could be stowed parallel to the floor and left wall farthest from the jet exit.

Although the majority of wedge boards required were the standard 3 x 3 foot configuration shown in Figure 18, a considerable number had to be custom made because the room was not a standard rectangular shape. In fact, the right side wall, rear wall and ceiling were built at 3 degree angles relative to the front wall, left wall and floor to meet the requirements for reverberation tests. Also, the wall dimensions were not exactly multiples of 3 feet and in addition, boards had to be fitted around the exhaust collector.

The anechoic wedge boards were made by applying contact adhesive to the plywood panel and spraying the base of each wedge with the same adhesive. Application of the adhesive to the foam wedges by means of a paint spray gun was found to be far superior to application with a brush. The adhesive

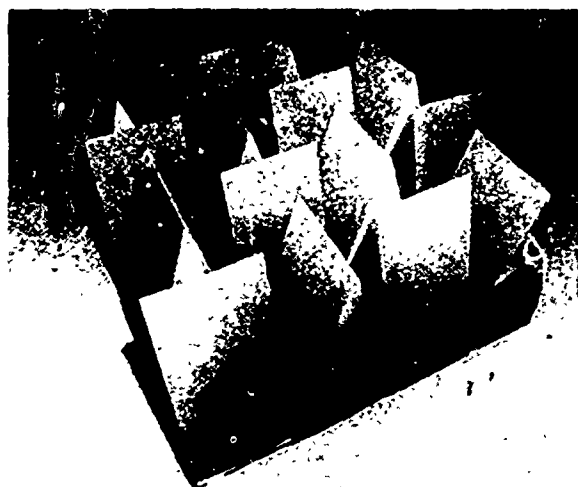


Fig. 18 Standard 3 Feet by 3 Feet Wedge Board

remained on the surface much more satisfactorily whereas a brush seemed to cause the adhesive to penetrate further into the foam, consequently not enough remained on the surface to create a good bond when applied to the board.

Threaded rods were screwed into anchor points on the walls located on three foot centers. Each board, with a hole at the center, was slipped over a rod and secured with a single washer and nut. Short stand-off legs were attached to the back corners of each board so that tightening the nut firmly positioned the board. This simple mounting arrangement allowed for removal of any board, whenever necessary, with a minimum of effort.

All corners of the room, except those around the periphery of the rear collector wall, were furnished with 14-inch blocks of foam to ensure that no resonant cavities would be produced where wedges on adjacent walls met.

At the periphery of the rear wall a different configuration was required. The wedge boards forming the rear wall were positioned six inches from the concrete wall creating the air gap required to distribute intake cooling and entrainment air. A six-inch gap was required between the rear false wall wedges and those attached to the ceiling, floor and side walls in order to allow the free flow of intake air. To ensure that sound waves generated during testing could not be reflected from any hard wall surface behind this six-inch gap, special elongated wedges were attached to the side wall, floor and ceiling boards to extend behind the rear false wall.

In order to ensure that the crane would not impair the anechoic quality of the room during testing, in addition to placing the crane as far from the jet and the microphones as possible, a special anechoic cover was designed and constructed. Because of the inaccessibility of the crane in its stowed configuration, this cover, like the crane, had to be remotely controlled from the door. A "clam-shell-like" cover was built from 1/2-inch plywood stiffened with aluminum angle. The cover was hinged on two axes as shown in Figure 19 and pulled over the crane by a motor connected through a cable and pulley system to the top edge of the cover. Since the cable was required to pass over the telescopic boom of the crane, extra cable was

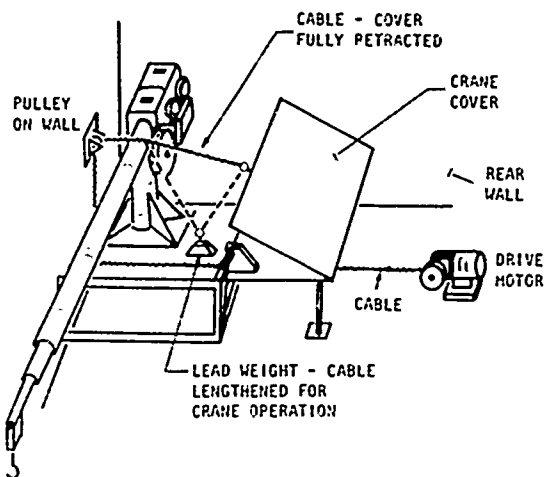


Fig. 19 Schematic of Cable System to Operate Anechoic Crane Cover and Allow Free Operation of Crane When Retracted

required when the cover was retracted, so that the crane would be raised without breaking the cable. This was achieved by threading a lead weight free to slide on the cable between the cover and the wall pulley as shown in Figure 19. When the crane was to be used the cover would be retracted and the motor run until the lead weight rested on the floor. This would allow sufficient extra length in the cable for complete operation of the crane and obviate any possibility of undesirable slack in the cable. The telescopic boom of the crane was permanently wrapped with 4 inches of acoustic foam which completed the anechoic cover.

Figure 20 shows the crane stowed under its anechoic cover and Figure 21 shows details of the entrance door.

Completion of the crane cover and its remote operation system left only one task to be accomplished before initial acoustic evaluation tests could be conducted; namely, the installation of a sound source and travelling microphone system which is discussed in Paragraph 11-9.1. Two additional tasks were required to be accomplished before jet noise tests could be initiated. These were, (1) the construction of the air supply ducting and (2) installation of the microphone system. These phases are discussed in Section 11-8 and Paragraph 11-9.2, respectively.

11-8 Design and Installation of the Air Supply System

The control of mean flow parameters is one of the most critical aspects of a jet noise test, since the mean flow pressure and temperature directly control the jet velocity.

The supersonic heated jet tests to be conducted in this facility required that a system be built capable of supplying a controlled flow of air to the 2-inch diameter jet nozzles at pressure ratios up to 7.4 (approximately 105 psi) and at stagnation temperature ratios up to 4.6 representing about 2000°F.



Fig. 20 Crane Under Anechoic Cover Just Prior to Closing



Fig. 21 Entrance Door Details

11-8.1 Design and Fabrication of the Air Supply System

The main air supply continuously delivers 20 pounds per second of clean, dry air at 300 psi. In addition, storage tanks retain 12,000 pounds of air at 300 psi for higher demands. The main air, initially controlled with a 4-inch automatic regulating pressure control valve located within the acoustics laboratory serves three systems: (1) the jet noise facility, (ii) the small anechoic room, and (iii) a flow measurement facility located out-

side the building. This main control valve isolates all three facilities from most pressure demand fluctuations in other facilities, such as the low speed wind tunnel. Downstream of this valve, cold air is delivered to the Marquardt Sudden Expansion (SUE) Propane Burner through a 2-inch automatic regulating control valve. This burner operates best at relatively high pressure and if test requirements dictate low flow, hot air is bled off at the burner exhaust stack through a 2-inch manually controlled high temperature (1200°F) valve.

A plan view schematic of the new jet noise facility is shown in Figure 22. In order to control both pressure and temperature to a high degree of accuracy for jet noise tests, hot and cold air are mixed just downstream of the burner. The 2-inch cold air valve is automatically regulated by plenum pressure and the new 2-inch hot air valve (nominally temperature limited to 1500°F) is controlled by plenum temperature. These servo controls provide ideal regulation of test pressure and temperature simultaneously.

Initial design of the hot air supply system utilized the super alloy Hastelloy X in order to withstand air temperatures up to 2000°F. It consisted of a 4-inch supply line from the SUE burner which carried the air through the outside wall into the laboratory area, followed by a diffuser leading to a 24-inch diameter 48-inch long muffler, followed by a 24-inch diameter, 48-inch long section in which an electric after-heater was to be installed. Downstream of this was a conical contraction to a final settling chamber or plenum at the end of which the jet nozzles would be attached inside the anechoic room. The maximum air temperature to be supplied by the SUE burner was to be limited to 1500°F because of the control valve temperature limit. The electric after-heater was included in the design considerations to raise the air temperature to the required maximum of 2000°F. In view of both the estimated high cost and long lead time for supply of this material, a compromise design was arrived at, such that a refractory lining inside the 1/4-inch thick 304 stainless steel ducts could be used. All ducts except the 4-inch supply line were fabricated from 1/4 inch stainless steel and lined with 2 inches of vacuum formed, or mold formed, Kaowool ceramic material (used primarily in furnace applications up to 3200°F), the foot long sections being sealed with ceramic cement. By wrapping all assembled ducts with a further two inches of Kaowool blanket, the metal temperature would be maintained below 800°F in all proposed test operations of the facility and also the thermal loss of the system would be minimized. The 4-inch line from the SUE burner to the diffuser was made from schedule 40 Inconel 600 pipe and wrapped with 4 inches of Kaowool ceramic blankets to prevent excessive heat loss.

The muffler section was designed to minimize the propagation of upstream valve, burner and pipe noise into the anechoic room. Virtual elimination of this upstream noise is a most important requirement to ensure meaningful jet noise measurements. The muffler was made with two concentric 2-inch wide annular tubes and a central 4-inch tube inserted into a Kaowool lined 24-inch internal diameter 4-foot long duct. Each tube consisted of an inner wall of stainless steel mesh lined with Kaowool ceramic paper used to retain a filling of Kaowool blanket. The outside was then wrapped with

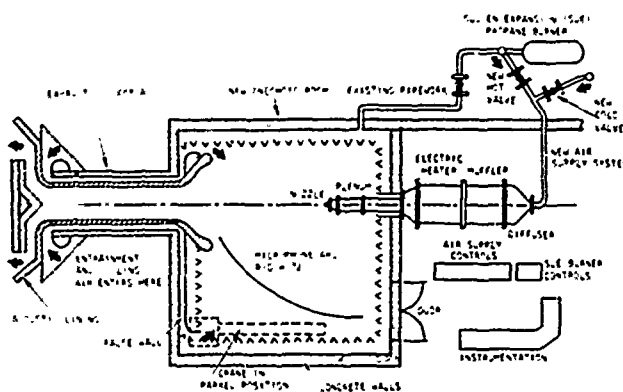


Fig. 22 Plan View Schematic of the New Facility

another layer of ceramic paper and finished with an outer sleeve of stainless steel mesh. The ends were retained with rings of 1/8 inch thick high temperature gasket material and stainless steel locking wire.

Details of fabrication of the muffler section are shown in Figure 23. The complete installation wrapped with Kaowool insulation is shown in Figure 24.



Fig. 23 Completed Muffler Section



Fig. 24 Air Supply Ducting Installed and Wrapped with Heat Insulating Material

The electric heater section is required to have a large heating surface area in order to achieve the required heat transfer and is to be designed for minimum production of turbulence or other noise generation mechanisms. Since it is very difficult to accurately predict the heat transfer coefficients of any heater element, consistent with the philosophy applied to other aspects of the facility design, model heater tests were planned. Initial testing of one type of rectangular element has indicated that the preliminary design should be capable of providing the required temperature increase. At this time samples of a more efficient (and more desirable from the turbulence point of view) half-round element have been ordered for similar evaluation. The electric heater section in the current configuration simply serves as an additional plenum.

11-8.2 Alignment of the System with the Exhaust Collector

In order to ensure that the flow would be aligned with the exhaust collector, an alignment system using a 1 mw continuous wave laser was devised. The laser was mounted on the central axis of the exhaust collector. A pair of cross wires were positioned at the entrance to the parallel section of the collector.

The air supply duct was roughly positioned through the front wall from the laboratory. A mirror was secured to the flange plate and cross wires were attached to the mirror indicating the position of the nozzle centerline. The laser was turned on and the ducting was maneuvered until the laser beam was reflected from the center cross wires on the mirror, back along its length to the cross wires in the exhaust duct entrance. In this way the jet axis was aligned to better than 1/2 degree accuracy.

11-8.3 Provision for Forward Arc Noise Measurements

In order to determine the effects of noise radiated in the upstream direction, particularly in connection with shock-associated noise investigations, provision had to be made to move the jet exit plane closer to the exhaust collector in order that microphones could be placed as far as 150° from the downstream jet axis. This required that a 10 foot extension to the plenum be made.

11-9 The Systems for Acoustic Measurements

This section is divided into two parts. The first part deals with the special installations for acoustic performance evaluation tests associated with the anechoic quality of the room and the second part deals with the microphone installation to be used for jet noise measurements.

11-9.1 Acoustic Performance Evaluation System

In order to check the performance of the room and to determine the best location for the microphone support structure for jet noise measurements, a movable travelling microphone system and stationary sound source was devised. This system consisted of a small electric motor mounted on a wooden strut just behind the proposed position of the jet exit plane. A support bracket and pulley designed to be attached to the wedge boards or sprinkler pipes was made. A cable, whose length could be adjusted, was

attached to the wooden strut at the jet exit plane and secured to the pulley bracket. A 1/2 inch B&K 4133 microphone was mounted by means of teflon bushings on this cable so that it would run freely. Another cable was run from the microphone carrier over the pulley on the pulley bracket to a take-up spool on the motor shaft. In this way the microphone could be traversed from close to the jet exit plane outwards in any selected direction toward and into the troughs between wedges or from the wedges toward the jet exit plane. A further refinement of mounting a deflection box on the wooden strut and attaching its cable to the microphone carriage allowed microphone position to be ascertained. Using the microphone output signal and the logarithmically converted signal from the deflection box, a sound pressure level versus position plot was recorded on an X-Y recorder during each test run.

Initially a loudspeaker was used as the sound source, but later an acoustic driver unit which was much more representative of a point source was used. The arrangement with loudspeaker source is shown in Figure 25.

In addition to the discrete frequency and 1/3 octave band random frequency spectra measured for a number of different microphone paths in the room (discussed in Section 11-10), a cold subsonic jet was also used as the sound source and a similar series of tests was carried out. The results of the tests are discussed in Section 11-10.

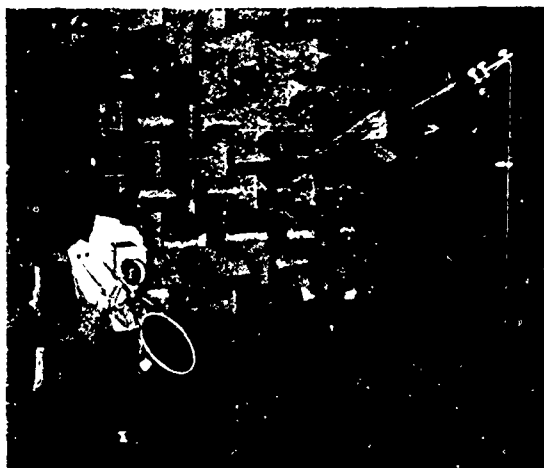


Fig. 25 Traversing Microphone System (with Loudspeaker) for Acoustic Performance Evaluation Tests

11-9.2 Jet Noise Measurement System

Based on the results of the inverse square law tests to be discussed in Section 11-10, the microphones were required to be mounted 72 jet diameters from the exit plane in order to be in both the acoustic and geometric far-fields of the jet exhaust. Accordingly, a microphone boom made from an arc of 3/4 inch stainless steel tubing was installed in a room diagonal so that the microphones would not be within the wedge near field. The boom was supported rigidly and located accurately by using adjustable struts as shown in Figure 26. Initially the microphones (twelve mounted in 7 1/2° intervals from 15° to 97 1/2° to the downstream jet axis) were attached directly to the tube by means of standard chemical

retort-stand clamps. During the preliminary jet noise measurements, an interference problem created by reflections from the microphone boom was discovered at about 400 Hz. The interference resulted in a 3.5 dB reduction in jet noise in the 400 Hz 1/3 octave band. This problem was experimentally determined to be eliminated when the microphones were moved 8 to 10 inches forward of the boom. Accordingly, the original boom was removed, modified slightly to have an increased radius and remounted closer to the wedges. The microphones were then attached to the support boom by extension tubes approximately 1 foot long so that they were still located at 72 nozzle diameters, but were significantly forward of the mounting boom. The final installation is shown in Figure 26.

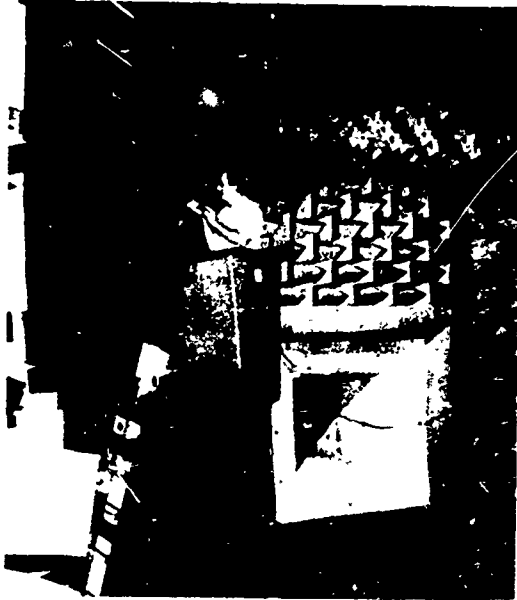


Fig. 26 Microphone Boom Arrangement

11-9.3 Data Acquisition System

A twelve channel 1/2 inch 8K microphone system was installed consistent with the requirements of the type of tests to be performed in the new facility. Bruel and Kjaer (Type 4133) microphones with FET cathode followers (Type 2619) were mounted on the microphone support boom at $7\frac{1}{2}^\circ$ intervals from 15° to $97\frac{1}{2}^\circ$ from the downstream jet axis. The recording system as shown in Figure 27 incorporated a twelve channel 8K model P-220 microphone power supply unit. The responses of these microphones were recorded simultaneously on a 14-channel Honeywell Model 7600 FM tape recorder at 120 inches per second (ips). An Ampex Time Code Generator and Search Controller was used for input to channel 14 to expedite the location of data on tape for subsequent analysis. Provision was made to monitor the response of any selected microphone on an oscilloscope during recording to ensure that the system was functioning correctly.

Before any test runs were made an SPL signal of approximately the same level as the test noise was applied to each microphone using a Photocon Model PC-135 calibrator, and recorded on tape to provide an absolute reference level for data reduction.

The atmospheric absorption corrections to be

applied to the measured jet noise spectra will vary with the environmental conditions (relative humidity and temperature) in the anechoic room. The magnitudes of these corrections at all one-third octave frequencies from 5 kHz to 40 kHz will be derived experimentally at the end of every test run as follows. Using a compact high frequency driver unit, the SPL at each frequency of interest will be measured at two convenient distances, say 3 feet and 12 feet, from the sound source using two microphones permanently mounted on the axis of the driver unit. For frequencies above 5 kHz, both measurement points will be in the acoustic far-field of the sound source, and hence, any additional decay over and above the familiar inverse-square law decay in the SPL's measured at these two locations will give the atmospheric attenuation at the frequency under test. In this manner, it will be possible to obtain accurate atmospheric attenuation calibrations for all tests carried out in the facility.

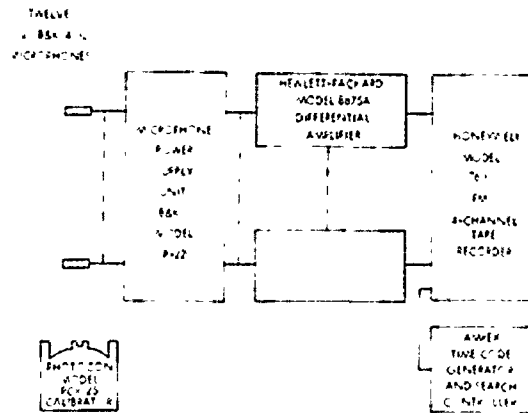


Fig. 27 Sound Pressure Instrumentation and Recording System Schematic

The noise data analysis system utilizes a Hewlett-Packard Model 8804-A Real Time 1/3 Octave Audio Spectrum Analyzer. The data reduction block diagram is illustrated in Figure 28. In order to obtain the 1/3 octave spectra from 200 Hz to 40 kHz, the tape speed was reduced to 30 ips on playback. The 1/3 octave levels were then recorded on digital magnetic tape using a Hewlett-Packard Model 2547A Digital Coupler connected to a Kennedy Model 1406 Incremental Tape Recorder for later detailed analysis using a data reduction program developed for use on the Univac 418 digital computer. This program incorporates the microphone frequency response corrections and atmospheric absorption corrections. The results are finally displayed to include test conditions and computed jet flow parameters, 1/3 octave acoustic spectra, and computed overall sound pressure levels. The day-to-day repeatability of the complete measurement and analysis system is ± 0.5 dB.

11-10 Facility Performance Evaluation Tests

11-10.1 Exhaust Collector Noise Attenuation Measurements

A multilayer lining arrangement as described in Sections 2 and 6 was adopted for the reasons outlined therein. This type of duct presents a difficult problem in regard to attenuation measurements. Any microphone system installed in the duct will

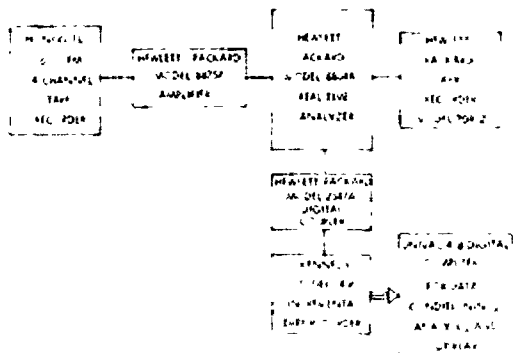


Fig. 28 Jet Noise Data Analysis System Schematic

invariably be affected by higher order duct modes of propagation. Total power attenuation measurements are hampered by the duct end terminations presented at one end by an anechoic room and at the other end by an outdoor environment.

Thus, a simple test arrangement was adopted which, although not perfect perhaps for discrete frequency noise, was considered to be sufficiently accurate to provide a means to establish noise reduction between the outside and inside. The method chosen was to position loudspeakers five feet from the outside exhaust duct openings and to compress the sound levels at each opening such that a constant 90 dB, in-phase amplitude was obtained at each exit point over a frequency range from 150 Hz to 10 kHz. Microphones were then positioned on the exhaust duct centerline at various axial locations, with the inner-most microphone actually in the anechoic room at the location of the 15° microphone. Figure 29 shows the layout of the measurement system.

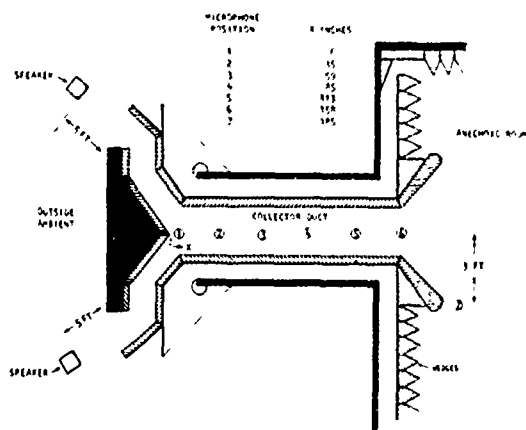


Fig. 29 Test System Layout for Exhaust Collector Attenuation Measurements

The swept frequency SPL measurements showed marked evidence of higher mode propagation cut-off effects but still the SPL decayed at a constant rate down the duct. For clarity, the results are presented in Figure 30 in terms of the separate attenuation of the three distinct components of the system in 1/3 octave bands. These components were (i) the initial bend at the outer end, (ii) the parallel duct section, and (iii) the "bend" between

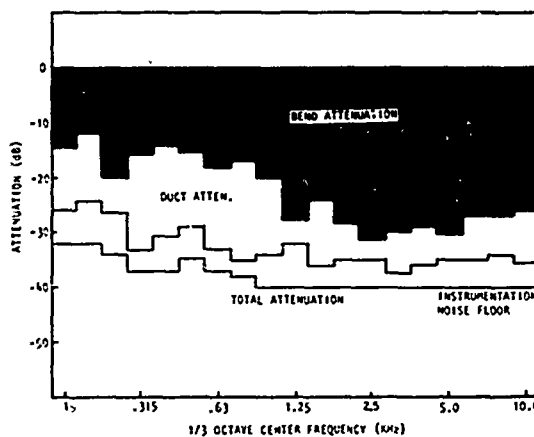


Fig. 30 One-Third Octave Attenuation Spectra of Exhaust Collector Sections

the duct "line of sight" axis and the microphone arc measurement point in the room.

As can be seen the initial bend provides the most attenuation, particularly above 1 kHz. At the higher frequencies the instrumentation noise level was reached at about 40 dB down for the microphone at the 15° measurement point (number 7).

In an attempt to estimate the probable levels of outside ambient noise, a time history was taken during a "typical" day. The maximum observed level of 78 dB overall occurred when a low flying jet aircraft passed over the facility. It was concluded that this type of interference would not intrude on the interior room microphone measurements, since the exhaust duct attenuation will reduce the outside noise level in the room to below the room ambient. One source of 85 dB occurred when a lawn mower approached the duct termination, but this source is considered to occur sufficiently rarely or may be appropriately diverted so as to present no problem.

11-10.2 Anechoic Room Performance Evaluation Tests

In order to confirm the design criteria and to ensure the accuracy of the subsequent jet noise measurements, the facilities were subjected to rigorous performance evaluation tests at appropriate stages. The major results are given below.

1. The background (or ambient) noise in the anechoic room was measured with a 1 in. B&K microphone (Type 4131), which has a dynamic range of 15 to 146 dB. The overall SPL in the room is 45 dB and the corresponding 1/3 octave spectrum from 50 Hz to 10 kHz is shown in Figure 31.

2. In addition to the detailed collector attenuation tests described in Paragraph 11-10.1, a crude test was conducted where the attenuation produced by the lined exhaust collector was approximately determined by subjecting the outside end of the collector tunnel to a broadband noise and measuring the 1/3 octave SPL spectrum at the entrance to the tunnel and inside the room at the collector entrance. The two spectra are also shown in Figure 31. The overall noise reduction of the collector exhaust system for this crude test was 47 dB, being

20 dB in the 200 Hz band and increasing to approximately 60 dB in the 10 kHz band.

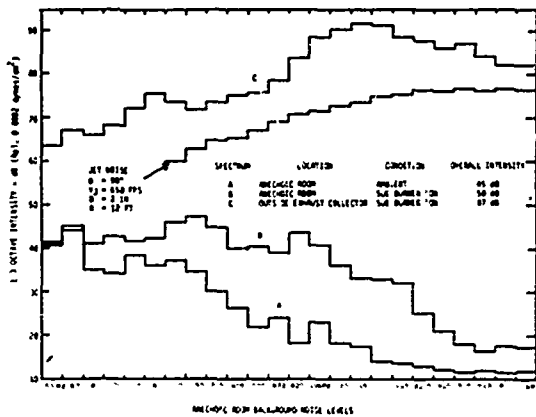
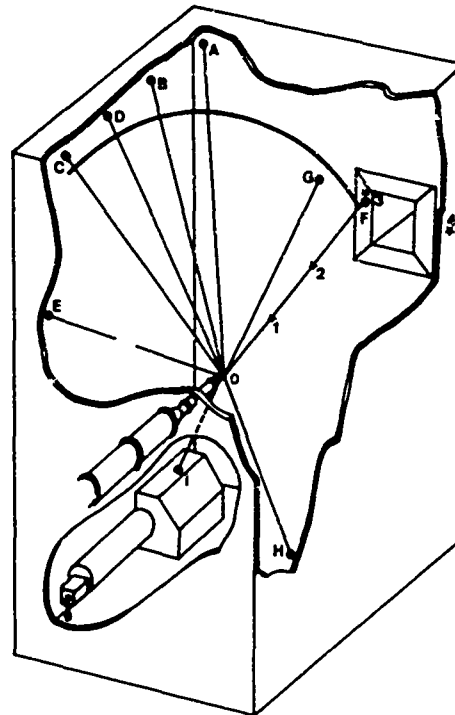


Fig. 31 Anechoic Room Background (or Ambient) Noise Spectra

3. In order to evaluate the anechoic quality of the room and to ensure that the proposed microphone distance of 12 feet (72D) is in the *acoustic* far field, an audio driver unit placed at the nozzle exit location was used as the sound source (i.e., point source) and the intensity vs. distance plots along several directions were obtained with the traversing microphone arrangement described in Paragraph 9.1. The microphone was traversed along the nine different directions shown in Figure 32, and for each of these traverses, measurements were made of the SPL fall-off as a function of distance, both for a pure tone noise source and for a one-third octave filtered white noise source. Along each of these traverses, the two sets of results (i.e., for pure tone and for filtered one-third octave) were in general, identical. Furthermore, the results along various directions from the sound source were essentially similar. A typical set of the intensity-distance plots at various frequencies is presented in Figure 33. It can be seen from this figure that the cut-off frequency of the room is below 200 Hz and that at a distance of 12 feet, the microphone is in the *acoustic* far field at all frequencies (above 200 Hz) of interest.

4. Using the same traversing microphone arrangement, a cold jet ($V_j/a_0 = 0.85$) was used as the sound source in a second series of tests to determine the limits of the *geometric* far field. The intensity-distance plots at various one-third octave frequencies were measured at four angles to the jet axis, namely 15°, 25°, 45° and 90°. Here again, the results along different directions were similar, and so only one set of results (90°) is presented in Figure 34. At distances greater than 9 ft. from the nozzle exit plane, the intensity conforms to "inverse-square law", except at frequencies above 8 kHz, where the decay is somewhat sharper because of the increasing atmospheric attenuation with frequency. Hence, it is established that for frequencies above 200 Hz, the acoustic interference produced by sources distributed over a finite region of the jet exhaust flow does not affect the "inverse-square law" decay of intensity for observer distances greater than approximately 54 nozzle diameters.

In conclusion, therefore the far-field criteria



- OA - OI Directions along which Inverse Square Law Tests were conducted with acoustic driver source.
- I - 4 Positions at which background noise levels were measured.
- OA,OB,OF,OG Directions along which Inverse Square Law Tests were conducted with cold jet source.

Figure 10.4 Microphone Traverse Geometry for "Inverse-Square Law" Tests

Fig. 32 Microphone Traverse Geometry for "Inverse-Square Law" Tests

tests described above have established that, at the proposed distance of 12 feet ($R/D = 72$) from the nozzle exit plane, the microphones will be both in the *acoustic* as well as the *geometric* far fields of the jet exhaust.

11-10.3 "Acoustic Cleanliness" Tests

The "acoustic cleanliness" or internal noise aspect of the rig was examined in the first instance by employing the usual method of measuring the noise from a cold convergent nozzle at 90° to the jet axis and studying its velocity dependence. The overall SPL is plotted against the jet efflux velocity V_j in Figure 35. It can be seen that the overall SPL follows the V_j^8 law within 1 dB between the velocities of 400 and 1000 fps, whereas at velocities outside this range, the levels are higher. At velocities above 1000 fps, the levels are higher clearly due to the presence of shock-associated noise. At velocities below 400 fps, however, a careful examination of the one-third octave spectra, together with the combined spectrum of background and instrumentation noise of the complete measuring system as shown in Figure 36, revealed that at these low jet velocities, the low and high frequency ends of the spectra were being lifted by the instrumentation noise.

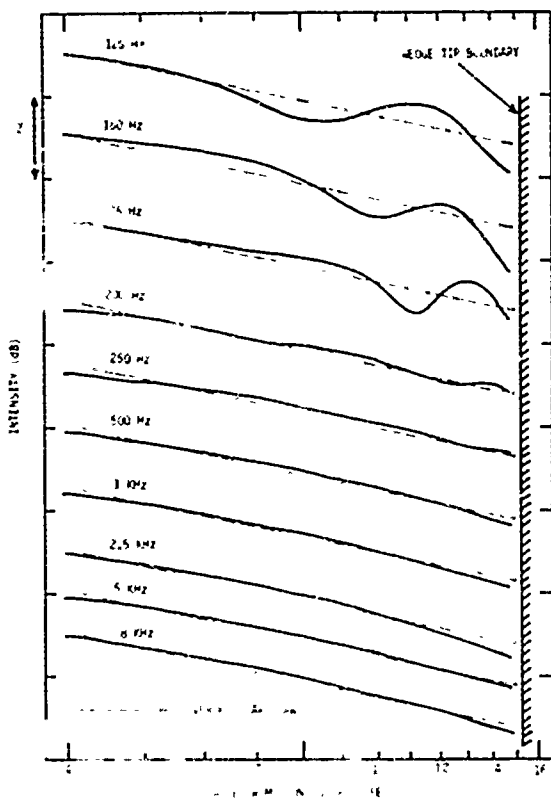


Fig. 33 Intensity-Distance Plots with Point Sound Source

In order to qualify this observation, the same series of mixing noise spectra were measured, this time with a minimum amount of instrumentation, i.e. a 1/2-inch B&K microphone, a 1/3-octave analyzer and a level recorder. The corresponding spectra at jet efflux velocities from 300 to 1240 fps, together with the new background/instrumentation noise spectrum are presented in Figure 37. It can be seen that the instrumentation noise spectrum is much lower in level this time and hence the mixing noise spectrum for $V_j = 300$ fps is no longer contaminated by the instrumentation noise, except at the lower frequency end due to the presence of a.c. line frequency and its harmonics. At this stage, therefore, it appears that the acoustic cleanliness for cold operation of the rig is not affected by internal noise, at least down to 300 fps, where the tests were terminated.

Having established the influence of the measuring instrumentation noise on low velocity jet noise measurements, we can proceed to produce additional evidence for the lack of any significant internal noise levels. Once again, the tests described below were carried out with the basic instrumentation system, consisting of 1/2-inch B&K microphones, a 1/3-octave analyzer and a level recorder, so that the instrumentation noise was kept to a minimum.

In order to establish the magnitude of the internally generated noise at a low value of jet exit velocity ratio ($V_j/a_0 = 0.32$), both cold and hot, a systematic study was carried out and a typical set of results at 45° to the jet axis is presented in

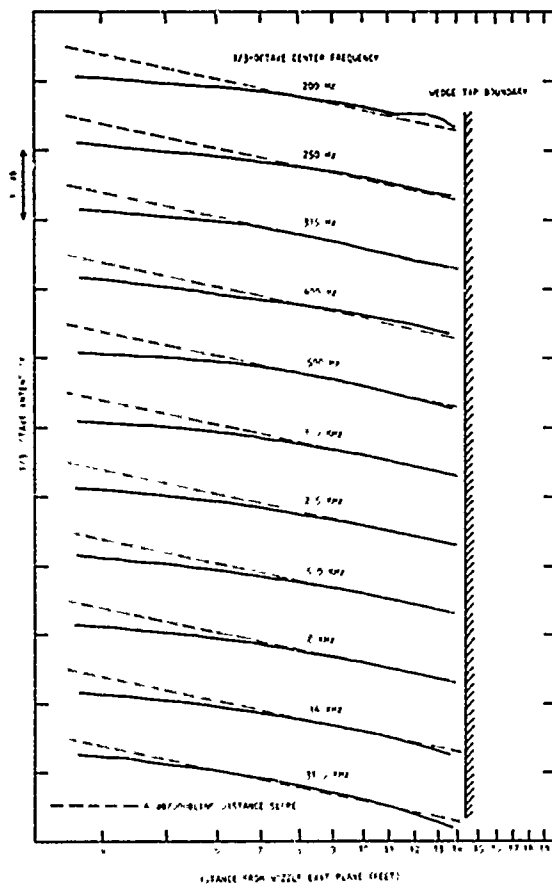


Fig. 34 Intensity-Distance Plots with Cold Jet: $D = 2$ in., $V_j/a_0 = 0.85$, $\theta = 90^\circ$

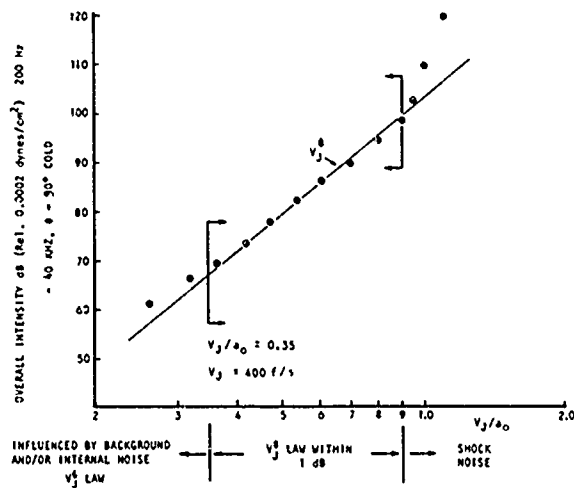


Fig. 35 Velocity Dependence of Overall Intensity at 90° to the Jet Axis

Figure 38. The background/instrumentation noise is given by spectrum A in this figure. Spectrum B represents the turbulent mixing noise for the 2-inch diameter cold jet at $V_J/a_0 = 0.32$. The internal noise for this jet operation condition was estimated by increasing the nozzle diameter to 4 inches and keeping the mass flow through the pipe-work constant. The jet velocity is therefore reduced by a factor of 4, and from the relationship

$$I \propto D^2 V_J^8$$

for the turbulent mixing noise, it can be calculated that the mixing noise will be 42 dB down in this case, while the internal noise will be essentially unaltered. The resulting spectrum C shown in Figure 38, therefore, represents the combined background/instrumentation/internal noise contribution and it will be observed that it is much lower in magnitude than the corresponding mixing noise spectrum B.

Having estimated the internal noise for the cold jet, it is necessary to repeat the exercise for the heated case, since the internal noise spectrum will be different due to the presence of combustion noise. The mixing noise from the heated 2-inch diameter jet ($T_J/T_0 = 2.8$, $V_J/a_0 = 0.32$) is given as spectrum D in Figure 38. This spectrum exhibits the characteristic increase over the corresponding cold jet spectrum B. In order to confirm that this increase is a genuine effect of heating,

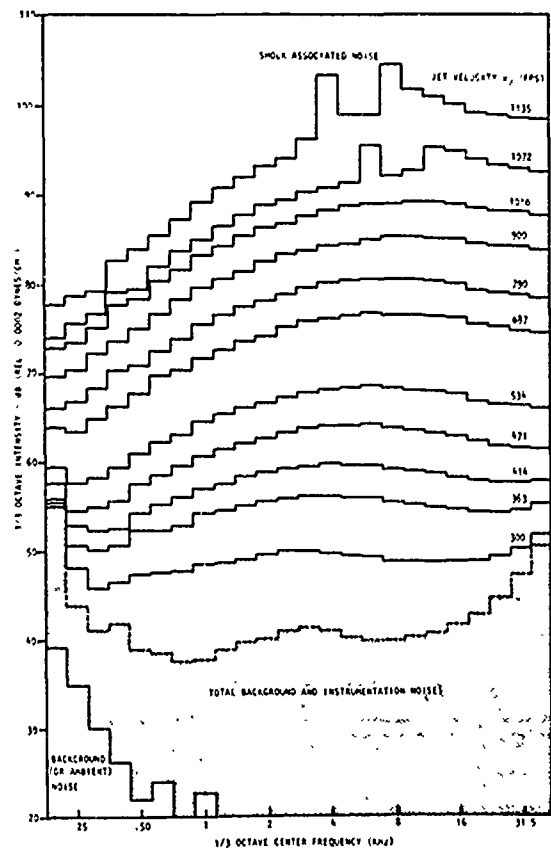


Fig. 36 Jet Noise Spectra at $\theta = 90^\circ$ for Various Jet Velocities

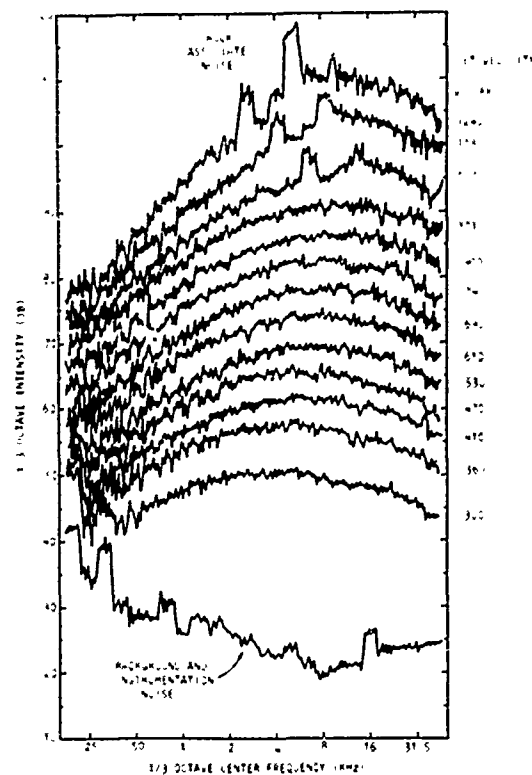


Fig. 37 Jet Noise Spectra at $\theta = 90^\circ$ for Various Jet Velocities - Cold

	V_J/a_0	T_J/T_0
A	0.32	1.0
B	0.32	1.0
C	0.32 (effective)	1.0
D	0.32	2.8
E	0.32 (effective)	2.8

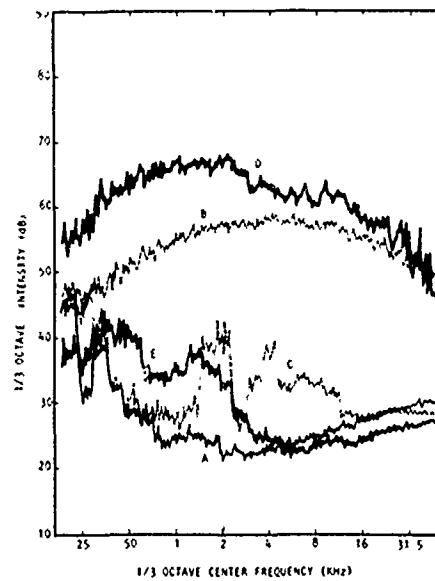


Fig. 38 Turbulent Mixing Noise and Internal Noise Spectra at $\theta = 45^\circ$, Cold and Hot

and not a direct result of the increase in internal noise, the nozzle diameter was increased to 4 inches as before and the mass flow through the pipe-work was kept constant. The resulting spectrum E therefore represents the combined background/instrumentation/internal noise contribution for this heated jet, and once again it is much lower in magnitude than the corresponding mixing noise spectrum D.

In conclusion, therefore, it has been established that the internally generated noise, for cold as well as hot operation of the facility, is not significant at least down to $V_J/a_0 = 0.32$. All data for $V_J/a_0 > 0.32$ obtained from this jet noise rig represent true turbulent mixing noise, unadulterated by internal noise. Due to the limitations imposed by the background and instrumentation noise, however, the lower limit of V_J/a_0 in jet noise experimental programs will be restricted to 0.35.

11-10.4 Jet Performance (or Operating Conditions) Envelope

In order to emphasize the wide range of jet operating conditions that the present facility is capable of providing for supersonic hot jet noise research, a performance chart is presented in Figure 39.

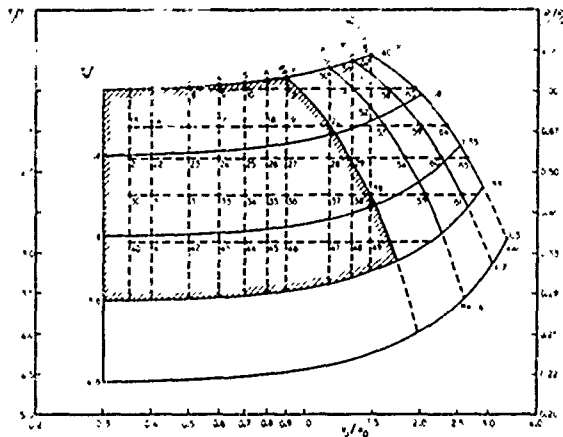


Fig. 39 Jet Performance Envelope

The diagram essentially shows the ranges of jet static temperature ratio T_J/T_0 (and hence also jet density ratio ρ_J/ρ_0) and jet exit velocity ratio V_J/a_0 that can be obtained with the available ranges of stagnation temperature ratio T_R/T_0 and pressure ratio P_R/P_0 . The lower limit of V_J/a_0 (where a_0 is the ambient speed of sound) is set by the measuring instrumentation noise discussed earlier. The four nozzles tested to date are the $M = 1$ convergent nozzle and the $M = 1.4, 1.7$ and 2.0 convergent-divergent nozzles. Noting that the maximum stagnation temperature available at the present time is 1500°F , with pressure ratios up to 8, the portion of the chart for $T_R/T_0 \leq 3.6$ represents the test regime offered by the facility at the present time for jet noise investigations. This capability will be increased even further when the electric after-heater is installed in the near future. Stagnation temperatures of up to 2000°F are estimated and the corresponding additional test regime that the

facility will provide is shown in Figure 39 as the area between the $T_R/T_0 = 3.6$ and 4.6 curves.

For turbulent mixing noise studies, the nozzles must be operated at on-design pressure ratios so that the data will not be contaminated with shock-associated noise. The convergent nozzle can therefore be operated at any pressure ratio up to 1.89 and the corresponding ranges of T_J/T_0 and V_J/a_0 are shown by the shaded area of the chart. In other words, the $M = 1$ nozzle can be used to obtain jet exit conditions ($T_J/T_0, V_J/a_0$) at any point within this shaded area. In contrast, the three convergent-divergent nozzles can be operated at fixed pressure ratios only and hence the jet exit conditions available with these nozzles are represented by the three lines on the right of the shaded area. On the other hand, for shock-associated noise studies, it goes without saying that the nozzles can be operated at any combination of operating conditions within the envelope shown in the figure.

11-11 Conclusions

A new facility, anechoic at all frequencies above 200 Hz, has been designed and built for investigations into supersonic hot jet exhaust noise. There are several special features that make this facility unique:

1. The "acoustic cleanliness" tests have established that the operation of the facility, both cold and hot, is not at all affected by internal noise, at least down to 300 fps. Due to limitations imposed by the background and instrumentation noise, however, the lower limit of jet velocity ratio (V_J/a_0) in jet noise experimental programs will be set at 0.35.
2. The series of rigorous performance evaluation tests, carried out to ensure the accuracy of subsequent jet noise measurements, established that at the proposed distance of 72 nozzle diameters from the jet exit plane, the microphones will be both in the *acoustic* as well as the *geometric* far fields of the jet exhaust.
3. The air supply and air heater system are presently capable of supplying 1500°F air at pressure ratios up to 8 for testing supersonic nozzles. This sufficiently extends the range of current facilities to allow the determination of temperature effects on jet noise. In Appendix III, Tanna, Fisher and Dean have initially evaluated the effects of temperature on jet noise and the wide operating ranges of the facility were very aptly presented in that report. Figure 39 summarizes the performance (or operating conditions) envelope of the facility in terms of jet temperature and exhaust pressure ratio. The higher stagnation temperature ratios up to 4.6 will be reached upon installation of a 300 KW electric heater bank.
4. An acoustically lined exhaust collector injects entrainment air, through the outer channel of the coaxial duct arrangement, in quantities dictated by the particular jet operating condition with no special forced-air injection or fan system.
5. An air gap between the concrete rear collector wall and the false wall created by the wedge boards distributes this entrainment air symmetri-

cally into the room around the jet axis. The air-flow circulation velocities are maintained at a minimum so that the microphones are not affected. Cooling air is supplied for the room lining material during high temperature jet operations and room temperature gradients are kept to a minimum so that noise measurements are unaffected.

6. In addition to providing entrainment and room cooling air the exhaust duct provides an adequate anechoic termination for the jet and attenuates outside ambient noise sources sufficiently so that no

interference will occur even at the lowest noise levels at which measurements will be made in the room.

7. A "cherry picker" crane is used to gain access to instrumentation and test installations for calibration, test set-up modifications, and maintenance, thus eliminating the need for access platforms and their attendant reflection problems. The crane is stowed by remote control from the entrance door under an anechoic cover during all test operations.

APPENDIX III

EFFECT OF TEMPERATURE ON SUPERSONIC JET NOISE†

H. K. Tanna, M. J. Fisher* and P. D. Dean
Lockheed-Georgia Company
Marietta, Georgia

Abstract

The influence of temperature on the sound field of supersonic, shock-free jets is studied experimentally by measuring the turbulent mixing noise in the far field from four 2-inch diameter nozzles, operated in a carefully designed anechoic room which provides a free-field environment. The nozzles were operated at pressure ratios up to 7.40 and over the range of stagnation temperature ratios from unity to 3.3, thus providing exit velocity ratios in the range 0.35 to 2.8. In order to avoid the additional problems of convective amplification and refraction, the effects of temperature on mixing noise source strengths per se are established by examining the data at 90° to the jet axis only. In general, two sources of noise are apparent, one due to the familiar Reynolds shear stress fluctuations and a second attributable to density or temperature fluctuations promoted by the turbulent mixing of streams of dissimilar temperatures. Scaling laws for the velocity and temperature dependencies of the spectra of these noise components are derived and tested. Further, it is shown that these sources are not statistically uncorrelated as previously supposed, but are, it appears, highly correlated. The final predictions in general agree with the measured spectra within 1 to 2 dB.

III-1 Introduction

The influence of flow temperature on jet mixing noise has become a subject of considerable debate within the last two years. Previously, it was commonly accepted that the effect of heating, at a fixed jet efflux velocity, should lead to a noise reduction due to the reduction of the density in the Lighthill source term $\rho v_j v_j$. However, a carefully conducted series of experiments reported by Hoch et al [1] showed that this was true only at jet efflux velocities above about 0.7 times the ambient speed of sound. At velocities below this value, the noise levels increased progressively with increase of jet temperature. These findings have since been amply confirmed by other independent investigations. It has therefore been established that:

1. the effect of jet heating at low jet efflux velocities is to increase the noise radiated, and
2. the effect of jet heating at higher jet efflux velocities is to reduce the noise radiated.

Furthermore, the degree of agreement between the various independent investigators is such that it must now be fully accepted that the noise increase

at low speeds is an effect associated with the jet flow field, and not the result of "rig generated" or excess noise problems. What is not so clear, however, is the physical origin of these effects and their accountability in terms of the Lighthill acoustic analogy approach or other prediction methods.

A major problem in such studies is, of course, that the effects of temperature are relatively weak, particularly in the regime of subsonic jet efflux velocities. This, as we shall show later, is because the decreased contribution of noise due to fluctuating Reynolds shear stresses (the $\rho v_j v_j$ term) is largely compensated by an increased contribution from what we shall term "Temperature Fluctuation Noise." Thus in working in the range $0.5 \leq V_j/a_0 \leq 1.0$, it is often difficult to distinguish, from available experimental data, between a number of apparently contradictory theoretical models which have been published recently [2-6] and all of which claim to be in accord with published measurements.

The objective of the present study was therefore to extend the range of available data to include velocities in the range $0.35 \leq V_j/a_0 \leq 2.8$ with jet stagnation temperature ratios in the range from unity to values in excess of 3. Furthermore, in order to avoid contamination of data in the high velocity range by the presence of shock associated noise, four nozzles (diameter = 2 in.) were employed, namely a convergent nozzle for pressure ratios up to 1.89 and three convergent-divergent nozzles having design Mach numbers of 1.4, 1.7 and 2.0, respectively. These latter were operated only at their design pressure ratios, thus ensuring that observed trends and dependencies were due only to turbulent mixing.

The resulting test plan matrix is shown in Figure 1. It can be seen that by considering test points in each horizontal line it is possible to keep the jet efflux temperature constant while varying the efflux velocity. Conversely, each vertical line maintains constant efflux velocity while varying jet efflux temperature. Throughout this report data will be identified in terms of the test point numbers (TP), shown on Figure 1, an approach which it is hoped will assist the reader's interpretation.

†This research supported by the Air Force Aeropropulsion Laboratory and the U. S. Dept. of Transportation (Contract AF 33615-33-C-2032).

*Lecturer, University of Southampton and Consultant to the Lockheed-Georgia Company where this work was conducted.

Pages 143 and 144 are Blank.

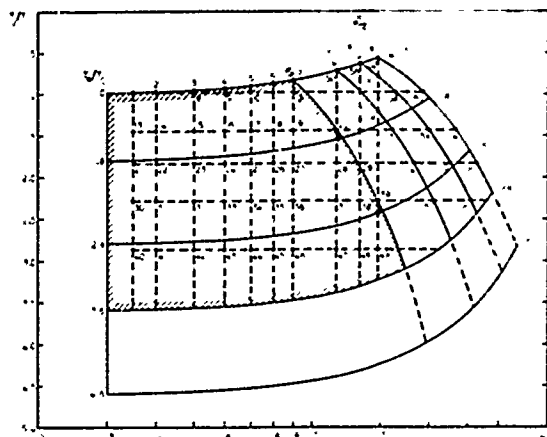


Fig. 1 Experimental Program Chart.

III-2 Facilities and Test Procedure

Much confusion about jet noise has arisen in the past as a direct result of inadequate facilities and insufficient knowledge and control of test conditions. The present facility was carefully designed accounting for other facilities' shortcomings and was guided by the stringent demands of on-going jet noise research at Lockheed. Prior to the design and construction of the facility, a one-sixth scale model of the anechoic room was constructed and a comprehensive series of flow visualization and temperature mapping experiments was conducted. The results of this model study dictated the design of the exhaust collector/muffler to provide entrainment and room cooling air in the quantities demanded by the jet operating conditions. The choice of acoustic wedge material and design was optimized by conducting an extensive series of performance evaluation tests in a specially built impedance tube.

A plan view of the complete hot jet noise facility is shown in Figure 2. The facility is described in detail in Appendix II, [7], and the major points are summarized below.

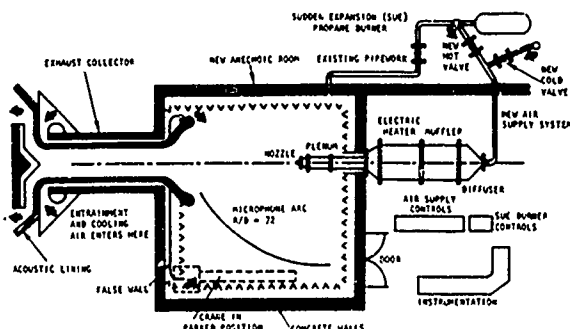


Fig. 2 Supersonic Hot Jet Noise Facility - Plan View.

The anechoic room measures 22' (long) x 20' (wide) x 28' (high) between concrete walls and the flame-retardant wedges are 18 in. long. The room is anechoic at all frequencies above 200 Hz. At the present time, the facility is capable of testing model jets of 2 in. diameter at stagnation temperatures up to 1500°F and pressure ratios as high as 8. The hot air is supplied by the Sudden

Expansion (SUE) Propane Burner. With the planned installation of an electric heater between the muffler and the plenum in the near future, it will be possible to increase the range of stagnation temperatures to 2000°F.

Three special features of the facility are:

1. an acoustically treated exhaust collector that sucks entrainment air through the outer channel in quantities dictated by the particular jet operating condition with no special forced-air injection or fan installation,
2. an air gap between the concrete wall and the false wall on the collector side of the room to distribute this entrainment air symmetrically around the jet axis, as well as to keep the room air-flow circulation velocities to a minimum, and
3. a "cherry-picker" crane used to gain access to instrumentation, etc. for maintenance, calibration and set-up, thus eliminating the need for access platforms. The crane is stowed by remote control under an anechoic cover during all test operations.

The jet/collector axis lies in the horizontal plane 16 ft. above the floor and is displaced by approximately 3.5 ft. from the center of the room. The microphone arc is installed in a diagonal plane in order to maximize the distance from the nozzle exit to 72 nozzle diameters (i.e., $R = 12$ ft. for 2 in. diameter nozzle), and at the same time to remain outside the near field of the wedges. For noise measurements in the forward arc ($\theta > 90^\circ$), provision has been made for moving the nozzle exit plane closer to the exhaust collector by adding an extra plenum section. Thus, the facility is capable of measuring the noise at all angles to the jet axis between 15° and 150° .

III-2.1 Facility Performance Evaluation Tests

In order to confirm the design criteria and to ensure the accuracy of the subsequent jet noise measurements, the facilities were subjected to rigorous performance evaluation tests at appropriate stages. Once again, the results of these tests are described in detail in Appendix II, [7], and only the major findings are summarized below:

1. The overall SPL of background (or ambient) noise in the anechoic room is 45 dB.
2. The attenuation produced by the lined exhaust collector was approximately determined by subjecting the outside end of the collector tunnel to a broadband noise and measuring the 1/3-octave SPL spectrum at the entrance to the tunnel. The measured noise reduction of the collector was 47 dB, being 20 dB in the 200 Hz band and increasing to approximately 60 dB in the 10 KHz band.
3. In order to evaluate the anechoic quality of the room and to ensure that the proposed microphone distance of 12 ft. (72D) is in the acoustic far-field, an audio driver unit placed at the nozzle exit location was used as the sound source (i.e., point source), and the intensity vs. distance plots at various one-third octave frequencies were obtained with a traversing microphone arrangement. These plots established that the cut-off frequency

of the room was 200 Hz and that at a distance of 12 feet, the observer was in the acoustic far-field at all frequencies (above 200 Hz) of interest.

4. Using the same traversing microphone arrangement, a cold jet ($V_j/a_0 = 0.85$) was used as the sound source in a second series of tests, and the intensity-distance plots at various one-third octave frequencies were measured at four angles to the jet axis. At distances greater than 9 ft. from the nozzle exit plane, the intensity conformed to "inverse-square law," except at frequencies above 8 KHz where the decay was somewhat sharper because of the increasing atmospheric attenuation with frequency. Hence, it was established that for frequencies above 200 Hz, the acoustic interference produced by sources distributed over a finite region of the jet exhaust flow does not affect the "inverse-square law" decay of intensity for observer distances greater than approximately 5λ nozzle diameters.

5. The "acoustic cleanliness" or internal noise aspect of the rig was examined by employing the usual method of measuring the noise from a cold convergent nozzle at 90° to the jet axis and studying its velocity dependence. It was found that the overall SPL followed a V_j^8 law within 1 dB between the velocities of 400 and 1000 fps, whereas at velocities below 400 fps the levels were higher. Two points need to be made here. First, a careful examination of the spectra at velocities below 400 fps, together with the combined spectrum of background and instrumentation noise, revealed that at these low jet velocities, the low frequencies were being lifted by the room ambient or background noise and the high frequencies were being lifted by the instrumentation noise. Hence, it appears that the acoustic cleanliness of the rig is not at all affected by internal noise; at least down to 300 fps, where the tests were terminated. Due to the limitations imposed by the background and instrumentation noise, however, the lower limit for V_j/a_0 in the test program will be 0.35. The second point to be made here is that although the results followed the V_j^8 law within 1 dB over the velocity range of 400 to 1000 fps, a $V_j^{7.5}$ slope also agreed with the measurements equally convincingly. Hence, it was decided to study the corresponding spectral results. The spectra were first collapsed on the V_j^8 basis, and then on the $V_j^{7.5}$ basis. It was observed that while the first collapse resulted into closely spaced parallel curves, the second collapse was convincingly better. It appears therefore that the $V_j^{7.5}$ power law is more appropriate. This point is discussed in greater detail in the later sections of this paper. For the moment, however, it is important to realize that deriving velocity dependencies from overall results, especially over a limited range of velocities, could lead to misleading conclusions, and it is more appropriate to examine the spectral results.

III-2.2 Data Acquisition

In the present experimental program, twelve 1/2 inch B&K microphones Type 4133 with FET cathode followers Type 2619 were mounted on the microphone arc at $7\frac{1}{2}^\circ$ intervals from 15° to $97\frac{1}{2}^\circ$. The responses were recorded simultaneously on a 14-channel Honeywell FM tape recorder at 120 inches per second (ips). In order to obtain the 1/3-octave spectrum from 200 Hz to 40 KHz using a

Hewlett-Packard real time 1/3-octave audio spectrum analyzer, the tape speed was reduced to 30 ips on playback. The 1/3-octave levels were then recorded on an incremental tape recorder for subsequent detailed analysis using a data reduction program developed for use on the Univac 418 digital computer. This program incorporates the microphone frequency response corrections and atmospheric absorption corrections. The results are finally displayed to include test conditions and computed jet flow parameters, 1/3-octave acoustic spectra, and computed overall sound pressure levels. The day-to-day repeatability of the complete measurement and analysis system is ± 0.5 dB.

III-2.3 Experimental Program Chart

The test point diagram, introduced earlier and shown in Figure 1, is now described in a little more detail. The diagram essentially showed the ranges of jet static temperature ratio T_j/T_0 (and hence also jet density ratio ρ_j/ρ_0) and jet exit velocity ratio V_j/a_0 that can be obtained with the available ranges of stagnation temperature ratio T_R/T_0 and pressure ratio P_R/P_0 . The lower limit of V_j/a_0 is set by the performance of the facility, discussed earlier. The four nozzles employed are the $M = 1$ convergent nozzle and the $M = 1.4, 1.7$ and 2.0 convergent-divergent nozzles. Since the maximum stagnation temperature available at the present time is limited to 1500°F , the portion of the chart above the $T_R/T_0 = 3.6$ curve represents the regime used in the present test series, while the portion of the chart below this curve represents the additional regime that will be available in the near future when the electric heater is installed.

In the present study of turbulent mixing noise, the nozzles must be operated at on-design pressure ratios so that the data will not be contaminated with shock-associated noise. The convergent nozzle can therefore be operated at any pressure ratio up to 1.89 and the corresponding ranges of T_j/T_0 and V_j/a_0 are shown by the shaded area of the chart. In other words, the $M = 1$ nozzle can be used to obtain jet exit conditions ($T_j/T_0, V_j/a_0$) at any point within this shaded area. In contrast, the three convergent-divergent nozzles can be operated at fixed pressure ratios only and hence the jet exit conditions available with these nozzles are represented by the three lines on the right of the shaded area.

An important feature of high temperature flows which must not be overlooked is the variation of the specific heat ratio γ with temperature. For dry air, the value of γ is 1.40 at ambient temperature and it decreases steadily to 1.31 at 2000°F . This variation is not negligible in the current calculations of jet flow parameters. For example, if the $M = 1.4$ nozzle is operated at the stagnation temperature of 2000°F , the values of T_j/T_0 and V_j/a_0 calculated by assuming $\gamma = 1.40$ would underestimate the actual values by approximately 5%. Hence, it was essential to incorporate the variation of γ with temperature in the preparation of the chart of Figure 1.

Having prepared this chart, the task of selecting the test conditions for a systematic study of the influence of temperature on mixing noise was relatively straightforward. A total of 65 jet exit

conditions (T_J/T_0 , V_J/a_0) were in fact chosen, and these are identified by test point numbers (TP) in Figure 1. For each TP, the jet operating conditions (T_R/T_0 , P_R/P_0) were first calculated by using $\gamma = 1.40$. Having obtained the first estimate of the stagnation temperature ratio T_R/T_0 , the correct value of γ was then used to calculate the more accurate values of T_R/T_0 and P_R/P_0 .

III-3 Theoretical Considerations

We have already alluded above to a degree of conflict between a number of theoretical models which have been presented recently, each of which claims to follow the observed trends of the noise as a function of temperature. With the exception of Mani [6], who considers the acoustic power spectra, the remainder concentrate on the noise radiated at 90° to the jet axis in the interest of avoiding additional, and still poorly understood, problems of convective amplification and refraction. The present authors endorse and therefore follow this philosophy in the belief that an improved fundamental understanding of the influence of temperature on mixing noise source strengths per se must not be further confused by refractive or other influences. Thus, while the test program of Figure 1 included acoustic measurements at all angles between 15° and 97.5° to the jet axis, only those at 90° are considered in the present context.

The first attempt to rationalize the observed increase of noise with increasing temperature at low jet speeds by other than purely empirical devices, appears to be due to Lush [2], a summary of which is also given in [3]. To follow this approach and those of [4] and [5], it is convenient to express Lighthill's acoustic analogy equation for sound generation in an arbitrary fluid flow (neglecting viscous stresses) in terms of pressure. In the absence of body forces and fluctuating mass addition it is:^{*}

$$\frac{\partial^2 p}{\partial t^2} - a_0^2 \nabla^2 p = a_0^2 \frac{\partial^2}{\partial x_i \partial x_j} (\rho v_i v_j) + \frac{\partial^2}{\partial r^2} (p - a_0^2 \rho). \quad (1)$$

Following standard procedures this equation predicts a far field acoustic pressure which scales according to

$$p(r, t) \sim \frac{1}{r} \frac{\partial^2}{\partial t^2} [\rho v_r^2 + (p - a_0^2 \rho)]_{t-r/a_0} \quad (2)$$

Lush in his approach to the problem chose to split the density fluctuation into a portion which was isentropically related to the pressure and a remainder due to entropy fluctuations. Thus, equation (2) becomes

$$p(r, t) \sim \frac{1}{r} \frac{\partial^2}{\partial t^2} [\rho_s v_r^2 + p(1 - (\frac{a_0}{c_s})^2) + \frac{\rho_s a_0^2 s'}{c_p}] \quad (3)$$

*A list of symbols is included in the Section III-11

With the assumptions that:

1. The source region density can be taken as the geometric mean of that in the jet potential core and that of the ambient fluid (i.e., $\rho_s = (\rho_j \rho_0)^{1/2}$).
2. The middle term of the rhs of (3) is unimportant,
3. The entropy fluctuations, s' , are proportional to the difference of the mean entropy values across the shear layer, and
4. The remaining two terms represent uncorrelated sources,

Lush tested the resulting scaling law for the intensity model,

$$I = A \left(\frac{V_J}{a_0}\right)^6 + B \left(\frac{V_J}{a_0}\right)^4. \quad (4)$$

In the above equation, the anticipated temperature dependencies of A and B are respectively

$$A \propto \left(\frac{T_J}{T_0}\right)^{-1} \quad \text{and} \quad B \propto \left(\frac{T_J}{T_0}\right)^{-1} (\log_e \frac{T_J}{T_0})^2. \quad (5)$$

We also note for future reference that for practical values of the jet static temperature ratio, T_J/T_0 , the second dependence can be approximated by

$$B \propto \left(\frac{T_J - T_0}{T_J}\right)^2. \quad (6)$$

The dependences predicted by equations (4) and (5) were examined in considerable detail and found to conform in an acceptable manner to the measured data then available, the majority of which was for subsonic jet efflux velocities. A comparison with the current data is presented in Section III-4.

Morfe [4], in considering a more general problem, has also alluded to the observed variations of jet noise with temperature. The starting point of his analysis is again equation (1). However, it is also claimed that if, in deriving (1) the influences of viscosity and heat conduction are neglected, then entropy must be conserved in the jet flow in a true Lagrangian reference frame. Hence, density and pressure are related more generally by

$$\frac{D^2 p}{Dt^2} = a^2 \frac{D^2 \rho}{Dt^2}. \quad (7)$$

Development of this approach leads Morfe to conclude that for a jet flow in which temperature or density inhomogeneities exist, two source terms will exist. The first is $\rho_0 v_i v_j$, which is the familiar Reynolds shear stress term, but with the difference that the density is now to be evaluated at ambient temperature and not at some estimated source region temperature. The second term is of the form

$$\frac{\rho - \rho_0}{\rho} \frac{\partial p}{\partial x_i}$$

which with the assumption that the pressure fluctuations scale as $\rho_s V_J^2$, leads to an acoustic intensity dependence for this term of the form

$$\left(\frac{T_s - T_0}{T_s}\right)^2 \left(\frac{V_J}{a_0}\right)^6$$

The differences between Lush's model and this model are of significance. First, Lush suggests a decreased contribution from the Reynolds shear stress term (the $(V_J/a_0)^8$ term) as the jet efflux temperature increases. Morfey, however, suggests that this term remains independent of temperature. Second, although both models predict the presence of an additional noise source if the jet temperature is different from that of the ambient, the velocity dependencies are different, being $(V_J/a_0)^4$ and $(V_J/a_0)^6$, respectively. It must also be pointed out that Morfey's model, as it stands, would not predict the observed decrease of noise with increased jet temperature at high velocities. He argues however that at these higher speeds the wavelength of the higher frequency sound becomes small compared to the shear layer thickness. In this situation the expression for acoustic intensity from Reynolds shear stress fluctuations, namely

$$I \sim \frac{\rho_s^2 V_J^8}{\rho a^5} \quad (8)$$

should be evaluated in its entirety at the source temperature. Thus, it is suggested that at high jet efflux velocities the lower frequency sound should be independent of jet temperature, while the higher frequencies should diminish as $(T_0/T_s)^{7/2}$. This indeed may appear a rather attractive possibility in view of the empirical observation by Hoch et al [1] that the noise output at the highest jet velocities diminished as $(T_0/T_J)^2$ which is close to the suggestion above if one assumes, as Lush has, that the source temperature is proportional to the square root of the jet efflux temperature.

The final theoretical model which deserves attention in the light of the present work is that published recently by Lilley [5]. In this work the wave equation (1) is re-derived utilizing a conservation of energy equation in addition to the usual mass and momentum equations. The result essentially is to replace the pressure term on the rhs of equation (1) by a combination of enthalpy and density. The predicted scaling law for the intensity is then obtained as

$$I \sim A \left(\frac{V_J}{a_0}\right)^8 + B \left(\frac{V_J}{a_0}\right)^6 + C \left(\frac{V_J}{a_0}\right)^4 \quad (9)$$

which appears to offer a compromise between the work of [2] and [4]. It is also shown that the value of C/A is similar to the ratio of the fourth and eighth power of velocity terms of Lush's expression, while B/A is relatively negligible if the stagnation enthalpy of the jet flow is much higher than that of the ambient air. It was concluded therefore that while the $(V_J/a_0)^6$ term does exist, the range of velocities over which it is of significance would be too limited to make its presence clearly apparent in general experimental comparisons.

It was against this background of previous work that the present investigation was undertaken. One thing had become clear. The essential differences between the various scaling laws arose principally because of the manipulations of the $(p - a_0^2)$ term in equation (1) in terms of different sets of flow variables. However, in each case, having established a set of source terms each investigator then assumed that the sources so represented were uncorrelated in the statistical sense. As we shall demonstrate later, correlation between source terms is clearly apparent from the measured data and it is probably in the neglect of such effects that many of the apparent differences between the various approaches have arisen.

In this light therefore two important principles were established at the outset of this work:

1. The source terms to be scaled should be chosen such that, as far as possible, an independent check of the character and dependence of each could be carried out in some appropriate regime of flow velocity and temperature.

2. In the light of Morfey's suggestion that high and low frequencies might behave differently, all analysis should be performed in terms of spectra instead of merely utilizing overall sound pressure levels.

III-4 Presentation of Data

In the course of this investigation, data from a total of more than sixty test points were measured and analyzed, covering the range of variables shown in Figure 1. The purpose of this section is to present a few typical results in order to display, in a preliminary manner, the major effects of temperature on the noise spectra and the variation of these effects throughout the speed range.

Figure 3 shows a comparison of measured spectra at low speed, $V_J/a_0 = 0.4$, for the isothermal jet (TP 2, see Figure 1) and at the highest temperature employed (TP 41). The isothermal jet shows the characteristic broad band spectrum while the effect of elevated temperature is clearly to provide a significant noise increase particularly in the lower frequencies.

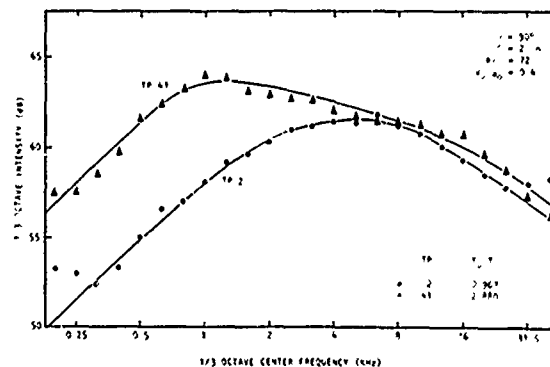


Fig. 3 Effect of Temperature on Jet Noise at Low Velocity ($V_J/a_0 = 0.4$).

Results for a medium velocity, $V_J/a_0 = 0.8$, are shown in Figure 4. Here all measurements on the constant velocity line between TP 6 and TP 45 have

been included. At first sight it is tempting to conclude that the lower frequency portion of the spectrum is independent of temperature, while clearly the higher frequencies decrease progressively with increased temperature. Indeed this would be in full accord with the suggestions of Morfey outlined above if one assumes that at this velocity the fluctuating Reynolds stresses are the dominant contributors to the noise field.

However, a more careful review of the data, at a series of velocities in this region, indicated that this is an oversimplified view. As can be seen from Figure 4 the levels at these lower frequencies first decrease as one proceeds from TP 6 to TP 18 and then begin to increase again as the temperature is further increased. As we shall see later, this is because the decrease of the Reynolds shear stress contribution with increased temperature is more than compensated by the temperature fluctuation noise.

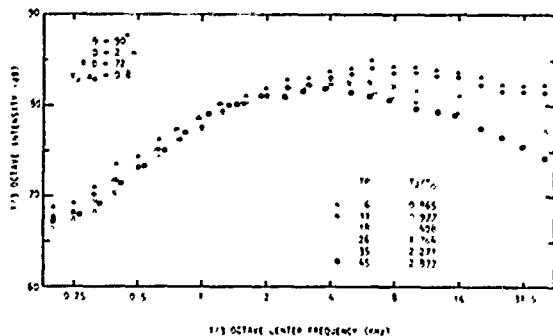


Fig. 4 Effect of Temperature on Jet Noise at Medium Velocity ($V_j/a_0 = 0.8$).

Confirmation that the Reynolds shear stress contribution (i.e., $\rho v_i v_j$) does decrease progressively with increased temperature is shown in Figure 5.

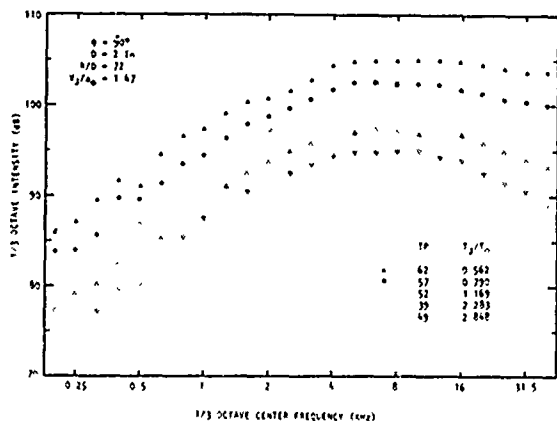


Fig. 5 Effect of Temperature on Jet Noise at High Velocity ($V_j/a_0 = 1.47$).

As can be seen from Figure 1 this data for $V_j/a_0 = 1.47$, covering the vertical line from TP 62 to TP 49 (Figure 1), yields the largest range of jet efflux temperature available in the present test series. Furthermore, irrespective of the theoretical model chosen one would anticipate maximum contribution from this source term at these high velocities. The fact therefore that a progressive decrease of level at all frequencies with in-

creasing temperature is clearly apparent at this high, but constant, jet efflux velocity does indicate a temperature dependence for this particular source mechanism, contrary to Morfey's suggestion that the low frequencies should be temperature independent.

One further point regarding the data of Figure 5 must be made at this stage. It will be noted that in the high frequency range, above 10 KHz, the spectrum for TP 52 actually crosses that for the lower temperature TP 57. It was thought at first that this was indicative of shock associated noise, due perhaps to poor "on-design" operation of this particular $M = 1.40$ nozzle. However, a systematic study of other data indicated that this apparently erroneous high frequency contribution occurred irrespective of the velocity line considered and was always associated with the test point on that line for which the jet efflux temperature was closest to the ambient temperature. To put the point another way, it was observed that the rate of decrease of spectral level above 10 KHz was always at a minimum when the jet was operated so that the jet efflux temperature was close to ambient. When the jet temperature was different from the ambient, irrespective of the direction of this difference, a more rapid decrease was observed. We shall return to this point again towards the end of this paper.

To summarize therefore, the major points revealed by this preliminary data review are:

1. The effect of operating the jet at high temperature and low speed is to generate an additional noise source whose spectral characteristics are distinctly different from those of the Reynolds shear stress contribution (Figure 3).

2. At high speeds where the Reynolds shear stress contribution is anticipated to predominate, the progressive decrease of measured levels with increasing temperature over the entire frequency range (Figure 5) suggests that this contribution is indeed temperature dependent.

From the latter in particular, therefore, it appeared that the current data agreed more with the type of model postulated by Lush [2] than that of Morfey [4]. Hence, it was decided to compare the overall sound pressure levels measured in this present series with the prediction method given in [3]. This involves essentially the use of equations (4) and (5) of the present paper, the actual values of the quantities A and B being obtained from the best fit theoretical curves given in Figure 11 of reference [3].

The result of this comparison is shown in Figure 6. The major result is clearly for the theoretical model to overestimate the measured levels for values in excess of about 100 dB. Furthermore, because of the strong dependence of these levels on jet velocity, it is possible to define the area of the experimental program chart, shown in Figure 1, from which they arise. They are in fact all points for which $V_j/a_0 > 1$. However, it should also be noted that the tendency for the measured points to be below the prediction occurs irrespective of whether convergent or convergent-divergent nozzles are employed to obtain these velocities. In the region where the levels are below about 100 dB (i.e., $V_j/a_0 < 1.0$), the agreement is generally

excellent (except at very low velocities), the majority of the points agreeing within ± 1 dB. Of course, since this is the range of velocities for which data for this particular prediction technique were derived, this agreement demonstrates only that the data of the present test series are compatible with those of previous independent investigations.*

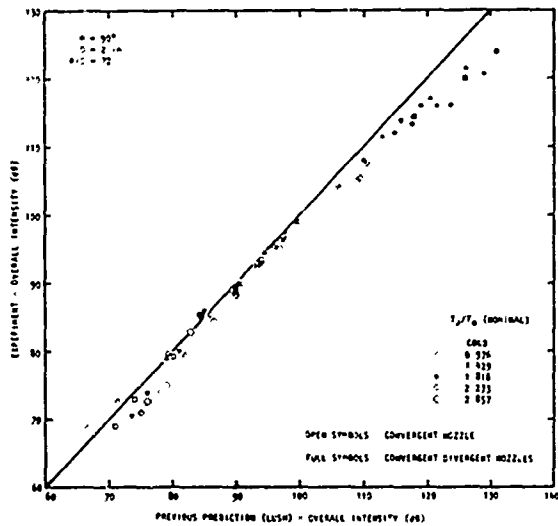


Fig. 6 Comparison of Experiment with Previous Prediction Model (Lush): Overall Intensity at $\theta = 90^\circ$.

An important feature is in fact revealed by the comparison presented in Figure 6. We have already stated that irrespective of the theoretical model adopted one would anticipate that the Reynolds shear stress contribution ($\rho v_j v_j$) would predominate at high velocities. The fact therefore that Figure 6 does not show good agreement at high velocities indicates that either the velocity or temperature dependence or both of these terms are incorrectly predicted by equations (4) and (5). The first essential step therefore is to establish the correct scaling for the Reynolds shear stress term by utilizing the data where the additional temperature (or entropy) source would be negligible.

III-5 The Model

To this end the following scaling law model was adopted. Following previous discussion we anticipate the amplitude of the far-field acoustic pressure at a fixed large distance from the nozzle to scale in accordance with

$$p = \frac{\partial^2}{\partial t^2} [\rho_s v_r^2 + (\rho - a_0^2 \rho)]. \quad (10)$$

We now divide the density fluctuations into a portion ρ'_A , which are due to any acoustic pressure fluctuations in the source region and which are therefore isentropically related to pressure (i.e., $\rho'_A = a_0^2 p'$). The remaining density changes, ρ'_T , are assumed to be those due to temperature fluctuations at constant pressure, promoted by the turbulent

mixing of the jet efflux with the ambient air. Thus equation (10) becomes

$$p = \frac{\partial^2}{\partial t^2} [\rho_s v_r^2 + \rho' (1 - \frac{a_0^2}{a_s^2}) - a_0^2 \rho'_T]. \quad (11)$$

This division sheds some light on the physical significance of the middle term on rhs of (11). It occurs as a result of the existence of acoustic pressure fluctuations in a source region which is at a temperature different from that in the far-field. It remains as a finite source however only if the temperature difference is maintained. The existence of the same amplitude pressure fluctuations in a source region at ambient temperature would not yield such a source. It is very tentatively suggested therefore that this term represents an effective source which in some way describes the transmission of acoustic waves between media of differing sound speeds. We shall present more circumstantial evidence to support this view later, but for the moment this "effective source" will be ignored in favor of the remaining two. If finally it is assumed that the amplitude of the temperature fluctuation promoted density changes ρ'_T are proportional to the change of mean density across the shear layer, then for the present experiments in which the mean static pressure was constant across the shear layer, we may write

$$\frac{\rho'_T}{\rho_0} \propto \frac{\rho_J - \rho_0}{\rho_0} = -\left(\frac{T_J - T_0}{T_J}\right) \quad (12)$$

This then permits us to write equation (11) in a form suitable for a scaling law investigation, namely

$$p = K_1 \left(\frac{\rho_s}{\rho_0}\right) \left(\frac{V_J}{a_0}\right)^2 \left(\frac{V_J}{a_0}\right)^n + K_2 \left(\frac{T_J}{T_0}\right) \left(\frac{V_J}{a_0}\right)^2, \quad (13)$$

where K_1 and K_2 are constants to be determined empirically. It will also be noted that, for the moment, the power law dependence on velocity of the Reynolds shear stress term has been left to be determined. The $(V_J/a_0)^2$ portion of the dependence arises from the second time derivative on the assumption, confirmed later, of the Strouhal number dependence of the acoustic radiation. The value of n , however, depends essentially on the variation of mean square turbulence level with velocity.

III-6 Scaling Laws and Master Spectra

III-6.1 Reynolds Shear Stress Noise

III-6.1.1 Velocity Dependence

Equation (13) suggests clearly that the velocity dependence of the Reynolds shear stress contribution should be obtained from data for which the jet efflux temperature is equal to the ambient. In this case the second term on the rhs of (13) is precisely zero as would be the middle term of (11) had we retained it. The velocity dependence was therefore obtained from spectra measured along the horizontal line of Figure 1, joining test points 1 and 63. An initial attempt to collapse these

*Although Lockheed-Georgia Co. results were cited in [3], those results were obtained in a previous investigation prior to the utilization of the current larger and improved anechoic facility.

spectra on the usual basis of plotting

$$SPL(\omega) - 80 \log_{10} \left(\frac{V_J}{a_0} \right) \text{ vs } \frac{fD}{V_J}$$

was not entirely successful. It was found that a series of accurately parallel curves resulted, but with a clearly pronounced trend for the values to decrease with increasing speed. In fact, between $V_J/a_0 = 0.5$ and 2.0 a 3 dB spread had resulted. It may appear, at first sight, that a difference of 3 dB over a velocity ratio of four is unimportant. However, it must be pointed out that on the basis of regarding the source temperature as a geometric mean of the jet efflux and ambient temperatures, this 3 dB decrease would correspond to a ratio of $T_J/T_0 = 2.0$, which is not an insignificant temperature rise.

A 3 dB discrepancy on an eighth power basis over a velocity increased by a factor of four suggests that a more accurate power law would be $(V_J/a_0)^{7.5}$. This was examined and found to collapse the spectra over the entire velocity range to an accuracy of ± 1 dB, this range being principally a scatter within experimental tolerance, rather than a consistent trend as for the previous case. The resulting spectrum, scaled to $(V_J/a_0) = 1$ for future use as outlined below, is shown in Figure 7. A computer program, described below, was designed to use this spectrum as input and then to calculate anticipated spectra for any other velocity (and later temperature) using the relationship,

$$S(\omega) = S(\omega_s) \left(\frac{V_J}{a_0} \right)^{7.5}, \quad (14)$$

where $\omega/\omega_s = V_J/a_0$ and $S(\omega_s)$ is the "master Reynolds shear stress noise spectrum" shown in Figure 7.

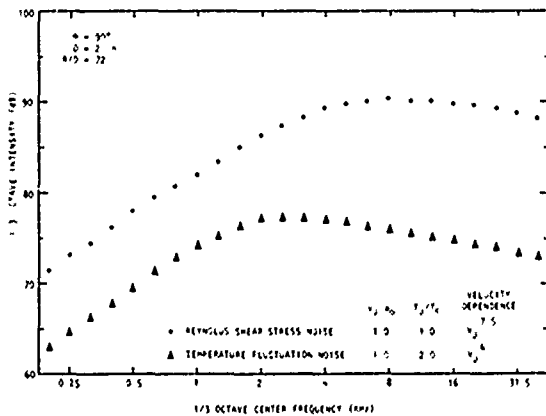


Fig. 7 Master Spectra for Reynolds Shear Stress Noise and Temperature Fluctuations Noise.

The utility and accuracy of this technique is shown in Figure 8, where a direct comparison is made between the predicted and measured spectra between TP 8 ($V_J/a_0 = 0.5$) and TP 63 ($V_J/a_0 = 2.0$).

It is necessary nevertheless to attempt to justify a power of $V_J^{7.5}$ rather than the normal V_J^8 . First, it should be mentioned that in reference [3] a similar problem was experienced with data from an

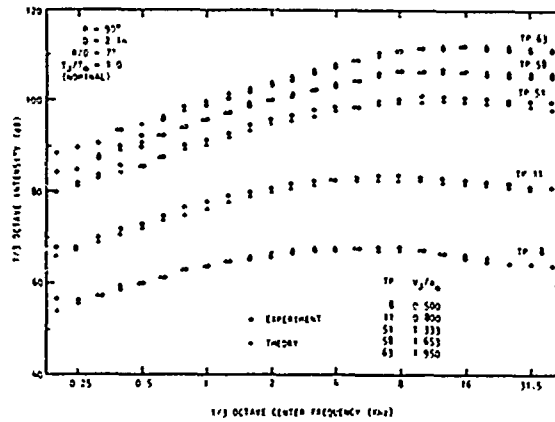


Fig. 8 Shear Stress Noise ($T_J/T_0 = 1$): Comparison of Measurements with Theoretical Model.

unheated jet when attempts were made to replot the data on a linear rather than the normal logarithmic (dB) amplitude scales, so that the suggestion of a velocity index slightly less than eight is not peculiar to the present data. We very tentatively attribute it to a minor reduction in the relative turbulent intensity as the jet velocity increases. Consideration of equations (11) and (13) indicate that the presently postulated $V_J^{7.5}$ law would correspond to a relationship between the rms turbulence level and jet velocity of the form

$$\sqrt{v_r^2} \propto V_J^{0.875}$$

To put these numbers into perspective this suggests that the normally accepted peak turbulence level of 14.5% measured at velocities of order $V_J/a_0 = 0.5$ might decrease to about 12% at $V_J/a_0 = 2.0$. This point should certainly be re-examined when Laser Doppler Velocimeter measurement techniques of sufficient accuracy at these higher speeds become available.

III-6.1.2 Temperature Dependence

Having established a velocity scaling law for the isothermal jet, the next problem was clearly the examination of the temperature dependence of the Reynolds shear stress contribution. Equation (13) clearly indicates that this should be performed at high velocity to minimize the relative contribution of the temperature fluctuation term. It was therefore decided to investigate the dependence in terms of the data previously presented in Figure 5 (i.e., $V_J/a_0 = 1.47$). This offers the additional advantage of yielding jet efflux temperatures on both sides of ambient in the range $0.56 \leq T_J/T_0 \leq 2.88$. The first attempt employed the previous concept of assuming that the source density was the geometric mean of the jet efflux and ambient density. The result of plotting the relevant relationship, namely,

$$SPL(\omega) + 10 \log_{10} \frac{T_J}{T_0} \text{ vs frequency}$$

is shown in Figure 9. It is clear that while compared to Figure 5 the data spread is much reduced,

a consistent trend still exists, indicating perhaps that the source temperature variation has been underestimated.

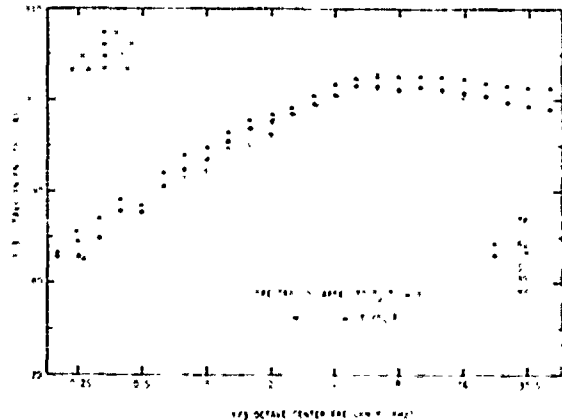


Fig. 9 High Velocity Spectra Collapse Using $T_s/T_o = (T_J/T_o)^{1/2}$

This is of course a feature to be expected from the geometric mean approach, in spite of its power law convenience. This is demonstrated in Table 1 below where estimates of source temperature based on geometric and arithmetic means of jet efflux and ambient temperature are compared.

Table 1. Source Temperature Models

T_J/T_o	$T_s/T_o = \sqrt{T_J/T_o}$	$T_s/T_o = (T_J+T_o)/2T_o$	$T_s/T_o = 0.7(T_J/T_o - 1) + 1.0$
	Geom. Mean	Arith. Mean	Current Prediction
1.5	1.224	1.25	1.35
2.0	1.414	1.50	1.70
3.0	1.732	2.00	2.40
4.0	2.000	2.50	3.10
5.0	2.236	3.00	3.80

If similar temperature profiles are assumed, then the effect of utilizing geometric means is essentially to "push" the source further towards the outside of the shear layer. At this point it was decided to utilize some well known properties of jet shear layers to find an alternative method of estimating the required source temperatures. The region of maximum turbulent intensity occurs at a point where the mean velocity is of order 0.7 times the jet efflux velocity. If this is the major source region, and assuming that temperature and velocity profiles are rather similar, the logical choice for a source temperature is

$$T_s = 0.7 (T_J - T_o) + T_o \quad (15)$$

The effect of this choice as a function of jet static temperature ratio is also shown in Table 1, where it is clear that considerably higher source temperatures result.

The result of employing the correction,

$$SPL(\omega) + 20 \log_{10} \left(\frac{T_s}{T_o} \right)$$

[where T_s is given by (15)],

to the data of Figure 5 is shown in Figure 10. In comparison with Figure 9 it appears that a much improved collapse has been obtained. Values of source temperature were henceforth based on this relationship. Some scatter does still exist in the higher frequencies and we shall return to this point later.

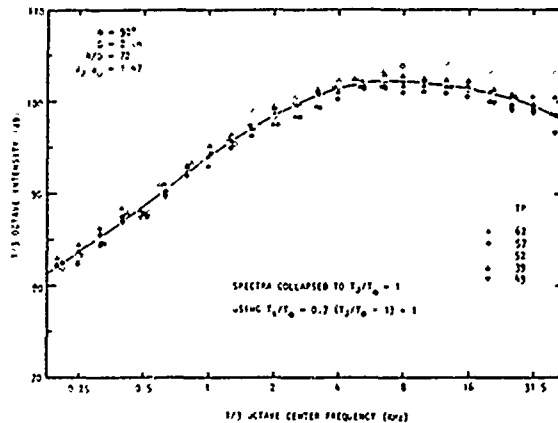


Fig. 10 High Velocity Spectra Collapse Using $T_s/T_o = 0.7 (T_J/T_o - 1) + 1$

III-6.1.3 Total Dependence

To summarize, it appears that the acoustic intensity generated by the Reynolds shear stress contribution varies in accordance with

$$I \sim \left(\frac{T_s}{T_o} \right)^{-2} \left(\frac{V_J}{a_o} \right)^{7.5} \quad (16)$$

where $T_s = 0.7 (T_J - T_o) + T_o$.

Spectral levels generated by this component can be calculated from the expression

$$S_m(\omega) = S_m(\omega_s) \left(\frac{T_s}{T_o} \right)^{-2} \left(\frac{V_J}{a_o} \right)^{7.5}, \quad (17)$$

where $\omega/\omega_s = (V_J/a_o)$ and $S_m(\omega_s)$ is the master Reynolds shear stress spectrum shown in Figure 7.

III-6.2 Temperature Fluctuation Noise

The remaining problem is clearly to define the spectral characteristics and levels to be associated with the temperature fluctuation noise spectrum which was so clearly apparent in Figure 3. Furthermore, as can be shown from the data in this velocity range the extra contribution will be dominant if the temperature scaling of the Reynolds shear stress term given in (16) above is accepted. That is, the spectrum given in Figure 3 for TP 2 must be reduced by a further 7.3 dB to obtain an estimate of the Reynolds shear stress contribution at TP 41 for which $T_s/T_o = 2.316$. Thus, it appeared that in the region of test points 30, 31, 40 and 41 the measured spectra could, for all practical purposes, be regarded as those due to the temperature fluctuation source alone. The spectra measured at these four test points were then scaled in accordance with the assumed dependence of this term given in equation (13) to a common velocity,

$V_j/a_0 = 1$, and ratio of temperature difference to jet efflux temperature, $\Delta T/T_j = \frac{1}{2}$, with, of course, due allowance for Strouhal number scaling of the frequencies. The resulting mean curve, labelled temperature fluctuation noise master spectrum is shown in Figure 7, while the actual data points showed a scatter of up to 1 dB about this mean line.

It is, of course, readily admitted that this is not conclusive proof that this is the correct scaling for this term. The jet conditions are necessarily rather similar — the maximum difference in the scaling factors being only 3.8 dB. However, within this limitation the contribution of the temperature fluctuation term can be written as

$$S_T(\omega) = S_T(\omega_s) \left(\frac{2\Delta T}{T_j}\right)^2 \left(\frac{V_j}{a_0}\right)^4, \quad (18)$$

where $S_T(\omega_s)$ is the "master temperature fluctuation noise spectrum" given in Figure 7 for $V_j/a_0 = 1$ and $\Delta T/T_j = \frac{1}{2}$ and as before, $\omega/\omega_s = V_j/a_0$.

The crucial test however is to see whether the sum of the contributions given by equations (17) and (18) will predict the measured spectra over the entire velocity and temperature range. This is discussed in the following section.

III-7 Comparison of Model with Experiment

III-7.1 Uncorrelated Sources

In order to test the scaling laws of equations (17) and (18) for the contributions of Reynolds shear stress and temperature fluctuation noise, respectively, a computer program was prepared which calculates the scaled contribution of each source separately and then sums the two. The quantity calculated initially was therefore

$$S(\omega) = S_m(\omega_s) \left(\frac{T_s}{T_0}\right)^{-2} \left(\frac{V_j}{a_0}\right)^{7.5} + S_T(\omega_s) \left(\frac{2\Delta T}{T_j}\right)^2 \left(\frac{V_j}{a_0}\right)^4, \quad (19)$$

where $S_m(\omega_s)$ is the master shear stress noise spectrum of Figure 7 and $S_T(\omega_s)$ is the corresponding temperature fluctuation source spectrum. It should be noted here that equation (19) makes the implicit assumption that the two noise sources are completely uncorrelated in the statistical sense.

A comparison between the theoretical levels from equation (19) and those measured is shown in Figure 11 for selected points on the constant T_j/T_0 line joining TP 30 and TP 55. This is chosen as typical because it encompasses a regime where the relative importance of the two terms of equation (19) "switch-over" entirely through this velocity range. It can be seen that while agreement is reasonable at the extremes of velocity (i.e., TP's 30 and 55) there is a definite tendency for the calculation to underestimate the measured levels for the intermediate velocities over a large middle frequency regime.

In inspecting the computer output, which lists the contribution from each of the terms of (19), as

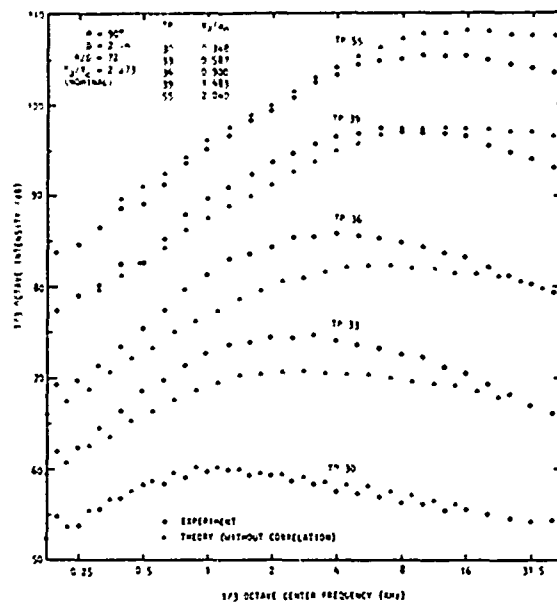


Fig. 11 Comparison of Experiment with Theory: Without Correlation Between Source Terms.

well as their sum, over the entire test point range, the reason for this discrepancy became clear. It was noted that the type of difference noted in Figure 11 for TP's 33, 36 and 39 was always at a maximum when the two terms were making equal contributions, and then diminished progressively as either term began to dominate. This suggested strongly that the two source terms were not uncorrelated as assumed universally but were indeed statistically interrelated.

III-7.2 Effect of Source Correlation

To demonstrate this effect of correlation, consider two time functions $a(t)$ and $b(t)$, representing the amplitude dependence of far-field pressure due to the two source terms considered above. The resulting acoustic pressure is therefore

$$p(t) = a(t) + b(t) \quad (20)$$

so that the mean square pressure or intensity is

$$I = \overline{a^2(t)} + 2 \overline{a(t)b(t)} + \overline{b^2(t)} \quad (21)$$

where $\overline{\quad}$ denotes a time average. Hence, defining a correlation coefficient

$$R(a,b) = \frac{\overline{a(t)b(t)}}{\sqrt{\overline{a^2(t)}} \sqrt{\overline{b^2(t)}}}, \quad (22)$$

the equation for intensity becomes

$$I(t) = \overline{a^2(t)} + 2R(a,b) \sqrt{\overline{a^2(t)}} \sqrt{\overline{b^2(t)}} + \overline{b^2(t)}. \quad (23)$$

The uncorrelated source assumption made above, of course, corresponds to $R(a,b) = 0$. We see there-

fore from this expression that the difference in far-field intensity generated by two correlated and uncorrelated sources, respectively, will be at a maximum when they are of equal strength and this difference will diminish as either begins to dominate. Furthermore, this maximum difference is 3 dB.

The computer program was therefore modified to include this effect using essentially equation (23), where $a^2(t)$ and $b^2(t)$ represent the first and second terms on the rhs of (19) respectively and, after some initial investigation, putting $R(a,b) = 1$. The effect of this modification is shown in some detail in Figure 12 for TP 36, that is, for the worst case in Figure 11.

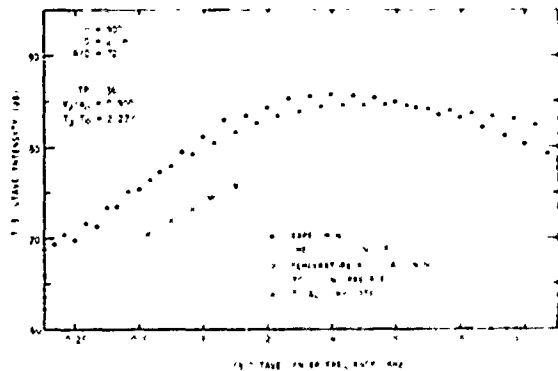


Fig. 12 Effect of Correlation Between Source Terms on Predicted Spectrum.

It can be seen that indeed over the range where the maximum discrepancy occurred, the contributing terms are almost of equal strength and as we have seen previously their uncorrelated total fall below the measured values. By contrast the assumption that they are perfectly correlated yields calculated values within 1 dB of those measured over the majority of the spectrum. We might also note in passing that the middle term of equation (23) has a velocity dependence of the form $(V_j/a_0)^{5.75}$. It would in fact have been $(V_j/a_0)^6$ had we persisted with the usual $(V_j/a_0)^8$ power law for the Reynolds shear stress contribution. While this point has not been followed up in any detail it does suggest that the appearance of sixth power dependences in the work of Morfey [4] and Lilley [5] arise because in using further equations, beyond those of momentum and mass conservation, this coupling or correlation between $\rho v_j v_j$ and ρ_T^2 has been implicitly included in these equations. The question still remains nevertheless as to whether or not their resulting source terms are really uncorrelated.

For the moment, however, we shall content ourselves with the question "Is it physically plausible to assume unity correlation between these two postulated noise mechanisms?" We believe the answer is affirmative on the basis that it is the Reynolds shear stress which produces the turbulent mixing, which according to the present model, is the process which mixes the hot jet efflux with the cooler ambient air, thus giving rise to the postulated density fluctuations at constant pressure.

111-7.3 Correlated Sources

The effect of including the correlation effect on the previous comparison of Figure 11 is shown in Figure 13. It may appear at first sight that one set of difficulties have merely been replaced by others. The comparisons at TP's 33, 36, and the lower frequency portion of TP 39 are much improved. By contrast those at TP's 30 and 55 are very much worse.

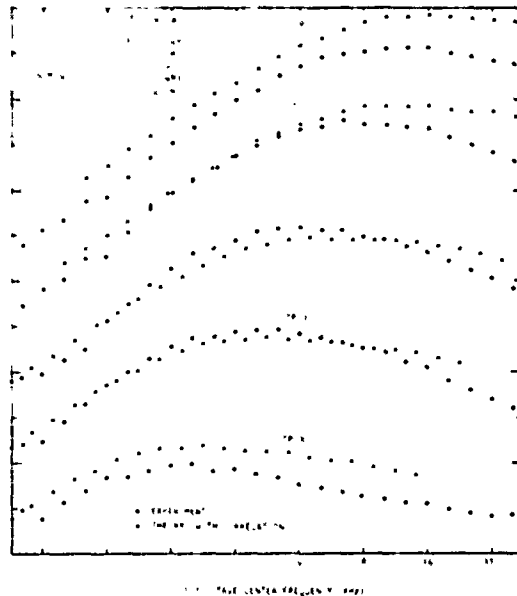


Fig. 13 Comparison of Experiment with Theory: With Correlation Between Source Terms.

The problem at the lower velocity (TP 30) was of course to be anticipated. The master spectrum for the temperature fluctuation noise was obtained directly by scaling data from this vicinity of the test point diagram. On the basis of our previous assumption of uncorrelated sources it was reasonable to assume that these spectra were almost entirely due to temperature fluctuation noise, the estimated Reynolds stress contributions being a little more than 10 dB below these measured levels. However, as a little consideration of equation (23) will show, a contribution which is 10 dB down, while making little contribution in its own right, does add an appreciable contribution in the coupling term $2\sqrt{a^2(t)}\sqrt{b^2(t)}$. It must be concluded therefore that the master spectrum for the temperature fluctuation component, Figure 7, is a little (-2 dB) high in some places as a result of the neglect of this effect.

Confirmation of this suggestion is shown in Figure 14, which is the lowest speed, highest temperature test point available. It can be seen that while the uncorrelated source prediction follows the data consistently, as it should if we have done our arithmetic consistently, the effect of adding the correlation term is to raise the predicted level by about 2 dB. It was, of course, extremely tempting at this point to "judiciously adjust" the master spectrum of this source to obtain better agreement. However, since this could be done only by trial and error with no independent check of the

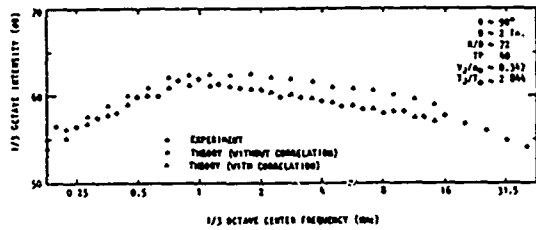


Fig. 14 Effect of Correlation on Temperature Fluctuation Noise Spectrum.

subsequent validity, this temptation was resisted in favor of awaiting higher temperature test point data, planned for the near future. Of course, as the jet velocity increases, the seriousness of this discrepancy diminishes and thus all comparisons were continued on the basis of the spectra of Figure 7.

111-7.3.1 Effect of Mach Number

A problem of a more fundamental nature however appeared to be associated with the now clear over-estimation of the lower frequencies for TP 55, Figure 13. A review of the data indicated that this type of discrepancy was always most noticeable with a combination of high Mach number (high pressure ratio) and high temperature ratio, and hence caused us to review our assumptions regarding the variation of the source temperature T_s . The relationship $T_s = 0.7 (T_J - T_0) + T_0$ essentially assumes both that the sources remain at the same point in the shear layer and that the static temperature profiles remain similar irrespective of Mach number.

A little consideration suggests that the latter is probably not very realistic. Let us suppose instead that it is the Mach number and total temperature profiles which remain similar irrespective of Mach number. Furthermore, merely to permit comparison with our previous assumptions, we suppose the source to be located at the point where

1. The local Mach number is 0.7 times the jet Mach number, and

2. That at this point, r_s , the ratio of total temperature to the total temperature at the nozzle exit plane is

$$\frac{T_T(r_s) - T_0}{T_T(r=0) - T_0} = 0.7. \quad (24)$$

We can now substitute for the ratio of static to total temperatures to obtain

$$\frac{T_s}{T_0} = \frac{0.7 f(M) \frac{T_J}{T_0} + 0.3}{f(0.7M)} \quad (25)$$

$$\text{where } f(M) = [1 + \frac{\gamma-1}{2} M^2]. \quad (26)$$

Thus to a close approximation we obtain

$$\frac{T_s}{T_0} = \frac{0.7 [1 + 0.2M^2] \frac{T_J}{T_0} + 0.3}{[1 + 0.1M^2]}, \quad (27)$$

which clearly approximates to our original expression for T_s/T_0 as the Mach number diminishes.

Table 2 below shows the influence of these assumptions on the values of T_s/T_0 as a function of both Mach number and jet static temperature ratio T_J/T_0 .

Table 2. Values of T_s/T_0

Mach Number	$\frac{T_J}{T_0} = \frac{1}{2}$	$\frac{T_J}{T_0} = 1.0$	$\frac{T_J}{T_0} = 2$	$\frac{T_J}{T_0} = 3$
0	.650	1.00	1.70	2.40
1.0	.655	1.04	1.80	2.56
1.4	.655	1.06	1.87	2.68
1.7	.660	1.09	1.94	2.81
2.0	.665	1.11	2.01	2.92

It is clear that within the limits of the assumptions made, there is a clear tendency for the calculated source temperatures to increase above the $M = 0$ estimates employed previously whenever both the Mach number and the temperature ratio are high. The test point in question on Figure 13, TP 55, which is the Mach 1.40 nozzle at $T_J/T_0 = 2$ has in fact been recalculated using the value of T_s/T_0 given in Table 2 above. The improved correlation with experiment is shown in Figure 15. The number of data points for which this type of phenomenon was observed in the present test series was really too limited to ensure that the explanation provided above is correct and further studies are required.

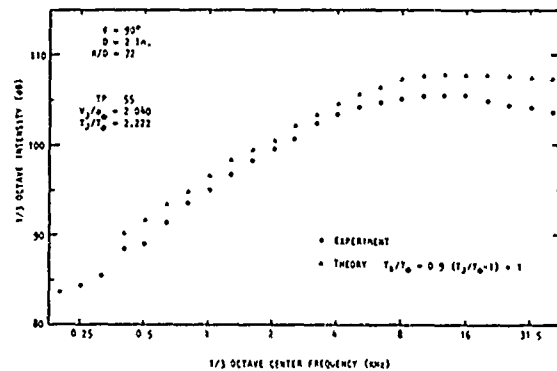


Fig. 15 Effect of Mach Number (and hence Source Temperature) on Predicted Spectrum.

This is confirmed in Figure 16, which shows the comparison of calculated and measured spectra for a constant $V_J/a_0 = 1.33$ covering the range on the test point chart from TP 56 to TP 48. Reference to Table 2 will show that for this constant velocity line, the differences in the original and speculative source temperatures are relatively negligible and indeed no discrepancy between the calculated and measured spectra exists over the majority of the frequency range.

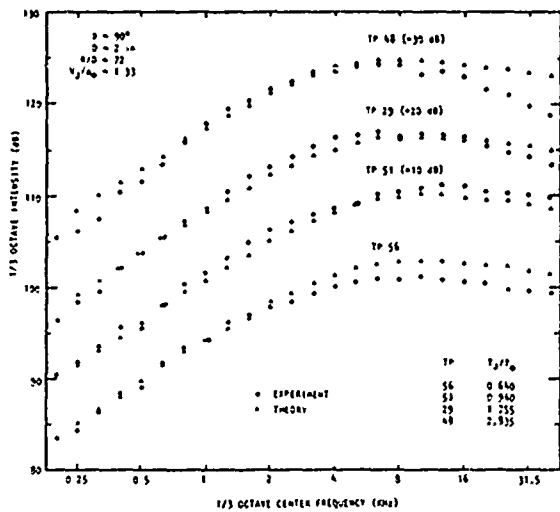


Fig. 16 Effect of Temperature Difference ($T_j - T_o$) on High Frequencies.

111-7.3.2 Effects of Temperature Difference on High Frequencies

At high frequencies, however, a definite trend is apparent for TP's 56 and 48 for the calculations to overestimate the measured levels. It is to be noted carefully, furthermore, that this occurs whenever the jet efflux temperature is significantly different from the ambient irrespective of the sign of that difference. It cannot therefore be explained in terms of the arguments involving modification of temperature dependences for the high frequency sound. This should yield a consistent trend as one proceeds up Figure 16 and not a phenomenon which occurs only at the extremes.

It is currently speculated that this effect is in some way associated with that term of equation (11) which we have implicitly ignored, namely

$$p' \left(1 - \frac{a_o^2}{a_s^2} \right).$$

We have already argued that this term appears to describe the transmission of pressure fluctuations between media of dissimilar sound speeds. In Figure 16 we see that the effect in question is absent for the isothermal and near isothermal case TP 51. However, it does occur for TP's 56 and 48, that is when the sound speeds are dissimilar. Furthermore, it occurs principally above a frequency of about 10 KHz, that is when the acoustic wavelength is of the order of one inch or less. This distance is comparable to the distance between the region of maximum turbulent intensity and the edge of the shear layer towards the end of the potential core for the present 2 in. diameter jet. It seems probable therefore that at these frequencies there is an interaction between the acoustic field and the flow. A proper description of this phenomenon is still required. In terms of the acoustic analogy, however, it appears, from the current data, to be a negative source term, perhaps a term in antiphase with $p'v_j$. It is apparently of importance only when the wavelength of the sound is less than the shear layer depth and when the temperature at the

source is significantly different from that of the ambient fluid.

111-7.3.3 Overall Levels

The final comparison between calculation and experiment to be presented in this paper is that for the overall sound pressure levels. These have been calculated by summation of contributions from the third octave bands obtained by the methods described above. This is shown in Figure 17 and should be compared with a similar diagram shown in Figure 6, which was obtained using the data and methods of [2] and [3]. It can be seen that an overall improvement in the degree of agreement is obtained. However, some discrepancies are still apparent at the extremes. At low velocities corresponding to levels less than 80 dB, the current overprediction of up to 2 dB is undoubtedly a result of the difficulties with the temperature fluctuation noise spectrum described in relation to Figure 14. It is felt that these can be eliminated once the higher temperature low speed data became available to yield an improved estimate of the basic spectrum of this noise source.

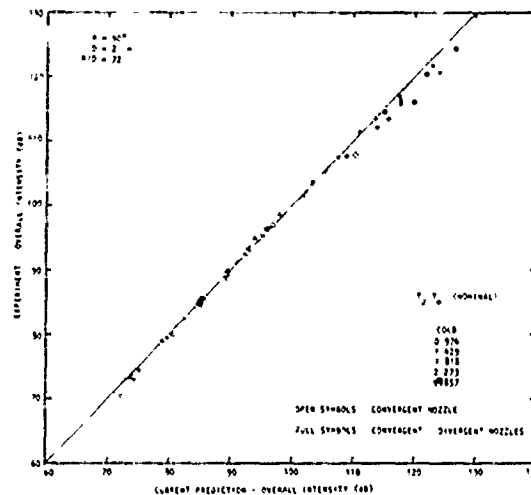


Fig. 17 Comparison of Experiment with Current Prediction Model: Overall Intensity at $\theta = 90^\circ$.

At the high speed end, the principle and most basic source of error is undoubtedly the tendency of the current model to overestimate the measured levels above about 10 KHz whenever the jet efflux temperature is significantly different to the ambient temperature, Figure 16. Future studies must clearly concentrate on a better understanding and quantification of this effect.

111-8 Summary and Conclusions

The principle objective of the work reported herein was to study the influence of temperature on the noise generated by shock-free jets over the extensive range of temperatures and velocities shown in the test point diagram, Figure 1. The major conclusions of this study are:

1. In general two sources of noise are apparent, one due to the familiar Reynolds shear stress fluctuations and a second attributable to density or

temperature fluctuations promoted by the turbulent mixing of streams of dissimilar temperature. This latter dominates the measured noise at low velocity and high temperature.

2. Scaling laws for the spectra at 90° to the jet axis of these noise components are respectively

a). Reynolds shear stress noise contribution:

$$S_m(\omega) = S_m(\omega_s) \left(\frac{T_s}{T_0}\right)^{-2} \left(\frac{V_J}{a_0}\right)^{7.5} = \overline{a^2(t)}$$

where $\frac{\omega}{\omega_s} = \left(\frac{V_J}{a_0}\right)$;

$S_m(\omega_s)$ is the master shear stress noise spectrum given in Figure 7* and for the majority of cases tested,

$$\frac{T_s}{T_0} = 0.7 \left(\frac{T_J}{T_0} - 1\right) + 1.$$

b). Temperature fluctuation noise contribution:

$$S_T(\omega) = S_T(\omega_s) \left(\frac{2\Delta T}{T_J}\right)^2 \left(\frac{V_J}{a_0}\right)^4 = \overline{b^2(t)}$$

where $S_T(\omega_s)$ is the master temperature fluctuation noise spectrum given in Figure 7.

3. A major new finding of this work is that these sources are, not statistically uncorrelated as previously supposed, but are, it appears, highly correlated. The resulting spectrum, when both are contributing significantly, must therefore be calculated from

$$S(\omega) = \overline{a^2(t)} + 2 \sqrt{\overline{a^2(t)}} \sqrt{\overline{b^2(t)}} + \overline{b^2(t)}.$$

4. The use of these relationships, in conjunction with the spectra given in Figure 7, is in general capable of predicting the measured spectra at 90° to the jet axis to an accuracy of 1 to 2 dB.

During the course of this work several new features of noise from jet mixing have become apparent. The most controversial is undoubtedly the observation that a velocity index of 7.5 appears more appropriate than the normally accepted eighth power. For the majority of practical purposes the difference is negligible, but not in relationship to a study of jet temperature effects. We tentatively attribute the lower index to a reduction of relative turbulent intensity by about 2% between a jet velocity of 500 and 2,000 fps. It is emphasized however that no proper confirmation of this currently exists.

A second important feature revealed by this work is that, while the expedient of regarding the temperature in the jet source region as a geometric

mean of the jet efflux and ambient temperatures is attractive in terms of power law analysis, it progressively underestimates the reduction of noise with increased temperature ratio. The current philosophy of using the relationship given in b) above does, by contrast, appear to be both consistent with our knowledge of jet structure and to provide an acceptable scaling law relationship. The only exception appears to be at high nozzle Mach numbers and temperature ratios where the marginally more complex relationship

$$\frac{T_s}{T_0} = \frac{0.7 [1 + 0.2M^2] \frac{T_J}{T_0} + 0.3}{[1 + 0.1M^2]}$$

appears more appropriate. It is emphasized that this is not an empirical relationship, but is based on the assumption that it is the Mach number and total temperature profiles which obey similarity relationships. The quantity of data, however, for which the source temperature calculated from the above relationship differed significantly from that obtained for $M = 0$ was too limited to really test this relation. Nevertheless, the trend is in the correct direction.

The principle new finding from this work is the observation that the Reynolds shear stress noise and that due to the temperature (or density) fluctuation are correlated. The fact that this is so does not appear at all strange when one remembers that both are intimately associated with the turbulent mixing process. It is tentatively suggested that it is, at least partially, the neglect of this effect which has caused the apparent divergence between the various theoretical studies cited herein.

The only fundamental discrepancy between the present model and the experimental data is the former's tendency to slightly overestimate the spectral levels above about 10 KHz (2" diameter nozzle) whenever the jet efflux temperature is significantly different from the ambient. Discrepancies of up to 5 dB at 40 KHz have been observed to date. The fact that this occurs irrespective of the sign of the temperature difference and only when one would expect the source's acoustic field (i.e., $kr > 1$) to be within the flow tempts us to the conclusion that this represents a phenomenon of acoustic energy transmission between two fluids of dissimilar temperatures and hence sound speeds. Equally tentatively we attribute it to the $\rho'(1 - a_0^2/a_s^2)$ term of Equation (11) which has not been included in our numerical studies. More work to examine this phenomenon further is clearly required.

In summary, we hope to have revealed in the course of this paper some of the physical processes associated with noise generation in shock-free jet flows over a broad range of jet velocities and temperatures. The numerical work does, we believe, provide a major foundation stone for the prediction of noise from such flows over the range of flow properties normally experienced in practice. Of course, the present study covers only the radiation at 90° to the

*It should be noted that all data given in this paper are for a 2 in. diameter nozzle with the measurement point at seventy-two diameters. The normal scaling laws must therefore be applied for other measurement configurations.

jet axis and further similar studies to extend these rather basic concepts to other angles of observation must be continued. In particular, a more detailed understanding of the conflicting roles of convective amplification and refraction must be established before complete prediction techniques of the accuracy obtained here can be contemplated.

III-9 Acknowledgements

This study forms a part of the larger program on supersonic hot jet noise research conducted at Lockheed-Georgia Company and financed by the AFAPL/ DOT under Contract F33615-73-C-2032. The authors wish to express their sincere acknowledgements to Mr. H. E. Plumblee, the Program Manager, and Mr. R. H. Burrin, the Principal Investigator, for all their help and to Mr. L. V. Mazzarella, who operated the test and data acquisition facilities.

III-10 References

1. Hoch, R. G., Duponchel, J. P., Cocking, B. J. and Bryce, W. D., "Studies of the Influence of Density on Jet Noise." Journal of Sound and Vibration, Vol. 28, No. 4, pp. 649-668, June 1973.
2. Lush, P. A., Fisher, M. J., and Ahuja, K. K., "Noise from Hot Jets." Proceedings of the British Acoustical Society, Spring Meeting, 1973.
3. Fisher, M. J., Lush, P. A. and Harper-Bourne, M. "Jet Noise." Journal of Sound and Vibration, Vol. 28, No. 3, pp. 563-585, June 1973.
4. Morfey, C. L., "Amplification of Aerodynamic Noise by Convected Flow Inhomogeneities." To be published in Journal of Sound and Vibration, 1973.
5. Lilley, G. M., "On the Noise from Jets." Proceedings of the AGARD Conference on "Noise Mechanisms", Brussels, September 1973.
6. Mani, R., "The Issue of Convective Amplification in Jet Noise." Proceedings of the AGARD Conference on "Noise Mechanisms", Brussels, September 1973.
7. Burrin, R. H., Dean, P. D. and Tanna, H. K., "A New Anechoic Facility for Supersonic Hot Jet Noise Research at Lockheed-Georgia." Paper to be presented at the 86th meeting of the Acoustical Society of America. October 1973.

III-11 List of Symbols

a, a_0, a_s local, ambient, source region sound speed

A, B	functions of jet static temperature ratio (T_J/T_0)
C_p	specific heat at constant pressure
$\partial/\partial t, D/Dt$	partial, total time derivative
D	nozzle diameter
$f(M)$	function of Mach number M
I	acoustic intensity
M	nozzle Mach number
p	pressure
p'	acoustic pressure fluctuations in source region
P	absolute pressure
P_R/P_0	pressure ratio
r, R	source-observer, microphone distance
S'	entropy fluctuation
$S_m(\omega)$	Reynolds shear stress noise spectrum
$S_T(\omega)$	temperature fluctuation noise spectrum
$S(\omega)$	total noise spectrum
t	time
T	absolute temperature
T_J/T_0	jet static temperature ratio
T_R/T_0	stagnation (or reservoir) temperature ratio
T_s, T_T	source, total temperature
v_j	fluid velocity components
v_r	component of fluid velocity in the direction of the observer
V_J/a_0	jet exit velocity ratio
γ	ratio of specific heats
ΔT	$= (T_J - T_0)$
θ	observer angle to downstream jet axis
ρ, ρ_0, ρ_s	fluid, ambient, source region density
ρ_T'	density fluctuation due to temperature fluctuation (at constant pressure)
$\rho v_i v_j$	Reynolds shear stress tensor
ρ_J/ρ_0	jet exit density ratio (potential core)

LASER VELOCIMETER FOR SUPERSONIC JET TURBULENCE AND TURBULENCE SPECTRA RESEARCH

D. M. Meadows, M. C. Whiffen, D. M. Smith and W. T. Mayo, Jr.*
 Lockheed-Georgia Company
 Marietta, Georgia

IV-1 Introduction

For a number of years conventional techniques of anemometry such as the hot-wire or pitot tube have proven highly satisfactory methods for measuring air flow at low speeds and under limited environmental conditions. However, analytical and experimental understanding of more complex aerodynamic and acoustic phenomena has improved to the stage that the limitations of these methods of measurement are now too restrictive. The limitations are basically caused by the need to insert a mechanical device in the airstream. When inserted in the airstream, the mechanical device and its supports will often not only alter the flow characteristics being measured, but will also frequently suffer mechanical damage where they are subjected to high-speed and high-temperature flows. The physical device also has the disadvantage that it provides the measurement over a relatively large region rather than at a point.

Laser anemometry seeks to resolve many of these problems by providing an instrument which will measure, by optical means, the velocity of microscopic particles introduced in the flow. The flow is therefore not disturbed except for the introduction of very small particles at a low seeding density, and optical techniques can ensure that the volume in which the velocity is measured is small compared with conventional techniques.

There are a number of optical techniques for remotely detecting the velocity of particles, and these techniques are now well documented in the literature⁽¹⁾. The technique to be described in this report is based on an interference pattern of light formed in the measurement volume region by intersecting two coherent monochromatic light beams. These intersecting beams interfere with one another producing alternate constructive and destructive bands of light (see Figure 1). As a microscopic particle passes through this region, light is scattered from the particle and is detected by a photo-sensor. The sensor output signal is a burst of radio frequency energy whose frequency is proportional to the spacing of the interference pattern fringes and the vector velocity of the particle (Figure 2). Since the spacing of the fringes is fixed by the geometry of the optics, the particle vector velocity is readily derived from the signal frequency.

If a second set of fringes is oriented at right angles to the first, a cross-hatch pattern results as shown in Figure 3, and a velocity vector may then be computed which is perpendicular to the first vector. The second interference pattern may be formed using a different wavelength of light such that its signals are readily distinguishable from those of the first pattern. These different wavelengths do not necessarily require different lasers, but may be derived from a laser that operates with several color lines present simultane-

ously; most argon lasers, for example, provide this feature.

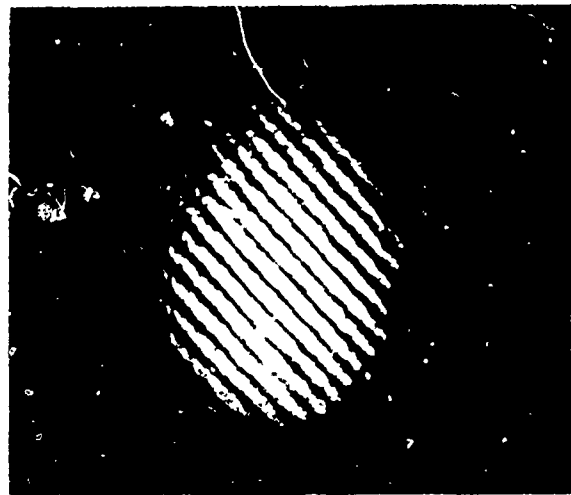


Fig. 1 Interference Fringe Pattern

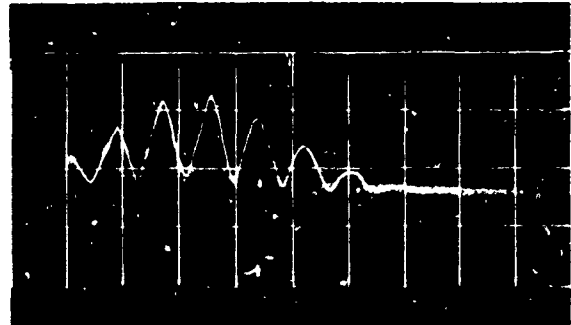


Fig. 2 Detected Particle Signal

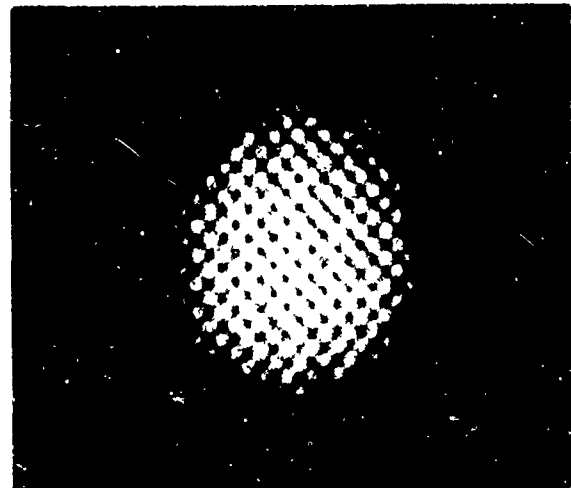


Fig. 3 Orthogonal Fringe Pattern

*Science Applications, Inc., and Consultant to Lockheed-Georgia Company.

Pages 160, 161 and 162 are Blank; 163

At the beginning of the design phase of the Lockheed-Georgia velocimeter, the major objectives were:

- o to measure flow velocities within the jet over a range of 1 to 2,000 feet per second,
- o to provide 2 orthogonal velocity vectors at the same point,
- o to derive auto- and cross-correlation functions for these vectors, and
- o to measure turbulence intensity and power spectra.

These objectives have all been met, with a number of other features added beyond those originally planned; for example, the system also has the capacity to provide cross-correlation of single velocity vectors at two spatially separated points. A complete set of specifications for the system is included in Paragraph IV-3.6 describing "System Specifications."

IV-2 System Concepts

In the preliminary design of the LV it was necessary to decide which of the two classical analysis methods should be used to derive estimates of the power spectral density. The first method, which is logically simplest, is to perform a spectral analysis directly upon the sampled velocity time histories. The second method is to measure correlation functions and apply a Fourier transform to these functions to derive the required power spectra. The decision as to which of these to use is based upon the fundamental question of whether a single-particle detection LV can produce velocity samples fast enough to describe the velocity time history in real time. A discussion by Lorens⁽²⁾ indicates that the mean data rate necessary to reconstruct the velocity time history from random time sampling within 1% is 200 times the highest frequency content of the signal. To achieve this accuracy for 20 kHz spectrum content therefore would require 4 MHz mean sampling rate. State-of-the-art electronic techniques require approximately two microseconds to evaluate and record data due to a single particle passing through the measurement volume. Typical measurement volume transit times for a particle range from 5 microseconds at 100 fps to 1/4 microsecond at 2000 fps. Since the maximum theoretical rate at which data can be processed is less than 500 kHz (based on 2 microseconds processing time per particle), it appeared that the velocity time history could not be reconstructed accurately from single particle data and thus the analysis should proceed indirectly by way of correlation functions to estimate power spectra.

In order to confirm this important conclusion, since it would dictate the design of the complete data system and also to estimate the data rates actually available, a detailed study of the statistics of particles in the measurement volume was undertaken. This study is outlined and discussed in Paragraph IV.2.1.

In addition to the important area of particle statistics, another major area of concern is that of particle dynamics discussed in Paragraph IV-2-2. This describes the characteristics of particles

used to seed the flow and their frequency response in high temperature, high velocity jet exhausts.

IV-2.1 Particle/System Statistical Analysis

In order to investigate the problems associated with attaining high data rates, it is necessary to evaluate the effect of all possible combinations of particle/measurement volume interactions. Of the possible combinations, only one is considered to be acceptable, that is, when a single particle crosses at least eight fringes in the measurement volume. All other combinations are considered to produce bad data and also consume valuable data processing time and reduce the valid data rate. These bad data are usually caused either by particles which intersect fewer than eight fringes (see also Section IV-3) or by more than one particle passing through the measurement volume at one time.

A probability model of the particle/electronics system was derived after introduction of some simplifying assumptions. First, it was assumed that all particles travel in the direction of the mean fluid velocity. From this assumption, the measurement volume was defined by the area of the $1/e^2$ incident intensity surface projected normal to the flow. Ideally, the measurement volume should have a sharply defined shape, as shown by the dashed lines in Figure 4(a), with a flat top and bottom such that all particles intercept at least the fixed number of fringes necessary for a valid measurement. Actually the shape is closer to an ellipsoid, as shown, which results in a definite projected area where a particle travelling in the direction of nominal flow cannot intercept the required number of fringes, leading to unusable data. The ratio of the good hit area, A_g , to the total area, $A_g + A_b$, is defined as the measurement volume efficiency, E :

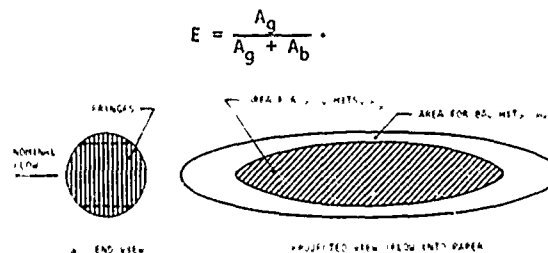


Fig. 4 Measurement Volume Sections

There are a number of different events which can occur during the processing time associated with one particle. The probability as a function of seeding density, of the various occurrences is defined for a single data processing period, t_p . The possible occurrences considered are:

- P_{nh} - Probability that no particles intercept the measurement area, $A_g + A_b$.
- P_h - Probability that one or more particles intercept the total measurement area, $A_g + A_b$.
- P_t - Probability that 2 or more particles are resident in the total measurement volume during the transit time, t_t , of one particle.

- P_g - Probability that one or more particles intercept area A_g .
- P_m - Probability that two or more particles sequentially intercept a part of the total measurement area, $A_g + A_b$, during the maximum time allowed for a particle to pass eight fringes, t_m .
- P_b - Probability that one or more particles intercept area A_b .
- P_v - Probability of obtaining valid data from one particle.

The total probability of all events in the processing interval t_p is the sum of the probabilities of no hits in time t_p , one valid data point, one good hit invalidated by a second concurrent particle and one bad hit whose 8-fringe count may or may not be completed by a second particle before the maximum time expires.

Details of the derivation of these probabilities are given in Appendix IV-C.

The probabilities are presented graphically in Figure 5 for a range of practical values for t_p , t_m , t_d and c , each using the transit time t_t resulting from 100 to 3000 fps particles.

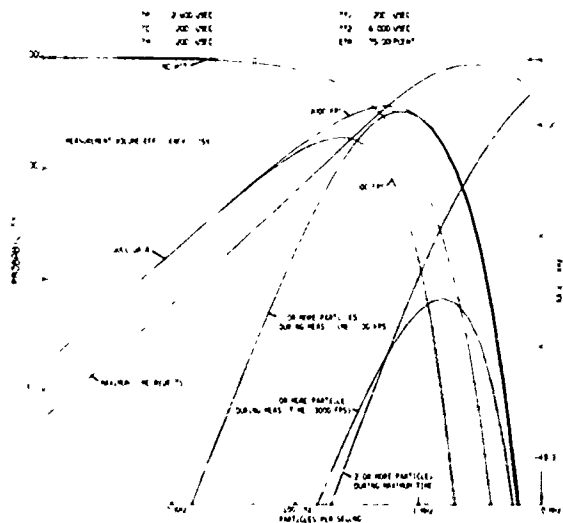


Fig. 5 Particle Probability Curves

The abscissa represents λ , the average rate of particles passing through the measurement area. The ordinate is the probability that a particular processing time period is occupied by data derived from the various types of occurrences being considered. Neglecting transit time overlap effects, this probability is also analogous to the average rate of these occurrences per unit time, since for a probability of 1.0 we have filled all the processing time periods giving a rate of $1/t_p$.

The right hand ordinate shows the rate of the occurrences for a t_p of 2.4 microseconds. It can be seen that for any given measured velocity there is a seeding rate at which the probability of receiving a single particle in the measurement

volume and obtaining 8 good counts reaches a maximum value. This is the curve showing the probability of good data for measured velocities of 100 to 3000 fps. If the particle rate is lower than this optimum, the probability of good data is limited by the number of particles passing through the measurement volume. If the particle rate is higher than the optimum, the good data is limited by the increased probability of multiple particles in the measurement volume eliminating significant possibilities of good data from a single particle.

The curves for different flow velocities indicate that at lower flow velocities the probability of valid data is reduced. This is because the lower velocity resulted in longer transit time in the measurement volume and an increased probability of particle interference.

An important result is evident from the curves of Figure 5. It indicates that even with electronics capable of processing data at a steady throughput rate of 400 kHz, the maximum probability of achieving good data during one particle processing interval is under 20%. Thus, the maximum possible rate of valid data to the data acquisition system is below 100 kHz. It is therefore totally out of the question to consider reconstruction of the velocity time history with 20 kHz bandwidth using a single-particle detector. This forms what is probably the most important finding from the system conceptual studies. It immediately precludes the use of direct spectral analysis, either analog or digital, for frequencies exceeding 2 kHz. The physical impact of this conclusion is that one must resort to the method of correlation analysis as the means of deriving turbulence frequency spectra.

IV-2.2 Seeding Particle Requirements

Since the LV derives its signals from microscopic particles embedded in the fluid flow, it is essential that the particles follow the flow. Additionally, it is a basic requirement under the contract that the particles be capable of surviving severe environments such as temperature as high as 2000°F. The following sections contain a discussion of these and other critical problem areas regarding seeding particle requirements.

IV-2.2.1 Particle Response

Berman(3) has analyzed the response of particles embedded in a turbulent gas flow. His analysis shows that for solid particles the phase and amplitude response relative to the turbulence is approximately an inverse function of the density ratio of the particle material, ρ_p , to the gas, ρ_f , and the square of the particle diameter (assumed to be spherical). Melling(4) arrives at similar conclusions with a somewhat more simplified approach. Figure 6 was prepared from Melling's expression for amplitude, η , and phase, β , response:

$$\eta = \frac{x}{x^2 + 1}$$

$$\beta = \tan^{-1} \left(-\frac{1}{x} \right)$$

where
$$x = \frac{28 N_s^2}{\rho_p / \rho_f}$$

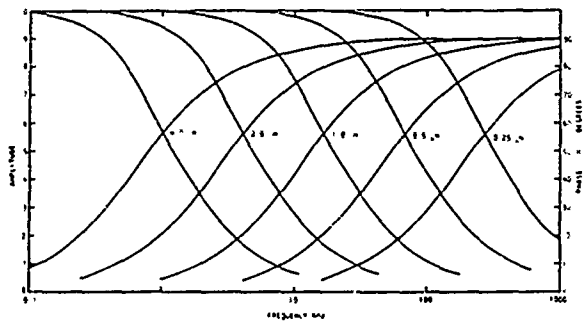


Fig. 6 Particle Response Curves

and

$$N_s = \frac{v}{\omega d^2}$$

where v is the kinematic viscosity of the gas, ω is frequency of turbulence and d is the diameter of the particle. From Figure 6 it is evident that the response of particles greater than 1.0 micron is inadequate to describe turbulence frequencies in the 20 kHz range. In fact, reasonable arguments can be made that the particle size should be less than 0.25 micron. Unfortunately, the problem is not as clear as the curves would make it appear. First, the response parameters must be considered in the light of their effect upon the turbulence spectra which are desired. The velocity accuracy required must be dependent upon the turbulence intensity. The value which is used to estimate the correlation is the difference between the absolute velocity measurement and the mean of the sample. Since small turbulence intensities result in small deviations from the mean, more accuracy is required for the same signal-to-noise ratio (the ratio of scattered light received by the photo-multiplier to photo-multiplier noise) to achieve the same correlation accuracy. Secondly, although phase deviations can be tolerated in the auto-correlation estimate if the particles are of a single size, in practice their distribution of sizes may vary by a factor of 4 at two standard deviations. This leads to additional errors due to the variation in phase delays. Third, the particles' response as shown in Figure 6 considers the movement of the particle relative to the gas. In practice the gas has considerable velocity with respect to the LDV, hence, turbulence frequencies are Doppler shifted upwards. The LDV in this case measures higher frequencies than those to which the particles are responding or conversely, for a given indicated frequency from the LDV, the particles are actually responding to some lower frequency. This phenomenon reduces the particle response requirements by significant factors depending upon the turbulence intensity at the frequency of interest. These are factors which will be the subject of future study.

IV-2.2.2 Availability and Suitability

Many particle materials are being used with LDV systems. They include abrasive powders, fly ash, smoke, aerosols, pollen and others. Since the study of high temperature (2000°F) jets is required in this program, only solids such as aluminum oxide and fly ash are suitable since their melting points are sufficiently high (aluminum oxide or alumina,

Al_2O_3 , melts at 3720°F). Of these two, the alumina is the most desirable because of its availability in the sizes required. Fly ash, however, does have an advantage over alumina in that it has a somewhat lower density, 2.5, as opposed to 3.9 for alumina.

The required particle size has been determined by considering two constraints. The particle must be large enough to scatter sufficient light to produce signals with good signal-to-noise ratios, SNR, and must be small enough to follow the high frequency turbulence perturbations within the flow. The previous discussion indicates that alumina particles must be less than one micron if they are to follow high frequency turbulence. Preliminary experiments with the LDV system in the backscatter mode have shown that good signal to noise ratios are possible with nominal 0.5 micron particles. Mie scattering curves⁽⁵⁾ along with experimental observations show that an increase of order 10 in SNR is realizable in the 30° off-axis forward scatter mode. Since this mode is to be used for future experiments, sufficient SNR is anticipated for particles in the sub-micron range.

IV-2.2.3 Particle Agglomeration

Dispersion of sub-micron sized particles is a problem area which must also be addressed. This includes both the introduction of the particles into the air flow and assurance that they are dispersed as single particles. The latter has been the subject of several experiments. Figure 7 shows various types and sizes of alumina particles. Some of these particles were injected into an air flow and samples of their dispersion taken by collection on adhesive surfaces exposed to the flow. Agglomeration is clearly shown in Figures 7(a) and 7(b).

In an effort to reduce agglomeration, crushed alumina particles were mixed with flame phase silica (CAB-O-SIL). Figures 7(c) and 7(d) show samples of these particles collected from the air flow. Note the dispersion and absence of agglomeration. This particular sample was taken on an adhesive surface positioned normal to the flow. Since the smaller particles were able to follow the flow and were therefore not deposited on the surface, we see only the largest particles in the distribution along with any significant agglomerations. The median of this distribution of particles is 0.5 micron with 1.0 micron as the upper two standard deviation point.

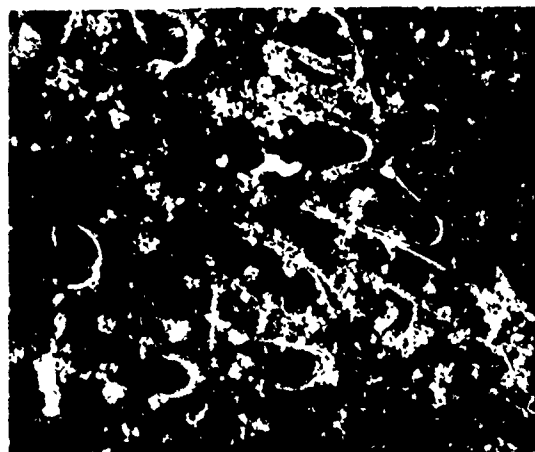


Fig. 7(a) 0.5 Micron Microgrit GB-2500 100X

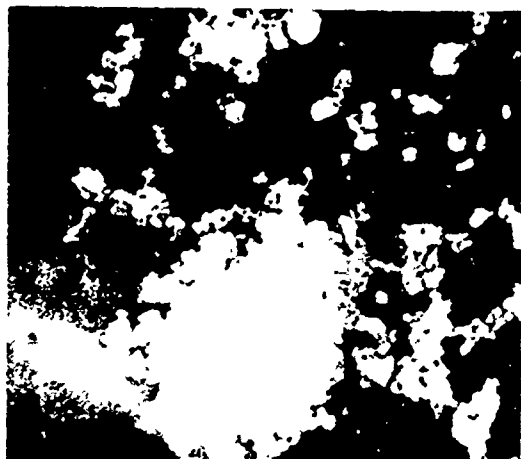


Fig. 7(b) 0-1 Micron Microgrit WCA 5000X

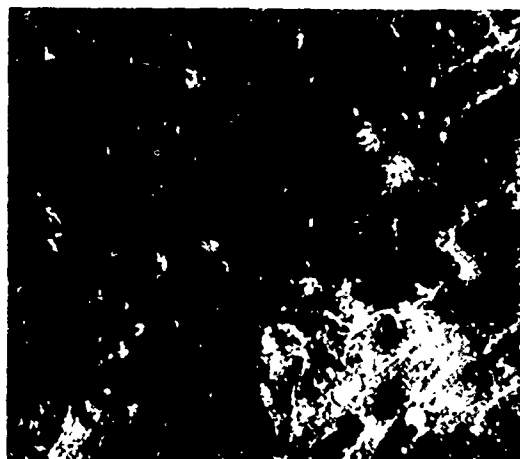


Fig. 7(c) 0-1 Micron Alumina Mixed with CAB-0-SIL 200X

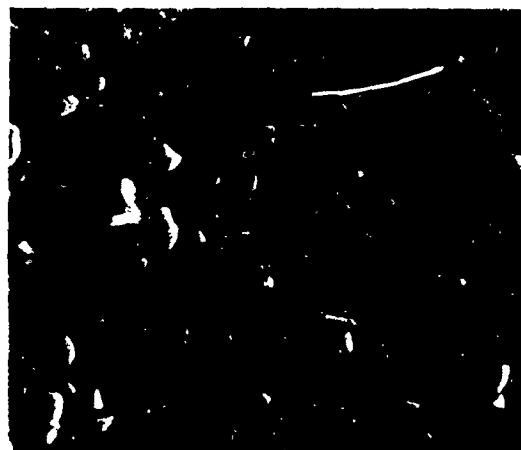


Fig. 7(d) 0-1 Micron Alumina Mixed with CAB-0-SIL 8000X

IV-3 System Description

The Lockheed laser Doppler velocimeter (LDV) system design, shown in block diagram form in Figure 8, consists of two optical electronic channels which detect particle velocities as two orthogonal vec-

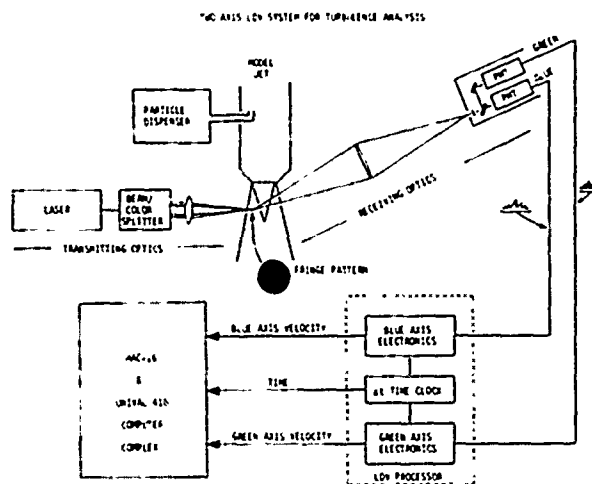


Fig. 8 Laser System Block Diagram

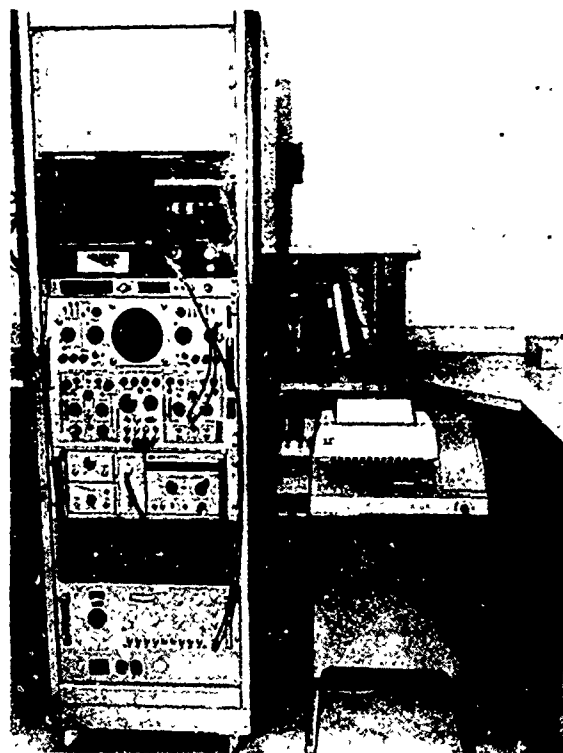


Fig. 9 LDV Processor

tors. The measurement volumes for these vectors are coincident but are separated electronically by using two different wavelengths (colors) which are detected by separate photo-detectors. The electronic processor, Figure 9, measures the time required for a particle to pass eight fringes in the measurement volume region. Certain tests are also applied to these data to eliminate ambiguities and to assure that only valid data are accepted. Valid output data from the electronic processor consist of two 16-bit digital words: the time for the particle to pass through eight fringes for each axis (from which velocity is derived) and the elapsed time since the last valid data point. These data are retrieved by a mini-computer and stored on a 500,000 word disk. The data are subsequently processed by the mini-computer to provide "real-time" information

to the operator in the form of mean velocity, turbulence intensity and, if desired, a histogram listing of velocity samples. The data on the disk is made available to a second computer for computing power spectrum and various correlation functions.

The Lockheed-Georgia laser velocimeter as described in the following sections is based on four major system advances: (1) a set of unique and highly efficient color separator/beam splitter optics — these optics provide the basis for generating the multicolor laser beams necessary for multivector capability; the optics are self-aligning, extremely stable and virtually eliminate cross-talk between vector channels; (2) extremely high speed processing electronics using a 500 MHz clock rate, and error checking circuitry; (3) direct coupling of the LDV to an on-line, high data rate mini-computer which provides unusual flexibility in data formatting, changing or adding additional outputs or calculations, and in data collection; (4) an advanced random sampling data processing program which allows power spectra to be derived from data whose average sampling rate is far below the Nyquist criterion; this particular feature represents perhaps the most significant aspect of the total LDV program.

The laser velocimeter, mounted on the jet test stand, is shown in Figure 10. While the system features optional forward scatter, off-axis forward scatter, and backscatter modes of operation, only the off-axis forward scatter configuration is shown in the photograph.

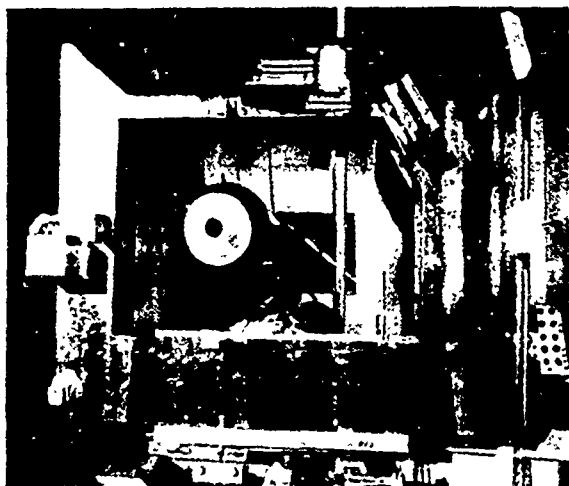


Fig. 10 LDV Test Configuration

IV-3.1 Particle Dispenser

The particles are introduced into the air flow in the plenum chamber, well upstream of the nozzle. The air velocity is sufficiently low at this point to allow a homogeneous dispersion of the particles. They are injected in the upstream direction to assure that residual injection accelerations do not affect the velocity measurements. The injection device is a converted abrasive unit designed for abrasive etching of small devices. It is shown in Figure 11. The unit uses a vibration device to sift the powder into a small plenum where it enters a stream of dry nitrogen and then into the nozzle

plenum. Injection rate is controlled by both the differential pressure between the nitrogen supply and the nozzle plenum, and the vibration level of the sifter. Both of these controls are located on the operations console, remote from the injection device itself.

The particles presently being used for turbulence analysis are alumina mixed with CAB-0-SIL to reduce agglomeration. The alumina particles are distributed from 0 to 1 micron. Initial results, discussed in this report, indicate response and agreement with hot wire spectra to frequencies approaching 20 kHz. Extensive experimental studies of the effect of particle size and distributions on measured spectra are in progress.

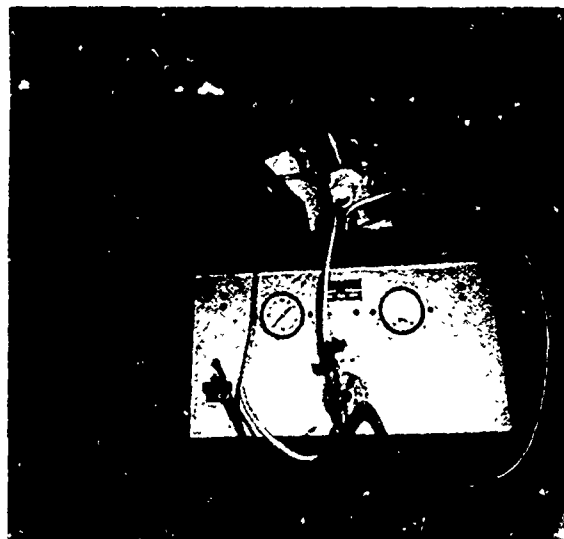


Fig. 11 Particle Dispenser

IV-3.2 Optics System

Figure 12 shows the plan view of the optical system for the laser velocimeter. The optional receiving configurations are illustrated on the diagram: a forward-scatter lens position, a 31° forward-scatter lens position, and a 13° back-scatter lens position. The laser used in the system is a Spectra Physics Model 164-03 Argon laser which provides 4 watts of multimode power. The laser beam is brought from the backside of the test fixture mounting frame through a periscope and up to a beam diameter adjusting telescope. A pinhole has been included in the telescope assembly to provide spatial filtering of the beam. A series of lens are available for this assembly which provide beam diameter changes from .75 to 3 millimeters. This capability allows a trade-off to be made between measurement volume size and the total number of interference fringes contained within the volume. Normal settings for the telescope are such that the dimensions of the $1/e^2$ measurement volume are approximately 0.3 mm by 1.0 mm with a total number of fringes of 33.

One of the key components in Lockheed's LDV is the beam splitter/color filter assembly. This unit provides the ability to derive two independent and orthogonal velocity vectors from the air flow by means of color separation techniques. Color sepa-

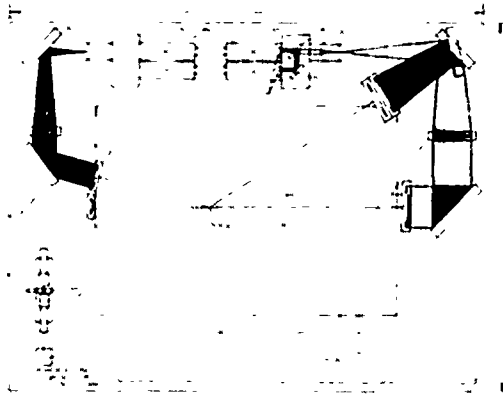


Fig. 12 LV Optical Configuration

ration was selected in lieu of other candidate techniques due to the ease of implementation and also due to the high probability of achieving very low cross-talk between the two velocity data channels. The other candidate techniques evaluated, but rejected, were (a) orthogonal polarization and (b) frequency shifting of light in one channel with respect to the other.

The beam splitter/color filter assembly separates the two predominant lines of the argon laser, 4880 Å and 5145 Å, into 4 beams - 2 blue and 2 of green. The 4 beams are positioned in a rectangular pattern with beams of the same color positioned diagonally across from one another as shown in Figure 13. Figure 14 shows the optical arrangement. The incoming beam from the argon laser impinges on a neutral beam-splitter flat and is split into two equal power beams; the second optical flat on the right provides pathlength compensation. The two beams which emerge from the beam-splitter contain a number of spectral lines. Figure 14(b) shows the path of one of these multimode beams and the method used for color separation. The color separation optics consist of two optical flats with 2 interference filter coating sections on the same surface: a transmit-green/reflect-blue section and a transmit-blue/reflect-green section. The incoming beam is color separated at the first surface of the optical flat with blue light being reflected and green light transmitted to the second surface and then reflected. At the second optical flat, the opposite effect occurs with blue light being transmitted and green light reflected.

The optical geometry provides very efficient removal of all unused wavelengths in separately located reflection beams which are later blocked. The cross talk is minimized by the fact that each beam used is transmitted through a narrow band filter coating twice. The geometry also provides coherence path length compensation.

Upon leaving the beam splitter/color filter assembly, the beams are simultaneously focused and caused to cross by the transmitting lens. The result of this is to create two coincident ellipsoidal measurement volumes whose cross-section is as shown earlier in Figure 3.

As mentioned previously, three alternate receiving configurations are available. The off-axis configu-

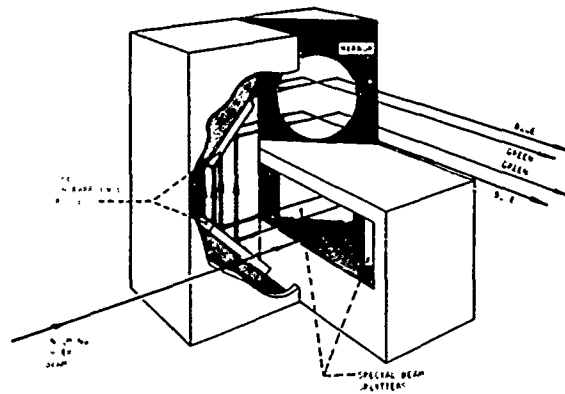


Fig. 13 Beam Splitter Assembly

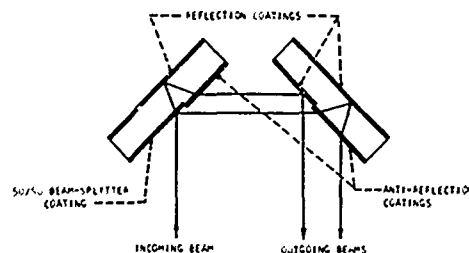


Fig. 14(a) Beam Splitter Flats (Lower Pair in Fig. 13)

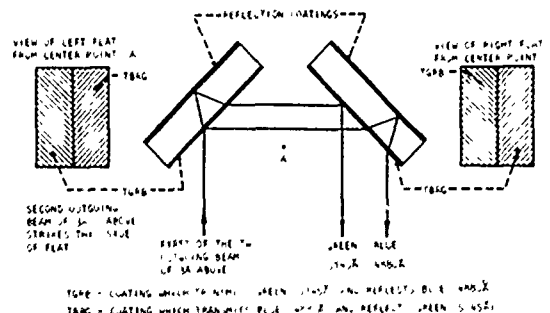


Fig. 14(b) Color Separation Flats (Vertical Pair in Fig. 13)

rations provide an advantage in that the elongated measurement volume can be effectively reduced in size. This occurs since the effective measurement volume is defined by the intersection of the transmitting and receiving focal volumes. Figure 15, which illustrates this effect, is a photograph of the measurement volume created by the intersection of one light beam sent through the transmitting system and a second beam sent back through the receiving optics. Each of the alternate receiving configurations has been used, although the back-scatter mode has been predominant in the early phases of the contract program. It is anticipated that the forward scatter modes will provide some distinct advantages in received power where the jet velocity is extremely high.

The light scattered by the microscopic particles passing through the measurement volume is collected

and transmitted to the photomultiplier assembly. This assembly, diagramed in Figure 16, utilizes a 45° interference filter, along with conventional interference filters in front of each photomultiplier tube, to separate the scattered light from the two measurement volumes. This particular configuration provides low cross-talk between the velocity vector channels. The two colors are separated by a measured power ratio of 0.0001. It should also be noted that a further reduction in cross-talk is provided in the receiving electronics by the zero crossing detector where the larger signals effectively determine zero crossing points and make the effects of additive interference negligible.



Fig. 15 Measurement Volume (Artificially Illuminated)

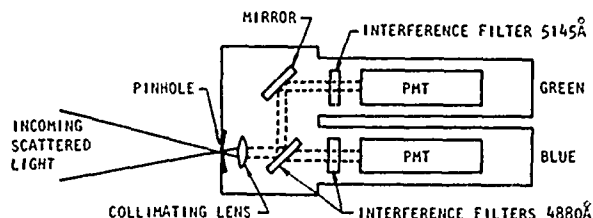


Fig. 16 Photomultiplier Assembly

IV-3.3 Electronics

The system block diagram of the LDV electronics is shown in Figure 17. The output from the optics system, in the form of light scattered from particles crossing the blue and green fringe patterns, is converted by separate photomultiplier tubes into electrical signals as shown in Figure 18. The signal is processed through the high pass filter to eliminate the DC pedestal and other undesirable signal characteristics. The resulting RF burst is amplified and input to both threshold and zero-crossing detectors. If the input exceeds the threshold setting, a gate is enabled allowing the output of the zero-crossing detector to clock the fringe counter. The output of the fringe counter is a pulse whose period is equal to 8 cycles of the received signal. This pulse is subsequently used to gate a 500 MHz clock which drives a 13-bit binary counter. The 13-bit counter serves the function of

quantizing the 8-cycle time interval into 1 nano-second increments and converting the time interval into a digital word.

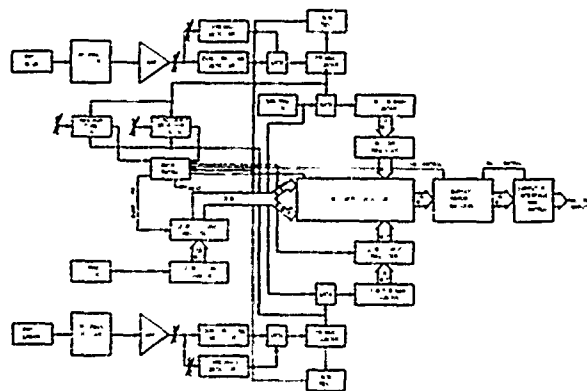


Fig. 17 Electronics Block Diagram

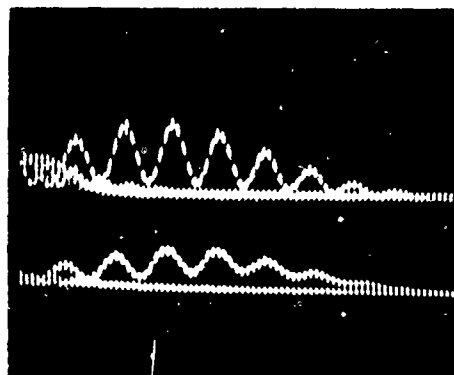


Fig. 18 Particle Signals on Orthogonal Channels

If the maximum allowable time is not exceeded and the particle ambiguity tests are successfully passed, the 16-bit word selector selects and loads two words containing both channels of velocity and the elapsed time into the buffer memory. The coincidence detector decides whether the measurements from each channel occurred sufficiently close together in time to be recorded with the same elapsed time since the preceding data transfer. The elapsed time from the last data transfer is measured by counting 1 MHz clock pulses. Whenever data is transferred, the 12-bit time count is stored in the 12-bit storage register for transfer to the buffer storage. At the same instant, the counter is reset and begins counting on the next clock pulse. If the time counter reaches its maximum count, an extra word pair containing the maximum count is output to the selector and the counter is reset.

The buffer memory provides temporary storage and accumulates a block of data for transfer to the computer memory. Since the buffer has independent input and output controls, the LDV can process particles as they appear without being limited by the maximum computer input rate. Although the average data rate is limited by the computer input rate, the Poisson time distribution can still be approximated since measurements as close together as 2 or 3 microseconds will be recorded and buffered by the silo memory.

IV-3.4 Data Validation

From the system probability model it can be seen that if maximum good data rates were to be realized, some method or methods were required to inhibit the recording of the various types of erroneous data. These tests were, of course, considered in the development of the model since each requires some processing time to perform. The types of erroneous results which must be inhibited are: data resulting from the passage of two or more sequential particles within the period t_m and data resulting from the passage of two or more simultaneous particles.

The electronic processor operates by measuring the time period required for the particle to pass a fixed number of fringes. Should the particle pass through the edge of the measurement volume, it is possible that it will not pass enough fringes and therefore the electronics are detained, awaiting completion of the count. A second particle may complete the count, but, of course, the data is invalid. Two tests are incorporated to eliminate these data. First, the maximum time gate automatically terminates the count and invalidates the data after sufficient time has elapsed to measure the slowest particle of interest. Second, a 4/4 test is applied. This test consists of comparing the time for the first half of the fringe count with the time for the last half. If this time differs by more than a fixed percentage (3%) the data is considered invalid.

Errors resulting from simultaneous particles have been treated extensively in the literature(6-9) from the standpoint of tracking LV systems. For the purposes of the single particle detector, a simplified sum of two interfering particles has been examined. Figure 19 shows typical calculated curves from the addition of two sinusoidal signals representing the light scatter of two simultaneous particles passing through the measurement volume. The frequency of one has been varied and the signature as seen by the electronics of the resulting signals plotted. Note that the zero crossing detector would not receive a periodic signal. In this case not only is one pulse of the series effectively missing, but also a phase delay of about 180° is introduced. The 4/4 test eliminates the vast majority of erroneous data from simultaneous particle interference of this type. The possibility still exists, however, that no phase shift is accumulated and the same number of zero crossings is lost on either half of the fringe count. In this case although the 4/4 test would validate erroneous data, in practice the probability is extremely small. If, however, this is found to be a limitation to the system, the electronics is provided with accommodations to incorporate a second test to measure the time for an odd ratio of the fringe count such as 3/5.

IV-3.5 Data Processing

A detailed discussion of the data processing equipment and software is contained in Section IV.4 of this report; only a brief description is included at this point in order to aid the reader in visualizing the total LV system. From the LV processor, block diagrammed earlier in Figure 17, two digital words are transmitted to the computer facility for each valid velocity measurement. These words include 10 bits of 8-fringe period data for each of two channels and 12 bits of time data. The time data

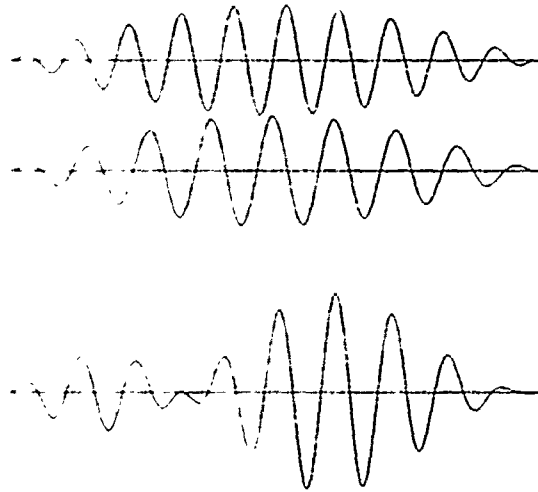


Fig. 19 Particle Signal Interference

is the elapsed time since the previous valid velocity measurement. The two words are input to a Lockheed Electronics Company MAC-16 mini-computer. This mini-computer is controlled by a teletype at the LV location and is provided with a $\frac{1}{2}$ million word high speed disk memory upon which all of the data are recorded. It is capable of maximum throughput rate of 37,000 words/second. A set of data may consist of up to 40,000 words which are recorded on disk directly from the LV processor. The run times for a set of data are typically 1 to 5 seconds. Following the run, the mini-computer calculates the mean and standard deviation of the data, along with a velocity histogram, if desired, and outputs these data to the teletype.

Permanent storage and analysis of the data is performed by a Univac 418 computer which also has hardware access to the MAC-16 disk. Permanent storage is maintained on magnetic tape and software provides the correlation and spectral analysis. Basically the analysis consists of first removing the mean velocity from each measurement, leaving only the velocity deviation from the mean which contains all the turbulence spectra data. The correlation function is estimated by an algorithm which tabulates the lag products $v(t) \cdot v(t+\tau)$, for sample pairs separated by time τ . τ is computed from the elapsed time data associated with each velocity.

The turbulence spectra are computed by taking the Fourier transform of the correlation function. The correlations and spectra are presented on a graphics CRT display which is part of the Univac 418 system and may be retained for hard copy by punched paper tape. A CALCOMP plotter is used to prepare the final copy.

IV-3.6 System Specifications

Velocity range:	1 to 4,000 fps
Accuracy:	0.1% at 125 fps
	0.2% at 250 fps
	0.4% at 500 fps
	0.8% at 1000 fps
	1.6% at 2000 fps
	3.2% at 4000 fps

Two orthogonal velocity vectors (u, v)

Effective measurement volume:

A cylindrical volume with a radius of 0.3×10^{-3} M, and length of approximately 1.0×10^{-3} M (with off-axis receiving optics)

Data outputs:

Sampled velocity: $u_1, u_2, \dots, v_1, v_2, \dots$
(given as an array of samples taken).

Mean velocity: \bar{u}, \bar{v} , and \bar{u}, \bar{v} resultant.

Turbulence intensity:

$$\frac{(x_1 - \bar{x})^2 + (x_2 - \bar{x})^2 + \dots + (x_n - \bar{x})^2}{n - 1}$$

where $x = u$ or v .

Histogram of velocity: a plot is provided for u and/or v .

Autocorrelation function:

$$R(\tau) = \frac{1}{T} \int_0^{T-\tau} x(t) x(t + \tau) dt$$

where $x = u$ or v .

Power spectrum:

$$S(f) = \int_0^{T_{\max}} R(\tau) e^{-j2\pi f\tau} dt$$

Cross-correlation function:

$$R_{uv}(\tau) = \frac{1}{T} \int_0^{T-\tau} u(t)v(t + \tau) dt$$

Cross-spectral density:

$$S_{uv}(f) = \int_0^{T_{\max}} R_{uv}(\tau) e^{-j2\pi f\tau} dt$$

Three dimensional positioning of the measurement volume anywhere in the flow is possible.

IV-4 Data Collection and Analysis

The following paragraphs describe programs currently available for processing data received from the LV electronics package. These programs were all written to use existing Lockheed computer configurations with minimum changes to the system structures. Considerable attention has been given throughout the development of the system to safeguard data against computer failures, etc. which potentially require a run to be repeated. The programs may be re-entered manually at three different places to recover from potential problems. These re-entry points have been successfully used throughout the program in optimizing data

collection and analysis procedures.

One Lockheed capability which has been used extensively on this project is the visual examination of data by computer graphics. By this means, insight has rapidly been gained into the behavior of complicated algorithms and a level of confidence in the procedures achieved which would have been impossible without such a tool. During program development, much valuable time in plotting erroneous results has been saved by the ability to preview data before plotting. During production use of this facility, graphics will continue to be used to preview data in order to reduce the quantity of data sent for hard-copy plotting.

IV-4.1 Theory

The technique used for computing estimates of power spectra from random samples of two time histories was independently conceived by the authors at Lockheed-Georgia Company and by W. T. Mayo at Texas A & M University⁽¹⁰⁾ and subsequently developed cooperatively into a practical algorithm. It is important to note that the theory upon which the power spectra analysis is based rests on the assumption that the data of interest is derived from a statistically stationary process. Results of preliminary experimental tests have confirmed the validity of this assumption.

The initial objective of the analysis program is to convert the randomly-occurring samples obtained from the laser velocimeter into a form suitable for input to an implementation of the Cooley-Tukey Fast Fourier Transform⁽¹¹⁾. This program seeks to solve the discrete equation

$$S(\omega) = \Delta\tau \sum_{k=0}^{N-1} R(k) e^{-\frac{j\omega k}{N}} \quad \omega = 0, 1 \dots N-1$$

where the sequence $R(k)$ is a complex array representing a correlation function sampled at regular intervals $\Delta\tau$, and $S(\omega)$ the resulting complex array representing the signal power spectral density. It should be noted at this point that the autocorrelation function of any one signal is an even function of time and will produce the required real power spectrum from the transform if $R(-k)$ is appended to $R(k)$ in the input array. The cross-correlation function of two signals, however, is not an even function, and produces a complex power spectrum.

As indicated by Mayo, the method used to compute the series $R(k)$ is best described by an algorithm rather than an equation. The emphasis in designing this algorithm has been on speed of execution without compromising accuracy or, in an experimental configuration, flexibility. The object is to establish three arrays, DXX, DXY and DYY, each containing N entries, with each element representing the sum of lagged products $\Delta\tau$ apart; where N and $\Delta\tau$ are chosen to satisfy the Nyquist criterion. This requires that the effective sampling rate, $1/\Delta\tau$ should be double the highest significant frequency content of the data if spectrum folding is to be avoided. The Fourier transform automatically selects the maximum frequency to satisfy this criterion,

$$f_{\max} = 1/2\Delta\tau,$$

and provides N samples of the spectrum, giving an effective spectrum resolution of $\Delta f = 1/2N\Delta t$.

The basic process of updating the correlation arrays with a pair of samples $\{x(t), y(t)\}$ and $\{x(t + \tau), y(t + \tau)\}$ is to compute the product $x(t) \times y(t + \tau)$ and add it to the sum DXX, compute $y(t)y(t + \tau)$ and add it to DYY, compute $y(t + \tau) \times x(t)$ and add it to DXY, and increment the array showing the number of products in each element where for example $x(t)$ represents the axial velocity at the same point.

The velocity data samples are processed serially in the order which they are taken. A time history out to the maximum delay time of interest is maintained at all times. As each sample is processed, it is first correlated with itself to update the first correlation element. The time to the previous element is then resolved onto the correlation time grid and the pair is used to update that element. Subsequently, the next element in the history is processed and updated until the accumulated delay exceeds the maximum delay of interest. The function computed may then be described as:

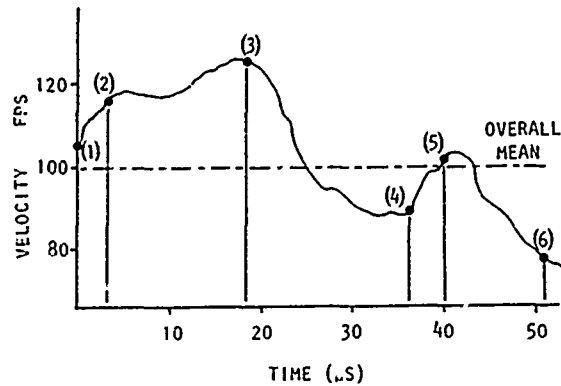
$$D_i = \sum_{k=1}^{IHT_i} x_k y_{[k + (i-1)\Delta t]}$$

where D_i represents the i 'th element of DXX, DXY or DYY, and IHT _{i} represents the number of entries in that element.

Figures 20(a), (b) and (c) illustrate the accumulation of a small number of samples to produce DXX (note: only 6 samples are shown out of 20,000 normally taken). Figure 20(a) shows the velocity time history with an overall mean of 100 fps sampled at random intervals. Figure 20(b) shows the tabulated data from the LV and Figure 20(c) shows the process of accumulating these values into the correlation function. For example, in processing sample number 6, its product with itself is entered for $\tau=0$, sample 5 was 11 μ S earlier giving a product at $\tau = 10$, sample 4 was 15 μ S earlier giving an entry at $\tau = 20$ etc. If this were a complete series, the sequence $R(k)$ would be:

$$R(k) = \frac{DXX_0}{6} \frac{DXX_1}{4} \frac{DXX_2}{4} \frac{DXX_3}{3} \frac{DXX_4}{2} \frac{DXX_5}{1}$$

Experience has shown that the major factor in the accuracy of the power spectra computed from correlation functions accumulated as summed lagged products is the number of products summed into each interval. During early experimentation with synthetic data, it was suspected that the process of permitting all data with random time intervals to be entered in the "nearest" grid slot was introducing errors which affected the computation results. Subsequent experimental evidence, which is supported by the theoretical analysis of other investigators, has shown that if this is significant at all, it affects only the shortest delays and therefore the very high frequency end of the spectrum. A more serious result of discarding those data which do not fall close enough to the Δt grid points in order to correct this effect is to reduce the amount of data accumulated in the correlation function. The computation time required to make this decision was also significant.



20(a)

Sample Number	Time Since Last Sample (μ Sec)	Deviations From Mean (fps)
1	10	+5
2	3	+15
3	16	+27
4	17	-8
5	4	6
6	11	-20

20(b)

Entries Due To Sample #	$\tau = 0$	10	20	30	40	50
1	5 x 5					
2	15 x 15	15 x 5				
3	27 x 27	27 x 15	27 x 5			
4	-8 x -8		-8 x 27	-6 x 15	-8 x 5	
5	6 x 6	6 x -8	6 x 27	6 x 15	6 x 5	
6	-20 x -20	-20 x 6	-20 x -8	-20 x 27		-20 x (15+5)
	DXX ₀	DXX ₁	DXX ₂	DXX ₃	DXX ₄	DXX ₅

20(c)

Fig. 20 Correlation Function Example

For these reasons, the logic inserted in the analysis program to allow the correlation latitude to be varied has been removed. The analysis is consequently faster and uses the minimum amount of data to establish a given accuracy of the spectral density function.

Having computed discrete estimates of the correlation functions, the problem has been transformed to the familiar one of computing the power spectral density from a regularly sampled correlation function. Considerable knowledge has been accumulated and published on this subject and the following is a brief distillation of those portions considered to be relevant to our particular problem. The basic result of much discussion in this field is that some knowledge of the characteristics of the data is required before it can be properly processed. For example, if some discrete frequencies are known to be present and must be detected individually, then the filtering which provides the most resolution is required whereas, if only the smooth envelope of the spectrum is required, considerable amounts of unnecessary "noise" can be removed.

Since the exact expression for the Fourier transform requires an infinite length correlation function, the process of transforming a finite

correlation function of length T_m implicitly assumes a correlation window function. The most obvious function is the "Zero'th" window, using the nomenclature of Blackman and Tukey(12):

$$Q_0(\tau) = 1 \quad \tau \leq T_m$$

$$= 0 \quad \tau \geq T_m$$

whose effect is to convolve the resulting spectrum with the function

$$Q_0(f) = 2T_m \frac{\sin(2\pi f T_m)}{2\pi f T_m}$$

which is plotted on Figure 21. Among the other functions tried, the most effective and that currently in use for the data being processed is the Hamming window

$$D(\tau) = 0.54 + 0.46 \cos(\pi\tau/T_m) \quad \tau < T_m$$

$$= 0 \quad \tau \geq T_m$$

which transforms to:

$$Q_3(f) = 0.54 Q_0(f) + 0.23 [Q_0(f + \frac{1}{2T_m})$$

$$+ Q_0(f - \frac{1}{2T_m})]$$

which is also plotted on Figure 21. The horizontal scale of Figure 21 is normalized to $2fT_m$ so that the integer values indicate the spacing at which spectrum samples will be produced by the Fourier transform.

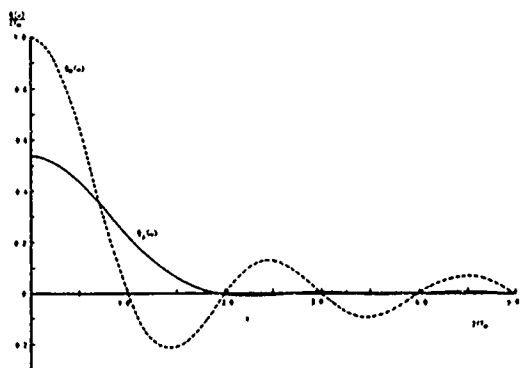


Fig. 21 Spectral Window Functions

Three of the most common window functions together with the "default" or "Type 0" window are currently available in the analysis program, and the effect of each upon a spectrum taken from a 0.63 inch jet is shown in Figure 22.

Figure 22(a) shows the spectrum using the "Type 0" window. Figures 22(b), (c) and (d) show the effect of "Type 3" or Hamming window, the "Type 2" or Hann window and the "Type 1" or Bartlett window respectively. Since the overall structure of these windows is similar, it is not surprising that their effect is distinguishable only in detail, but the difference from "Type 0" is remarkable.

A secondary study to determine the effect of truncating the data is shown on Figures 22(e) and (f). The correlation function was truncated respectively to one-half and one-third of its original length and the Bartlett window applied with the expected loss of definition of the data.

In addition to these analytic windows, two other smoothing processes are applied before displaying the resulting power spectra. The first, which may be suppressed if there is reason to suspect the presence of sharp spikes in the data, is designed to improve the presentation of smooth spectra by applying a running average over ten points of the spectrum. The second is an integral part of the conversion from the linear output of the Fast Fourier Transform to the more conventional log frequency/log amplitude (dB) plots. Since the frequency distribution of the data is linear and the log plot has a large concentration of points at the high-frequency end, an algorithm was introduced to coalesce all points to be plotted within a specified mantissa tolerance. The effect of this smoothing is most graphically observed on those spectra having spikes at high frequency where the amplitude of the spikes is reduced by averaging with points of lower amplitude. By adjusting the width of the mantissa tolerance, these effects can be minimized.

IV-4.2 Computer Configurations

Figure 23 shows the configuration of the laboratory data acquisition and processing system as augmented to include the LV. The Central MAC is an LEC MAC-16 computer used as a data management and switching center. Its capabilities have been expanded recently by the addition of a 4-channel multiplexed data channel (MDC), two channels of which are used to handle high-speed data throughput from the LV to the disk file. The computer also supports a file management system for the disk used by the Univac processor and by the other experiments at remote terminals. Its memory will be expanded from 4K to 8K words in the near future. The Univac 418 system is a 32K 18-bit word processor on which most of the Company's research into computer graphics was done in the late 1960's, and is still used for concept development. Except for time-critical subroutines, all analysis on this machine is written in FORTRAN IV, a feature facilitating the translation of the analysis to other computers. The graphics language used by this program to drive the display is a machine-independent FORTRAN graphics language, FLING.

IV-4.3 Data Management

The success of the LV data processing system in producing reliable spectra relies upon the rapid collection of a large volume of data. Although the Nyquist criterion does not apply to randomly sampled signals as will be discussed below, current experience indicates that in order to achieve reliable results, it is necessary to maintain a relatively steady sample rate of the same order as the bandwidth of the data of interest. The sample rate necessary to meet these requirements would be less demanding if it were a regular rate at which synchronous writing of the disk could be maintained. With the irregular arrival rate of the data, however, it became necessary to use a special disk handler whereby the sector to be written on next is

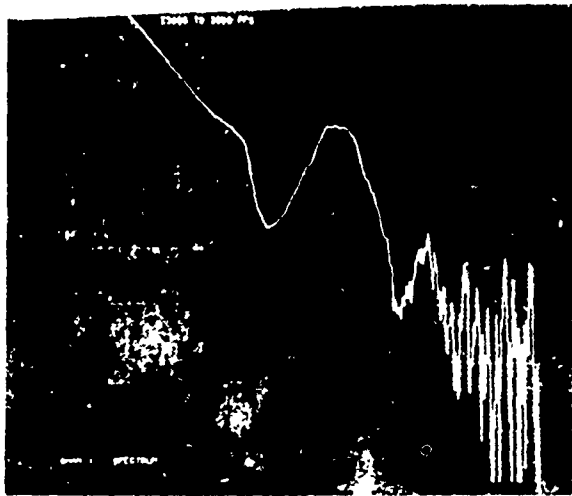


Fig. 22(a) Window Function Study - Type "0" Rectangular Window

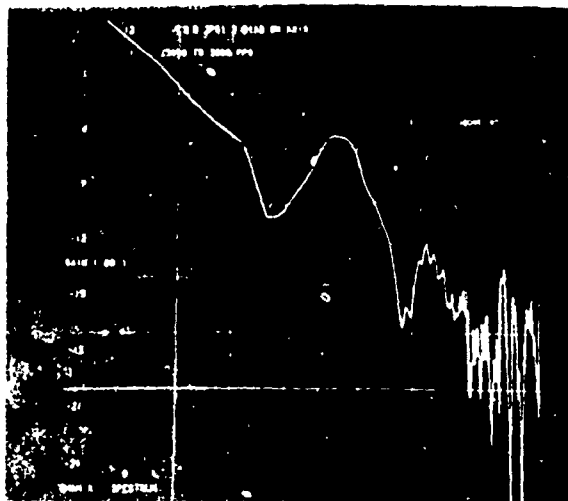


Fig. 22(d) Window Function Study - Bartlett Window

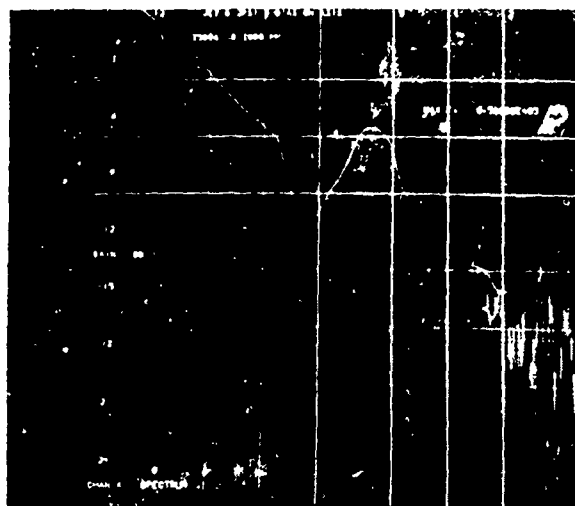


Fig. 22(b) Window Function Study - Hamming Window

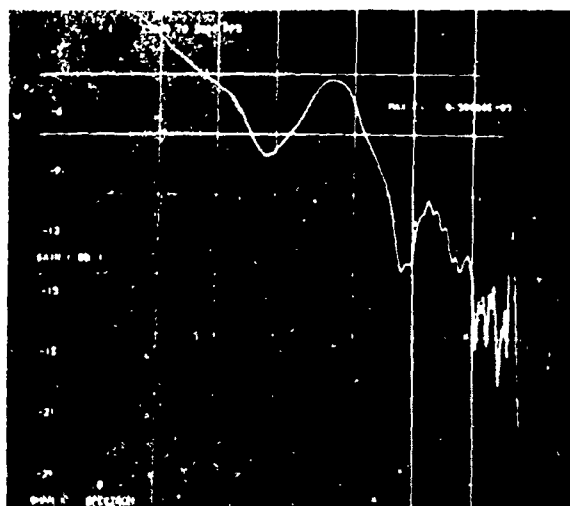


Fig. 22(e) Window Function Study - Bartlett Window Half Truncated

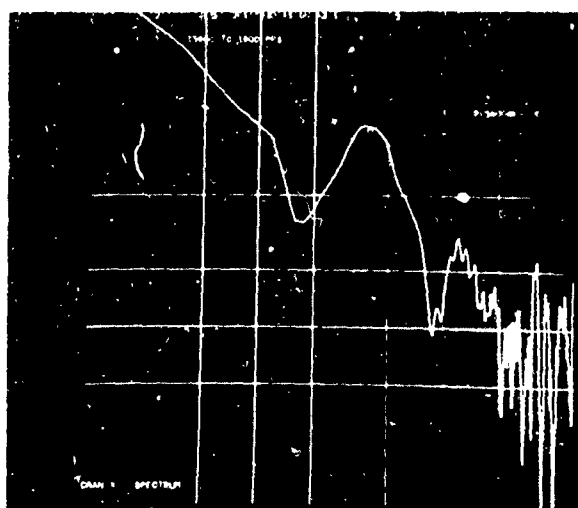


Fig. 22(c) Window Function Study - Hann Window

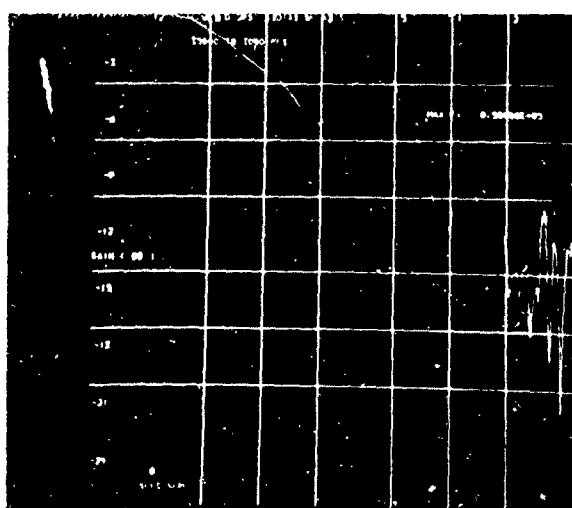


Fig. 22(f) Window Function Study - Bartlett Window 2/3 Truncated

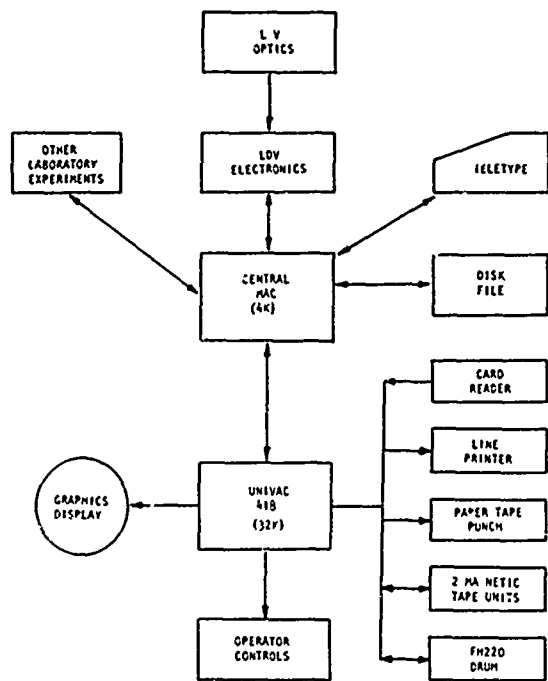


Fig. 23 Data Processing Block Diagram

determined, logic is used to select an available track, and as soon as a block of data becomes available the data is written and then further writing at that sector/track is prohibited. The synchronous transfer rate to the disk for 16-bit words is 75 kHz in its current configuration, and the above logic permits a maximum throughput rate of half this, 37.5 kHz. The maximum sample rate for two channels which, with the associated time data, require two 16-bit words for each sample is therefore 18.75 kHz. This is considered satisfactory for data with bandwidths above 20 kHz especially when data buffering in both the electronics and the central MAC permit short bursts of data at rates above 200 kHz.

The data collection process is initialized by requesting the LV handler at the teletype, and entering the appropriate run data. After checking the system to ensure that previously stored runs have been successfully retrieved and stored, the handler awaits the start of the first run. When that run completes, the list of sequential locations of each block of data is processed to retrieve the data, compute the mean and standard deviation of the run and re-store it in one of seven sequential files. The probability density distribution of samples versus velocity for each channel are printed for immediate review. It is then decided whether to store or scrap the run and the start of the next run is awaited. Currently, 20,000 samples of each channel are stored as contiguous 100-word blocks. The disk handler automatically caters for occasional disk writing errors or data area overflows by requesting the next sector. If the resulting delay is such that the LV buffer is caused to overflow, the run is automatically terminated and restarted from the beginning. This is necessary to preserve the time continuity of the data.

If the Univac 418 is ready to retrieve data,

when a file is completed on the disk, it is re-called, reformatted and stored on digital magnetic tape. The reformatting at this point discards all data beyond three standard deviations from the mean and recomputes the mean velocity. The data format is also changed from the two-word format of Figure 24(a) to the three-word format of Figure 24(b). The mean of this data for each channel is printed for comparison with that of the raw data.

When a data tape is available for processing, the operator prepares a data card indicating which data set on the tape to process and the parameters associated with the processing and initializes the processing. During processing, if further runs are completed, the processing is suspended to retrieve and store the data.

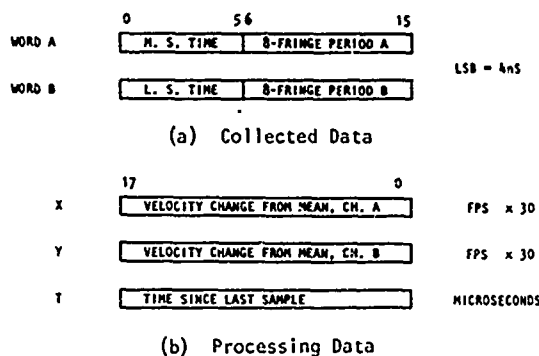


Fig. 24 Data Word Formats

IV-4.4 Results

In order to establish the validity of the system design and operation, a number of major functional tests have been performed.

The first of these was used during the development of the data analysis software before the electronics and data acquisition portions were available. It involved supplying the data analysis program with a data tape simulating the information on two LV channels. This simulated data was also used in a study of the effect of reduced measurement accuracy on the resulting spectra.

The second test included the electronics by applying specific frequency modulated signals to the data channel input and using the jet seeding and particle detection to provide a "natural" random sampling of this signal. The carrier frequency provided a simulated mean flow velocity, and the modulating signal represented flow perturbations about that mean.

The third functional test was performed using the complete LV system on a small jet excited by a loudspeaker. The results of the second and third tests were combined in a study of the effect of data rate upon the measured mean velocity.

The LV was then exercised in a number of configurations in the laboratory and the spectra compared with those from a hot-wire anemometer. The results are included in this section.

IV-4.4.1 Simulated Data

A digital program was written to prepare a data tape with characteristics similar to those to be produced by the data acquisition system operating on real jet turbulence. This simulation program was used to generate the input to and output from a linear filter with frequency characteristics similar to those expected of the data. The input to this filter was a pseudo-random binary sequence whose power spectrum approximates that of white noise in the frequency range of interest and the complete process of generating the input signal and simulating both the filter and Poisson sampling process was performed in the same program. The theoretical characteristics of the filter and its digital simulation are shown on Figure 25. The detailed derivation of the filter, the relationship between the filter input and output signals and the simulated sampling process are given in Appendix IV-A. The curves showing the auto-correlation function and power spectral density of each channel, the cross-correlation function and cross-spectral density between channels and the histograms of the time between samples are shown in Figure 26. Figure 26 (a) and (b) show the auto-correlation and power spectral density of the pseudo-random binary signal which closely approximates that of white noise. Figures 26(c) and (d) show the cross-correlation function and cross-spectral density which approximate the impulse response and complex frequency response of the filter model, the latter added to Figure 26(d) for comparison. Figures 26(e) and (f) show the auto-correlation and power spectral density of the filter output; the latter adequately approximates the squared magnitude of the filter frequency response (superimposed on the curve) above 300 Hz. Figure 26(g) shows the histogram of the time between particles indicating the typical Poisson distribution.

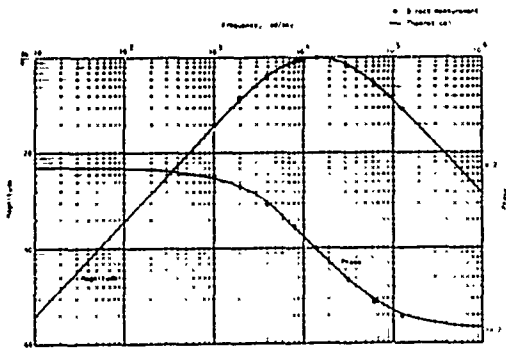


Fig. 25 Digital Filter Frequency Response

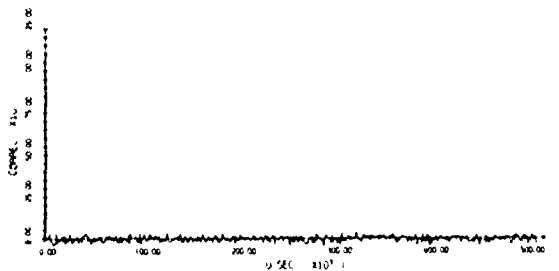


Fig. 26(a) Synthetic Data - Filter Input Auto-correlation

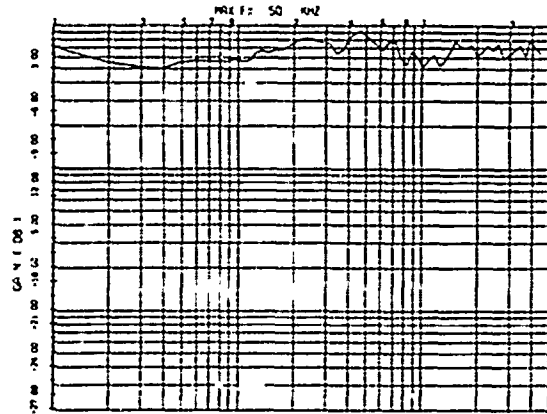


Fig. 26(b) Synthetic Data - Filter Input Power Spectrum

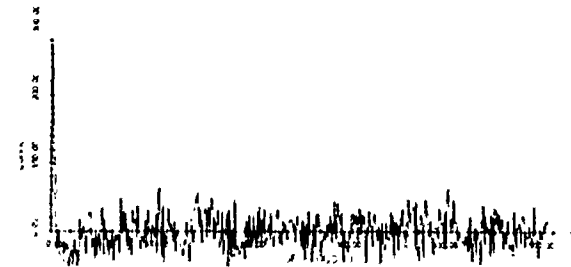


Fig. 26(c) Synthetic Data - Filter Cross-correlation

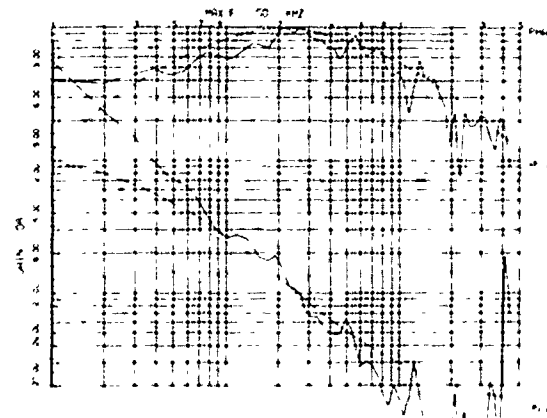


Fig. 26(d) Synthetic Data - Filter Cross Spectral Density

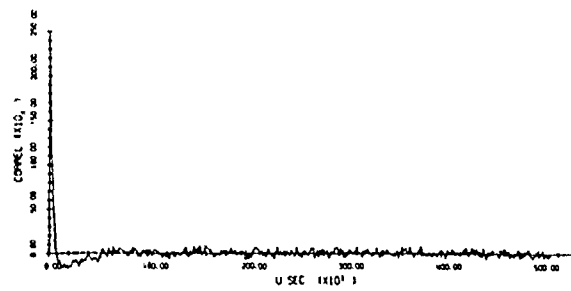


Fig. 26(e) Synthetic Data - Filter Output Auto-correlation

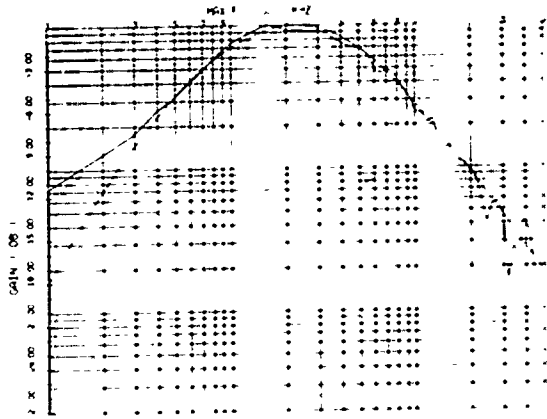


Fig. 26(f) Synthetic Data - Filter Output Power Spectrum

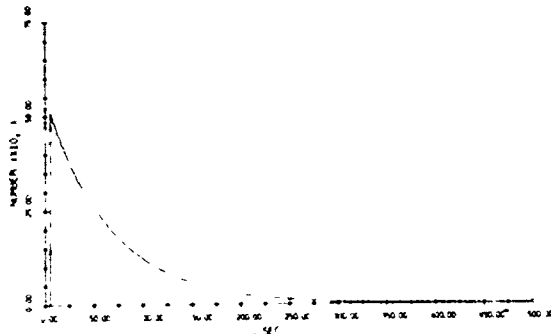


Fig. 26(g) Synthetic Data - Histogram of the Time Between Samples

IV-4.4.2 Data Amplitude Inaccuracy

A small temporary patch was added to the analysis program to allow a variable number of the low-order bits of the velocity samples to be masked out without changing the mean flow velocity. One hundred sixty records from the synthetic data discussed in Paragraph IV-4.4.1 giving a minimum correlation function count of 1042 samples per grid point were used as the test data set and Figure 27 shows the result of successively removing an increasing number of data bits. The original synthetic data was designed to contain as many bits of significance as actual measurements under typical conditions — velocity deviations of 100 fps providing twelve bits of accuracy. The curves show that while the spectrum above 2 kHz remains virtually unchanged, the low-frequency end is progressively destroyed by removing up to 10 of the twelve bits of significance in the data.

IV-4.4.3 Frequency Modulation Inputs

In order to provide accurate calibration of the complete data sampling and analysis procedures, an experimental configuration was established for replacing the particle signal input with the signal from an FM oscillator. The particle detection logic was retained to provide the real sampling intervals and the experimental seeded jet was run during the tests giving mean sample rates between 5,000 and 10,000 particles per second. Figure 28

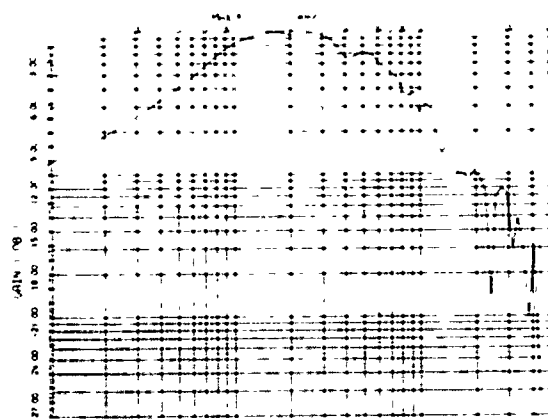


Fig. 27(a) Accuracy Study - 0.1% Reduction

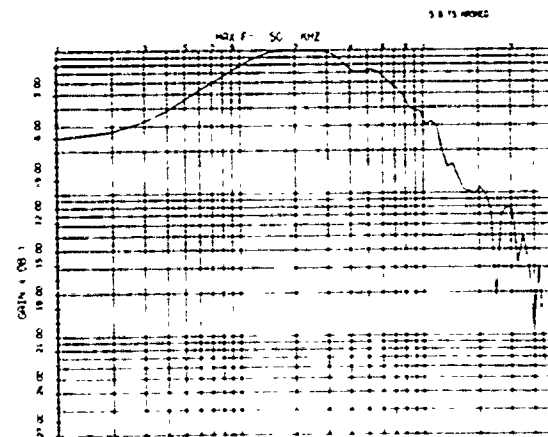


Fig. 27(b) Accuracy Study - 0.8% Reduction

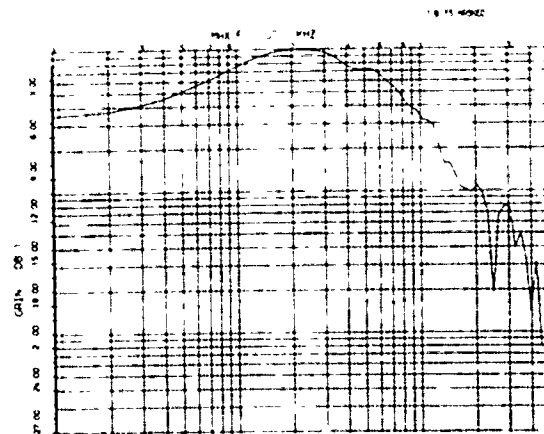


Fig. 27(c) Accuracy Study - 3.1% Reduction

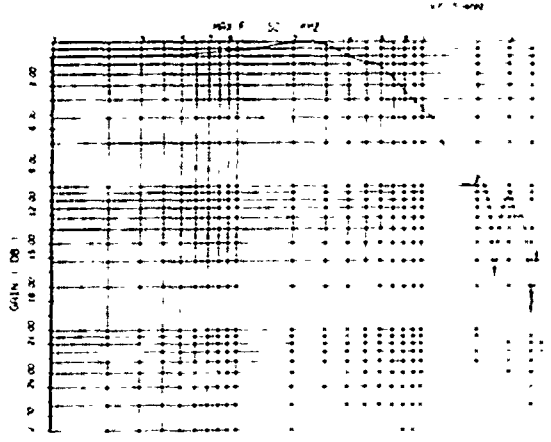


Fig. 27(d) Accuracy Study - 12.5 Reduction

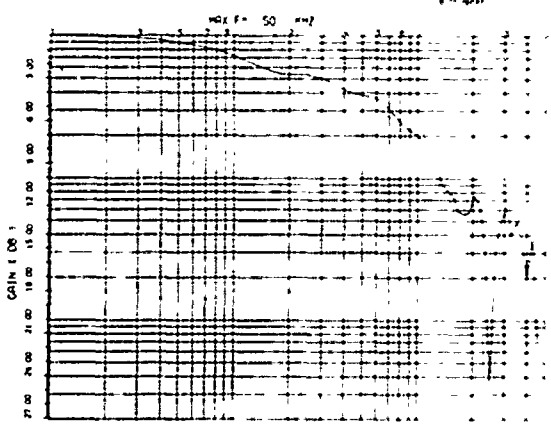


Fig. 27(e) Accuracy Study - 25 Reduction

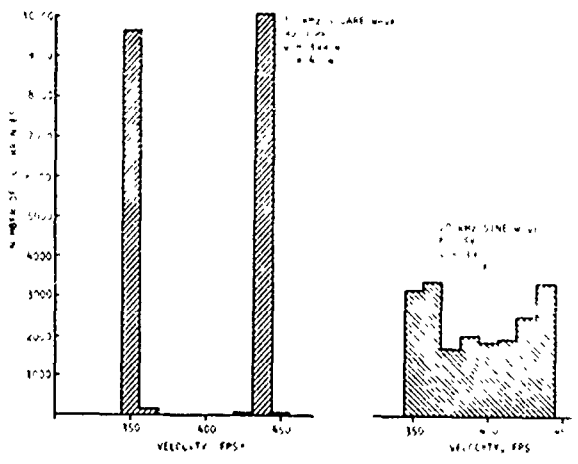


Fig. 28 10 kHz Square Wave, 20 kHz Sine Wave
 Mean = 399.4, $\sigma = 40.4$, Mean = 395.4,
 $\sigma = 25.6$, Velocity Sample Distributions

shows the means and distribution of velocity samples returned to the teletype as soon as the run was completed for two of the signals. The center frequency of the signal was 12.4 mHz which converts to a simulated mean velocity of 398.7 fps. The curve for the square wave shows the expected dis-

tribution of samples at the extremes of the velocity excursion from the mean while that for the sine wave approximates the theoretical double-peaked amplitude distribution of a sinusoidal disturbance.

In total, the results of seven runs are shown on figure 29. A caption is included on each figure listing the conditions of each run and the data presented at the teletype after the run was completed. Figures 29(a) and 29(b) show the computed spectrum and correlation function of the 500 Hz sine wave excitation. The correlation function closely approximates a cosine wave with the value of 0.99, indicating the exact rms value of the perturbation, 680 (fps), and the spectrum indicates a peak with the correct value with a bandwidth of approximately 200 Hz as predicted by the characteristics of the Hamming window function. Figures 29(c) and 29(d) show the results of a 1 kHz square wave excitation for which the correlation function should be the triangular wave indicated.

Classical Fourier series theory indicates that the spectrum due to this should have the odd harmonics present at amplitudes 9.5, 14, 17 and 19 dB below the fundamental, and these values are closely approximated on the spectrum. Figures 29(e), 29(f), and 29(g) show the results due to a 5 kHz sine wave including the distribution of time between samples typical of all this sequence of runs showing a mean sample rate of approximately 6 kHz. As discussed in Paragraph IV-4.1, in order to reduce the density of data on the log-log plot of the spectra, a simple zone averaging is employed which for smooth spectra is significant, but reduces the amplitude of spikes which occur in the smoothed region. The curves of Figures 29(e), 29(h) and 29(i) show increasing evidence of this as the frequency (and therefore data density) increases. In order to verify that the amplitude ratios in the spectrum due to the 10 kHz square wave were correct out to the limit of the analysis, reference was made to the original linear amplitudes of the spectrum which showed values of 197, 18.6 and 6.7 at 10 kHz, 30 kHz and 50 kHz respectively representing ratios of 10 dB and 15 dB from the fundamental on the log-log scale.

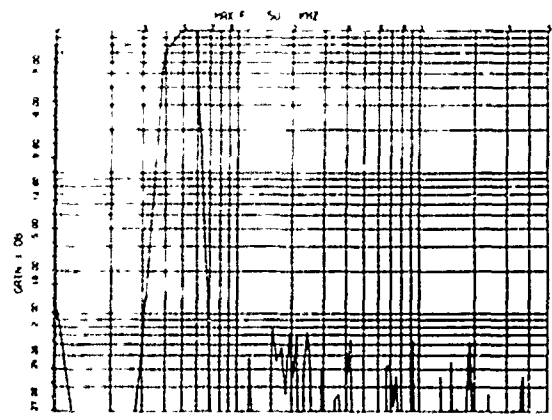


Fig. 29(a) FM Excitation - 500 Hz Sine Wave Spectrum, Mean = 406.1, fp, $\sigma = 25.6$

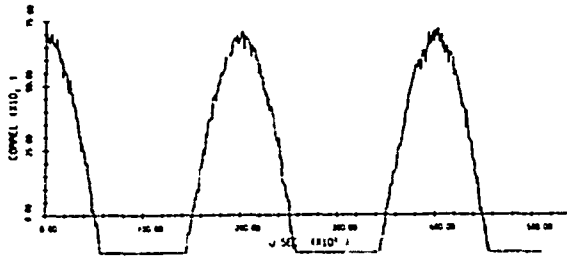


Fig. 29(b) FM Excitation - 500 Hz Sine Wave Correlation

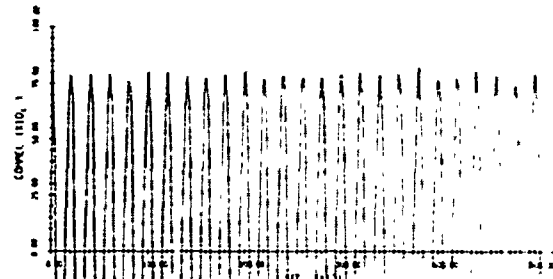


Fig. 29(f) FM Excitation - 5 kHz Sine Wave Correlation

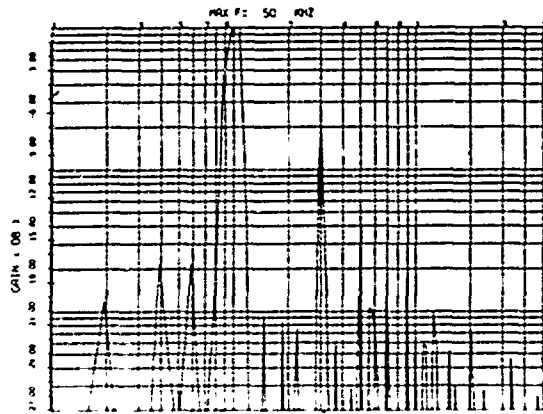


Fig. 29(c) FM Excitation - 1 kHz Square Wave Spectrum, Mean = 407.1 fps, σ = 36.2

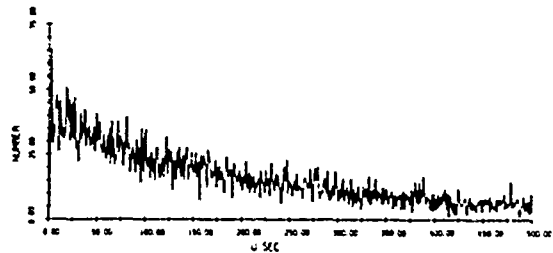


Fig. 29(g) FM Excitation - 5 kHz Sine Wave Histogram of Time Between Samples

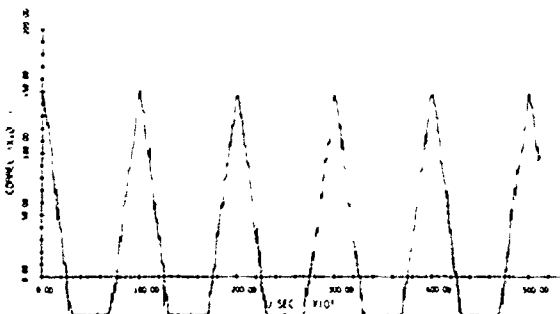


Fig. 29(d) FM Excitation - 1 kHz Square Wave Correlation

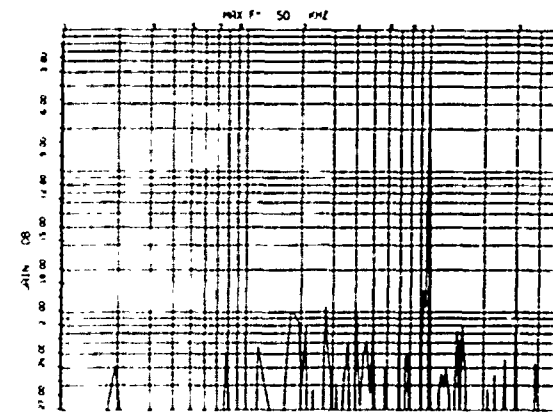


Fig. 29(h) FM Excitation - 10 kHz Square Wave Spectrum, Mean = 399.3 fps, σ = 40.4

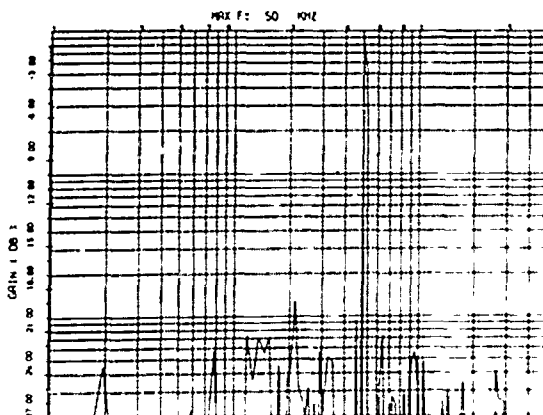


Fig. 29(e) FM Excitation - 5 kHz Sine Wave Spectrum, Mean = 407.3 fps, σ = 25.6

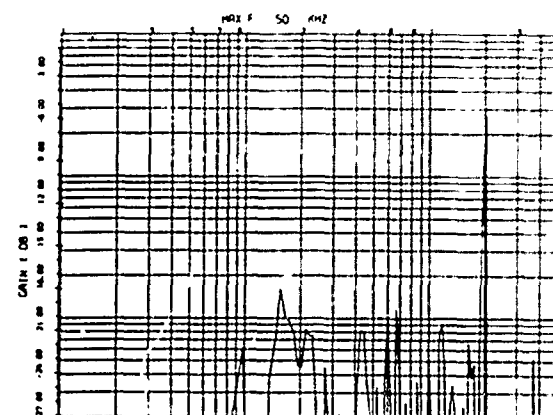


Fig. 29(i) FM Excitation - 20 kHz Sine Wave Spectrum, Mean = 395.3 fps, σ = 25.6

IV-4.4.4 Loudspeaker-Excited Jet

The test configuration used was a small compressed-air jet with a plenum chamber to which a 100-watt acoustic driver was connected. The jet was run at a mean velocity of 403 fps and LV runs taken at various excitation frequencies and amplitudes. Two typical spectra resulting from these runs are shown as Figures 30(a) and 30(b) representing excitation at 850 and 4400 Hz respectively. The power spectrum resulting from the unexcited jet is shown on Figure 30(c). As expected, the results indicate that spikes, at the excitation frequencies, have been added to the normal jet turbulence spectrum.

IV-4.4.5 Effects of Data Rate

One of the major contributions of the laser velocimeter software analysis program has been its verification of the fact that with random-time sampling and single-particle detection, power spectra can be computed with frequency content much higher than the mean rate of collection of the data. In principle at least, if the sampling process is purely Poisson, arbitrarily low data rates may be used, and the same power spectra will eventually result. Practical considerations of the stability of the flow being measured, the requirement to record the time between samples with a finite word length and the overall time to perform the experiment put a lower bound on the possible mean rate. Other considerations concerned with the probability of two particles appearing in the measurement volume and the rate at which data can be accumulated place an upper bound on the usable mean data rate. Between these bounds, it has been established that power spectra for certain classes of perturbation about steady flow can be measured. The relationship between the variability of power spectra and the rate at which data is taken will be pursued when more experimental data is available.

One question about which there has been some concern is whether the measured mean flow velocity is biased by the existence of more velocity samples higher than the mean than samples lower than the mean. This is related to the question of whether one should use the arithmetic mean velocity of each particle or compute the mean time to cross the measurement volumes and use it to compute a mean velocity (the harmonic mean velocity). Appendix IV-8 represents a somewhat simplified theoretical argument which indicates that the use of the arithmetic mean is equivalent to assuming that the flow perturbation is a purely compressible phenomenon whereas using the harmonic mean implies a totally incompressible flow. The discussion then reduces to the physical description of the behavior of the flow during the perturbation being measured.

An analysis made in an attempt to shed some light upon this discussion produced some interesting results. A small program was written to subdivide the samples taken on a selected run into groups of 30 and compute the mean velocity of each group and the mean rate at which the group of data were accumulated. The data were plotted as mean velocity against data rate as shown in Figure 31, and it was observed that there was a small gradient apparent in the data grouping equivalent to a correlation between sample mean and data rate. The program was expanded to include a least-squares fit

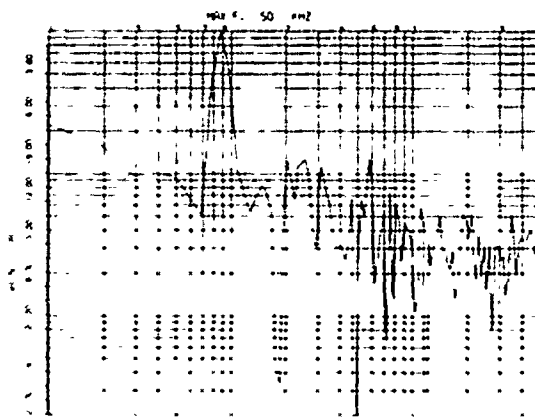


Fig. 30(a) Loudspeaker-Excited Jet - 850 Hz,
Mean = 403.8 fps, $\sigma = 57.2$

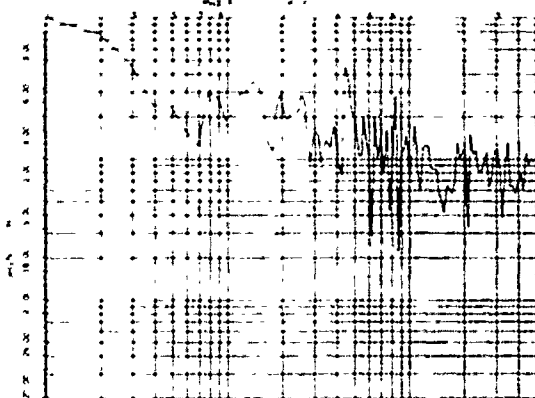


Fig. 30(b) Loudspeaker-Excited Jet - 4400 Hz
Mean = 402.1, $\sigma = 54.3$

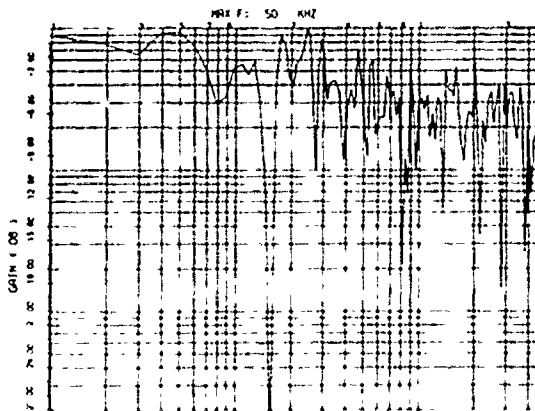


Fig. 30(c) Unexcited Jet, Mean = 404.2 fps,
 $\sigma = 44.3$

to a straight line and run for two series of similar measurements in the 0.25 inch jet. The first series was the set of data using an acoustic driver as described in Paragraph IV-4.4.4 and the second, the frequency modulation inputs described in Paragraph IV-4.4.3 where the data format and sample distribution were unchanged but the actual physical sampling process was removed. Figure 32 is a tabu-

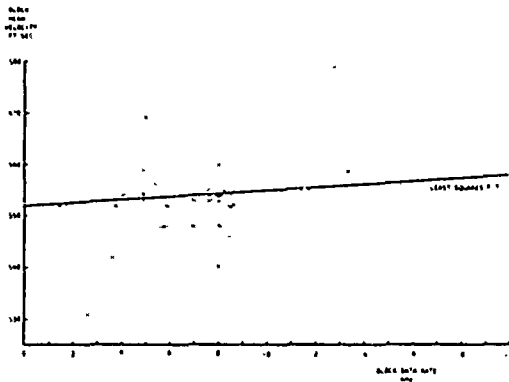


Fig. 31 Mean Velocity vs Data Rate for Blocks of 30 Samples

Run ID	Least Square Slope Loudspeaker Runs
24-2	0.3004×10^{-3}
24-3	0.2317×10^{-3}
24-4	0.7038×10^{-3}
24-5	0.7626×10^{-4}
26-6	0.2857×10^{-3}
24-7	0.2765×10^{-3}
24-8	0.1958×10^{-3}
25-1	0.9862×10^{-4}
25-3	0.5063×10^{-4}
25-4	0.1291×10^{-3}
Mean Slope	0.2348×10^{-3}

Run ID	Least Square Slope Frequency Modulation Runs
22-6	0.3799×10^{-4}
22-7	-0.2079×10^{-4}
22-4	0.5439×10^{-6}
22-5	-0.4375×10^{-4}
22-9	-0.1082×10^{-3}
23-1	0.7076×10^{-4}
23-2	0.3406×10^{-4}
Mean Slope	-0.3673×10^{-5}

Fig. 32 Table of Least Squares Slopes

lation of the results of these two studies. The studies were then repeated using the harmonic mean velocity in place of the arithmetic mean without significant change in the results.

The results of this study show that even when the data flows relatively smoothly, there are large variations in the rates at which small groups of data are accumulated, ranging from under 500 Hz to almost 20 kHz at a nominal rate of approximately 8 kHz. Within these samples, if the complete seeding and sampling procedure is used, there is a small positive correlation between the mean velocity of a sample and the rate at which the sample was taken. This correlation amounted to approximately 1% of the mean velocity over the extremes of the data rates sampled and was not materially affected by computing the harmonic mean velocity. It was, however, removed by performing analysis on data taken with the sampling process detached from the velocity measurement. This indicates that there is indeed some phenomenon in the LV sampling process which correlates data rate with measured velocity.

IV-4.4.6 Comparison with Hot-Wire Anemometer

The first measurements comparing the LV with a hot-wire anemometer were taken in a jet with 0.63 inch diameter driven by compressed air. Although the flow characteristics in such a jet are not sufficiently predictable for rigorous comparison, measurements were made on the axis of the jet two diameters from the nozzle with both a hot-wire anemometer and a single LV channel, each oriented at 45° to the mean velocity.

The hot wire measured a mean speed of 360 fps at the 45° axis which resolves to an axial mean speed of 508 fps. The velocity sample distribution from the LV is shown in Figure 33 and the power spectra measured by each method are compared on Figure 34. The bandwidth of the filter used on the hot-wire spectrum analyzer was 100 Hz.

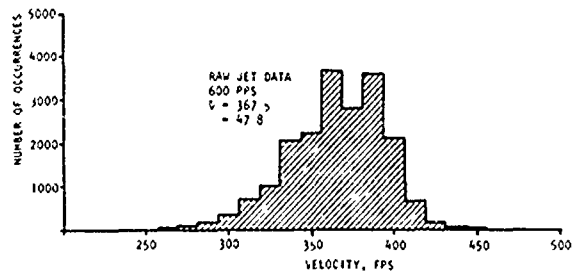


Fig. 33 Hot-Wire Comparison - Velocity Sample Distribution

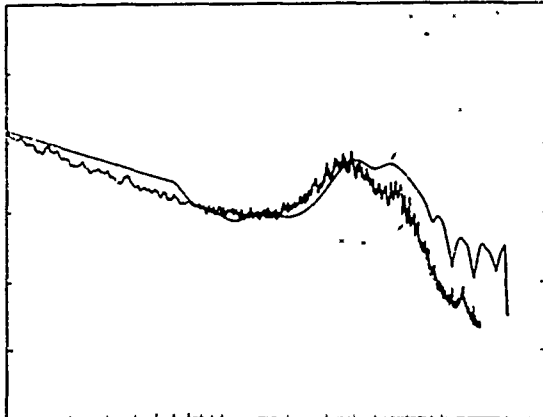


Fig. 34 Hot-Wire Comparison - Power Spectral Density, Mean = 367.5 fps, $\sigma = 47.8$

IV-5 Conclusions

The laser velocimeter has been proven to be able to provide a method of measuring not only instantaneous and mean velocities and turbulence intensity but also power spectra over a broad band of frequencies. Paragraph IV-3.6 (System Specifications) summarizes the system hardware capabilities and defines data which may be obtained as system outputs.

The major technological challenge during this contract period was in achieving turbulence spectrum in the LV over a range of frequencies from low frequency up to 20,000 Hertz. It was determined early in this development program that the method of deriving power spectra would not be by way of reconstructing the time history of the turbulent flow. To derive satisfactory power spectra by this means would require a sampling rate of approximately 4 MHz which of course is totally unacceptable. By resorting to correlation processes, it has been proved to be possible to achieve power spectra with bandwidths of 20,000 Hz with sample rates of only 5 to 10 kHz.

This has been validated by three methods. First, the total electronics, computer, and computer software were simultaneously checked to determine the bandwidth of the total system, independent of flow or particle characteristics. The results of this test showed that the system was capable of measuring power spectrum up to at least 50,000 Hz and down to 300 Hz, the low frequency limit being determined by FFT frequency spacing (see Paragraph IV.4.4.3). The second validation of the system involved not only the system characteristics but the characteristics of the flow and particles as well. In this case, a small jet was modulated by a loudspeaker using single frequency tones. In each case the tones were readily identified within the processed spectrum (see Paragraph IV.4.4.4). The third method of validation was a comparison with hot-wire data. The laser velocimeter data compared quite well with the hot-wire data (see Paragraph IV.4.4.6). The small jet used in making these comparisons contained a significant frequency content out to approximately 10 kHz.

A major area of study during the second half of the contractual period will be to complete investigation into the effects of particle response on the computed power spectrum. Since the laser velocimeter system has been validated in its performance out to 50 kHz, it would be practical to evaluate particle response through theoretical investigations and a series of laboratory experiments. The results of spectrum measurements in different conditions show a frequency range limited more by the power at each frequency than by any absolute frequency value. A "white noise" level occurs between 20 and 24 dB below the peak frequency level masking any significant information below that. The cause of this phenomenon and techniques for reducing the level and minimizing its effect remain to be investigated.

The effects of various parameters associated with the system have been studied. Those aspects of classical signal analysis related to window functions which apply to this analysis are presented in this report. On practical data from the test jets considered, the Hamming window without arithmetic smoothing has been used with most success. The difference between this window and those due to Hann and Bartlett is not, however, large on this type of data. A study to determine the effects of inaccurate measurement of the velocity produced some surprising results. While the measured standard deviation of velocity and the high-frequency end of the spectrum were unchanged with data limited in accuracy up to 25%, the low frequency end of the spectrum displayed a marked change raising the relative power below 2 kHz. This effect is somewhat complicated by the change of mean velocity which would affect the very low frequency components but remains a significant measure of the effect of inaccurate data upon the power spectra. A third study, investigating the relationship between the rate at which a set of velocity samples was taken and the mean of the sample, also produced surprising results. It showed that for a series of runs taken in a small jet the mean rate at which sets of 30 samples were taken varied from under 500 to almost 20,000 per second. It also showed that there was a small positive correlation between the rate at which the samples were taken and the mean velocity of the sample. On average, this was approximately 2% of the mean velocity over the extremes of the rate distribution. Further study of this phenomenon is also required.

After absolute calibration runs on the test stand have been completed, the LV system will be ready to record jet characteristics throughout the operational regime of the facility.

IV-6. Acknowledgements

The completion of this system would have been impossible without the efforts of a large number of dedicated people in the Lockheed-Georgia Company. Special mention is made of J. H. Ivester and E. C. Mills for their creative ingenuity in designing the electronics; of C. R. Huie in his support of the laser, seeding and optics; of P. D. Dean and L. Mazarella in providing advice, support and data related to hot-wire anemometry.

References

1. Stevenson, W. H., Redijo, M. K. and Zamitt, R. E., "Bibliography on Laser Doppler Velocimeters: Theory, Design and Applications," Laser Doppler Velocimeter Workshop, Purdue University, March 1972.
2. Lorens, C. S., "Recovery of Randomly Sampled Time Sequences," Correspondence with IRE Transactions on Communications Systems, April 1962.
3. Berman, N. S., "Particle Fluid Interaction Corrections for Flow Measurement with a Laser Doppler Flowmeter," NASA CR-124254.
4. Melling, A., "Scattering Particles for Laser Anemometry in Air," Imperial College of Science and Technology, ET/TN/B/7 (1971).
5. Born, M. and Wolf, E., "Principles of Optics," Fourth Edition, Pergamon Press, New York, 1970.
6. Allen, J. B., "Estimation of the Frequency of Laser Velocimeter Signals," Ph.D. Dissertation Georgia Institute of Technology, January 1973.
7. George, W. K., "An Analysis of the LDV and Its Application to the Measurement of Turbulence," Ph.D. Thesis, John Hopkins University (1971).
8. Dunrani, T. S. and Gneoted, C. A., "Statistical Analysis and Computer Simulation of Laser Doppler Velocimeter Systems," IEEE Trans. on Inst. and Meas. Vol. IM-22, No. 1, (1973).
9. Mayo, W. T. Jr., Laser Doppler Flowmeters - A Spectral Analysis, Ph.D. Dissertation, Georgia Institute of Technology, May 1969.
10. Mayo, W. T., Jr., Shay, M. T., and Riter, S. "An Introduction to the Estimation of Power Spectra from Single Particle LDV Data," presented at the Oklahoma State University Workshop on Laser Anemometry, June 11, 1973, Stillwater, Okla. See also final Report USAF Arnold Engineering Development Center Contract F40-600-73-C0003.
11. Brigham, E. O. and Morrow, R. E., "The Fast Fourier Transform," IEEE Spectrum, Dec., 1967.
12. Blackman, R. B. and Tukey, J. W., "The Measurement of Power Spectra from the Viewpoint of Communications Engineering," Dover, New York, 1959.
13. Kuo, Benjamin C., "Analysis and Synthesis of Sampled Data Control Systems," Prentice-Hall, 1963.
14. Nixon, F. E., "Principles of Automatic Controls," McMillan, 1958
15. Golomb, Solomon W., "Digital Communications with Space Applications," Prentice-Hall, 1964.
16. Papoulis, A., "Probability, Random Variables, and Stochastic Processes," McGraw-Hill, 1965.

APPENDIX IV-A

Simulated Data Model

The first step in the simulation process is writing a data tape containing two channels of data whose individual and combined statistics are known. The signals selected were the input to and output from the digital model of a linear filter.

IV-A.1 Filter Model Characteristics

The particular filter used was selected to provide a spectrum similar to that expected from the LV:

$$H(S) = \frac{KS}{(S+a)(S+b)}$$

with a gain K of 37700 and break frequencies a and b of 1000 Hz and 5000 Hz, or 6283 rad/sec. and 31416 rad/sec. The frequency response of this filter is shown on Figure 25.

The digital model of this filter was created by using the z-transform technique fully described in Reference 13. The results of this are summarized as follows:

We require H(S) combined with a zero-order hold:

$$H_0(S) = \frac{1}{S} (1 - e^{-TS})$$

where T, the sampling period, is 1 μ S.

$$\begin{aligned} H(Z) &= \sum H_0(S) H(S) \\ &= \frac{K(1 - e^{-TS})}{(S+a)(S+b)} \end{aligned}$$

from tables in Reference 13,

$$H(Z) = \frac{K(1 - e^{-TS})}{b-a} \left[\frac{Z}{Z - e^{-aT}} - \frac{Z}{Z - e^{-bT}} \right]$$

$$\frac{a_1 Z^{-1} + a_0 Z^{-2}}{b_0 + b_1 Z^{-1} + b_2 Z^{-2}}$$

where $a_1 = K(e^{-aT} - e^{-bT}) / (b-a)$

$$a_0 = -a_1$$

$$b_0 = 1$$

$$b_1 = (e^{-aT} + e^{-bT})$$

$$b_2 = e^{-(a+b)T}$$

If x(t) and y(t) are the input to and output from this filter whose sampled histories have Z-transforms X(Z) and Y(Z), these are related to H(Z) by the expression

$$Y(Z) = H(Z) X(Z).$$

by taking the inverse Z-transform and inserting the

expression for $H(Z)$, we obtain

$$b_0 y_n + b_1 y_{n-1} + b_2 y_{n-2} = a_1 x_{n-1} + a_2 x_{n-2}$$

where x_n and y_n are the values of $x(t)$ and $y(t)$ sampled at time nT . From this expression, an algorithm was derived for computing y_n given the two previous values of x and y :

$$y_n = \frac{a_1}{b_0} x_{n-1} + \frac{a_2}{b_0} x_{n-2} - \frac{b_1}{b_0} y_{n-1} - \frac{b_2}{b_0} y_{n-2}$$

Figure A-1 shows the values of y_n plotted when the inputs are

- (a) $x_1 = 10000, x_i = 0, i \neq 1$
- (b) $x_i = 1$ if $i \geq 0, x_i = 0, i < 0$
- (c) $x_i = iT$ if $i \geq 0, x_i = 0$ for $i < 0$
- (d) $x_i = \sin(i f)$ for $i > 0, = 0$ for $i < 0$
where $f = i0,000T$ radians.

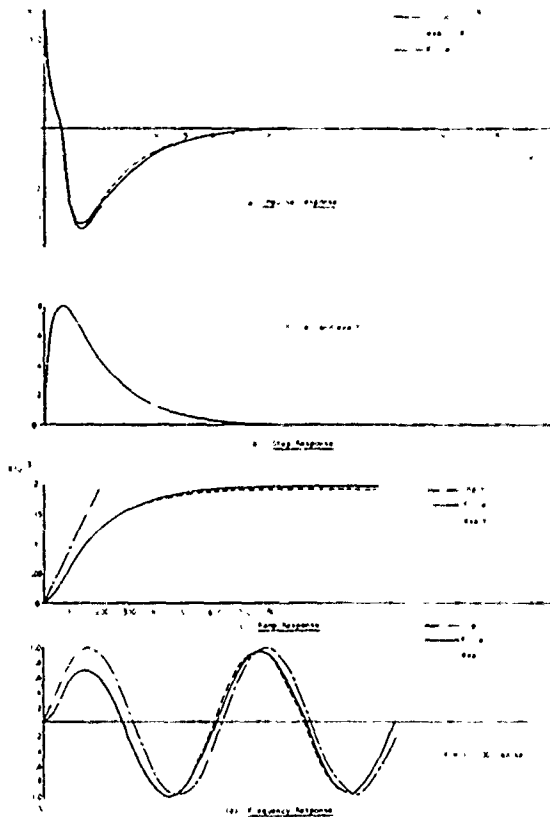


Fig. A-1 Filter Characteristics

Also plotted on the same charts are the responses of the linear filter $H(S)$ computed from tables in Reference 14:

$$\text{Impulse response: } g_i(t) = \frac{K(b e^{-bt} - a e^{-at})}{b-a}$$

$$\text{Unit step response: } g_s(t) = \frac{K(e^{-at} - e^{-bt})}{b-a}$$

$$\text{Ramp response: } g_r(t) = \frac{K}{ab} \left(1 + \frac{b e^{-at} - a e^{-bt}}{a-b} \right)$$

Frequency response at frequency ω_1 :

$$g_f(t) = \frac{AT_1 \omega_1^2 e^{-t/T_1}}{(T_2 - T_1)(1 + T_1^2 \omega_1^2)} - \frac{AT_2 \omega_1^2 e^{-t/T_2}}{(T_2 - T_1)(1 + T_2^2 \omega_1^2)} + \frac{A \omega_1^2 \cos(\omega_1 t - \psi)}{(1 + T_1^2 \omega_1^2)(1 + T_2^2 \omega_1^2)}$$

where

$$A = \frac{K}{ab\omega_1}, T_1 = 1/a, T_2 = 1/b,$$

$$\psi = \tan^{-1} T_1 \omega_1 + \tan^{-1} T_2 \omega_1$$

IV-A.2 Selection of Input Waveform

In order that the filter output signal should have a known power spectral density, it was decided that the input to the filter should be band-limited white noise. One form of white noise which is very conveniently generated on a digital computer is a pseudo-random binary sequence whose generation and properties are described in Reference 15. The particular sequence used was the 16-bit maximum-length sequence generated by feeding back bits 10, 12, 13 and 15 of a 16-bit register. The binary signal resulting from observing any bit of this register and setting $x_n = 1$ if the bit is 1 and $x_n = -1$ if the bit is zero is a periodic signal with period T' given by

$$T' = (2^{16} - 1) T$$

where T is the clock period of the register.

The auto-correlation function for this signal is defined by the relation

$$R(\tau) = \frac{1}{T'} \int_{-T'/2}^{T'/2} X(t) X(t+\tau) dt$$

It can be shown (Ref. 15) that this is evaluated as

$$R(\tau) = (1 - \tau/T) \quad \text{for } \tau \leq T$$

$$= -1/N \quad \text{for } \tau > T$$

where N is the number of samples period, $2^{16} - 1$ in this case. This function is diagrammed on Figure A-2.

The power spectrum of this signal is quoted in Reference 15 as:

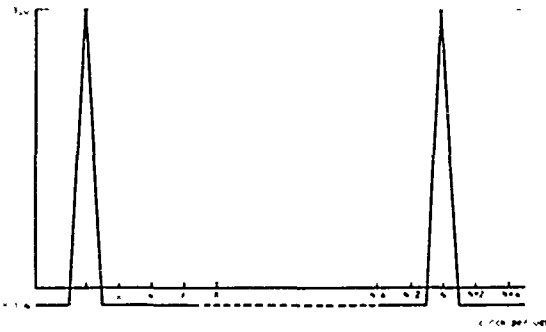


Fig. A-2 Auto-correlation Function of a Pseudo-Random Binary Sequence

$$\phi(\omega) = \frac{(N+1)}{N^2} \frac{\sin(\frac{\omega T}{2})^2}{\frac{\omega T}{2}} \sum_{\substack{n=-\infty \\ n \neq 0}}^{\infty} \delta(\omega - \frac{2\pi n}{NT}) + \frac{1}{N^2} \delta(\omega)$$

where $\delta(t)$ is the Dirac delta function. This is a line spectrum with frequencies at multiples of the fundamental frequency

$$\omega_0 = \frac{2\pi}{NT}$$

Evaluating this in the frequency range of interest and noting that the basic frequency ω_0 is 96 rad/sec. and the maximum frequency of interest is 10^6 rad/sec., we assume the spectrum to approximate a continuous spectrum with a constant level of $1/N$ except at $\omega = 0$ where it is zero.

The maximum error in this assumption is at the highest frequency where $\alpha = \omega T/2 = 0.5$ and $\sin \alpha/\alpha = .927$ giving an error of $1 - (.927)^2 = 14\%$.

Similarly, if NT is very large in comparison with the system response time, the auto-correlation function may be approximated by the Dirac delta function:

$$R(\tau) = \frac{1}{N} \delta(\tau)$$

In the system selected, Figure A-1 shows the filter response to be stable after less than 1 mS, which is small compared to the 65 millisecond sequence period, thus justifying the above assumptions.

IV-A.3 Filter Input and Output Relationship

Reference 15 lists the standard input-output relationships for a linear system. If $x(t)$ and $y(t)$ are the input and output of a filter, $h(t)$ its impulse response, and $H(\omega)$ its frequency response, $h(t)$ and $H(\omega)$ are related by the Fourier transform pair

$$h(t) = \frac{1}{2\pi} \int_{-\infty}^{\infty} H(\omega) e^{i\omega t} d\omega$$

$$\text{and } H(\omega) = \int_{-\infty}^{\infty} h(t) e^{-i\omega t} dt$$

Similarly, the Wiener-Khintchine relations for auto-correlation $R(\tau)$ and spectral density $S(\omega)$ are the transform pair

$$R(\tau) = \frac{1}{2\pi} \int_{-\infty}^{\infty} S(\omega) e^{i\omega \tau} d\omega$$

$$\text{and } S(\omega) = \int_{-\infty}^{\infty} R(\tau) e^{-i\omega \tau} d\tau$$

The output of a linear system is related to its input by the following conversion:

$$y(t) = \int_{-\infty}^{\infty} x(t-\theta) h(\theta) d\theta$$

We will use the result derived above that the auto-correlation function of $x(t)$, the pseudo-random binary signal, is a series of impulse functions occurring at such a low frequency that each system response to that stimulus may be treated in isolation. The suffix xx is added to indicate the correlation of x with x :

$$R_{xx}(\tau) = \frac{1}{N} \delta(\tau)$$

whose power spectral density is then given by

$$S_{xx}(\omega) = \frac{1}{N} \quad \text{A-3.1}$$

in the frequency range of interest.

The output auto-correlation function and power spectral density are standard deviations:

$$R_{yy}(\tau) = \int_{-\infty}^{\infty} \int_{-\infty}^{\infty} h(\theta) h(\mu) R_{xx}(\tau - \mu + \theta) d\mu d\theta \quad \text{A-3.2}$$

$$\text{and } S_{yy}(\omega) = H(\omega)^2 S_x(\omega) \quad \text{A-3.2}$$

The cross-correlation and cross-spectral densities may also be derived as follows from the definition of auto-correlation:

$$R_{xy}(\tau) = \lim_{T \rightarrow \infty} \frac{1}{T} \int_{-T/2}^{T/2} x(t) y(t+\tau) dt$$

Substituting for $y(t+\tau)$:

$$R_{xy}(\tau) = \lim_{T \rightarrow \infty} \frac{1}{T} \int_{-T/2}^{T/2} x(t) \int_{-\infty}^{\infty} x(t+\tau-\theta) h(\theta) d\theta dt$$

and since x and h are continuous with respect to t , τ and θ , the order of integration may be changed:

$$R_{xy}(\tau) = \int_{-\infty}^{\infty} h(\theta) \lim_{T \rightarrow \infty} \frac{1}{T} \int_{-T/2}^{T/2} x(t) x(t+\tau-\theta) dt d\theta$$

which contains the definition of $R_{xx}(\tau-0)$

$$\therefore R_{xy}(\tau) = \int_{-\infty}^{\infty} h(0) R_{xx}(\tau-0) d0$$

With the value for R_{xx} substituted, this becomes

$$R_{xy}(\tau) = \frac{1}{N} h(\tau)$$

and by transformation,

$$S_{xy}(\omega) = \int_{-\infty}^{\infty} \frac{1}{N} h(\tau) e^{-j\omega\tau} d\tau$$

or
$$S_{xy}(\omega) = \frac{1}{N} H(\omega) \quad A-3.3$$

Equations A-3.1, A-3.2 and A-3.3 are the known relationships which the analysis program reconstructs from the random sampling process.

IV-A.4 Sampling Process Model

The assumption was made that the process of obtaining a sample of the fluid velocity in the measurement volume by detecting the presence of a particle and measuring its velocity is a Poisson sampling process with a mean sample rate λ which would be constant over any measurement run. This assumption has been adequately justified by sample distributions recorded during actual data runs [compare Figures 26(g) and 30(g)]. This means that the probability, P , that the number of velocity samples $n(T)$ occurring in time interval T is equal to k is given by

$$P \{n(T) = k\} = e^{-\lambda T} \frac{(\lambda T)^k}{k!}$$

where λ is the mean rate of arrival of samples (16). In order to simulate this sampling process correctly, we are required to know the statistics of the random variable τ' , the time between adjacent velocity samples. In particular, we wish to know the density function $f(\tau)$ which is defined as the limit of the probability that τ' lies in the small interval $[\tau, \tau + \Delta\tau]$:

$$f(\tau) = \lim_{\Delta\tau \rightarrow 0} \frac{P\{\tau \leq \tau' \leq \tau + \Delta\tau\}}{\Delta\tau}$$

This may also be regarded as the probability that time between particles is between τ and $\tau + \Delta\tau$.

The function $f(\tau)$ is derived in Reference 16 by defining a random variable Z as the time between the two particles surrounding a fixed time t_0 and showing that the density of Z is given by

$$f_z(z) = \lambda^2 z e^{-\lambda z}$$

The logic is then extended to the variable X measuring the time between any two samples where

$$f_x(x) = \lambda e^{-\lambda x}$$

The density function required for this analysis is therefore

$$f(\tau) = \lambda e^{-\lambda\tau} \quad A-3.4$$

In order to model this distribution under the added constraint that there is a minimum value for τ caused by the finite processing time of the electronics, a second random generator is created with statistics independent of that used to excite the filter. By using a portion of the storage register for this sequence, a random number with uniform distribution is obtained. This distribution may then be shaped to any desired distribution such as that of equation A-3.4 by reference to a suitable table. The numbers resulting from this generation process specify the number of samples of the filter process to be ignored before the next sample is accepted for storage. The digital filter is therefore driven regularly by a clock and sampled at intervals simulating the required Poisson process.

APPENDIX IV-B

Mean Flow Rate Calculation

We are provided with a sequence of samples V_i of a flow velocity separated by known intervals $\Delta\tau_i$ and require to compute a number of statistics of the flow including an estimate of the mean flow velocity \bar{V} . The exact expression for \bar{V} is:

$$\bar{V} = \frac{1}{T} \int_0^T V(t) dt$$

where $V(t)$ is the instantaneous flow velocity and T is the duration of the experiment.

Since the flow is sampled as described above, the simplest approximation to the sampled flow is to hold V_i constant for the period $\Delta\tau_i$. The estimated mean velocity, \bar{V}' , then becomes:

$$\bar{V}' = \frac{1}{\sum_{i=1}^N \Delta\tau_i} \sum_{i=1}^N V_i \Delta\tau_i$$

where T has been replaced by the sum of the increments of time.

It is necessary to make some assumptions about the relationship between V_i and $\Delta\tau_i$ in order to evaluate this expression.

Assumption A

If V_i and $\Delta\tau_i$ are independent random variables, it can be shown that the expected value of their product, $E(V_i \Delta\tau_i)$ is the product of their expected values $E(V_i) E(\Delta\tau_i)$ and since X ,

$$E(X) = \frac{1}{N} \sum_{i=1}^N X_i$$

then

$$\begin{aligned} \sum_{i=1}^N V_i \Delta t_i &= NE(V \cdot \Delta t) \\ &= N \cdot E(V) \cdot E(\Delta t) \\ &= \frac{1}{N} \sum_{i=1}^N V_i \sum_{i=1}^N \Delta t_i \\ \bar{V}_A^1 &= \frac{1}{N} \sum_{i=1}^N V_i \end{aligned}$$

which is the *arithmetic* mean of the sequence V_i .

Assumption B

If V_i is related to Δt_i by the expression

$$V_i \Delta t_i = K$$

where K is an arbitrary constant, the estimated mean velocity becomes:

$$\begin{aligned} \bar{V}_B^1 &= \frac{NK}{\sum_{i=1}^N \Delta t_i} \\ &= \frac{K}{\bar{\Delta t}} \end{aligned}$$

where the mean period $\bar{\Delta t}$ is given by

$$\bar{\Delta t} = \frac{1}{N} \sum_{i=1}^N \Delta t_i$$

\bar{V}_B^1 is therefore the *harmonic* mean velocity given by

$$\frac{1}{\bar{V}_B^1} = \frac{1}{N} \sum_{i=1}^N \frac{1}{V_i}$$

Physical Significance

The physical significance of assumptions A and B can be related to the characteristics of the fluid in which the particles which provide the velocity samples are suspended. If it is first assumed that the particles are mixed homogeneously with the fluid, assumption A that V_i and Δt_i are independent says that when the fluid accelerates, its density correspondingly reduces in order to prevent any correlation between V_i and Δt_i , i.e., that the flow is compressible. Assumption B that $V_i \Delta t_i$ is constant says that on average, the distance between particles and therefore the fluid density remains constant as the flow speed increases locally, an example of incompressible flow.

*Definition of the probabilities is given in Section IV-2.1.

Conclusion

It can therefore be concluded that by using the arithmetic mean of the velocity samples, one is assuming the flow to be compressible. The arithmetic mean period (or harmonic mean velocity) is used for incompressible flow.

APPENDIX IV-C

Derivation of Particle Probabilities

For any given particle density,

$$P_h + P_{nh} = 1^* \quad C.1$$

and P_h can be further divided into either good hits, P_g , in A_g or bad hits, P_b , in A_b

$$P_h = P_g + P_b \quad C.2$$

The probability of valid data is defined as the probability that particles which intercept A_g are not disturbed by a second particle and is,

$$P_v = P_g \cdot (1 - P_t) \quad C.3$$

Particles which intercept A_g but whose signals are disturbed by a second particle should be rejected by the data validation tests. The probability of these is $P_g \cdot P_t$. The bad hits, P_b , are divided into those that exceed t_m , $P_b \cdot (1 - P_m)$, and those whose count of B is completed by a second or more particles before t_m , $P_b \cdot P_m$. The total probability of these occurrences may be written as,

$$\begin{aligned} 1 &= (1 - P_h) + P_g \cdot P_t + P_g (1 - P_t) \\ &\quad + P_b \cdot P_m + P_b \cdot (1 - P_m) \end{aligned} \quad C.4$$

Assuming that the distribution of the particles in the flow is truly random, the Poisson distribution can be used to quantize these probabilities. This is a standard assumption and, as will be demonstrated later, is verified by experiment. The Poisson form is,

$$p(n; \lambda t) = e^{-\lambda t} \frac{(\lambda t)^n}{n!}, \quad C.5$$

where n is the number of particles occurring and λ the mean rate of arrival of particles per unit time, t .

The probability of a hit, P_h , is then the probability of obtaining at least one particle in the measurement space in time t_p .

$$P_h = \sum_{n=1}^{\infty} p(n; \lambda t_p) = 1 - p(0; \lambda t_p) \quad C.6$$

The probability of no hits, P_{nh} , is of course, $p(0; \lambda t_p)$.

The particle rates desired for the single particle LV necessarily restrict the hits in the measurement area to small numbers. Each one of these hits must be examined by the electronics for validity by either a frequency stability test or the t_m test. Although the time required to perform the stability test, t_d , is small compared to t_p , t_m can be either longer or shorter than the data processing period, t_p , depending on the minimum velocity required. For the experiments planned in this program, the velocities are such that we assume $t_m < t_p$.

In order to describe P_g we must consider that the system can only examine a limited number of particles during t_p . If we consider only t_m test rejects, then this number, n , is the integer value of t_p/t_m . Using the binomial notation to describe the probability that K of the n particles will pass through A_g , where the probability of any single particle passing through A_g , ($K = n = 1$), is E , we can write,

$$b(K;n,E) = \frac{n!}{K!(n-K)!} \cdot E^K(1-E)^{n-K} \quad C.7$$

where

$$P_g \Big|_{t_p/t_m} = \sum_{n=1}^{t_p/t_m} p(n;\lambda t_p) \cdot b(1;n,E). \quad C.8$$

We must also consider the probability, P_m^1 , that one particle may pass through A_b followed by another through $A_g + A_b$ before t_m . If these events were to continue throughout t_p , the number of particles which can be examined is $\approx t_p/t_d$. The probability of these events allows n to be $> t_p/t_m$ and limited by t_p/t_d . It may be expressed in binomial notation as,

$$P_m^1 = b(n - t_p/t_m;n,P_m \cdot b(n - t_p/t_m;n;1-E)). \quad C.9$$

The probability of these occurrences is,

$$P_g \Big|_{t_p/t_d} =$$

$$\sum_{n=t_p/t_m+1}^{t_p/t_d} b(n - t_p/t_m;n,P_m^1(\lambda t_m)) \cdot p(n;\lambda t_p) \cdot b(1;n,E). \quad C.10$$

Combining these equations we get the total probability of a good hit:

$$P_g = \sum_{n=1}^{t_p/t_m} p(n;\lambda t_p) \cdot b(1;n,E) + \sum_{n=t_p/t_m+1}^{t_p/t_d} b(n - t_p/t_m;n,P_m^1(\lambda t_m)) \cdot p(n,\lambda t_p) \cdot b(1;n,E). \quad C.11$$

Of these particles, only those not disturbed by a second particle may be considered as valid data as shown by equation C.3. An expression for P_t and P_m must now be derived.

P_m is the probability that two or more particles intercept the total area, $A_g + A_b$, during the maximum time gate, t_m .

$$P_m = \sum_{n=2}^{\infty} p(n,\lambda t_m) = 1 - p(0,\lambda t_m) - p(1,\lambda t_m). \quad C.12$$

Similarly P_t is the probability that two or more particles intercept the measurement area during the transit time, t_t , of one particle.

$$P_t = \sum_{n=2}^{\infty} p(n;\lambda t_t) = 1 - p(0;\lambda t_t) - p(1;\lambda t_t) \quad C.13$$

where $t_t = N_f d/V$, N_f is number of fringes in the measurement volume, d is their spacing and V is the particle velocity.